VILNIUS UNIVERSITY
CENTER FOR PHYSICAL SCIENCES AND TECHNOLOGY

Tadas
MATIJOŠIUS

Tribological investigation of biocompatible nanostructured coatings and lubricating materials

DOCTORAL DISSERTATION

Natural Sciences,
Chemistry N 003

VILNIUS 2020

This dissertation was written between 2015 and 2019 at the Department of Chemical Engineering and Technology of Center for Physical Sciences and Technology. The research was supported by Research Council of Lithuania.

Academic supervisor:
Dr. Svajus Asadauskas (Center for Physical Sciences and Technology, Natural Sciences, Chemistry, N 003)

This doctoral dissertation will be defended in a public meeting of the Dissertation Defence Panel:
Chairman – **Acad. Prof. Habil. Dr. Albertas Malinauskas** (VMTI Center for Physical Sciences and Technology, Natural Sciences, Chemistry, N 003)
Members:
Doc. Dr. Kristina Kantminienė (Kaunas University of Technology, Natural Sciences, Chemistry, N 003)
Dr. Danutė Kaušpėdienė (VMTI Center for Physical Sciences and Technology, Natural Sciences, Chemistry, N 003)
Prof. Dr. Juozas Padgurskas (Vytautas Magnus University, Technological Sciences, Mechanical Engineering, T 009)
Prof. Dr. Jaunius Urbonavičius (Vilnius Gediminas Technical University, Natural Sciences, Biochemistry, N 004)

The dissertation shall be defended at a public meeting of the Dissertation Defence Panel at 1 p.m. on 6th March 2020 in auditorium D401 of the Center for Physical Sciences and Technology.
Address: Saulėtekio av. 3, LT-10257, Vilnius, Lithuania. Tel. +370 5 264 8884; e-mail: office@ftmc.lt.

The text of this dissertation can be accessed at the libraries of Center for Physical Sciences and Technology and Vilnius University, as well as on the website of Vilnius University: www.vu.lt/lt/naujienos/ivykiu-kalendorius

VILNIAUS UNIVERSITETAS
FIZINIŲ IR TECHNOLOGIJOS MOKSLŲ CENTRAS

Tadas
MATIJOŠIUS

Tribologiniai tyrimai įvertinant biosuderinamų nanostruktūrinių dangų bei tepamųjų medžiagų savybes

DAKTARO DISERTACIJA

Gamtos mokslai,
Chemija N 003

VILNIUS 2020

Disertacija rengta 2015–2019 metais Fizinių ir technologijos mokslų centre Cheminės inžinerijos ir technologijų skyriuje. Mokslinius tyrimus rėmė Lietuvos mokslo taryba.

Mokslinis vadovas:
Dr. Svajus Asadauskas (Fizinių ir technologijos mokslų centras, gamtos mokslai, chemija, N 003)

Gynimo taryba:
Pirmininkas – **akad. prof. habil. dr. Albertas Malinauskas** (VMTI Fizinių ir technologijos mokslų centras, gamtos mokslai, chemija, N 003)
Nariai:
doc. dr. Kristina Kantminienė (Kauno technologijos universitetas, gamtos mokslai, chemija, N 003)
dr. Danutė Kaušpėdienė (VMTI Fizinių ir technologijos mokslų centras, gamtos mokslai, chemija, N 003)
prof. dr. Juozas Padgurskas (Vytauto Didžiojo universitetas, technologijos mokslai, mechanikos inžinerija, T 009)
prof. dr. Jaunius Urbonavičius (Vilniaus Gedimino technikos universitetas, gamtos mokslai, biochemija, N 004)

Disertacija ginama viešame Gynimo tarybos posėdyje 2020 m. kovo mėn. 6 d. 13 val. VMTI Fizinių ir technologijos mokslų centro D401 auditorijoje. Adresas: Saulėtekio al. 3, LT-10257, Vilnius, Lietuva. Tel. +370 5 264 8884; el. paštas: office@ftmc.lt.

Disertaciją galima peržiūrėti Fizinių ir technologijos mokslų centro, Vilniaus universiteto bibliotekose ir Vilniaus universiteto interneto svetainėje adresu: https://www.vu.lt/naujienos/ivykiu-kalendorius

ABBREVIATIONS

a.	Acid
ALD	Atomic Layer Deposition
CCD	Charge-Coupled Device
COF	Coefficient of Friction
CVD	Chemical Vapor Deposition
DC/RF	Direct-Current/Radio-Frequency
DI	Deionized
DLC	Diamond-Like Carbon
DMEM	Dulbecco's Modified Eagle Medium
ECM	Extracellular Matrix
EDS	Energy-Dispersive X-Ray Spectroscopy
EDTA	Ethylenediaminetetraacetic acid
FAME	Fatty Acid Methyl Ester
FTIR	Fourier-Transform Infrared Spectroscopy
FWHM	Full Width at Half Maximum
GDP	Gross Domestic Product
GIXRD	Grazing Incidence X-Ray Diffraction
HV	Vickers Hardness
ID	Internal Diameter
IPA	Isopropanol
OD	Outside Diameter
PBS	Phosphate-Buffered Saline
PDLS	Periodontal Ligament Stromal
PL	Photoluminescence
PTFE	Polytetrafluoroethylene
PVD	Physical Vapor Deposition
RGD	Arginine-Glycine-Aspartic acid
RH	Relative Humidity
SEM	Scanning Electron Microscopy
SERS	Surface-Enhanced Raman Spectroscopy
TDMAH	Tetrakis (dimethylamino) hafnium
TDMAT	Tetrakis (dimethylamino) titanium
UHV	Ultra-High Vacuum
UV	Ultraviolet
XPS	X-Ray Photoelectron Spectroscopy
XRD	X-ray Diffraction

CONTENTS

INTRODUCTION

The losses caused by friction and wear often exceed 2% of GDP, therefore the aim is to create surfaces that are resistant to abrasion and usage of lubricants will be minimal. Friction between moving surfaces depends on many parameters: load, sliding velocity, roughness, hardness, elasticity, the viscosity of a lubricant and so on. However, one of the most important is chemical transformation, especially for wear. Tribology deals with a combination of all these parameters and processes. Therefore detailed research on the chemical aspects has great importance not only in the transport and other technical sectors but also in biomedicine. Teeth, bone, joint damage become one of the increasing problems in the world. Over two million bone tissue surgery procedures are performed every year [1] and the worldwide market for dental implants is estimated at 12–18 million [2]. Up to 10% of implants are rejected within the first days or several years, but depending on conditions this number can reach 20% or more [3, 4].

Bioceramic materials (Al_2O_3, ZrO_2) are often used in medicine for dental, bone and joint implants due to their chemical inertness, biocompatibility, high hardness and mechanical resistance. However, despite its widespread usage, bioceramics are bioinert. Therefore cell adhesion and interaction with biological tissues might be insufficient. It is useful to use porous and rough surfaces to enhance cell-biomaterial interaction.

One of the most commonly used methods for the formation of porous Al_2O_3-based coating is aluminum anodizing (electrochemical oxidation), which increases surface hardness, corrosion resistance, provides better dyeing, adhesion and other characteristics. The use of titanium, zirconium, steel and other alloys in medicine is limited not only by the high cost but also by the complicated mechanical treatment. The density of Al is much lower than Ti or Zr and equal to 2.70 g/cm³, 4.51 g/cm³ and 6.52 g/cm³, respectively, therefore the lightness and lower weight of Al might be more in demand for both medical devices, e.g. implants and other details. High purity Al (> 99.999%) is expensive and has poor mechanical properties because its hardness 2–3 times lower than Al alloys. Anodized coatings with porous structure increase cell adhesion and biocompatibility [5, 6]. In addition, the porous surface of the anodized coating can lead to the ingrowth of damaged bone tissues, which increases mechanical stability and load distribution.

In this investigation, the term “anodized coatings” is retained due to its widespread colloquial usage. However, those are cathodic processes, which lead to deposition of additional layers on metals, while anodic processes

result in surface etching and dissolution. In fact, the surface of anodized Al is partially dissolved and oxidized, so electrochemically it does not represent a true coating. However, during Al anodizing oxidation is so intense that it usually results in some growth of the surface. So topographically this resembles coating formation quite closely. Hence the term “anodized coating” is controversial electrochemically, but seems acceptable topographically. This is why it is used further in the text. Hard anodization is usually performed in sulfuric/oxalic acid electrolyte at low temperatures such as 0 °C. In this study, the term “hard anodization” was also used for Al anodization at 15 °C.

Hard (Type III) anodization, which is carried out in sulfuric/oxalic a. electrolytes at low temperatures allow to form solid Al_2O_3 coatings with a thickness exceeding 100 μm [7]. Despite its hardness, wear of anodized coatings remains one of the major problems in many industrial areas. In biological systems, wear must be avoided. Relative movement between the implant and surrounding tissues can lead to poor adhesion and rejection reactions. Cracks formed during friction and abrasion increase ion release and migration to surrounding tissues and organs, causing inflammation, bone erosion, and might be the reason for implant removal. Al^{3+} ions are toxic to the human body at high concentrations [8, 9], therefore the concentration of Al^{3+} ions should not exceed 1 mg/kg per day [10]. In addition, high levels of alloying additives (Mn, Cu, Fe, Zn, etc.) in industrial Al alloys might have a negative effect on cell adhesion and proliferation.

One of the most commonly used way to improve the wear resistance of anodized coatings is based on the formation of polytetrafluoroethylene (PTFE) barrier coatings, which reduce the Coefficient of Friction (COF) below 0.2. However, several major issues prohibit usage of PTFE coatings in biomedicine. The porous and rough anodized coatings are transformed into a flat layer, which is not favorable to cell adhesion due to the non-wetting nature of PTFE molecules. The deposition of biocompatible Ti layers on anodized coatings can be considered as an alternative.

Ti oxides and nitrides showed some effectiveness as protective, anti-frictional and anti-wear layers for various substrates [11, 12], including anodized coatings [13]. Several research groups have found that Ti-based layers effectively inhibit wear and reduce COF to 0.15 [12, 14]. The effectiveness of Ti/TiO_2 layers was showed on implants [15], fasteners [16], aerospace and marine applications [17], turbine engines [18]. For various technological purposes, their layers were deposited on anodized Al substrates when produced by sol-gel [19], magnetron sputtering [20], atomic

layer deposition (ALD) [21], hydrothermal [22] and other methods. Titanium dioxide (TiO_2) is chemically stable, insoluble, non-toxic and does not react with most acids, alkalis and organic compounds. Because of chemical stability [23], corrosion resistance [24] and biocompatibility [25] Ti layers commonly used in sensors, implants and other biomedical applications. The formation of Ti oxide layers enhances the direct implant-bone tissue interaction (osseointegration), prevents immune response and provides protection from the body medium. Although the wear resistance of biocompatible coatings has not yet been well studied and the friction and wear regimes in organisms have not yet been clearly identified, it is evident that biomedical products may come into contact with moving surfaces within the body as well as during transport and installation. It is important to investigate the most important tribological properties of biocompatible coatings. The synergistic effect of anodized coatings and Ti layers providing low surface friction and high biocompatibility is promising for the development of biomedical devices of a new generation. Nanostructured alloys could be employed as a cost-effective replacement for currently used expensive Ti osteosynthesis systems in dentistry and orthopedics.

In order to get closer to the friction conditions in biological systems, it is appropriate to investigate surfaces coated with lipids and other organic compounds since most of the compounds present in blood plasma and in the cellular composition can interact with nanostructured coatings [26]. The adsorption and migration of organic compounds into the pores of the anodized coating leads to tribofilm formation through chemical reactions providing low surface friction and wear. The migration of these compounds in various coatings is often studied by non-destructive Raman spectroscopy, which provides information not only on the structure and quantities of molecules but also on interaction with the coating.

Main goal

The aim of this work is to evaluate the most relevant chemical, physical, tribological and biocompatibility properties of nanostructured anodized coatings on industrial aluminum alloys and their interaction with the most important biolubricants.

Objectives

- To evaluate the influence of electrolyte and anodizing parameters on the topography and friction of the formed anodized Al_2O_3 coatings.

- To select the most appropriate cell lines for testing and to evaluate the biocompatibility properties of anodized and nanostructured coatings.
- To evaluate influence of Ti/TiO_2 surface layer on static and dynamic friction of anodized coatings.
- To compare the tribological properties of IVB group elements and nanothin layers of other transition metals on anodized coatings.
- Evaluate the suitability of Raman spectroscopy for migration of organic compounds into the pores of anodized coating.
- To evaluate the influence of the most important biolubricants on the tribological properties of anodized and nanostructured coatings.

Scientific novelty

- The biocompatibility of both Ti alloys and Al_2O_3 has already been extensively studied. However, the fact that industrial Al alloys contain alloying additives (Cu, Mn, Si, etc.) is not properly taken into account, while significant amounts of electrolyte remain in the coatings after anodization. The dissertation thesis demonstrates that nanothin layers of chemically inert Ti/TiO_2 improve the biocompatibility of anodized coatings by forming a barrier layer.
- Several groups have investigated the influence of Ti and TiO_2 layers on tribological properties, but these layers were almost unexplored on anodized Al coatings. So far it was detected only a slight improvement in tribological properties.
- Independent of the deposition method, e.g. ALD or sputtering, nanothin layers of Ti/TiO_2 significantly improve the tribological properties of the anodized coatings and reduce the COF to 0.2. Considering the layers of other elements, it was found that metals of IVB group have significantly better tribological properties than other transition metals, but Ti efficiency is incomparably higher.
- It has not yet been suggested that nanostructured coatings deposited on anodized Al with good biocompatibility and friction resistance can be successfully applied in biomedical applications to replace the currently used titanium alloys.
- The migration of organic compounds into the pores of anodized coating has not yet been monitored by Raman spectroscopy. This methodology has been successfully applied to investigate the penetration of dyes into the anodized foil as well as to select the tribologically most effective fillers for coating.

Statements presented for defense

1. Nanothin layers of Ti and its oxides improve the biocompatibility of anodized Al not only due to Ti bioinertness, but also because a barrier against the residual electrolyte inside the pores is formed. Low thickness of the layers helps in retaining rough surface topography which is favorable for cell adhesion.
2. Tribological properties of anodized coatings produced in sulfuric/oxalic a. electrolyte can be significantly improved by depositing nanothin layers of group IVB elements or their oxides. Layers of Ti or its oxides with the thickness from 10 to 100 nm demonstrate lower coefficients of friction than those on Al, anodized coatings or Ti substrates. The layers thinner than 10 nm or thicker than 0.5 μm show friction, which is similar or worse than that of the substrates. Friction reduction can also be observed with nanothin layers of Zr and Hf oxides. Those metals, which do not belong to IVB, such as Cr, Cu or Nb, do not demonstrate similarly beneficial effect on tribological properties.
3. Dry and severely starved lubrication on hard-anodized alumina can be significantly improved by capitalizing on the reactions between impregnated filler and the residual electrolyte within pores. Tribological properties of the filler itself have little influence, because new compounds are produced in the pores and eventually within the friction zone, which lead to tribofilm formation. Barrier layer on the top of the anodized coating is not essential for wear resistance, while deeper penetration of the filler, which can be monitored by Raman spectroscopy, is very important for better tribological properties.

Contribution of the author

- The procedures for preparation of Al alloys and electrolytes, anodizing and impregnation with lubricants as well as friction and wear tests were made by the author.
- The author contributed significantly to the surface analysis of anodized and nanostructured coatings and their preparation for publication using optical microscopy (part by L. Staišiūnas), scanning electron microscopy (by G. Stalnionis and A. Selskis), profilometry (part by L. Staišiūnas), X-ray energy dispersion spectroscopy (by G. Stalnionis), X-ray diffraction (by V. Pakštas), hardness measurements (by G. Bikulčius), X-ray photoelectron spectroscopy (by V. Jasulaitienė). Also directly contributed to the analysis and processing of the results of

biocompatibility studies (performed by A. Stirkė, J. Kavaliauskaitė and IMC researchers G. Pivoriūnas and A. Čebatariūnienė).

- Measurements of penetration of fillers into the pores of anodized coating of Al foil by Raman spectroscopy were performed by the author and I. Ignatiev. The text and graphic part of the dissertation and its summary were prepared by the author.

List of publications

1. Matijošius, T., Ručinskienė, A., Selskis, A., Stalnionis, G., Leinartas, K. and Asadauskas, S.J. (2016). Friction reduction by nanothin titanium layers on anodized alumina. *Surface and Coatings Technology*, 307, pp.610-621.
2. Matijošius, T., Asadauskas, S.J., Bikulčius, G., Selskis, A., Jankauskas, S., Višniakov, J. and Ignatjev, I. (2019). Determination of the dye penetration rate in porous aluminum oxide using Raman spectroscopy. *Coloration Technology*, 135(4), pp.275-282.

Other Publications

1. Bikulčius, G., Češunienė, A., Selskienė, A., Pakštas, V. and Matijošius, T. (2017). Dry sliding tribological behavior of Cr coatings electrodeposited in trivalent chromium sulphate baths. *Surface and Coatings Technology*, 315, pp.130-138.
2. Matijošius, T., Gedvilas, M., Gečys, P., Vozgirdaitė, D. and Asadauskas, S. (2018). Effects of electrolyte and Ti layers on static and dynamic friction of anodized alumina. *Proceedings of the International Conference BALTTRIB'2017*, 1, pp.199-206.
3. Nicolenco, A., Tsyntsaru, N., Matijošius, T., Asadauskas, S. and Cesiulis, H. (2018). Wear resistance of electrodeposited Fe-W alloy coatings under dry conditions and in the presence of rapeseed oil. *Green Tribology*, 1(1), pp.16-23.
4. Bikulčius, G., Češūnienė, A., Matijošius, T. and Selskienė, A. (2018). Dry sliding tribological behaviour of bilayer Cr/Cr coatings obtained in sulphate Cr (III) baths. *Transactions of the IMF*, 96(3), pp.130-136.
5. Jonauske, V., Stanionyte, S., Chen, S.W., Zarkov, A., Juskenas, R., Selskis, A., Matijosius, T., Yang, T.C., Ishikawa, K., Ramanauskas, R. and Kareiva, A. (2019). Characterization of sol-gel derived calcium hydroxyapatite coatings fabricated on patterned rough stainless steel surface. *Coatings*, 9(5), p.334.

6. Bikulčius, G., Češūnienė, A., Matijošius, T., Selskienė, A. and Pakštas, V. (2019). Investigation of the properties of Cr coatings deposited in an improved Cr (III) electrolyte. *Chemija*, 30(2), pp.69-77.

Participation in conferences

1. Matijošius, T., Čebatariūnienė, A., Pivoriūnas, A., Asadauskas, S., Miečinskas, P. Friction and biocompatibility studies of nanostructured titanium coatings using periodontal ligament stromal cells. *5th Conference of PhD Students and Young Researchers FizTech2015*, Vilnius, Lithuania, 22-23 October 2015 (oral presentation).
2. Matijošius, T., Ručinskienė, A., Asadauskas, S. Friction and wear of titanium in water and fatty acids. *Annual conference of Lithuanian chemists "Chemistry and Chemical Technology"*, Vilnius, Lithuania, 28-29 April 2016 (poster presentation).
3. Matijošius, T., Čebatariūnienė, A., Pivoriūnas, A., Miečinskas, P., Asadauskas, S. Impact of titanium layers on adhesion and friction resistance using periodontal ligament stromal cells. *6th Conference of PhD Students and Young Researchers FizTech2016,* Vilnius, Lithuania, 26-27 October 2016 (oral presentation).
4. Matijošius, T., Gedvilas, M., Gečys, P., Asadauskas, S. Static and dynamic friction evaluation of anodized aluminum surfaces. *Annual conference of Lithuanian chemists "Chemistry and Chemical Technology"*, Kaunas, Lithuania, 28 April 2017 (oral presentation).
5. Matijošius, T., Valsiūnas, I., Asadauskas, S. Anodizing of aluminum alloys in sulfuric and phosphoric acids and comparison of coating properties. *7th Conference of PhD Students and Young Researchers FizTech2017*, Vilnius, Lithuania, 24-25 October 2017 (oral presentation).
6. Matijošius, T., Gedvilas, M., Gečys, P., Vozgirdaitė, D., Asadauskas, S. Effects of Electrolyte and Ti Layers on Static and Dynamic Friction of Anodized Alumina. *The 9th International Conference "BALTTRIB'2017"*, Kaunas, Lithuania, 14-16 November 2017 (oral presentation).
7. Matijošius, T., Valsiūnas, I., Asadauskas, S. Anodization of Al Alloy in Phosphoric Electrolyte for Friction Reduction. *23rd Topical Meeting of the International Society of Electrochemistry*, Vilnius, Lithuania, 8-11 May 2018 (poster presentation).

8. Matijošius, T., Staišiūnas, L., Asadauskas, S. Friction Reduction on Anodized Alumina by Deposition of Ti Nanolayers. *The 4th edition of Nanotech France 2018 International Conference and Exhibition*, Paris, France, 27-29 June 2018 (oral presentation).
9. Matijošius, T., Kalužina, A., Bikulčius, G., Valsiūnas, I., Asadauskas, S. Comparison of liquid friction trends between steel and several bioceramic surfaces. *8th Conference of PhD Students and Young Researchers FizTech2018*, Vilnius, Lithuania, 17-18 October 2018 (oral presentation).
10. Matijošius, T., Valsiūnas, I., Asadauskas, S. Tribological destruction of anodized Al waste of different alloys in environment. *International Conference "EcoBalt 2018"*, Vilnius, Lithuania, 25-27 October 2018 (oral presentation).
11. Matijošius, T., Asadauskas, S., Bikulčius, G., Ignatjev I. Characterization of dyes during coating process of anodized alumina using raman spectroscopy. *International conference "Open Readings 2019"*, Vilnius, Lithuania, 19-22 March 2019 (oral presentation).
12. Matijošius, T., Valsiūnas, I., Stalnionis, G., Jasulaitienė, V., Asadauskas, S. Penetration of titanium into alumina nanopores after atomic layer deposition or magnetron sputtering. *Annual conference of Lithuanian chemists "Chemistry and Chemical Technology"*, Vilnius, Lithuania, 16 May 2019 (oral presentation).
13. Asadauskas, S.J., Matijosius, T. Friction reduction on anodized alumina by impregnating ashless fillers. *74th STLE (Society of Tribologists and Lubrication Engineers) Annual Meeting*, Nashville, USA, 19-23 May 2019 (oral presentation by Asadauskas).
14. Bražinskienė, D., Matijošius, T., Bikulčius, G., Asadauskas, S. Penetration of esters, derived from vegetable oils, into anodized coating for friction reduction. *21st International Conference "Advanced Materials and Technologies"*, Palanga, Lithuania, 19-23 August 2019 (poster presentation by Bražinskienė).
15. Matijošius, T., Kavaliauskaitė, J., Kazlauskaitė, A., Stirkė, A., Asadauskas, S. Influence of titanium and bioceramic coatings on cell adhesion. *9th Conference of PhD Students and Young Researchers FizTech2019*, Vilnius, Lithuania, 23-24 October 2019 (oral presentation).

1. LITERATURE REVIEW

High friction leads to surface wear, damage, deformation, increases energy loss. This is related not only to technological but also to economic aspects reducing the lifetime and increasing the cost of the materials and equipment. Friction problems include industrial applications as well as medical devices which leads to the inflammatory process, implant loosening, and rejection. Various coatings are often applied to protect surfaces from friction, increases materials durability, physical, mechanical and chemical properties. In this study, anodized coatings were obtained by electrochemical oxidation (anodization) using industrial Al alloys.

1.1 Tribology and biotribology

Tribology is the multidisciplinary science on wear, friction and lubrication of interacting surfaces in relative motion, which includes many fields: materials science, chemistry, engineering, biomedical science, physics, etc. Friction is the force resisting the relative motion between systems in contact when solid surfaces or fluids sliding against each other. The friction force is linearly dependent on the applied (normal) load. Therefore, the ratio between friction force and normal force (i.e. load) gives COF, which value mostly varies from 0.1 to 1.0. Since tribology involves interacting surfaces of artificial systems, biotribology deals with biological systems. Friction objects in the human body include articular cartilage, synovial joints, dental implants, braces, blood vessels, heart pumps, catheters, bio-probes, skin, contact lenses, tendons, muscles, and many other biological objects.

High friction problems in biotribology related to dental implants and articular cartilage. Tooth enamel, which is made mostly of hydroxyapatite (crystalline calcium phosphate, $Ca_{10}(PO_4)_6(OH)_2$), can reach from 10–20 N to 50–150 N loads during a normal chewing cycle [27]. The initial COF of enamel reaches 0.11 under 20 N load [28]. The most common materials for dental implants include Ti and bioceramic surfaces (i.e. Al_2O_3, ZrO_2) which are non-toxic, chemically stable and provide good biocompatibility with living tissues. Biocompatible materials do not produce a toxic or immunological response when exposed to the body or bodily fluids. Moreover, these biomaterials increase osseointegration processes after fusion them into the jawbone. Much higher compressive loads from at least 300 N are present in articular cartilage when contact pressure reaches over 4 MPa [29]. Hyaline cartilage, which is present in joint surfaces able to reduce

COF to 0.002–0.02 [30, 31]. The composition of cartilage includes type II collagen, glycosaminoglycans and water. Aggrecan molecules of chondroitin sulfate and keratan sulfate glycosaminoglycan chains attached to hyaluronic a. due to high negative charge are forming hydrogels, which increases compressibility. Such low friction is based not only on cartilage structure but also on synovial fluid. It is a viscous, non-Newtonian fluid mostly based on hyaluronic a and lubricin present in the cavities of synovial joints. Biomaterials should provide good mechanical and antifrictional properties to reduce wear debris formation and osteolysis due to inflammation problems. Various combinations of materials are applied today: metal with metal, ceramic with ceramic, polymer with metal, polymer with ceramic. It was shown that ultra-high molecular weight polyethylene reduced COF to 0.09 under dry friction and 0.03 under lubricated friction conditions against ZnO_2 ceramic [32].

Soft tissues are also influenced by friction in contact with bone or implant materials. As shown by previous studies COF value between muscle and bone tissue can increase to 0.29–0.36 [33]. Much lower COF was estimated between stents and endothelial cells that form the interior surface of blood vessels. Studies showed that the endothelial layer was stable when COF reached 0.03, while COF values over 0.06 showed surface damage using 0.4 mN load and 300 μm/s velocity [34]. Other implants, i.e. contact lenses, which is based on silicone hydrogel have COF from 0.025 to 0.075 using 3–20 mN loads and 63–6280 μm/s velocities [35]. Friction is influenced not only on physical and chemical surface properties of biomaterials but also on tribological conditions and environment: load, velocity, motion trajectory (linear, rotary, oscillatory), temperature, friction regime (dry or lubricated), etc.

1.2 Dry and lubricated friction

There are no perfectly frictionless surfaces exists when two surfaces are in contact. Friction forces will always develop when surfaces are moving or attempting to move against each other. Two types of friction static or dynamic (kinetic) can occur under dry or lubricated friction conditions.

Static friction acts between two surfaces when there is no relative motion to each other, while dynamic friction acts between objects in motion. Dynamic friction is proportional to the normal force applied on the surfaces and is directed opposite to the relative motion of the surfaces. In general, dynamic friction is lower than static friction. This is explained by surface

asperities (i.e. roughness) and electrical charges between two surfaces requiring much higher energy to move the static object than the energy required to keep it in motion. Static friction is very important for dry surfaces especially in the industrial field when friction becomes intermittent. This includes transport (brake disks, engine, etc.) or industrial (fasteners, railings, etc.) applications as well as high-tech, e.g. robotics (casings, frame, etc.), medical (dental braces, crowns, etc.) and many other areas. According to literature, static friction depends on the mechanical properties of the material, surface roughness, a mutual dissolution of materials, contact time and presence of the extraneous bodies in the contact zone [36]. Surface elasticity is also an important factor for static COF. Elastic deformation occurs when the internal molecular structure of the material is self-reversing after removing the force or load, while plastic deformation shows an irreversible change in the internal molecular structure.

When two surfaces of different radii are in contact together some elastic deformation occurs and a small contact area is formed when the load is applied, Fig. 1.

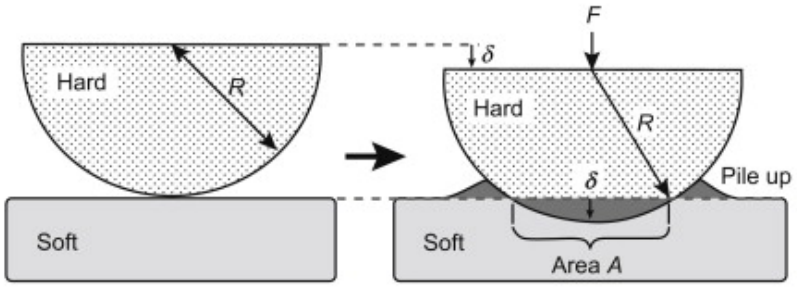

Fig. 1. *Elastic deformation using the sphere-on-flat geometry, adapted from [37]*

The surfaces experience high stresses, which are known as Hertz (Hertzian) contact stresses first studied by Hertz in 1881. He focused on non-adhesive contact where no tension force is allowed to occur within the contact area [38]. Hertzian contact stresses relies on four primary assumptions: I) The surfaces are continuous and non-conforming; II) The bodies are in frictionless contact; III) The strains are small and within the elastic limit; IV) Each body can be considered an elastic half-space, i.e. the contact area is small relative to the sizes of the bodies in contact. Non-adhesive elastic contact can occur between a sphere and a half-space, two spheres, two cylinders with parallel axes, a rigid cylinder and an elastic half-space, a rigid conical indenter and an elastic half-space. For Pin-on-Disc

(e.g. ball on plate) tribosystem, the theory of spherical/hemispherical deformation is most reasonable. According to Hertz contact modulus (Pa) for the spherical/hemispherical system is [39]:

$$E^* = \left(\frac{1 - \nu_1^2}{E_1} + \frac{1 - \nu_2^2}{E_2} \right)^{-1} \quad (1)$$

where E is the elastic modulus, in Pa; ν is Poisson's ratio. The subscripts 1 and 2 refer to the sphere and half-space respectively.

Therefore the diameter (d) of the contact area is:

$$d = \sqrt[3]{\frac{6PR}{E^*}} \quad (2)$$

where P is the indentation load, in Pa; R is the radius of the indenter, in m; E^* is a contact modulus, in Pa.

Elastic modulus also known as Young's modulus shows the stiffness of material under compression or tension and expressed as the ratio of stress and strain. Stress is the compression or tension per unit area when the force is applied while strain defines as the deformation or displacement of material. Poisson's ratio is the ratio of transverse contraction strain to longitudinal extension strain in the direction of stretching force, which values for most materials ranging between 0 and 0.5. Tensile deformation is considered positive and compressive deformation is considered negative.

According to Amontons' first and second laws friction force which is opposite to applied force is directly proportional to the applied load, but is independent of the apparent area of contact under dry friction conditions. A normal force (i.e. load) that is perpendicular to the surface depends on the mass of the object and the gravitational field strength, which is about 9.81 m/s^2 on Earth. When applied force is greater than the friction force, the object begins to slide represent the dynamic friction. Coulomb's law of friction state that dynamic friction is independent of the magnitude of the velocity (i.e. speed) when two surfaces slide against each other under dry friction conditions.

While static COF is an important parameter of dry friction, dynamic COF especially relevant to lubricated friction conditions. Lubricated friction occurs between two solid surfaces sliding against each other in the presence of lubricant fluid. Lubricants reduce surface friction and wear, dissipate the heat, transmitting forces or transporting foreign particles which are

generated when surfaces are moving. Stribeck curve represents three lubrication regimes: I) Boundary lubrication; II) Mixed or elastohydrodynamic lubrication; III) Hydrodynamic lubrication. Richard Stribeck and Mayo D. Hersey showed that lubricated friction is a non-linear function of the lubricant viscosity, sliding velocity and the contact load, see Fig. 2.

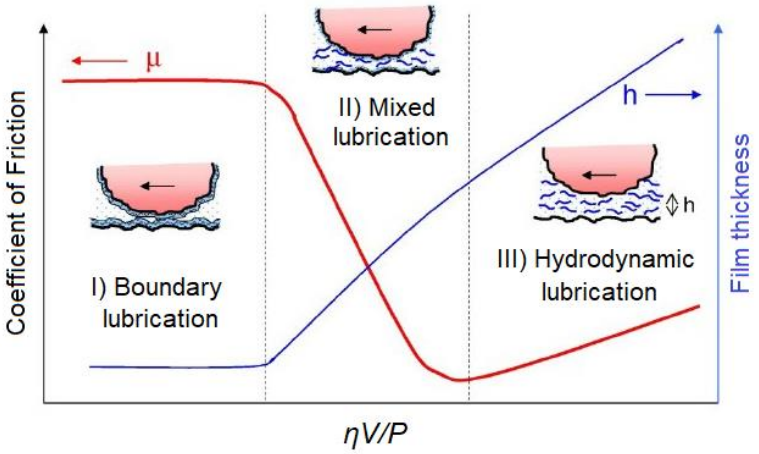

Fig. 2. *Stribeck curve model, where the friction coefficient (μ) and the fluid film thickness (h) are plotted as a function of velocity (V), lubricant viscosity (η) and load (P) for the boundary, mixed and hydrodynamic lubrication regimes; adapted from [40]*

Boundary lubrication defined the conditions then solid surfaces come into direct contact, load supported mainly by surface asperities rather than by the lubricant. The highly resistant film is formed between the moving solid surfaces and lubricant, which is capable of support the load and avoid major wear or breakdown. Boundary lubrication obtained under high loads, low velocities and/or low lubricant viscosities, then film thickness is thinner than surface roughness ($h < Ra$). Low thickness of the lubricant and high surface contact area leads to increased friction. Surface chemistry is especially important for boundary lubrication. In mixed or elastohydrodynamic lubrication conditions load is supported by both asperities and the liquid lubricant, when the film thickness is approximately equal to surface roughness ($h \approx Ra$). The surfaces undergo elastic deformation due to elastic strains at the contact at higher velocities. Such strain creates a load-bearing area, which provides an almost parallel gap for the fluid to flow through. The motion of the contacting surfaces generates a flow induced pressure, which

acts as the bearing force over the contact area. A viscosity of the fluid may rise considerably due to the high contact pressure. Hydrodynamic lubrication also known as full film lubrication regime occurs when the lubricant completely separates the surfaces with the film thickness much higher than surface roughness (h >> *Ra*), nearly 1 μm or even more [41]. Low friction obtained at high velocities without no surface wear. Any friction remaining comes from the cohesiveness of the oil molecules as they slide past each other. Applied load, velocity, and lubricant viscosity are the most important factors for film thickness. A lubricant with too high viscosity increases the oil's molecular friction, leading to higher operating temperatures and energy loss.

1.3 Lubricants

Lubricants are often used to reduce surface friction, wear, transfer generated heat or wear debris formation when surfaces are in mutual contact by providing a continuous fluid film. In general, lubricants could be classified as liquids, semisolids (greases) and solids. Although other classification methods based on the composition of the base oil or their application are also appreciable [42]. Liquid lubricants include mineral oils, synthetic oils and vegetable, and animal oils. Liquid lubricants, i.e. mineral oils, which are obtained by fractional distillation of petroleum and semisolid lubricants produced by emulsifying oils or fats with metallic soap (Li, Na, Al, Ca, etc.) are widespread in the industry, where thick lubricating film is required. This includes roller bearings, steam turbines, engine, gear, piston parts, and other applications. Lubricants contain up to 10% additives which act as antioxidants, anti-corrosive, anti-wear, anti-foaming, emulsifying or demulsifying agents [43]. Vegetable oils (i.e. soybean, rapeseed (canola), sunflower, corn) are an environmentally friendly alternative to mineral oils since they are not toxic to the environment and biodegradable. Lubrication properties of vegetable base oils are similar to those of mineral oils. As showed by previous studies, vegetable oils reduced COF to 0.1 or below depending on used additives and/or lubricating materials [44, 45]. However, the main disadvantages of vegetable lubricants include poor hydrolytic, thermal and oxidation stability. Lubricant type, viscosity, thermal (thermal stability, freezing point, boiling point, etc.) and protective (resistance to oxidation, corrosion, pressure, etc.) properties are the main characteristics for selecting an oil.

Solid lubricants are often applied in applications where contamination by lubricating oils or greases must be avoided. This includes powders and thin layers which reduces friction and wear of contacting surfaces and provides protection from damage [46]. Solid lubricants can be classified as inorganic lubricants (graphite, MoS_2, WS_2, BN, etc.), organic lubricants (i.e. polymers like PTFE), soaps (Ca stearate, Na stearate, etc.)), metals and its oxides including composites (Cu, Ag, Ti, TiO_2, B_2O_3, MoO_2, ZnO, etc.). Materials like graphite, molybdenum disulfide (MoS_2) and tungsten disulfide (WS_2) which have lamellar structures, can maintain low friction due to the anisotropic layered structure, covalent bonding within the adjacent lamellae and weak Van der Waals forces between them. Among the lamellar solids, MoS_2 and WS_2 have the best load-carrying capacity and low shear strength as thin layers on solid substrates. Sputtered MoS_2 layers showed COF reduction of 0.005−0.05 in vacuum conditions. In the native environment, where humid air is present, COF was increased from 0.15 to 0.30 suggesting that unsaturated bonds or other groups react with water and oxygen molecules leading to much higher friction [47]. WS_2 is used instead of MoS_2 when applications involve relatively higher temperatures due to higher resistivity to oxidation and better lubrication at elevated temperatures. MoS_2 oxidizes and decomposes into MoO_3 and SO_2 above 500 °C temperature [48].

Currently, treatment with fluoropolymers, such as PTFE become the most commonly used method to reduce friction and improve wear resistance of metallic (Al, stainless steel, steel alloys, brass, etc.) and non-metallic (glass, plastics, etc.) surfaces. Studies showed that PTFE reduces COF to less than 0.2 by functioning as a barrier lubricant [49, 50]. PTFE remains effective at temperatures from -200 °C for up to 260 °C [51], provides low friction and high chemical resistance which makes them suitable for aerospace, automotive, food and other industrial applications. However, several major issues prohibit usage of PTFE coatings in industry, because heating over 300 °C and manual rubbing are usually required to coat the polymer. Due to smooth and hydrophobic nature, PTFE is not the optimal substrate for cell adhesion, therefore several additional treatments are required to increase the wettability of the surface. Reactive surface groups such as hydroxyl, amino or carbonate can be formed on inert PTFE surfaces by using dry-chemical treatment (i.e. plasma etching [52]) and wet-chemical treatment (i.e. H_2O_2/H_2SO_4 [53]) methods to increase cell adhesion. Therefore, deposition of chemically inert metals like Ti or its oxides can be considered as an alternative.

Ti oxides and nitrides provides anti-frictional properties on various substrates, including stainless steel, Ti and anodized Al. Studies showed that Ti/TiO_2 layers of ~200 nm thickness sputtered on Ti6Al4V substrate reduced COF to 0.5 and assured stable friction for 10,000 cycles [15]. Ti-based multilayer coatings including TiN, TiSiN, TiSiCN, Ti/Cu/N have demonstrated much better wear resistance and low friction with COF 0.15–0.25 [12, 14]. Friction reduction to COF ~0.2 is significant for dry coatings which able to protect surfaces from incidental friction, wear, and abrasion. Anti-frictional properties of Ti/TiO_2 layers was already demonstrated in fasteners [16], gears [54] turbine engines [18], biomedical devices [15], aerospace or marine applications [17], robotic equipment [55] and etc.

Recently, Ti/TiO_2 layers gain recognition in medicine for dental implants [56], bone implants [57], stents [58] and other applications. The deposition of Ti/TiO_2 layers promotes osseointegration processes and a direct bonding between an implant surface and bone tissue interface [59, 60]. However, the new bone formation on the plain, native oxide layer of Ti is complicated in the early stage of osseointegration. Therefore, modification of surface chemistry and/or surface topography are required to increase biocompatibility and other desirable properties. Methods such as blasting [61], plasma spraying [62], etching [63] and anodic oxidation [64] were shown some effectiveness. Recent studies have demonstrated that porous anodized Al_2O_3 coatings exhibits good biocompatibility towards blood, epithelial, neuronal, muscle and connective tissues (i.e. fibroblasts, osteoblasts) [6, 65]. These nanostructures remarkably increase surface topography (i.e. roughness) and reinforce interactions between implant material and cells. Surface properties with desirable pore diameter and porosity can be adjusted by controlling anodization factors, such as a type of electrolyte, electrolyte concentration, temperature, voltage or current density. For various technological purposes, Ti layers have also been produced on anodized Al by sol-gel [19], magnetron sputtering [20], ALD [21] and other methods. Manipulation with nanopore sizes, their density, roughness, application of fillers or deposited layers and other parameters gives an opportunity to control wettability, permeability, biocompatibility, adhesion, friction resistance and other properties of anodized surfaces.

1.4 Formation of titanium and its oxides

Ti is group IVB transition metal, which is known for its high strength, lightweight and anticorrosive properties. When Ti is exposed to air, a passive

oxide film is spontaneously formed on its surface. The amorphous film is 5–10 nm thickness and contain three layers: TiO next to metallic Ti, Ti_2O_3 in the middle and anatase TiO_2 on the outer part [59]. The characteristics of the oxide film depend on the chemical composition, structure, morphology and mechanical properties of the material. TiO_2 is most stable, insoluble, non-toxic and chemically inert, resistant to most acids, alkalis and organic compounds [66]. It has three different polymorphs: rutile with tetragonal crystal lattice, anatase with tetragonal crystal lattice and brookite with orthorhombic crystal lattice, see Fig. 3.

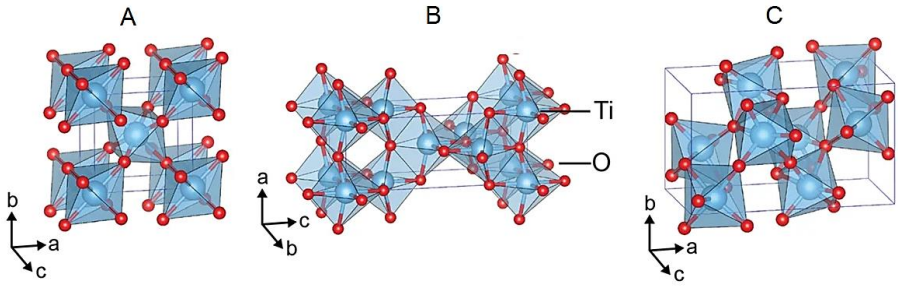

Fig. 3. *Three different polymorphs of TiO_2: rutile (A), anatase (B) and brookite (C). The small red spheres represent the oxygen atoms, the big blue spheres are the Ti atoms and the light blue polyhedral shapes show the orientation in space of the TiO_6 octahedra, adapted from [67]*

In general, the polymorphs of TiO_2 are composed of TiO_6 octahedra. Thermodynamically, rutile is the most stable polymorph of TiO_2 exhibiting lower total free energy than metastable phases of anatase or brookite. After heating, both anatase and brookite irreversibly transform to rutile. TiO_2 amorphous phase usually crystallized in anatase phase at temperatures above 400 °C, while transformation from anatase to rutile required temperatures over 600 °C [68]. Transformation to rutile is not instantaneous, it is time-dependent due to reconstruction processes. Transformation values ranging from 400 to 1200 °C can also be found and depends on deposition method, deposition conditions, precursors, materials used, the presence of impurities, crystallite size, surface contact area, heating rate [69–71]. The phase transformation process involves particle agglomeration and grain growth, which led to a change of polymorphs of TiO_2 [72]. During annealing, two grains of anatase attached to each other following by nucleation of rutile phase. After that, the growth of rutile begins resulting in phase transformation, which is related to a change of surface energy.

Agglomeration of small needle-like grains to a larger coarse grain significantly decreases surface energy of TiO_2 [73].

1.5 Titanium properties in biological fluids

When extracellular body fluids including blood and interstitial fluids come into contact with Ti, it attracts many water molecules, carboxylates as well as nitrates, phosphates or sulfates, which are often present in trace amounts. Such compounds easily adsorb or are reactively formed at the Ti surface as a consequence of many dangling bonds. The dangling bonds also referred to "immobilized free radicals" are very similar to free radicals, except since they are immobilized in a solid. Due to its reactivity they able to form new chemical bonds between Ti moieties and functional groups of other molecules. The formation of hydroxide ions (OH^-) on Ti surfaces can be induced by hydration processes due to chemisorption when OH^- groups are coordinately bound to the surface Ti cations or physisorption when water molecules are bound by weak hydrogen bonds at the oxide/hydroxide surface due to van der Waals forces. Hydroxide ions attached to metal cations possess acid or base properties depending on the type of the metal cations and the coordinate bonds with the cations. The interaction of multivalent Ti^{4+} ions with hydroxides provides amphoteric properties. Therefore, TiO_2 exhibiting both acid and base (alkaline) properties in water solution as well as under physiological conditions. Reaction (1) show the formation of negative charges on the surface and reaction (2) yields positive charges [74]:

$$Ti–OH + H_2O \rightleftarrows [Ti–O]^- + H_3O^+ \quad (3)$$

$$Ti–OH + H_2O \rightleftarrows [Ti–OH_2]^+ + OH^- \quad (4)$$

The surface charge of Ti depends on the pH of the aqueous solution. It is known that the isoelectric point of TiO_2 varies from 3.9 to 8.2 [75]. Small negative charge forms due to deprotonation of the acidic hydroxides at neutral pH while the basic and a large part of the acidic groups are still present in the neutral form. The alkaline solution provides more negative charges on the Ti surface by increasing pH.

Due to high chloride ion concentration in blood plasma of 113 mEq/L and in interstitial fluid of 117 mEq/L metallic materials starts to corrode much faster leading to pits and cracks formation on the surface. Corrosion reduces strength, increases permeability to liquids and gases which initiate relaxation of metal ions into the body fluid. Moreover, wear debris formation and microparticles accumulation often lead to cytotoxic and inflammatory

effects, mechanical instability, which end up by implant loosening and even rejection [76, 77]. The pH of extracellular body fluids is also an important parameter for biomaterials which varies from 7.35 to 7.45 [78]. Studies showed that pH decreases to about 5.2 after implantation and recovers to 7.4 within two weeks [74]. These changes are based on the isoelectric points of the biomolecules, such as proteins. It is commonly accepted that Ti exhibits high stability and corrosion resistance *in vitro* due to the ability of passive TiO_2 film formation. However, previous studies revealed that accumulation of Ti can occur in adjacent tissues near the implant indicating the relaxation of Ti ions and corrosion *in vivo*. Ti degradation is related to: (I) electrochemical factors due to high local acidity; (II) bacterial colonization; (III) mechanical factors which can lead to fretting and excessive wear of the surface and (IV) tribocorrosion as a result of a synergistic mechanism between chemical attack and mechanically-induced degradation [79–81]. Instead of pure Ti, the electrochemical reaction of Ti alloys such as Ti-6Al-4V, Ti-6Al-7Nb, NiTi also resulting of relaxation of metal ions (Al, V, Ni, etc.) which are toxic to the human body and able to accumulate in tissues and organs [82]. Corrosion resistance, physiological conditions (pH, chloride ion concentration, temperature, etc.), mechanical factors (cracks, surface abrasion, film adhesion), electrochemical effects (galvanic, pitting, crevice) and the cell concentration around biomaterials are the main factors which influence metal ions release [83].

1.6 Surface properties for cell interaction

The interactions between cells and their environment proceed through integrins (transmembrane glycoproteins) and extracellular matrix (ECM) proteins (vitronectin, fibrinogen, collagen, laminin, osteopontin, etc.) which provides Arg-Gly-Asp (RGD) tripeptide sites of arginine, glycine and aspartic a. required for cell attachment. Meanwhile, cell interaction with biomaterials is possible through the adsorbed protein layer. After implantation of biomaterials into a human body, the first stage of the reaction is non- a fibrous capsule around implant material [84]. The composition and structure of the protein layer depend on surface properties which play a critical role in determining cell behavior including adhesion, spreading and protein secretion. To promote cell -biomaterial interaction it is important to take into account the surface properties including chemical composition, wettability, surface charge, and roughness which allow maintaining normal conformation and bioactivity of adsorbed proteins.

Surface free energy shows the excess energy present at the surface of a material when compared to bulk. Therefore, surface energy will be higher if the bulk interactions are stronger, or if the surface exposure is greater. The material surface energy can be calculated from the contact angle measurements using a water drop test. Generally, a surface with high surface energy will cause good wetting and therefore result in a low contact angle. Moderate hydrophilic surfaces with water contact angle of 20° to 40° promote the highest levels of cell attachment when compared to hydrophobic surfaces with a contact angle over 90° [85]. Proteins spontaneously adsorbed on very hydrophobic surfaces acquire a denatured and rigid state, which is inappropriate for cell binding. In addition, very hydrophilic surfaces have limited cell adhesion, because proteins bind to surface with weak forces which lead to easy detachment. Surface charges showed the ability to control cellular response. Human umbilical vein endothelial cells had good adhesion to negative (COOH) or positive (NH_2) charged functional groups whereas cells adhered poorly on neutral molecules either hydrophilic (OH) or hydrophobic (CH_3) [86]. Other studies revealed that COOH and OH functional groups increase osteoblast adhesion and differentiation, NH_2 group promotes myoblast and endothelial cell proliferation and osteoblast differentiation, while CH_3 group promotes leukocyte adhesion and phagocyte migration [87].

Surface roughness is an important parameter on both tribological and biological properties. It can be divided into three levels: macro-roughness (Ra > 100 μm) also known as waviness, micro-roughness (Ra = 0.1–100 μm) and nano-roughness (Ra < 100 nm). The macro-roughness is directly related to implant geometry, which provides initial fixation and long-term mechanical stability. Surface roughness at the micro-scale promotes cell adhesion, local factor production (e.g. fibroblast growth factor, vascular endothelial growth factor) osteoblast differentiation and eventually leads to osseointegration and bone growth [88]. Micro-roughness in the range of 1–10 μm often selected for biomedical devices, e.g. implants, rather than smooth surfaces. When compared roughness of natural surfaces like a tooth and articular cartilage with Ra values of ~0.12 μm [89] and ~0.22 μm [90] respectively, roughness values for implants is much higher. Nanoroughness stimulates the adhesion, proliferation, and differentiation of cells. Various methods were developed to create micro- and nano-featured surfaces including acid etching, blasting, plasma spraying, anodization, etc.

Other techniques are related to surface modification and direct immobilization of biomolecules for a specific cellular response. Surfaces

functionalized with peptides containing RGD sequence promote cell attachment. ECM adhesion proteins including vitronectin, fibronectin, fibrinogen, laminin, collagen, osteopontin and bone sialoprotein can promote cell adhesion and enhance cell attachment via ligand–acceptor interaction [91]. Peptides showed some advantages over larger proteins since they are cost-effective and exhibit higher stability towards sterilization, heat treatment and pH. Growth factors like bone morphogenetic protein, fibroblast growth factor and etc. able to modulate cell behavior, in particular, proliferation and differentiation. Alternatively, surface modification with various layers including TiO_2 showed increased cell spreading, improved osseointegration and reduced migration of alloying additives from the substrate [92].

The material surface is important not only for cell attachment but also for better adhesion to the substrate. Since the "native" metallic surfaces usually are oxidized, contaminated, plastically deformed and non-uniform after the manufacturing process, surface treatment must be performed. In this study, Ti and TiO_2 and additional layers were deposited on bioceramic Al_2O_3 coatings obtained by anodic oxidation.

1.7 Anodization of Al alloys

Al is the most produced non-ferrous metal. Due to its reactivity, Al metal rapidly reacts with the oxygen present in the atmosphere at ambient temperatures by creating thin Al_2O_3 layer of 1–10 nm thickness. However, protective properties of Al is poor leading to rapid surface damage. Anodization is the most commonly used surface treatment method for Al alloys, which increase surface hardness, paintability, corrosion resistance and other technical features [93, 94]. Industrially, anodization is often carried out in sulfuric acid-based aqueous electrolytes, although anodization in oxalic a., chromic a., phosphoric a. and their mixtures are also quite widespread. When positively charged Al is attacked by anions (HSO_4^-, OH^-, $RCOO^-$, etc.), the metal electrochemically oxidizes mostly into Al_2O_3 by forming anodized coatings of various thickness, sometimes 100 μm or more. However, it is unable to obtain thicker than 200 μm anodized coatings due to the high resistivity of anodic Al_2O_3. Highly porous anodized Al_2O_3 coatings with vertical nanopores of uniform size and distribution are produced after anodization [56].

According to the standard specification for anodization (MIL-A-8625) there are three types for Al anodization. Type I anodization requires chromic

a. to produce coatings with 0.5 μm to 2.5 μm thicknesses. The electrolyte of H_2CrO_4 is often favored for aircraft applications due to the effective anti-corrosive properties of chromates. However, very high toxicity of Cr(VI) compounds [95] currently limit their applications by suggesting other potential alternatives, i.e. trivalent chromium (Cr(III)) plating [96]. Coatings obtained in sulfuric a. electrolyte at room temperature with a thickness between 1.8 μm to 25 μm is known as Type II anodization. While hard (Type III) anodization requires much lower temperatures to produce coatings from 25 to 150 μm thickness [97]. Hard anodization not only increase surface hardness, corrosion resistance, wear or abrasion resistance but also improve paintability and lubrication properties. Despite wide applications of hard coatings, currently, investigation also includes other anodization methods such as plasma electrolytic oxidation also known as micro-arc oxidation or spark anodization [98, 99], which requires at least 200 V to create thick coatings of 1700 HV hardness that is close to crystalline phase corundum [100].

1.7.1 Formation and structure of anodized coatings

Depending on the type of electrolyte, two types of anodized coatings can be produced. Non-porous barrier type oxide is formed in slightly acidic or neutral aqueous electrolytes of pH 5–7, i. e. boric a., ammonium borate or ammonium tartrate. Porous type oxide obtained in acidic and oxide dissolving electrolytes, such as sulfuric a., phosphoric a., oxalic a., chromic a., tartaric a., citric a. and etc. [101, 102]. Typical electrolytes used to produce porous type oxide coating have a pH<5.

The formation mechanism of porous type $Al_2O_3 \cdot xH^+[Anion]^- \cdot yH_2O$ (further Al_2O_3) was discussed further. At the beginning of the anodization, potential increases linearly while current density decreases due to the formation of the barrier type oxide (barrier layer), Fig. 4(a).

The high relaxation rate of Al^{3+} ions in the electrolyte with pH<5 leads to instability of the applied electrical field by forming many hemispherical pits, Fig. 4(b). At the maximum of potential, the breakdown of the tight barrier film occurs leading to the porous structure formation. Moreover, the shape of the pits even increases the dissolution rate of Al. This leads to field-enhanced or/and temperature-enhanced dissolution in the formed oxide, Fig. 4(c). Fig. 4(d) shows the steady-state growth of porous Al_2O_3 although at the end of anodization the current might decrease due to diffusion limits in the long pore channels. Differently, from deposition techniques, anodized coatings build-up from Al metal by letting to avoid delamination processes.

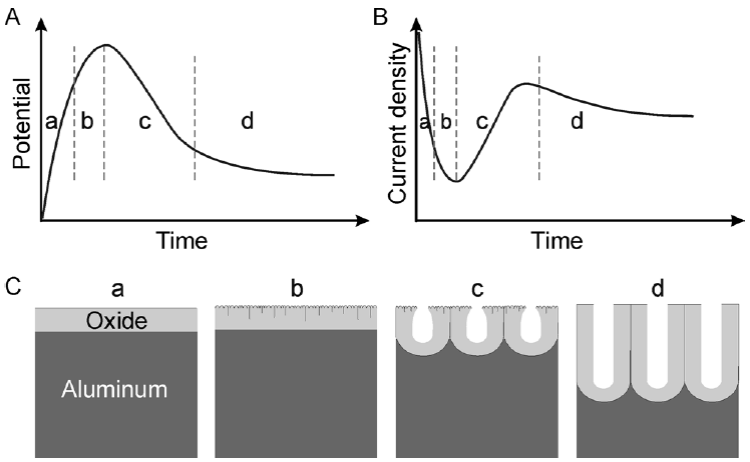

Fig. 4. *The kinetics of anodized porous Al_2O_3 growth in galvanostatic (A) and potentiostatic (B) regimes with the mechanism of the pore formation (C), adapted from [103]*

Before anodization Al surface must be cleaned usually using alkaline etching in hot NaOH solution to remove the natural oxide layer on the Al surface. Produced sodium aluminates are washed with deionized (DI) water:

$$2Al + 2NaOH + H_2O \rightarrow 2NaAlO_2 + 4H_2 \quad (5)$$

$$NaAlO_2 + 2H_2O \rightarrow NaOH + Al(OH)_3 \quad (6)$$

Following by cleaning and etching of aluminates in the nitric a. aqueous solution and rinsing in DI water again:

$$NaAlO_2 + HNO_3 \rightarrow NaNO_3 + HAlO_2 \quad (7)$$

$$HAlO_2 + 3HNO_3 \rightarrow Al(NO_3)_3 + 2H_2O \quad (8)$$

$$Al(OH)_3 + 3HNO_3 \rightarrow Al(NO_3)_3 + 3H_2O \quad (9)$$

When current is applied anodization process begins. After decomposition of acid (i.e. H_2SO_4), hydrogen ions starts moving to the negatively charged cathode where they are reduced to hydrogen gas:

$$2H^+ + 2e^- \rightarrow H_2 \quad (10)$$

The positively charged anode is Al which generates Al^{3+} ions and reacts with negatively charged oxide/hydroxide ions. It is generally accepted that the oxides simultaneously grow at both interfaces: at the metal/oxide interface by Al^{3+} transport and at the oxide/electrolyte interface by oxygen ion transport:

$$Al \rightarrow Al^{3+} + 3e^- \quad (11)$$

$$2Al^{3+} + 3O^{2-} \rightarrow Al_2O_3 \quad (12)$$

$$2Al^{3+} + 3OH^- \rightarrow Al_2O_3 + 3H^+ \quad (13)$$

The summary for the overall reaction of anodic oxidation showed below:

$$2Al + 3H_2O \rightarrow Al_2O_3 + 6H^+ + 6e^- \quad (14)$$

After anodization porous anodized coating is produced with a well ordered hexagonal structure, each cell contains a central pore perpendicular to the surface, Fig. 5.

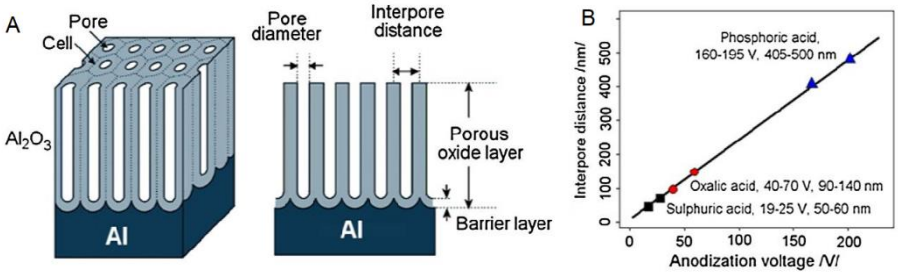

Fig. 5. *The structure of anodized coating (A) and the influence of anodization electrolyte on interpore distance (B), adapted from [104]*

The pore size and the interpore distance are mainly depending on the concentration of electrolyte, anodization voltage and electrolyte temperature. Next to the Al metal is a barrier layer which consists of nanocrystallites with sizes of 2–10 nm, hydrated Al_2O_3, anions, and water molecules [105]. The thickness of the barrier layer mostly depends on the anodization voltage, although there is a small deviation depending on the electrolyte and temperature. It is unable to exceed 1μm thickness of the barrier layer in the porous type oxides due to dielectric breakdown of the layers that occur at 500–700 V. Studies revealed that self-ordered porous Al_2O_3 structures can be obtained under specific conditions. Small nanopores with low interpore distance are obtained in sulfuric a. electrolyte at 19–25 V. Phosphoric a. used to produce wide pores with high interpore distance at 160–195 V.

According to X-ray diffraction (XRD) studies, anodized porous type Al_2O_3 coatings have an amorphous structure in general, although small amounts of crystal phases of γ-Al_2O_3 also could be detected with a grain size of ~20 nm if the anodization voltage reaches above 100 V [106]. γ-Al_2O_3 is traditionally considered as a cubic defect spinel type in which the oxygen atoms are arranged in a cubic close packing and Al atoms occupy the octahedral and tetrahedral sites. Al_2O_3 can exist in many forms including gibbsite (γ-$Al(OH)_3$) of monoclinic crystal system, boehmite (γ-AlO(OH)) of orthorhombic crystal system, diaspore (α-AlO(OH)) of orthorhombic crystal system, bayerite (α-$Al(OH)_3$) of monoclinic crystal system and α-Al_2O_3 of hexagonal structure. The porous anodized coatings obtained by only anodization processes are amorphous in nature but on heat treatment, phase

transformation toward the crystalline Al_2O_3 of γ, δ, θ, and α-phase will occur. The transformation to α-Al_2O_3 phase requires temperature over 1000 °C [107]. Anodized coatings do not exclusively contain Al_2O_3, the anions also are incorporated into the coating, which concentration depends on electrolyte. Anodized coatings obtained in H_2SO_4 electrolyte contains the highest amount of sulfates reaching up to 17% [108] while the ability to incorporate of phosphates, oxalates or chromates into anodized coating is much lower. Moreover, the purity of coatings significantly depends on the type of Al alloy.

Previous investigations by Masuda and Fukuda showed that it is able to obtain highly ordered anodized coatings of the hexagonal structure by self-organized growth mechanism under specific anodizing conditions [109, 110]. Masuda and Satoh developed a two-step anodization process which consists of first long-term anodization, followed by removal of obtained anodized coating with etching mixture of H_3PO_4 and H_2CrO_4 and reanodization [111]. The pits formed after first anodization act as the pattern for the pore formation of a much more regular structure. Although two-step anodization process requires relatively inexpensive laboratory equipment, it takes more time to produce a highly ordered hexagonal pore structure. Several approaches have been explored to modulate Al_2O_3 pore channels with different architectures. The multiple branched pore structure could be produced by multi-step anodization using different types of electrolytes, changing electrolyte concentration or temperature, a variation of applied voltage or current density during anodization or combining anodization and chemical etching [112, 113]. Another method i.e. pulse anodization, which is based on long low current pulses and short high current pulses allow to create pores with different diameters across the anodized coating [114]. The ability to control surface porosity with various nanopatterns are very favorable for nanostructured materials and devices.

1.7.2 Applications for anodized coatings

Highly ordered anodized coatings are characterized by chemical, thermal stability, hardness and high surface area. Advanced properties of porous coatings and membranes demonstrated wide applications in many areas including biomedicine for cell adhesion, implants and local drug delivery, chemical/biological sensing, molecular separation, catalysis, electronics, optics, photonics, solar cells, fuel cells and energy storage, Fig. 6.

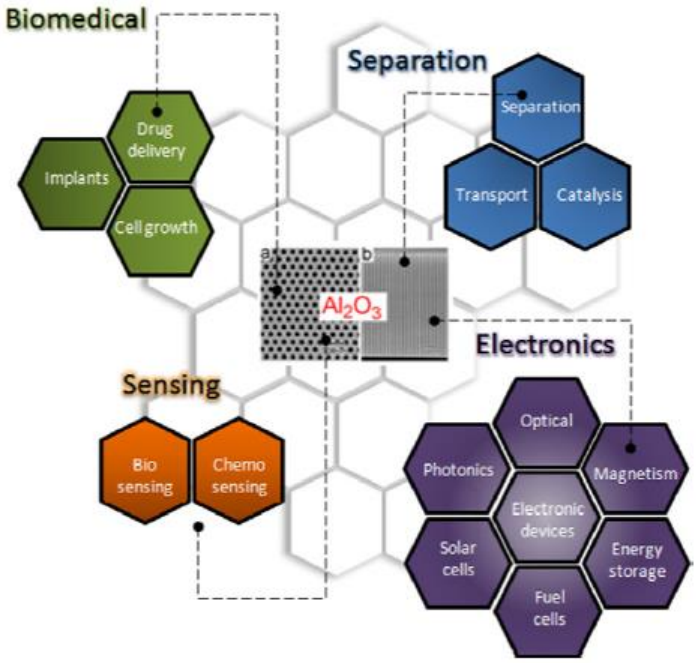

Fig. 6. *The structure and major applications of anodized coatings, adapted from [104]*

Due to the porous structure, anodized coatings can be easily modified using wet chemical synthesis (self-assembly processes, sol–gel coating, electrochemical deposition, etc.) or gas-phase modification (thermal vapor metal deposition, chemical vapor deposition (CVD), ALD, physical vapor deposition (PVD), etc.) techniques. Gas-phase techniques are widespread method to improve structural, physical and chemical properties of anodized coatings by depositing metals, metal oxides, composite materials or other compounds. Au, Pd, Pt, Ti/TiO_2 layers showed improved catalytic properties while magnetic properties can be improved with Ni or Co layers [104]. Ti based layers increased biocompatibility [115], reduced friction [13] and showed antibacterial effect [116] which is very favorable for biomedical devices. The ability to deposit various materials into the pores of anodized coating has many advantages. Bioactive surface layers based on TiO_2, hydroxyapatite might be useful for medicine, i.e. dental and orthopedic implants, as well as for photocatalysts and sensor applications [117]. Anodized coatings can be easily functionalized with peptides, enzymes, antibodies, DNA, fluorescent dyes, quantum dots, nanoparticles, lipid bilayers and other molecules. It was showed that organosilane modification

of anodized coatings not only influences surface wettability but also influences surface chemistry through reactive functional (i.e. amino, carboxy, aldehyde) groups.

Porous A_2O_3 coatings not only increases cell adhesion [6] but also acts as reservoir for various molecules including drugs [118], Ag nanoparticles [119] for antibacterial effect, growth factors for cell differentiation or proliferation [120] and even lubricants for friction reduction [121]. The importance of lubricating materials for tribology was highlighted subsequently.

1.8 Lipids

Lipids are biomolecules that are soluble in nonpolar solvents and do not dissolve in water. They can be classified into eight categories: fatty a., glycerolipids, glycerophospholipids, sphingolipids, saccharolipids, polyketides, sterols and prenols. Phospholipids are major structural elements of biological membranes composed of hydrophilic phosphate head and a hydrophobic tail of two fatty a. chains. Many lipids serve as a major energy reserve and are stored in adipose tissue, 98% of them are made up of triglycerides [122]. Other lipids serve as hormones and signaling molecules between cells, tissues, and organs. Over 500 lipids are found in blood plasma which includes mainly fatty a. and cholesterol. Since lipids are insoluble in blood plasma or other extracellular fluids, therefore they bound to proteins and form lipoproteins of various densities.

1.8.1 Lipid based biolubricants

Hydroxyl groups present on the anodized coating surface allow them to be easily modified with organic molecules for the desired functionality. Many lipids found in plasma and other tissues able to interact with biomedical devices. Properties of fatty a. and triglycerides were studied.

Fatty a. is a carboxylic a. with a long aliphatic chain containing from C_4 to C_{24} atoms, but C_{16} to C_{18} are most common [123]. Carbon numbers are generally restricted to even numbers because fatty a. are synthesized from two-carbon compounds as starting materials and elongated by simultaneous addition of two carbons. They found in animal and vegetable fats or oils. At physiological pH most weak acids, i.e. fatty a. are anions. In water, they form micelles due to amphipathic nature, which contains both hydrophilic (polar head groups) and hydrophobic (the long aliphatic chain) regions. Normal-phase (oil-in-water) micelles have the hydrophobic chains at the centre with their head groups located outside. Fatty a. that comprise

organisms generally have linear chains while branched fatty a. are very rare. Fatty a. can be either saturated or unsaturated. A fatty a. with no double bond is saturated, with a single double bond is monounsaturated and with more than one double bond is polyunsaturated. Unsaturated fatty a. can exist in the *cis* or *trans* configuration. The configuration is called *cis* when the hydrogen atoms are on the same side of the double bond, while in *trans* configuration hydrogen atoms are on opposite sides of the double bond. Despite of thermodynamic instability and lower melting point, natural unsaturated fatty a. often found in *cis* configuration.

The most common long chain saturated fatty a. are palmitic a. (16:0) and stearic a. (18:0), while for unsaturated fatty a. is oleic a. (18:1), linoleic a. (18:2) and linolenic a. (18:3) [124]. Saturated fatty a. of stearic a. and unsaturated fatty a. of oleic a. were chosen for tribological studies, see Fig. 7.

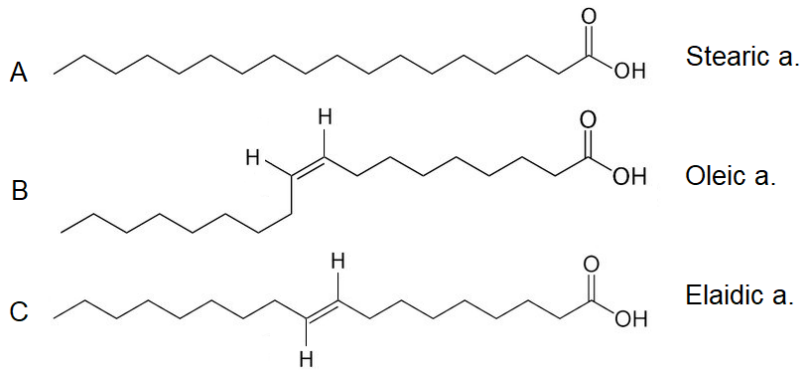

Fig. 7. *Structures of fatty acids: (A) stearic a. (saturated), (B) oleic a. (unsaturated, cis), (C) elaidic a. (unsaturated, trans); adapted from [125]*

Stearic a. (octadecanoic a.) and oleic a. (*cis*-9-octadecenoic a.) with 18 carbon atoms are most abundant compounds found in animal fats including triglycerides and phosphoglycerides with their concentrations up to 30% [126] and up to 50% [127] respectively. Solid state stearic a. represent tightly bound aliphatic chain molecules while oleic a. have a liquid state at room temperature because of loose molecules with a double bond at C9 atom. The stereoisomer of oleic a. is known as elaidic a. (*trans*-9-octadecenoic a.) obtained by partial hydrogenation or elaidinisation.

Fatty a. molecules are usually joined together in a group by forming triglycerides (triacylglycerols), wich are esters derived from three fatty a. and glycerol. Triglycerides are the main constituents of body fat found

mostly in adipose tissue. They play an important role in metabolism as energy sources and transporters of dietary fat and contain more than twice as much energy as carbohydrates. One of the investigated material was tristearin composed of three stearic a. molecules and glycerol. Tristearin found in three crystalline forms (polymorphs): α, β, and β′, which differs by their crystalline structure, melting point and thermodynamic stability, Fig. 8.

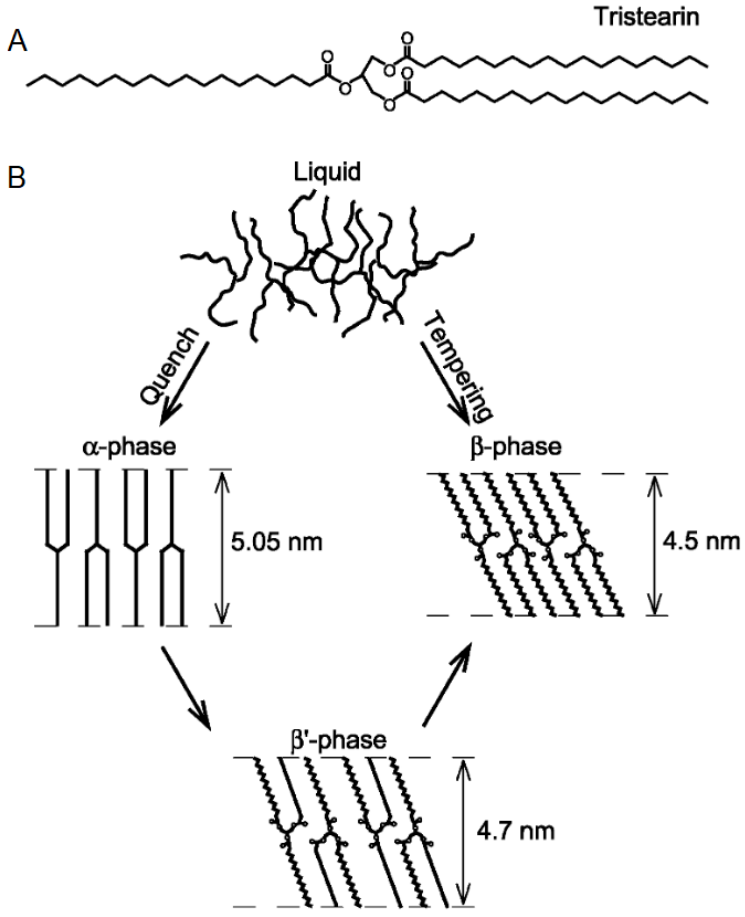

Fig. 8. *Molecular structure of tristearin (A) and its polymorphs (B), adapted from [128]*

Upon quenching (rapid cooling), tristearin forms meta-stable α-phase, which transforms into meta-stable β′-phase and finally to the stable β-phase. The direct path to β-phase transformation able to achieve by tempering or slow cooling to solid state. Tristearin showed “tuning-fork” conformation of

α (90° angle) and β′ (~70° angle) phases with random (loose) packing or moderate order respectively while stable β-phase has "chair" conformation (59° angle) with a tight packing and highest melting point of 73 °C. For α and β′ phases melting temperatures reaches 54 °C and 65 °C respectively. The β-phase crystals also are more ordered and larger when compared to other phase crystals. In general, the more disordered crystals with lower melting temperatures are formed by fast cooling while more organized crystals obtained by slower cooling [129].

The properties of solid state stearic a. and tristearin and liquid state oleic a. were shown in Table 1.

Table 1. *Properties of lipids*

Lipid	Molar mass, g/mol	Density at 20 °C, g/cm^3	Melting point, °C	Viscosity at 90 °C, mPa·s
Stearic a.	284.48	0.94	69.30	6.29
Tristearin	891.48	0.92	72.50	12.79
Oleic a.	282.46	0.89	13.00	4.85

It was shown that oleic a. have the lowest density and viscosity. For comparison, density and viscosity of oleic a. methyl ester, i.e. methyl oleate, is 0.87 g/cm^3 at 20 °C and 1.64 mPa·s at 90 °C respectively. This is even lower by comparing it with the tested lipids.

1.8.2 Friction of bio-based lubricants

Bio-based lubricants have been found to exhibit great lubricating properties over conventional mineral oils [130]. Due to renewability, biodegradability and non-toxicity they showed high potential for various applications including automotive, railroad, machinery, metalworking. In general, a lubricant should have high viscosity index, high flash point, low pour point, high oxidation stability and good corrosion resistance. Although vegetable oils have low chemical and oxidative stability, chemical modification such as hydrogenation or the use of antioxidants could solve those problems. Vegetable oils used for lubricants are mostly based on fatty a. and their esters. The narrow range of viscosity, low volatility and good friction properties make a vegetable oil a perfect candidate as lubricating material. It was shown that bio-based lubricants reduced friction on both steel [130] or Al_2O_3 [131] substrates with COF ~0.1. High polarity and fatty a. unsaturation with long and linear chains could increase better lubricity. The non-polar end of the fatty a. chain sticks away from the metal surface

while polar head attaches to the metal surface. Such arrangement results in the formation of a high strength monolayer film which reduces surface friction and wear [132]. However, studies showed that unsaturated fatty a. in the *cis* form have a lower ability to pack themselves close together, resulting in a weak protective film [133].

The ability to reduce surface friction and wear is based on tribofilm formation. Unlike the adsorbed film, which is formed by intermolecular forces between lipid and metal surface, tribofilm formation is influenced by tribochemical reactions and has different chemical composition, structure and tribological behavior [134, 135]. The lubricated friction depends not only on the chemical composition, structure and physical properties of the substrate and counterface but also on the tribological parameters including applied load, sliding speed, sliding distance, temperature and the chemical species in an environment. This suggests that the composition of anodized coatings ant electrolyte compounds might play an important role for tribofilm formation.

In general, tribofilms can be classified in four types: I) Tribofilms generated from the wear of the sliding surfaces; II) Tribofilms generated from the wear of the soft or lubricious constituents of a multi-phase or composite material; III) Tribofilms with different chemical composition and/or crystalline structure as a result of sliding contact; IV) Tribofilms generated due to tribochemical reactions between the wear products and the environmental species [135]. Tribofilms of the first type forms strong adhesive bonding to the worn substrate surface, which triggers high COF as detected on nitride coatings at the “run-in” friction stage [136]. For second type tribofilms, soft inclusions in the alloy structure act as lubricious films, which are transferred during sliding. Low friction was demonstrated with graphite particles [137] as well as MoS_2 particles [138] by forming a transfer film. In the third type, the tribofilm is formed depending on chemical reactions or phase transformation of the surface. The typical example is diamond-like carbon (DLC) coatings widely used in industrial, aerospace, medical and other applications due to low friction, wear and abrasion resistance. Sliding induced transformation from sp^3 diamond structure to sp^2 graphite structure significantly reduces friction with COF from 0.05 to 0.2 [139]. Tribofilm formation of the fourth type related not only to chemically reactive species such as oxygen or moisture but also includes lubrication. In lubricated sliding, fillers chemically adsorb and react with a surface by producing new compounds in the friction zone, which reduces friction and wear.

1.8.3 Migration of bio-based lubricants

The penetration of the lubricant into the pores of anodized coating might influence tribofilm formation and ability to sustain low friction. However, the detection of lubricant penetration is quite difficult and required specific methods. X-ray spectroscopy is not a very useful detection method for anodized coatings in cross-section area since organic molecules mostly consist of C, H and O atoms, which are widespread in any surroundings and able to contaminate the specimens. In previous study, penetration of methyl oleate in anodized coating of 6082 alloy was detected by confocal fluorescence microscopy using rhodamine B as a fluorophore. It was observed that impregnation possibly increases the penetration rate of methyl oleate for about two times using sonicated conditions rather than submersive procedure with depth of ~36 μm and ~15 μm respectively according to the fluorophore distribution [140]. However, some observations must be taken into account since the distribution of rhodamine B in the methyl oleate might be unequal due to different flowing rates. The sulfates or oxalates left in pores of anodized coating also might influence degradation, reduce the stability and fluorescent activity of fluorophore rhodamine B. Topografical features including pore size and surface porosity also very important for lubricant penetration rates into the anodized coating. Therefore, additional analytical methods are required to verify the measurements of the confocal fluorescence microscopy.

Raman spectroscopy is a non-destructive analytical method discovered by C. V. Raman in 1928. used to determine vibrational, rotational and other low-frequency modes of analytes. Raman provides detail information about chemical structure, crystallinity, phase, polymorphy and molecular interactions. When monochromatic light such as a laser is incident upon a sample it can be absorbed, reflected or scattered. Raman is based on inelastic scattering. Elastic scattered light at the wavelength corresponding to the laser line does not provide useful information about the material. As shown from the Jablonski diagram excited molecule can relax back down to the ground state and emit a photon of equal energy to that of the incident photon, which is known as Rayleigh scattering, Fig. 9.

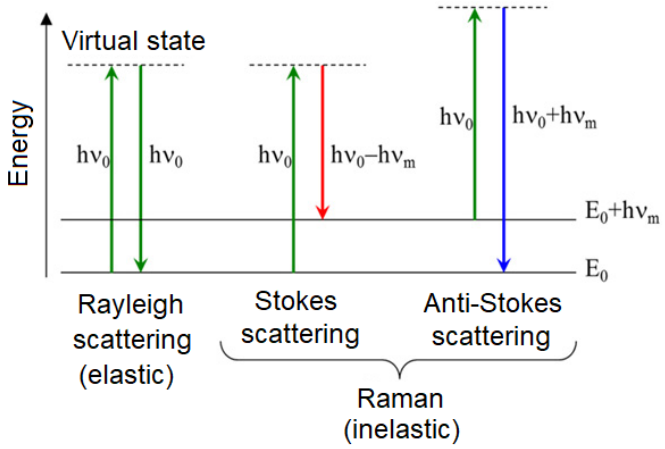

Fig. 9. *Jablonski diagram of quantum energy transitions for Rayleigh and Raman scattering, adapted from [141]*

However, a small amount of inelastic light (typically 0.0000001%) is scattered at different wavelengths known as Raman Scatter, which depends on the chemical structure of the analyte. Stokes Raman scattering occur when a molecule is relaxed to vibrational state and emit a photon with less energy (longer wavelength) than the incident photon. When a molecule from higher vibrational state is excited to a higher virtual state it can emit a photon with more energy (shorter wavelength) than the incident photon after relaxation. This effect is known as anti-Stokes Raman scattering. Only about 1 in 10^7 photons undergo Stokes Raman scattering while amount of anti-Stokes scattering is even lower. Although, the latter has the advantage to be less affected by the luminescence background. Most Raman measurements are performed considering only the Stokes shifted light because most molecules are found in the ground state at room temperature and have greater intensity. Raman scattering requires a change in polarizability, which describes the ability to respond to an electric field and acquire an electric dipole moment. The polarizability of a molecule increases with decreasing electron density, decreasing bond strength, and increasing bond length. Nonpolar bonds (e.g. C-C , C-H , C=C, N=N) are Raman active and polar bonds decrease in Raman activity as the electronegativity difference in the atoms in the bond increases. IR spectra provide complementary information about molecular vibrations due to active polar bonds (e.g. C-O , N-O , O-H). The choice of laser wavelength is very important for Raman spectroscopy because near infrared wavelengths decrease scattering coefficient. It is kown that wavelengths of 785 nm or 830 nm increase penetration depth and reduce

background fluorescence [142]. After disersion of the scattered light by diffraction grating Raman signal is collected using silicon based multichannel array charge-coupled device (CCD) detector. Raman spectrum give qualitative and quantitative information about the sample. The position of the peak correspond to the vibration of the functional groups and structure while its intensity correspond to concentration of the chemical species. The full width at half maximum (FWHM) of the peak show the structural disorder, defects and ctystallinity. In addition, the shift of band position is related to physico-chemical parameters such as phase or stress/strain as well as external parameters, i.e. temperature or pressure [143].

No sample preparation for solids, liquids and gases with ability using visible light are very favorable over other analysis techniques. However, the Raman signal is very weak, which leads to low sensitivity, making it difficult to measure low concentrations of the analyte. Surface-enhanced Raman spectroscopy (SERS) can significantly enhance Raman signals up to 10^6–10^{16} times [144]. SERS requires nanoscale roughened metal surfaces cover with or without nanoparticles typically made of gold [145], silver [146] or copper [147]. Laser excitation of these roughened metal nanostructures resonantly drives the surface charges creating a highly localized (plasmonic) light field. Resonance Raman scattering occurs when laser light is matched to the absorption maximum of the molecule. Previous studies showed that anodized coatings covered with gold, silver or copper can be manufactured into highly sensitive and low cost substrates for SERS [148, 149].

Raman spectroscopy could be used to evaluate the penetration of impregnated fillers into the anodized coating. Although the deposition of a metal layer could have a negative effect on penetration due to the pore closure, coatings with various pore sizes and patterns could be applied for evaluating the suitability of newly developed organic compounds.

2. EXPERIMENTAL

Most of the specimens were prepared by anodizing Al alloys and depositing nanothin layers of Ti/TiO_2 and other elements. Oxide layers were formed by ALD method. Magnetron sputtering device employed for deposition of Ti, Zr, Cu, Cr, Hf and Nb layers. Afterward, they were tested using ball-on-plate tribotesting. The biocompatibility of anodized and nanostructured coatings was evaluated by testing cell adhesion. The general concept of the experiments is presented in Fig. 10.

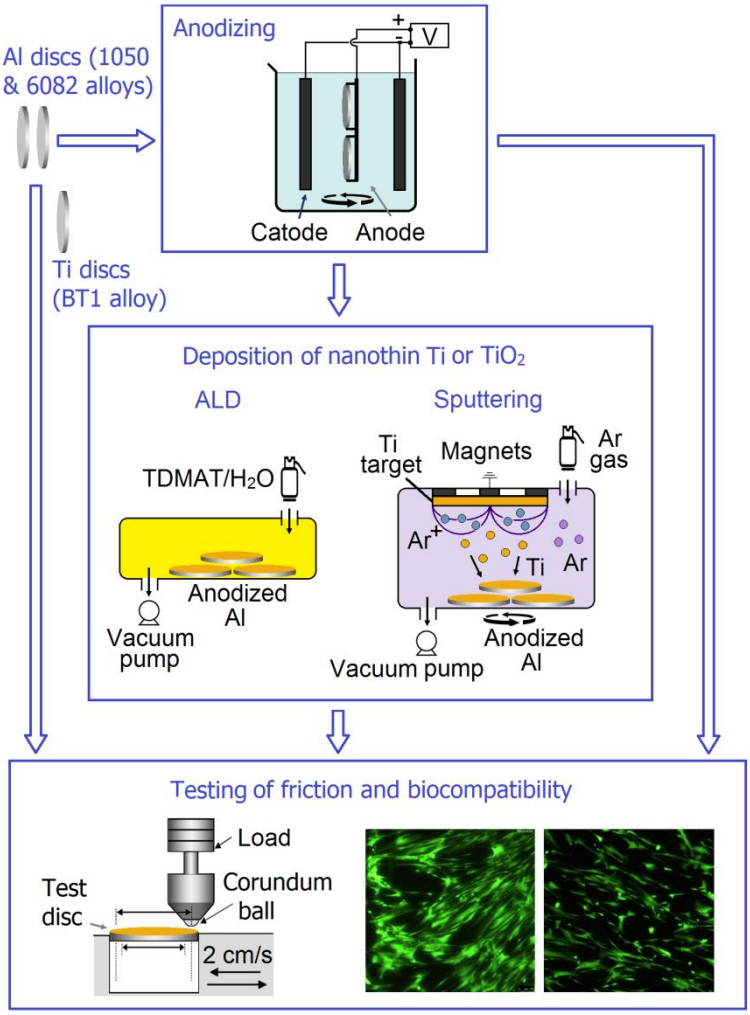

Fig. 10. *Schematic representation and the flow of specimens for nanostructuring, tribotesting and biocompatibility experiments performed during the study*

Many detailed explanations about materials, experiments and methods had already been presented in previous reports [131, 150–152].

2.1 Materials and cells

Industrial Al alloys, 1050 of 99.67% purity (0.25 wt.% Fe; 0.08 wt.% Si), 6082 of 96.72% purity (1.10 wt.% Si; 1.02 wt.% Mg; 0.61 wt.% Mn; 0.54 wt.% Fe), 7075 of 87.39% purity (7.74 wt.% Zn; 2.80 wt.% Mg; 2.08 wt.% Cu) with a sheet thickness of 2 mm and 16 mm OD from FXB-Niemet UAB (Lithuania) and 3003 of 98.51% purity (1.06 wt.% Mn; 0.30 wt.% Fe; 0.19 wt.% Si), 5005 of 97.59% purity (1.05 wt.% Mg; 0.86 wt.% Si; 0.38 wt.% Mn; 0.12 wt.% Fe) with a sheet thickness of 1 mm and 15 mm OD from Q-Lab Corporation (USA) were used as substrates. Polished Ti alloy BT1 (ASTM B 265; grade 37) of 96.32% purity (1.76 wt.% Mn; 1.75 wt.% Al; 0.11 wt.% Fe; 0.06 wt.% Si) and 1,5 mm thickness from SP MET UAB (Lithuania) was used as a control substrate for friction and biocompatibility tests. Al foil of 99.95% purity (0.03wt.% Fe; 0.02 wt.% Si) and 50 μm thickness (Russia) was used for penetration studies of impregnated compounds. Reagent grade salts and electrolytes were employed for the anodization and laboratory grade solvents were used for cleaning and degreasing of Al alloys.

Commercially available 99.99% Ti (Testbourne Ltd, UK), 99.20% Zr (Alfa Aesar, Germany), 99.90% Hf (Testbourne Ltd, UK), 99.95% Cr (Alfa Aesar, Germany), 99.99% Cu (Kurt J. Lesker, USA) and 99.80% Nb (Alfa Aesar, Germany) were used as sputtering targets for deposition. In ALD, compressed gas phase precursors 99% Tetrakis (dimethylamino) titanium (TDMAT) from Merck (USA) and 99.99% Tetrakis (dimethylamino) hafnium (TDMAH) from Strem Chemicals were used for TiO_2 or HfO_2 formation respectively.

The dyeing process was carried out with commercially available Sanodal Deep Black MLW and Sanodure Green LWN (Clariant, Switzerland) anionic dyes, hereafter referred as the “black dye” and “green dye”, respectively. Both dyes were dissolved in DI water with a concentration of 2 g/L. They represent widespread organic dyestuff compounds bearing the chromium-complexed azo moiety $Cr(R\text{-}N{=}N\text{-}R')_2$, typically with derivatized ortho-phenol substituents, in order to assemble color-producing conjugated chains and one or more anionic functional groups ($–SO_3H$, –Cl, –COOH, etc.) for better hydrophilicity, adsorption, and other properties.

Hanks balanced salt solution (0.185 g/L $CaCl_2 \cdot 2H_2O$ + 0.09767 g/L $MgSO_4$ + 0.4 g/L KCl + 0.06 g/L KH_2PO_4 + 0.35 g/L $NaHCO_3$; 8.0 g/L NaCl + 0.04788 g/L Na_2HPO_4; 1.0 g/L D-Glucose + 0.011 g/L phenol red · Na) of pH 7.2–7.6 from Carl Roth GmbH (Germany) was used for friction tests. Fluoropolymer-based DryFilm RA/IPA dispersion of 25% solids (DuPont) was reported to contain surfactants (CAS N° 65530-85-0, 24938-91-8 and 9002-84-0). The dispersion was agitated well before each use to achieve full homogeneity and applied as is or diluted with reagent grade isopropanol (Chempur, Czech) on volumetric basis of 25% to 2.5% solids. Technical grade oleic a. of 70% purity acquired from StanChem (Poland), stearic a. of 95% purity from Sigma (USA), tristearin of 80% purity from TCI (Japan) and fatty acid methyl ester (FAME) with ~60% methyl oleate (including ~20% methyl linoleate, ~9% methyl palmitate, ~5% methyl stearate, ~2% methyl linolenate, ~2% methyl laurate, <1% others) donated by Mestilla (Lithuania) were used for lubricated friction tests. Their structures are presented in Fig. 11.

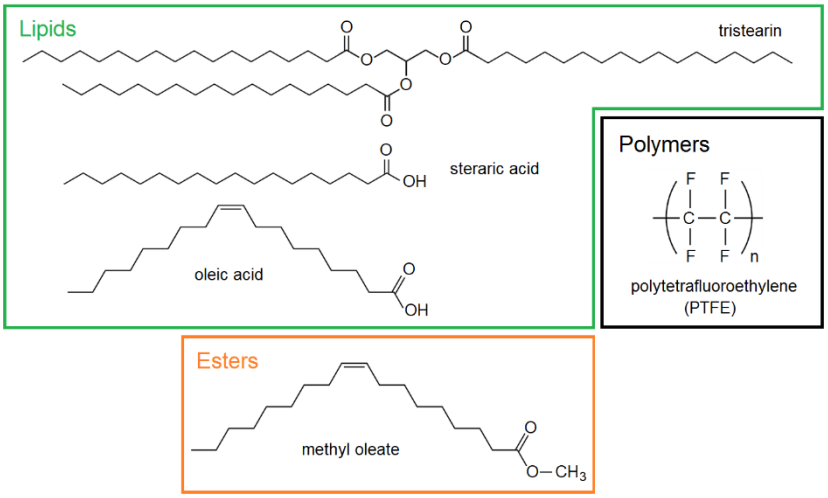

Fig. 11. *Chemical structures of investigated materials including lipids, esters and polymers*

Murine fibroblast cell line L929, human cervix carcinoma cell line Hep-2C (HeLa derivative) and Chinese hamster ovary cell line CHO-K1 were cultured in Dulbecco's Modified Eagle's medium (DMEM) (Corning, USA) supplemented with 10% fetal bovine serum (GE, USA). The cells were grown as a monolayer in plastic flasks (25 cm^2; Thermo Fisher Scientific, USA) at 37 °C in a humidified atmosphere containing 5% CO_2 until a

confluence of approximately 90% was reached. After that, the cells were washed with phosphate-buffered saline (PBS) and harvested by trypsinization (0.025% trypsin and 0.02% EDTA).

Primary periodontal ligament stromal (PDLS) cells were isolated from healthy periodontal tissues of 2 donors using explant outgrowth method [153]. The material was collected under the approval of the Lithuanian Bioethics Committee. The intact premolars of eighteen years old Caucasian woman were extracted because of orthodontic reasons. Periodontal ligament tissue was obtained from the middle third of the tooth root using surgical blades, minced, placed to the 35 mm diameter culture dishes and cultured in a low glucose DMEM supplemented with 10% fetal calf serum, 100 U/ml penicillin, 100 μg/ml streptomycin and 2 mmol/L L-glutamine (all from Biochrom, Germany). Hereinafter, this formulation will be referred as basal medium. Explant cultures were maintained at 37 °C in a humidified atmosphere containing 5% CO_2 with medium change routinely twice a week. For passaging cells were washed 3 times with PBS, harvested with 0.25% trypsin and 1 mmol/L EDTA solution (Gibco, Life technologies), resuspended in culture medium and plated onto cell culture flasks for expansion.

2.2 Anodization

Anodization was performed in aqueous H_2SO_4/oxalic a. or H_3PO_4 electrolytes. The H_2SO_4/oxalic a. electrolyte was used to produce relatively thick anodized coatings using Type III "hard" anodization procedure [93], while anodization in phosphoric a. electrolyte produces much thinner coatings. Beforehand Al discs were etched in an alkaline solution of 30 g/L NaOH + 25 g/L Na_3PO_4 + 75 g/L Na_2CO_3 for 45 s at 60 °C. After rinsing in DI water they were cleaned for 1–2 min in 30% HNO_3 and rinsed in DI water again. Then the discs were placed into the continuously mixed H_2SO_4/oxalic a. electrolyte (175 g/L H_2SO_4 + 30 g/L $(COOH)_2 \cdot 2H_2O$ + 55.5 g/L $Al_2(SO_4)_3 \cdot 18H_2O$) for 70 min at 2 A/dm^2 anodic current density. Anodization in 40 g/L H_3PO_4 electrolyte with or without additives (i.e. methanol, glycerol, citric a., tartaric a.) performed for 150 min at 120 V or 150 V at 15 °C. For optimal anodization conditions, current density was set at 1–3 A/dm^2, electrolyte temperature at 5–30 °C and anodization time from 30 min to 150 min. For surface treatment, Al alloys were etched in alkali/HNO_3 solution, Ar plasma using plasma surface treatment device (Diener electronic GmbH, Germany) at full power 50 W for 10 min or using

a combined treatment method with alkali/HNO_3 and Ar plasma. Some specimens were polished with 80 or 2500 grit papers before anodization.

Anodized coatings were periodically checked with CM-8825FN device (Guangzhou Landtek Instruments Co., China) to obtain up to 10 ± 5 μm thickness for phospho-anodization and 60 ± 10 μm thickness for hard anodization. After anodization, the discs were immersed into 170 W ultrasonic bath VTUSC3 (Velleman, Belgium) and sonicated at full power for 10 to 20 min in DI water without heat for rinsing. Then the discs were dried at 50 °C for 30 min and stored in a desiccator for 1 to 7 days for further experiments.

Al foil of 50 μm thickness was mounted in a special holder and anodized in sulfuric/oxalic a. electrolyte for 30 min. (partial anodization) or until the anodization current dropped to 0 (full anodization). A barrier layer with a growth rate of ~1.1 nm/V [154] formed during anodization assures mechanical integrity of the fully anodized Al foil. A vertical optimeter with a ± 1 μm measurement error was used to determine the thickness of the anodized coating. After anodization Al foil was dried at 60 °C for 60 min and stored in a desiccator for 1 to 7 days for further experiments.

2.3 Titration

The concentration of electrolytes was periodically checked by titration every three to six months to ensure concentration limits. The recommended concentration for H_2SO_4 is 15–20% [155], ~2–3% for oxalic a. [156] and ~4% for H_3PO_4 [157].

Concentrations of sulfuric and phosphoric a. were determined by colorimetric titration of 3 mol/L NaOH solution into H_2SO_4/oxalic a. or H_3PO_4 electrolytes in the presence of phenolphthalein. An indicator that is colorless in acid solution gives pink color in basic solution and remains for at least 15 s at the equivalence point. This shows that acid is completely neutralized with NaOH solution.

Determination of concentration of oxalic a. is based on oxidation and reduction reaction with potassium permanganate, which occurs in acidic medium. $KMnO_4$ is a powerful oxidizing agent, which turns oxalic a. into CO_2 gas and MnO_4^- is reduced to colorless Mn^{2+}. Self-indicator of 0.02 mol/L $KMnO_4$ gives a light pink color on the endpoint in the presence of H_2SO_4 at 60–70 ºC temperature.

0.1 wt.% aqueous solution of aluminon (aurintricarboxylic a. triammonium salt) was used for detection of Al^{3+} ions in the electrolyte. As

the $Al(OH)_3$ precipitates, it absorbs the aluminon reagent and assumes a red coloration known as a "lake," Fig. 12.

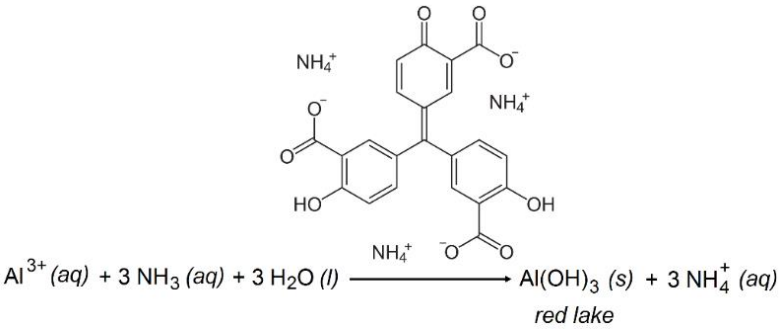

Fig. 12. *The reaction of aluminon for detection of Al^{3+} ions, adapted from [158]*

The test was made more specific by buffering the electrolyte to pH 4.5–5.5 with 3 mol/L CH_3COONH_4 to avoid interfere of uncommon metals (Pb, Zn, Co, Mn, Fe, Cr). The electrolyte was gently heated and pH was raised to 7.1–7.3 with 6 mol/L NH_4OH and $(NH_4)_2CO_3$ solutions [159, 160].

2.4 Atomic Layer Deposition

For TiO_2 layers, Al alloys were loaded into ALD system Fiji F200 (Cambridge NanoTech). Before deposition the discs of untreated alloys were etched in an alkaline solution for 45 s at 60 °C, neutralized for 1–2 min in 10% HNO_3 and rinsed in DI water to remove all impurities off the surface. Nanothin TiO_2 layers of 5 nm, 10 nm and 15 nm thicknesses were formed by a two-pulse process based on TDMAT chemisorption and its oxidation into TiO_2, Fig. 13.

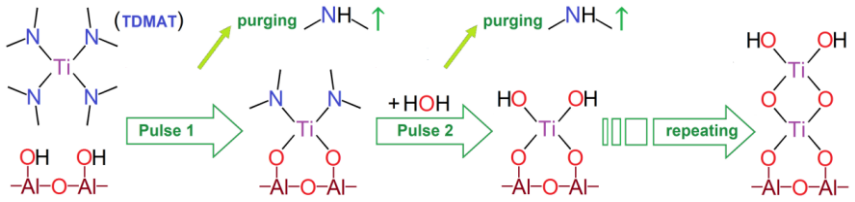

Fig. 13. *The scheme of the 2-pulse sequence of TiO_2 layer deposition, employed in ALD. Purging between the pulses is shown as removal of 2 moles of dimethyl amine. Pulse 1: TDMAT chemisorption with the release of two dimethyl amine molecules. Pulse 2: humid purge to hydrolyze chemisorbed monolayer into TiO_2 with the release of another two dimethyl amine molecules. Repeated pulses generate additional monolayers of TiO_2.*

Gas phase TDMAT served as a precursor of Ti-containing monolayer and water vapor as its oxidant. During Pulse 1, TDMAT was injected into the ALD chamber for 0.1 s, followed by purging with Ar gas. Then vapor of DI water was injected as Pulse 2 for 0.12 s and purged with Ar gas again, as itemized in Table 2.

Table 2. *Durations of pulses and injections with other parameters, selected for ALD deposition of investigated nanothin TiO_2 layers*

Deposited thickness	Duration, s								
	TDMAT Inject	Exposure to TDMAT	Ar purge	Water inject	Exposure to water	Ar purge	Cycle length	Total cycles	Total duration of ALD treatment
5 nm	0.10	45	55	0.12	45	55	200.22	100	5 h 33’42”
10 nm	0.10	15	20	0.12	15	20	70.22	250	4 h 52’35”
15 nm	0.10	13	15	0.12	13	15	56.22	375	5 h 51’22.5”

The deposition conditions for HfO_2 of 15 nm thickness were identical to TiO_2 deposition by using TDMAH as a precursor. The substrate temperature for the deposition of TiO_2 and HfO_2 was 250 °C under 30–35 Pa deep vacuum. The thicknesses of TiO_2 and HfO_2 layers were inferred from theoretical calculations, X-ray photoelectron spectroscopy (XPS) measurements and non-calibrated measurements using grazing incidence X-ray diffraction (GIXRD), so they should be considered approximate.

2.5 Sputtering

Deposition of Ti, Zr, Hf, Cr, Cu and Nb layers was performed by DC/RF magnetron sputtering device Univex 350 (Leybold Vacuum Systems, Germany). Before deposition the discs of untreated alloys were etched in an alkaline solution for 45 s at 60 °C, neutralized for 1–2 min in 30% HNO_3 and rinsed in DI water to remove all impurities off the surface. The specimens were placed into the rotary holder of the magnetron apparatus, the lid was closed and the chamber was vacuumized for at least 16 h before actual sputtering. The base pressure of the system was 250 μPa and the working pressure of Ar gas was kept constant at 250 mPa

maintaining substrate temperature at 12 °C. Thermal regime was balanced using two controls: 1) cooling by circulating cold water through the magnetrons and the specimen holder; 2) heating with integrated quartz halogen lamps, interfaced via programmable “SHQ15A TC/PID” controller (AJA International, USA). The distance of 20–25 cm between the target and specimens was too large to significantly affect the temperature of the substrate. Sputtering time, current and voltage were adapted to obtain a necessary thickness of Ti layers: 16 nm (t = 15 min, I = 100 mA, U = 421 V), 75 nm (t = 30 min, I = 200 mA, U = 420 V), 515 nm (t = 50 min, I = 1421 mA, U = 422 V) and 2.3 μm (t = 30 min, I = 400 mA, U = 375 V). Sputtering parameters of nanothin layers of other metals were listed next: 16 nm Zr (t = 7 min, I = 156 mA, U = 321 V), 75 nm Zr (t = 30 min, I = 154 mA, U = 323 V), 16 nm Hf (t = 13 min, I = 60 mA, U = 265 V), 75 nm Hf (t = 40 min, I = 105 mA, U = 285 V), 75 nm Cr (t = 40 min, I = 164 mA, U = 302 V), 75 nm Cu (t = 50 min, I = 70 mA, U = 367 V), 75 nm Nb (t = 25 min, I = 81 mA, U = 314 V). The target was cleaned with Ar^+ ions for 5–10 min at 100 W before sputtering to remove surface oxides, nitrides and other contaminants. The rotary sample holder with 6 specimens was turning during the sputtering process at 20 rpm to assure uniform patterns of deposited layers.

16 nm Ti layer was deposited in order to determine its weight by quartz crystal microgravimetry via resonator frequency change according to Sauerbrey ratio [161]. The resonator mass changes were translated into Ti layer thickness of 16 nm. Cross-sections of several discs were made and scanning electron microscopy (SEM) showed that 75 nm thickness was obtained, as described in §3. The deposition of the thickest Ti layer was performed by moving the specimens three times closer to the Ti target. Profilometry of the discs showed that 2.3 μm thickness was obtained, as described in §3. The average thickness of other metal layers (Zr, Hf, Cr, etc.) sputtered on Si plate was estimated from SEM or GIXRD measurements.

2.6 Biocompatibility studies

Before biocompatibility tests, untreated and anodized alloys were sterilized by steam autoclaving at 121°C for 15 min. Sterile Ti BT1 alloy samples were assembled into a custom-made sealed 6-well manifold (Center for Physical Sciences and Technology, Lithuania) for evaluation of most suitable cell line. The construct was sterilized by steam autoclaving (121°C

for 15 min) prior to every experiment. Ti BT1 alloy was used as a control specimen for biocompatibility studies. Ti BT1 alloy samples were embedded in the bottom panel of a construct, sealed with an O-ring and topped with an upper panel which formed a 6-well culture plate. Samples were prepared in duplicates. Suspension of 0.53 x 10^6/cm^2 cells was added on the metallic Ti BT1 alloys and samples were kept for incubation at 37 °C in a humidified atmosphere containing 5% CO_2 for 48 hours. The viability was determined using trypan blue staining and hemocytometry. The number of viable cells was counted by trypan blue exclusion in four quadrants of a hemocytometer. Trypan blue azo dye selectively colors dead cells blue due to high membrane permeability. The general scheme for cell preparation, adhesion and viability studies were showed in Fig. 14.

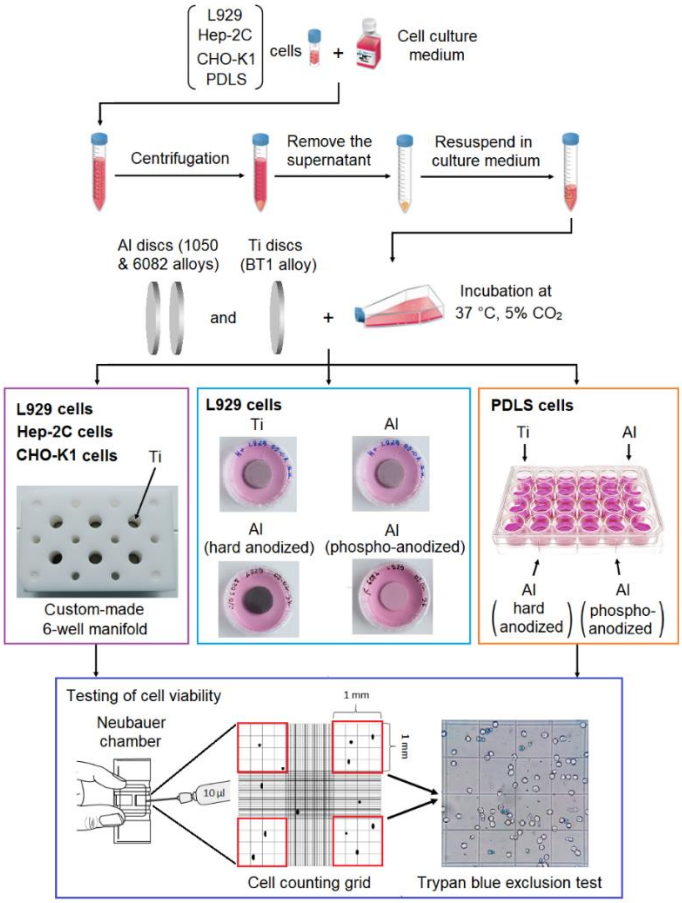

Fig. 14. *The procedure for cell preparation and evaluation of cell adhesion and viability*

Sterile Al and Ti alloy samples were placed into tissue culture plates (35 mm; Thermo Fisher Scientific, USA) for direct cell suspension interaction using cell line L929 ATCC CCL-1 (American Type Culture Collection, USA). Suspension of 0.075 x 10^6/cm^2 cells was added into culture plates and incubated at 37 °C in a humidified atmosphere containing 5% CO_2 for 48 hours. Incubated cells were further analyzed for morphology using Eclipse Ti-E microscope (Nikon, Japan) under 10× magnification.

For PDLS cells prepared alloy specimens were placed in the separate wells of 24 cell culture plates (Multiwell™, Falcon® Plates, Becton Dickinson Labware, USA) and 200 µl of the basal medium was added into each well. After 10 minutes, 300 µl of PDLS cell suspension was added onto each specimen. Growth kinetics of PDLS cells was measured by plating 4th passage cells at densities of 15000, 10000 and 8000 cells/1.9 cm^2 in replicate wells and counting the increase in cell number with time (after 24 h, 72 h, and 120 h respectively). Viable cells were counted by the hemocytometer (Fast-Read 102, Biosigma) using trypan blue (Sigma, USA) exclusion test.

For fluorescence imaging, after 48 h incubation, the specimens were stained with 1 µmol/L CellTrace™ Calcein Green (Invitrogen, USA). Fluorescent images of stained cultures were acquired with TCS SP8 DMI6000B microscope (Leica Microsystems) using DFC550 camera.

Statistical analysis for biocompatibility was performed using a one-way ANOVA analysis of variance followed by Bonferroni test using MaxStat Pro Statistics Software (Version 3.6). The statistical significance level was set at $p < 0.05$. Three independent experiments on 2 or 4 specimens obtained for cell adhesion to get statistically meaningful results indicated as significant ($*p < 0.05$), highly significant ($**p < 0.01$) and extremely significant ($***p < 0.001$) values.

2.7 Tribological tests

For tribological measurements, a Pin-on-Disc Tribometer (Anton Paar TriTec SA, Switzerland) was employed by utilizing a ball-on-plate linearly reciprocal configuration. As a stationary part, two types of 6 mm OD balls were used: 1) bearing steel 100Cr6 (96.5% purity, grade G100, hardness ~800 HV and roughness *Ra* 0.100 µm) and 2) corundum Al_2O_3 (99.8% purity, grade G16, hardness ~2900 HV and roughness *Ra* 0.025 µm) from RGP International Srl (Italy). The moving part was the Al disc, mounted on a pre-installed tribometer module. The linear reciprocal motion of 2 mm amplitude was maintained resulting in a track length of 4 mm and a total

distance of 8 mm for one reciprocal friction cycle. At 2 cm/s velocity each friction cycle produced approx. 100 data points of 'instantaneous' friction force, whose values remained sufficiently similar throughout the selected range of the reciprocal motion, i.e. the middle 80% segment [131]. The average dynamic COF value was calculated automatically by taking an arithmetical average of modular friction values for the central 80% segment of the path. COF was calculated from the ratio between friction force and normal force that is perpendicular to the surface (i.e. load). The results were presented as COF changes with progressing friction in terms of number of cycles. Corundum balls almost always have been used to measure the COF, therefore those conditions are not further mentioned in the results. In the case of steel balls were used, this is indicated in the description of the results.

Static COF was measured using 100 Hz data collection rate for improved sensitivity. COF data at such a high collection rate is strongly affected by surface roughness and debris particles [162, 163]. Therefore, fluctuations of COF curve were smoothened by averaging every 15 data points to get a representative segment of initial 10 friction cycles, Fig. 15.

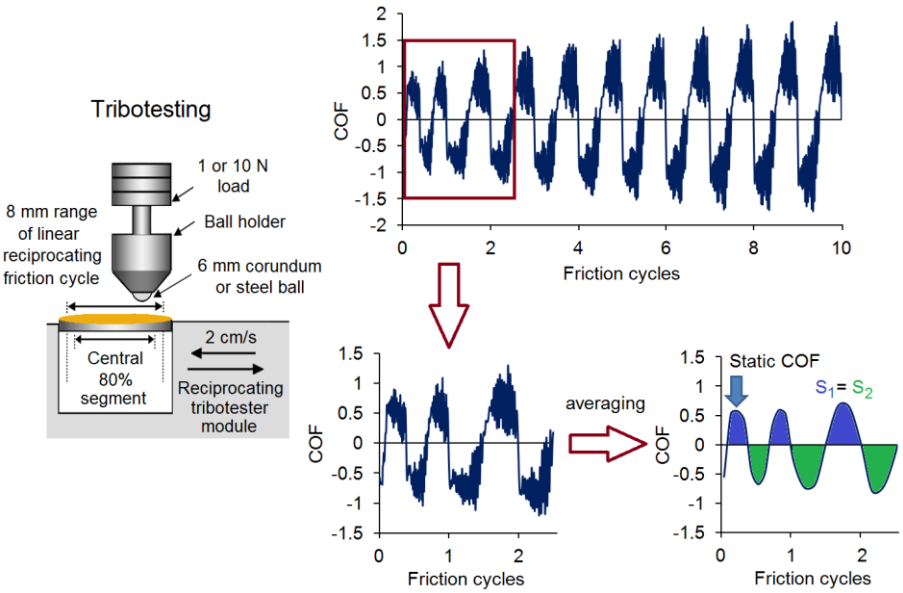

Fig. 15. *Scheme for tribotesting (left) and determination of static COF (right), adapted from [151]*

In the segment, the line of COF=0 was established with equal aggregates of ‘negative’ and ‘positive’ areas under the peaks. Static COF was determined at the maximum of initial value of the frictional force.

To ensure good reproducibility, each sample was tested 2 or more times at given conditions and the most representative runs were selected for the comparison between samples. The tribotesting parameters of 1 or 10 N loads, 2 mm amplitude and 2 cm/s velocity were held constant against a steel or corundum ball. Tribotest duration was either automatically limited due to excessive friction force because of an increase in COF, or stopped after a specified number of friction cycles, such as 10, 30, 500, 1000, etc.

Corundum balls have almost always been used to measure the COF, therefore these conditions are not mentioned further in the results. In the case of steel balls were used, this was indicated in the description of the results.

2.8 Microscopy studies

For optical microscopy analysis, a B-353 MET model with Optikam B2.0 digital camera was used (Optika SRL, Italy). Topographical changes were evaluated under 200× and 400× magnifications. No polarization or color filters were used.

SEM images were obtained using dual beam system Helios NanoLab 650 (FEI, Netherlands) with a Schottky type field emission electron source and a gallium (Ga) ion source at various magnifications from 1 500× to 350 000×. Thin layers of Cr were applied on all specimens in order to obtain the necessary electrical conductivity on the surface by using a magnetron sputtering device Quorum Q150T ES (Judges Scientific Plc, UK), which led to the Cr coating thickness of 2 to 3 nm. SEM images were used to determine the pore diameter, distribution and surface porosity. A number of pores were established by calculating the pores in 0.2 × 0.2 μm segments of the surface in 3–4 random areas to get the average pore density.

Porosity (%) was calculated using the following equation [157]:

$$\eta = \frac{S_{pore} \cdot n}{S_{ox}} \cdot 100\% \qquad (15)$$

where: S_{pore} is the average area of a pore opening, see eq (2), in μm²;

S_{ox} is the area of surface oxide, obtained as the 2D area selected for the calculation minus S_{pore} n (i.e. minus the area of pore openings), in μm²; n is a number of pores in the selected S_{ox} area.

The average area of a pore opening, S_{pore}, was calculated assuming a circular shape of the opening:

$$S_{ox} = \pi \cdot ID^2 / 4 \quad (16)$$

where ID represented an average Internal Diameter (ID) of the pore from SEM measurements, in μm.

Quantitative Energy-dispersive X-Ray Spectroscopy (EDS) was employed for elemental analysis using an INCA spectrometer with X-Max 20 mm^2 Silicon-drift detector (Oxford Instruments, UK). Elemental composition was reported as atomic weight percentage among investigated atoms (at.%) of Al, O, S, P, Si and Ti by excluding all other elements. EDS X-ray maps were recorded at 10 or 20 kV until a sufficient number of counts were collected to distinguish the most evident non-uniformities on the surface.

2.9 X-ray photoelectron spectroscopy

Elemental analysis of anodized coatings with Ti layers and its oxides was performed by XPS using an ESCALAB-MKII spectrometer (VG Scientific, UK). Non-monochromated Mg K (1253.6 eV) anode was used as an excitation source of photoelectrons, which was powered at 15 kV and 20 mA. The pressure in the analysis chamber was lower than $3 \cdot 10^{-7}$ Pa during spectral acquisition. The XPS core-level spectra of Ti 2*p*, O 1*s* and Al 2*p* were acquired at an analyzer pass energy of 20 eV with a 0.05 eV step and at a 90° take-off angle. The energy scale of the spectrometer was calibrated from the hydrocarbon contamination using the C 1*s* peak at 284.8 eV. The accuracy of the binding energy evolution was ± 0.1 eV. The sensitivity of the method used was 0.1 at.%. Ar^+ ion treatment for the surface cleaning was performed in the UHV preparation chamber at a pressure of $\sim 5 \cdot 10^{-4}$ Pa using a 3 kV Ar^+ beam energy at an angle of ~60°. Nanostructured coatings were etched at 20 μA/cm^2 current density with a rate of ~3 nm/min, while 20 μA/cm^2 and 50 μA/cm^2 current densities were used for etching of anodized coatings. The spectra calibration, processing, and fitting routines were done using Avantage software (5.962) provided by Thermo VG Scientific. Core level peaks of Ti 2*p*, O 1*s*, and Al 2*p* were analyzed using a nonlinear Shirley-type background. The spectra were then fitted with Gaussian-Lorentzian type functions.

2.10 Hardness measurements

Vickers microhardness of untreated Al alloys and anodized coatings, obtained at 5–30 °C temperatures in the sulfuric/oxalic a. electrolyte were measured using an indenter PMT-3 (Russia). Beforehand, the cross-section was done over disc-shaped anodized Al specimens. No cross-section was made for untreated alloys. HV was measured from the top side of the specimen. For anodized alloys, the side for HV evaluation was polished by 320–2500 grade emery paper using vertical and lateral movements to achieve a smooth surface. After cleaning in acetone, untreated and anodized 1050 and 6082 alloys, were placed into indenter for testing using a square-based diamond pyramid with an angle of 136°. High purity Al (99.99%) foil was used for HV calibration at 20 °C. The indenter load of 5 or 20 gf was maintained for 10 s to calculate HV (kgf/mm^2) using the following formula [164]:

$$HV = 2 \sin(\theta/2) \cdot P / d^2 \quad (17)$$

where θ is apex angle of diamond prism; P is load, kgf; d is diagonal of surface indentation mark, mm.

The average value of HV was calculated from 7 or more measurements of cleaned Al surfaces and anodized coatings.

2.11 Roughness measurements

The surface roughness (*Ra*) and depth of wear track were evaluated with a contact profilometer Surftest SJ-210 (Mitutoyo, USA) using a diamond needle of 2 μm tip radius, which was scanning the surfaces horizontally within 1.5 mm of the path. Image Plus™ software was used for data acquisition. The *Ra* was calculated from at least 5 measurements on different locations within the same specimen. Four specimens were used to determine average *Ra* on untreated and anodized samples without Ti layers, while 2 specimens were used to determine *Ra* of samples with Ti layers. For measuring the average elevation, the median planes were projected by equating the peak volumes above the planes with the void volumes underneath them.

2.12 Penetration studies of organic fillers

The Raman spectroscopy method was used to evaluate the penetration of methyl oleate through fully anodized Al foil. A small droplet of methyl oleate (~10 μL) was deposited on anodized foil and kept for one hour at

room temperature. After that excessive layer of methyl oleate was removed from a surface by microfiber paper. Raman spectrometer with confocal microscope inVia (Renishaw, UK) was used for spectra registration by using a diode laser of 785 nm beam as an excitation source. The system utilizes a backscattering configuration to collect the Raman signal through a microscope vertically. The beam was focused into a ~1 μm diameter spot on the surface of anodized Al foil with laser power of 4.5 mW. The laser beam was directed downwards by focusing the beam from the surface up to 54 μm in depth with a step size of 6 μm. A 50× microscope objective with short working distance of 0.3 mm and long working distance of 8 mm was used for signal collection at room temperature. Raman signal directed onto a grating (1200 l/mm) and dispersed on thermoelectrically cooled CCD detector. The migration of methyl oleate was detected on two anodized foils by testing three different places under the same spot. Each spectrum accumulated 10 scans with an integration time of 30 s, which were divided by the total accumulation time followed by subtraction of background. Raman peak positions were calibrated using a silicon wafer sample measured at 520–521 cm^{-1}.

For penetration studies of anionic dyes through fully anodized Al foil the near-IR diode laser operating at 785 nm was initially focused into a ~200 μm diameter spot of the anodized foil with laser power of 30 mW and the working distance of 7 mm, Fig. 16.

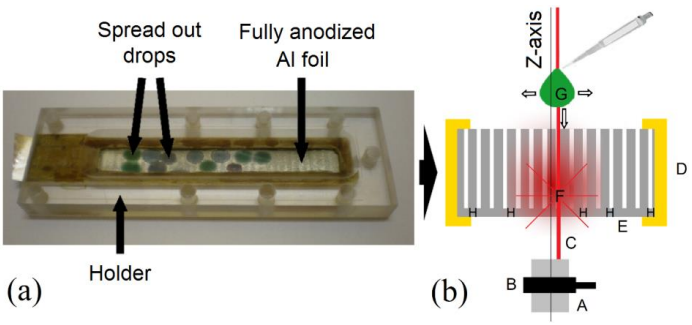

Fig. 16. *(a) Real image of the template (i.e. fully anodized Al foil) in the holder after dye was dropped onto it and Raman spectroscopy measurements were carried out; and (b) principal scheme of Raman spectroscopy measurements: A = fibre optic cable for working distance of 7 mm; B = holder, which shifts along the Z axis; C = 785 nm laser beam; D = holder with fixed position; E = the template, i.e. fully anodised aluminium foil of 70 μm thickness; F = approximate focus position of the laser beam; G = dye drop, with arrows showing overspread directions; H = barrier layer (~10–20 nm) of anodised part of Al foil. Not to scale, adapted from [152]*

Raman spectra were recorded with an Echelle type spectrometer RamanFlex 400 (PerkinElmer, Inc., USA) with a thermoelectrically cooled CCD detector and a fibre optic cable for excitation and collection of the spectra at room temperature. For all specimens, photoluminescence (PL) scans were recorded to establish the feasibility of Raman spectra collection. Before dye deposition the beam was advanced into the inside of anodized Al pores from the bottom until the intensity of background PL achieved the maximum value. The maximum PL was attained at the point of highest Al_2O_3 abundance, indicating that the beam's focus included the entire barrier layer. Periodically, Raman spectra were collected within 1 hour or less after dye deposition with a volume of 5 μL from 5 different spots. Each spectrum accumulated 3 scans with an integration time of 10 s and divided by the total accumulation time followed by subtraction of background fluorescence. The polystyrene standard (ASTM E1840) spectrum was used for calibration. Spectral analysis was obtained with Grams/AI 8 software (Galactic Industries Co, USA).

2.13 Impregnation of organic fillers

Raman spectra of bare lubricants including lipids, esters and polymers were obtained after deposition a droplet of 1 μL on a stainless steel plate.

Lipids (stearic a., oleic a. and tristearin), methyl oleate, lipid filler and 18Z filler were melted and the specimens were immersed for 1 hour at 90 °C. Afterward, the coated discs were suspended in the oven for at least 1 hour to ensure homogeneous distribution of the film on the surface. Visually only completely transparent layer of liquid or solidified (for stearic a. and tristearin only) film could be observed on the specimens without any agglomerations of white color.

Oleic a. films of 15 μm, 30 μm, 50 μm, 100 μm and 200 μm thicknesses were deposited on anodized alloys using analytical balances MXA 5/1 (Radwag, Poland). The required amount of oleic a. (g) was calculated using the formula:

$$m = S \cdot V \cdot \varrho \tag{18}$$

where S is surface area, cm^2; V is layer thickness, cm; ϱ is the density of oleic a., g /cm^3.

Coated discs were placed for 1 hour at 90 °C and stored in a desiccator for 24 hours before tribotesting.

2.14 Deposition of PTFE coatings

PTFE was applied with dilution from 2.5% to 25% solids in IPA. The anodized alloys were immersed for 15 minutes then removed and suspended vertically in air for 30 min. Per manufacturer's recommendation the dried specimens were placed into the tube furnace RS 80/500/11 (Nabertherm GmbH, Germany) at 310 °C for 10 min curing, then cooled in a furnace to ambient temperature.

3. RESULTS AND DISCUSSION

This chapter consists of four parts. The results outlined in the three parts support the appropriate defensive statement. The first part is dedicated to the selection and characterization of research objects.

3.1 Development of nanostructured anodized coatings on aluminum alloys and their characterization

During the investigation of chemical, tribological, biomedical and many other processes on anodized coatings, it is important to evaluate the structural, morphological and topographical properties of surfaces. Although the anodization of chemically pure Al and its surfaces are widely described, the anodized coatings using industrial Al alloys are much less studied in scientific research. Anodization of industrial Al alloys increases surface hardness, corrosion resistance by forming thick Al_2O_3 coating which has great potential not only for high-tech (robotics, aerospace, etc.) but also for biomedical applications. However, despite its hardness, protective properties of anodized coatings are poor leading to rapid surface wear under high loads. Some researchers [13] tried to incorporate TiO_2 nanoparticles into phospho-anodized coatings of just 6 μm thickness. In nanopores of 125 nm ID they were able to achieve nearly complete filling. The obtained coating had COF within 0.1–0.2 and much better resistance to wear. The tribological performance was just slightly better than that of a pre-compressed TiO_2 slab. This agreed with the expectations quite well, because the composite coating contained large amounts of TiO_2. In addition, the use of nanostructured coatings in biomedical applications is still very little studied. It is also important that the mechanisms of wear on porous coatings are significantly different from those occurring in the classical friction zones, therefore, the methods for the formation of tribofilms and wear reduction have not yet been clearly identified. Therefore, it is necessary to examine in detail various anodizing conditions and the morphology of nanostructured coatings.

3.1.1 Influence of alloy on anodized coatings

Low cost, easy workability and lightness of Al alloys offer many advantages in the industrial and medical field. High purity Al (>99.999%) has insufficient mechanical properties, while tensile strength and hardness are two times lower compared to commercially pure 1xxx series Al alloys (>99.5%) [165]. Al alloys can be grouped into 8 major categories depending

on alloying additives, but only the most suitable wrought Al alloys for anodization was chosen in this study are listed in Table 3.

Table 3. *Properties of Al alloys*

Al alloy	Al, wt.%	Fe, wt.%	Si, wt.%	Mg, wt.%	Mn, wt.%	Cu, wt.%	Zn, wt.%	Surface roughness *Ra*, μm	Vickers microhardness $HV_{0.02}$, kg/mm^2
foil	99.95	0.03	0.02	-	-	-	-	0.68 ± 0.09	38 ± 4
1050	99.67	0.25	0.08	-	-	-	-	0.99 ± 0.09	31 ± 4
3003	98.51	0.30	0.19	-	1.06	-	-	0.83 ± 0.13	28 ± 2
5005	97.59	0.12	0.86	1.05	0.38	-	-	0.81 ± 0.14	33 ± 5
6082	96.72	0.54	1.10	1.02	0.61	-	-	1.28 ± 0.08	139 ± 10
7075	87.39	-	-	2.80	-	2.08	7.74	0.86 ± 0.08	99 ± 10

Optical microscopy images revealed different topography of higher and lower purity Al alloys. It must be pointed out that the Al alloys used in this study were not mechanically pre-treated, i.e. they were not polished or abraded. The microscopy showed that surfaces contained high levels of various imperfections and grain-like inclusions appeared during the rolling process in alloy manufacture, Fig. 17.

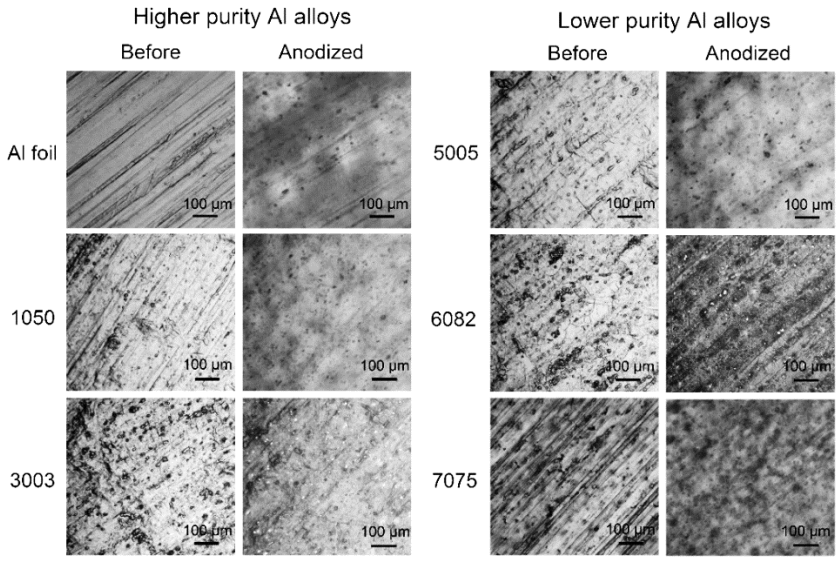

Fig. 17. *Optical microscopy images of higher purity (left) and lower purity (right) Al alloys before and after anodization in sulfuric/oxalic a. electrolyte*

Al foil, 1050 and 5005 Al alloys have more plain structure when compared to 3003 and 6082 alloys before and after anodization. Many cracks observed on 6082 alloy suggests that the content of alloying additives i.e. Si, Mg, Fe, Mn significantly affects the surface structure. Surface cracking of 6082 alloy remains even after anodization.

The surface roughness of untreated and anodized Al alloys was evaluated by a profilometer. Among all Al alloys, 6082 have the highest surface roughness reaching *Ra* value of 1.3 μm while mostly alloys have roughness about 1 μm or less, annex Fig. S1. Anodization has almost no influence on roughness despite some variations within the margin of errors.

Out of a variety of tested alloys, 1050, 6082 and Al foil were selected for detailed investigations. Al foil of 99.95% purity and 1050 alloy of 99.67% purity have the lowest content of additives as well as low surface hardness. For comparison, 6082 alloy has low purity and highest surface hardness. 1050 and 6082 Al alloys represent distinctly different materials, widely used in the metalworking industry. Commercially pure 1050 alloy is often used in the food and chemical industry, while 6082 alloys are applied to technical facilities where surfaces are exposed to high stresses and loads [166]. Both 1050 and 6082 alloys offer good anti-corrosive properties, but 1050 provides better plasticity and formability. Heat treatable 6082 alloys have higher strength and mechanical resistance primarily due to Mn, Mg and Si alloying additives. Vickers microhardness studies confirmed that 6082 is 4.5 times harder than 1050 alloy. Alloys 1050 and 6082 are more technologically applicable not only for the lower price, accessibility but also for the physical-mechanical properties.

Al discs and foil were anodized in a technologically widespread electrolyte of sulfuric and oxalic a. for Type III “hard” anodization. In this study, the target thickness for hard anodized Al alloys was 60 ± 10 μm. For comparison, phospho-anodized coatings obtained in H_3PO_4 electrolyte with or without additives were used since phosphates act as anti-wear compounds [167] and their anions are biocompatible to the human body [168].

Non-conductive anodized coatings were sputtered with 2–3 nm Cr layer for better electrical conductivity in order to obtain SEM images. As expected, SEM images revealed a porous structure of anodized coatings obtained after hard anodization, Fig. 18.

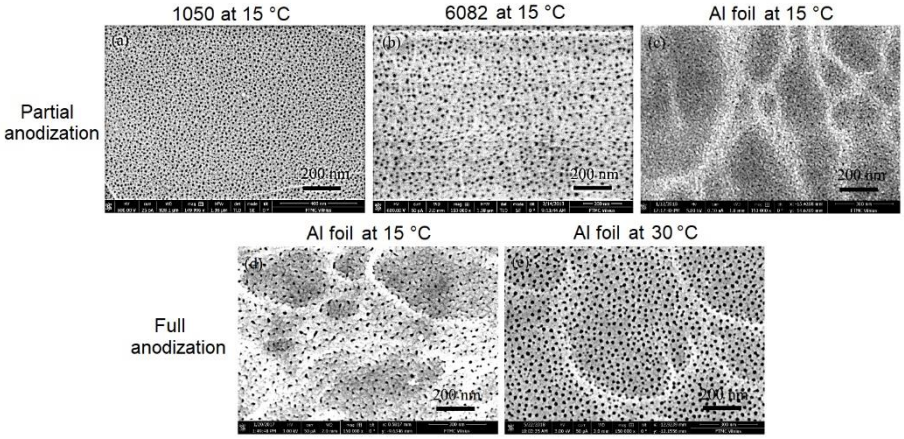

Fig. 18 *SEM images of surfaces of partially and fully anodized Al specimens in sulfuric/oxalic a. electrolyte. Partial anodization at 15 °C: (a) 1050 disc, (b) 6082 disc, and (c) foil. Fully anodized foils at (d) 15 °C and (e) 30 °C, adapted from [152]*

Size of the pores and distribution was clearly different, with their main characteristics given in Table 4.

Table 4. *Characteristics of surface pores obtained after partial and full anodization in sulfuric/oxalic a. electrolyte, adapted from [152]*

Alloy; anodization conditions	Thickness of anodized coating, μm	Pore diameter, nm	Pore density, pores/μm^2	Porosity, %
1050; partial at 15 °C	60 ± 1.0	6.5 ± 1.3	1560 ± 110	5.5
6082; partial at 15 °C	60 ± 1.4	15.0 ± 2.2	1040 ± 121	22.5
Al foil; partial at 15 °C	20 ± 1.1	7.6 ± 2.9	1207 ± 39	5.8
Al foil; full at 15 °C	70 ± 1.0	13.2 ± 2.1	530 ± 34	7.8
Al foil; full at 30 °C	68 ± 1.0	15.9 ± 2.5	770 ± 39	18.0

SEM data showed that pores in 6082 are at least twice as wide as those in 1050, with the porosity nearly four times higher in H_2SO_4/oxalic a. electrolyte. This shows that porosity not only depends on anodization conditions i.e. temperature, electrolyte concentration, current density, voltage, but also on substrate properties. When compared Al alloys to Al foil of partial anodization, pore diameters of 1050 alloy and Al foil was similar 6.5 nm and 7.6 nm respectively. This agrees well with the relatively high purity (>99.5%) of both Al foil and 1050 alloy in contrast to 6082 of only

96.72% purity with a pore diameter of 15 nm. In contrast to partial anodization of Al foil, full anodization has shown increased pore diameter (7.6 vs 13.2 nm). When anodization approaches nearly hollow pores in the Al foil, its ohmic resistance begins to increase rapidly and leads to higher spot temperatures within the pores. This accelerates the dissolution of Al_2O_3, resulting in larger pore diameters. Much wider pores and surface porosity can be obtained at higher temperatures due to the intensive chemical dissolution of Al_2O_3 in the anodization electrolyte [169].

After full anodization thickness of Al foil increased from 50 μm to 70 μm by suggesting that Al_2O_3 coating able to builds up on the top of Al surface, annex Fig. S2. The balance of two competing processes: formation and chemical dissolution of Al_2O_3 is crucial for the growth of porous anodized coating in the entire anodization process [170]. The theoretical volume expansion factor of the anodized coating is 1.6 when the formation current efficiency is 100%. However, the experimental values can range from 0.8 to 1.6 [111]. The volumetric growth of the anodized coating depends not only on anodization conditions but also on electrolyte and its concentration. SEM images of fully anodized Al foil confirms the expectation that pores are distributed equally without significant differences in pore distribution, density or thickness when comparing three different segments from the top, centre and bottom of cross-sectional analysis.

3.1.2 Influence of electrolyte on anodized coatings

Studies showed that the structure of anodized coatings significantly depends on the composition of Al alloys. However, electrolyte and anodization conditions also affect surface properties. SEM revealed that topography of Al surface was irregular and contained many grain-like inclusions formed after Al rolling process with surface roughness of 0.99 μm for 1050 alloy and 1.28 μm for 6082 alloy respectively. Alloying additives of Fe and Mn elements forming an intermetallic second phase that reduces the size of grain boundaries due to low solubility, which is 0.05% for Fe and 0.30% for Mn [171]. Grain boundaries (crystallites) generally accepted as 2D defects in a polycrystalline material. On 1050 and 6082 alloys grain boundaries of various sizes could be observed mostly less than 10 μm in size, Fig. 19. According to previous studies, the size of grain boundaries can exceed 100 μm which is common in 6000 series alloys [172]. Anodization in H_2SO_4/oxalic a. and H_3PO_4 electrolytes reduced the size of grains on both 1050 and 6082 alloys suggesting the formation of anodized coatings with randomly oriented crystallites.

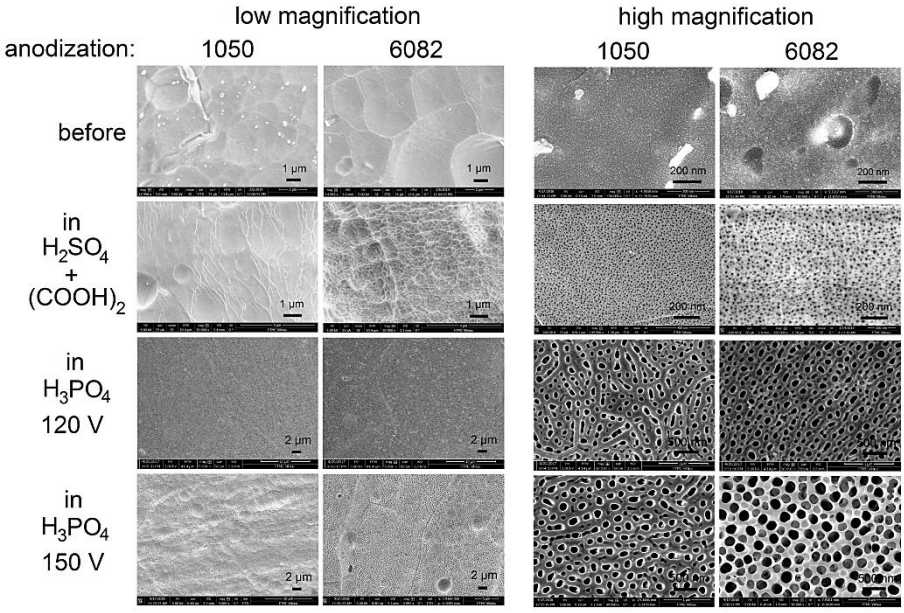

Fig. 19. *Topography of Al surfaces under low (left) and high (right) magnifications, evaluated by SEM, before and after anodization*

Surface nanotopography revealed significant changes in the structure of anodized coatings at high magnification using a different type of electrolytes. Anodized surfaces contain many pores, while untreated surfaces showed similar plain structure with grain-like inclusions of unretained alloying additives. According to results thick coatings with small pores (<20 nm) are produced in H_2SO_4/oxalic a. electrolyte, while thin coatings with large pores (>100 nm) are formed in H_3PO_4 electrolyte, see Table 5.

Table 5. *Characteristics of surface pores, obtained after anodization at 15 °C, adapted from [151]*

Electrolyte	Al alloy	Coating thickness, μm	Pore diameter, nm	Pore density, pores/μm^2	Porosity, %
H_2SO_4/oxalic	1050	59 ± 2	7 ±1	1560 ± 110	6
	6082	56 ± 2	15 ± 2	1040 ± 121	23
H_3PO_4 (120 V)	1050	7 ± 1	110 ± 23	22 ± 2	27
	6082	6 ± 1	119 ±14	25 ± 2	39
H_3PO_4 (150 V)	1050	15 ± 2	144 ± 11	19 ± 2	44
	6082	11 ± 1	203 ± 19	14 ± 2	83

Much wider pores can be obtained by increasing anodization voltage. When voltage was raised to 150 V in H_3PO_4 electrolyte surface porosity increased two times especially on 6082 alloys with average pore diameter over 200 nm. Such differences could have significant influence not only on adhesion of various layers including Ti or TiO_2 but also on tribological tendencies. Studies showed that independently of the type of electrolyte, voltage or anodization time surface roughness *Ra* values vary between 0.8 µm to 1.0 µm for 1050 alloy and 1.3 µm to 1.5 µm for 6082 alloy, annex Fig. S3. Despite somewhat higher roughness of 6082 alloy, *Ra* values were quite similar suggesting that effect of surface roughness on tribological and biological characterization should be negligible.

Additives in H_3PO_4 electrolyte was added to increase the coating thickness of anodized Al. According to studies, the optimal additive concentration is 1% [173]. The thickness of anodized coating increased 1.5 times after anodization in H_3PO_4 electrolyte with 1 wt.% glycerol at 150 V, see Fig. 20.

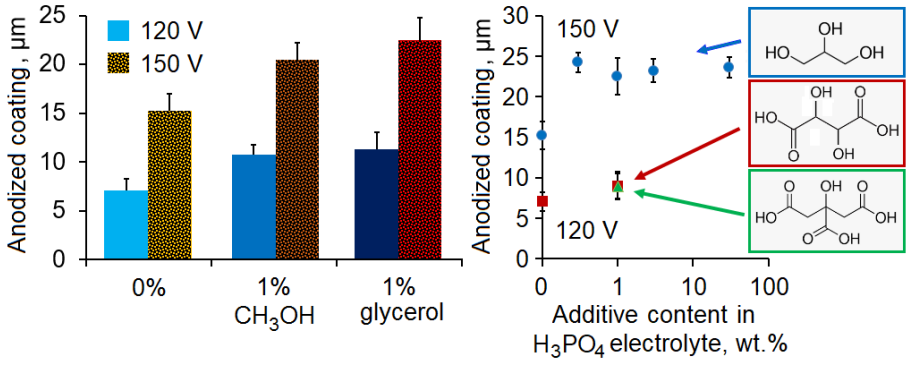

Fig. 20. *Influence of additives in phosphoric a. electrolyte (150 min at 120 V or 150 V) on anodized coating thickness of 1050 alloy*

However, thickness remains similar by increasing glycerol content even to 30 wt.%. It must be mentioned that coating thickness significantly depends not only on the type of electrolyte, bus also no anodization voltage. 150 V increased thickness about 2 times when compared to 120 V. Other additives including methanol, tartaric a., citric a. were less effective. Higher thickness of anodized coating related to the high viscosity of glycerol when compared to water (1500 cP vs 1.0087 cP at 20 °C), which reduces the dissolution rate of Al_2O_3 [174]. Methanol, which also showed a positive

effect maintains temperature changes at Al_2O_3/electrolyte contact area more efficiency due to a lower evaporating temperature than water [175].

3.1.3 Influence of anodization parameters on anodized coatings

As mentioned before, anodization conditions significantly influence the structure of anodized coating. Optimal conditions of porous coating formation for hard anodization at 15 °C temperature is showed in Fig. 21. An anodic current density of 2 A/dm^2 is suitable for both 1050 and 6082 alloys. No porosity with severe surface damage was observed on 6082 alloys at 3 A/dm^2 while the formation of irregularly shaped pores found after anodization at 1 A/dm^2 anodic current density.

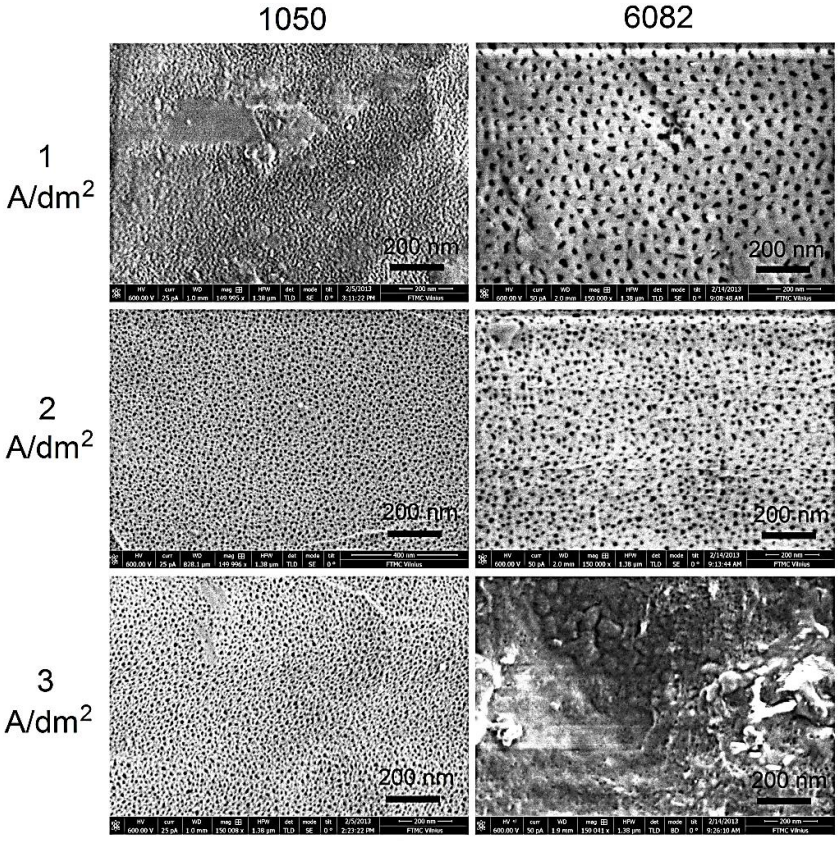

Fig. 21. *Influence of current density on anodized coating formation in sulfuric/oxalic a. electrolyte at 15 °C*

The thickness of anodized coatings is important for tribology and mostly depends on the type of electrolyte, alloy properties and anodization

conditions i.e. time, current density or applied voltage. The influence of anodization time and voltage on anodized coating thickness were shown in Fig. 22.

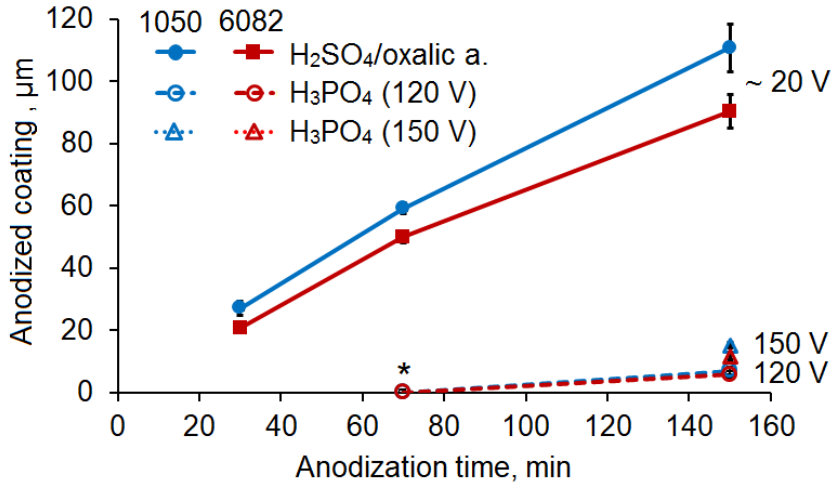

Fig. 22. *Influence of anodization time and voltage on the thickness of anodized coating at 15 °C. Values assigned for (*) are below the detection limit, measured by coating thickness meter and optical microscopy*

The thickness of porous Al_2O_3 increases in time by forming 90–110 µm and 10–15 µm anodized coatings in H_2SO_4/oxalic a. (~20 V) and H_3PO_4 (150 V) electrolytes after 150 min of anodization respectively. The thickness of phospho-anodized coatings was too low for its determination after 70 min of anodization by using a coating thickness gauge device and optical microscopy. When changing anodizing potential between 120 V and 150 V it was observed that higher thickness of the phospho-anodized coating can be much easier achieved with the latter, which also resulted in shorter durations. Two times thicker coatings were obtained by raising anodization voltage from 120 V to 150 V using H_3PO_4 electrolyte. The target thickness was set to 10 ± 5 µm for phospho-anodized coatings and 60 ± 10 µm for hard coatings produced in H_3PO_4 and H_2SO_4/oxalic a. electrolytes respectively. Anodized coatings with 60 ± 10 µm thickness are optimal for "hard" anodization showing much better reproducibility than thicker coatings. Despite that coating thickness is slightly lower on 6082 the differences are not significant for tribological circumstances.

Electrolyte temperature almost has no influence on the thickness of anodized coating by changing the temperature from 5 °C to 30 °C, despite higher variations at 30 °C, see Fig. 23.

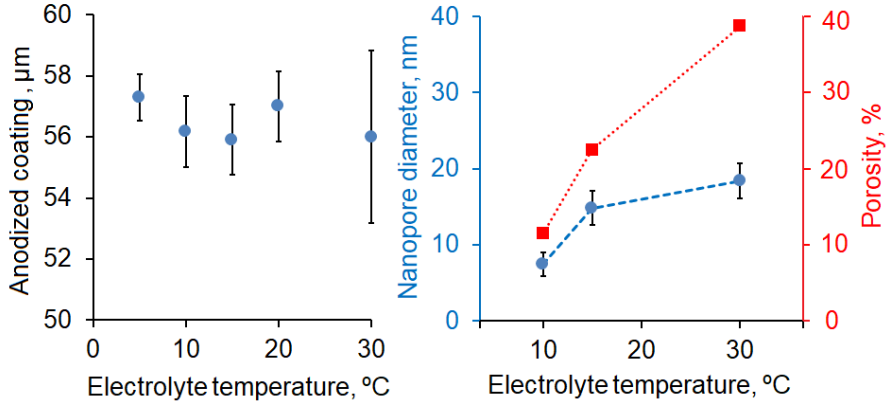

Fig. 23. *Influence of temperature in sulfuric/oxalic a. electrolyte on characteristics of anodized coating thickness (left) and surface pores (right) of 6082 alloy*

However, the surface structure of anodized coatings changes dramatically. Higher temperature increases dissolution rate of anodized coating leading to wider pore diameter and surface porosity. SEM images confirmed that pore diameter depends on electrolyte temperature. Small pores with less than 10 nm are obtained at 10 °C, while wider pores are produced at 30 °C of anodized 6082 alloys, Fig. 24.

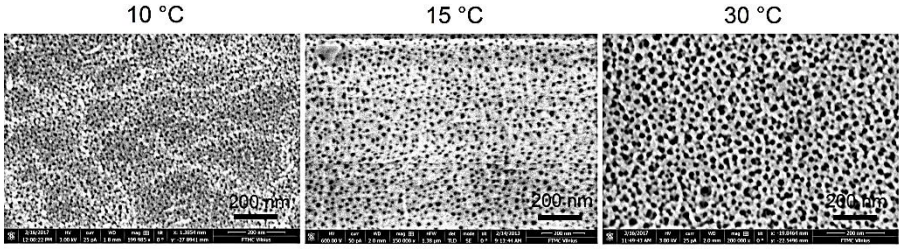

Fig. 24. *Influence of temperature on surface nanotopography of hard anodized 6082 alloys, evaluated by SEM*

Higher dissolution of hard anodized coatings often leads to pore merging and irregular pore structure.

The surface roughness of anodized coatings showed only slight variation against electrolyte temperature on both 1050 and 6082 alloys, Table 6.

Table 6. *Influence of anodization temperature in sulfuric/oxalic a. electrolyte on surface roughness (Ra) and hardness (HV)*

	Surface roughness *Ra*, μm		Surface hardness, HV	
Al alloy	1050	6082	1050	6082
Before anodization	0.99 ± 0.09	1.28 ± 0.08	31 ± 4	139 ± 10
Anodized at 5 °C	0.75 ± 0.09	1.48 ± 0.16	668 ± 51	579 ± 73
Anodized at 10 °C	0.79 ± 0.05	1.54 ± 0.08	541 ± 83	320 ± 44
Anodized at 15 °C	0.86 ± 0.09	1.49 ± 0.14	436 ± 22	279 ± 39
Anodized at 20 °C	0.71 ± 0.10	1.52 ± 0.09	358 ± 20	282 ± 28
Anodized at 30 °C	0.85 ± 0.06	1.13 ± 0.07	290 ± 28	253 ± 48

However, electrolyte temperature significantly influences the surface hardness. Wider pores obtained at higher temperatures gradually decrease the hardness of Al alloys.

3.1.4 Influence of surface preparation on anodized coatings

Surface preparation of Al alloys might influence the properties of anodized coatings, therefore surfaces were treated with alkali/HNO_3 solution, Ar plasma or using a combined treatment. Optical microscopy revealed that surface structure remains similar after different treatment methods, despite less homogeneity and higher surface roughness of 6082 alloys, Fig. 25.

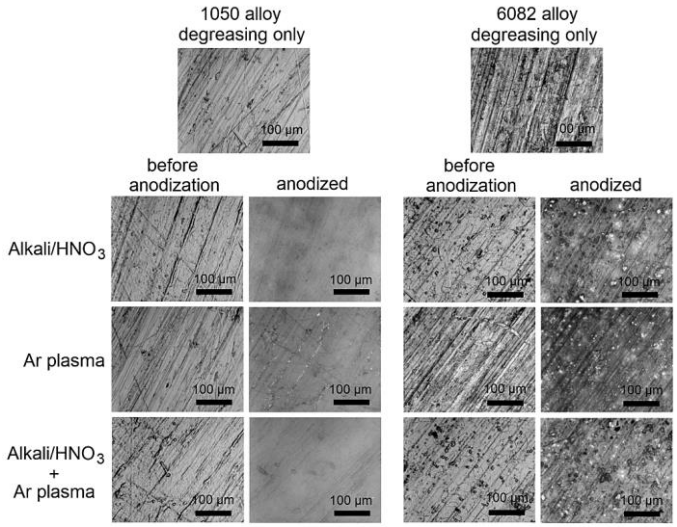

Fig. 25. *Optical microscopy images of 1050 (left) and 6082 (right) alloys before and after hard anodization using different surface treatment methods*

The surface structure of anodized coatings became smoother on 1050 alloys while rough surfaces with unretained alloying additives present as white spots obtained on 6082 alloys. Surface roughness measurements also confirm that anodization reduces roughness *Ra* value on 1050, but increases *Ra* on 6082 alloys, Table 7.

Table 7. *Influence of surface treatment of Al alloys on surface roughness (Ra) before and after hard anodization*

	Alloy	Before treatment	Alkali/HNO_3	Ar plasma	Alkali/HNO_3 + Ar plasma
Before anodization	1050	0.99 ± 0.09	0.92 ± 0.05	0.83 ± 0.10	0.87 ± 0.06
	6082	1.28 ± 0.08	1.02 ± 0.09	0.92 ± 0.08	1.20 ± 0.11
Anodized	1050	-	0.86 ± 0.09	0.73 ± 0.07	0.82 ± 0.09
	6082	-	1.49 ± 0.14	1.40 ± 0.18	1.55 ± 0.14

Despite different treatment methods surface cracking of 6082 alloys remains before and after anodization in H_2SO_4/oxalic a. electrolyte.

Al alloys before anodization were polished with 80 or 2500 grit paper to evaluate surface changes. Surface roughness with less than 0.5 μm was named as "low *Ra*", about 1 μm – "medium *Ra*" and about 7 μm – "high *Ra*", Table 8.

Table 8. *Influence of polished specimens on surface roughness (Ra) before and after hard anodization*

Surface roughness	Before anodization		Anodized	
Ra, μm	1050	6082	1050	6082
Low *Ra* (*2500 grit paper*)	0.22 ± 0.03	0.39 ± 0.03	0.49 ± 0.04	0.38 ± 0.03
Medium *Ra* (*non-polished*)	0.99 ± 0.09	1.28 ± 0.08	0.86 ± 0.09	1.49 ± 0.14
High *Ra* (*80 grit paper*)	7.18 ± 1.09	6.89 ± 1.27	7.28 ± 0.89	7.05 ± 1.22

Results showed that anodization did not affect *Ra* values significantly for both polished or non-polished specimens.

3.1.5 Deposition of thin layers by ALD and sputtering

Deposition of Ti/TiO_2 layers gains recognition in many areas including aerospace, marine and medical applications due to its chemical stability, biocompatibility, non-toxicity and antifrictional properties. Surface characteristics of deposited layers were described below.

TiO_2 layers of 5 nm, 10 nm and 15 nm thicknesses and Ti layers of 16 nm and 75 nm thicknesses were deposited either by ALD or sputtering. The term "nanothin layers of Ti/TiO_2" includes all possible oxides e.g. TiO_2, TiO, Ti_2O_3, etc., as well as Ti nitrides due to oxidation in a humid atmosphere. TDMAT precursor was used to produce TiO_2 monolayers via chemisorption and humidity purge. Despite that ALD process is much slower than sputtering and required from 100 to 375 alternating pulses for deposition of TiO_2 layers with 5 nm to 15 nm thicknesses, it has an advantage of depositing TiO_2 more deeper into the pores of anodized coating while sputtering builds Ti layers mostly on the surface. According to studies TiO_2 layers can penetrate into the pores with the aspect ratio of 1:2000 using ALD [176]. EDS study was carried out to compare Ti contents in ALD specimens those of sputtered ones, Table 9.

Table 9. *Elemental analysis of deposited Ti/TiO_2 layers before and after hard anodization*

Anodization and deposition	Alloy	Layer thickness, nm	Elemental composition at.%				
			Al	O	Ti	Si	S
only ALD (no anodization)	1050	10	96.58	3.36	0	0.03	0.02
	6082	10	95.52	3.78	0.01	0.68	0.01
only anodization (no deposition)	1050	0	26.89	69.33	0	0	3.78
	6082	0	32.13	63.40	0	0.41	4.06
Anodized + ALD	1050	5	30.53	64.47	1.16	0.04	3.80
	6082	5	30.32	63.75	1.69	0.32	3.92
Anodized + ALD	1050	10	31.87	62.65	1.28	0.03	4.17
	6082	10	31.17	62.73	1.84	0.36	3.90
Anodized + ALD	1050	15	31.93	62.53	1.41	0.05	4.08
	6082	15	31.61	62.17	1.97	0.34	3.91
Anodized + sputtered	1050	16	31.51	64.66	0.35	0	3.47
	6082	16	31.09	64.39	0.38	0.38	3.77
Anodized + sputtered	1050	75	30.69	63.48	1.77	0.01	4.05
	6082	75	31.26	62.54	1.89	0.39	3.92

On the surfaces before anodization EDS could not quantify Ti concentration with reasonable accuracy, because this analytical method mostly measures the elements from a 1–2 μm interval of depth into the substrate. Consequently, not many atoms from the Ti layer on the top could be registered by EDS. In the case of anodized coatings, EDS of nanostructured surfaces showed a substantial presence of Ti both in sputtered and ALD specimens.

Although, TDMAT penetration into the pores is not likely to be linear, Ti content increases by increasing the thickness of TiO_2 layer. Content of Ti is at least 1.5 times higher on anodized 6082 alloy than 1050 due to two times wider pores obtained in H_2SO_4/oxalic a. electrolyte. Theoretical values of Ti contents on a flat surface of 1 μm thickness can be calculated, assuming that EDS sampling depth is 1 μm. Then the nanothin layers with 5, 10 and 15 nm thicknesses should contain 0.17, 0.34 and 0.51 at.% Ti respectively. This is several times lower than the values, recorded by EDS. TiO_2 layers of 15 nm thickness, obtained by ALD, are quite comparable to Ti layers of 16 nm thickness, obtained by sputtering. However, EDS analysis showed at least four times lower content of sputtered Ti. This suggests that TDMAT penetration into the pores of anodized coating was much more intensive than that of Ti clusters in case of sputtering. After deposition of 75 nm Ti layers, Ti content increased over 4.5 times, which is well correspond to layer thickness.

In addition, Ti distribution also was obtained on anodized Al as shown by EDS mapping, Fig. 26.

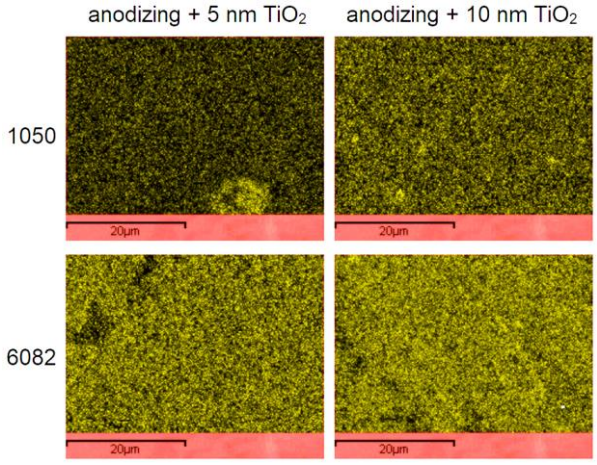

Fig. 26. *Distribution of Ti (light color) on the surfaces of hard anodized coatings after ALD, using TDMAT precursor*

Deposited Ti layers were quite uniform despite some grain-like inclusion of alloying additives. Zones with different Ti concentrations are more evident on 1050 than 6082, which suggests that various porosity patterns could be produced during anodization. However, the fluctuations in uniformity of Ti distribution are not dramatic, with the exception of 5 nm Ti layer on 1050, which has some spots of high Ti contents. Nevertheless, even the latter specimen shows that at least some Ti is present in all surface areas on micro-scale. EDS mapping confirms the expectation that pores with the diameters of 7 nm (1050) and 15 nm (6082) were most likely overfilled during deposition of 10 nm or thicker layers, leading to continuous coverage of TiO_2 on the surface.

Since industrial Al alloys were employed, the anodized coating should not be expected to contain exclusively Al_2O_3. In addition, EDS shows high amounts of sulfur in the anodized coatings exceeding 4%. The walls of nanopore are coated with hydrated hydroxy sulfates and hydroxy oxalates of various structures. This layer mostly contains complexes and soaps of Al, Mg and other alloy elements with many variations of hydration and ligand arrangements. It could be assumed for simplicity that all the complexes and soaps are represented just by $Al_2(SO_4)_3 \cdot 18H_2O$, although the presence of this particular soap is extremely unlikely in the actual nanopore. In such case the layer thickness can be calculated to approach 9 nm and the nanopore cross-section can be depicted as shown in Fig 27.

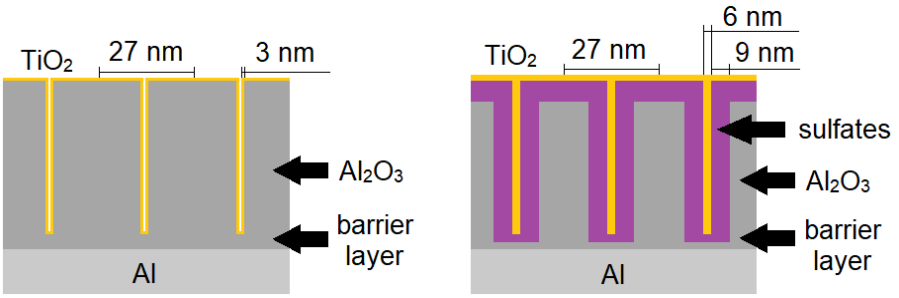

Fig. 27. *Theoretically expected layer of TiO_2 (left) on anodized 1050 and suggested effect of various sulfates (and oxalates) assuming negligible void volumes (right)*

However, such an amount of the octadecahydrate is unlikely, because the pore ID is too small for its accommodation. Residual sulfates and other salts might have an impact on cell adhesion and tribology, but industrially it would be hard to eliminate them from the anodized coatings by washing out with pores as narrow as 15 nm ID or less. Nevertheless, the continuous layer

of TiO_2 on the surface is likely to prevent hydroxides, salts and alloy elements from direct exposure to the surrounding medium.

SEM images complement EDS findings by showing the disappearance of pore openings with deposition of just 5 nm of TiO_2 layer by ALD, Fig. 28. It must be noted that all specimens were sputtered with 2–3 nm Cr for electrical conductivity in order to obtain SEM images. This could also contribute to the disappearance of the pore openings, so it cannot be stated with certainty that the pores were completely overfilled during 5 nm deposition by ALD. However, it is very likely that deposition of 10 nm and 15 nm TiO_2 layers are forming a continuous film on the surface.

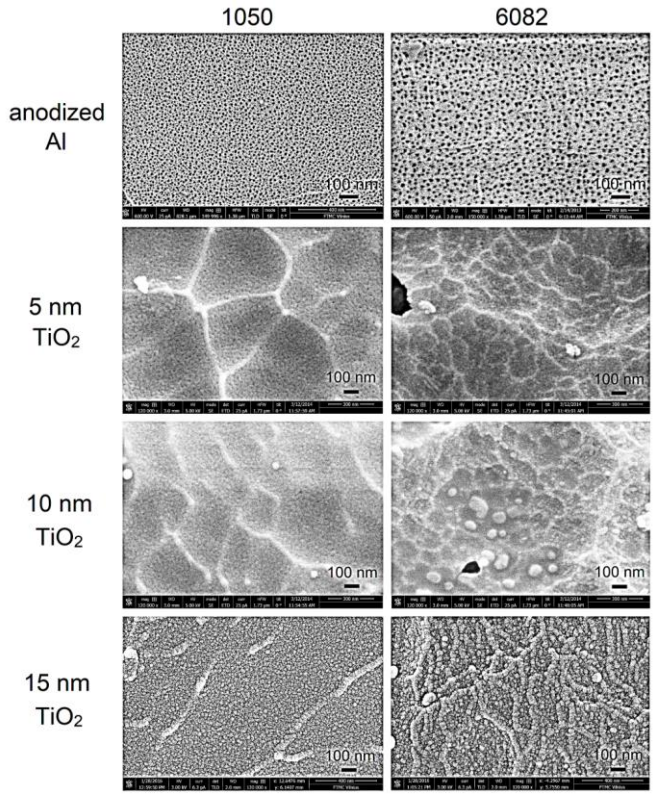

Fig. 28. *SEM images of hard anodized 1050 and 6082 alloys with and without nanothin TiO_2 layers, deposited by ALD*

Interestingly, the surfaces appear relatively uniform and homogeneous on nanostructured 1050 without significant nanoscale segmentation. Some microscale patterns are visible, most likely due to the grain boundaries. On anodized 6082 the segmentation proceeds on a much lower scale with

elongated patterns about 50 nm wide and hundreds of nanometers in length. This suggests that anodized 6082 alloy has lower homogeneity on nanoscale level than anodized 1050, possibly a result of more abundant and diverse alloy components. Occasional anodization defects up to 300 nm in size were visible on 6082 as dark voids, which were most likely produced during anodization as a result of unevenly dissolved alloying elements. These anodization non-homogeneities eventually generated voids in TiO_2 layers as well. However, on micro-level these defects were less significant, as evident from elemental mapping, Fig. 26. Although surface homogeneity was not perfect on nanoscale, microscale factors have much higher importance for friction zone interactions and cell adhesion mechanisms.

The surface roughness of nanostructured coatings was evaluated further. Despite that anodized 6082 was somewhat rougher than 1050, yielding *Ra* values of ~1.5 μm and ~0.85 μm respectively, the deposition of Ti/TiO_2 layers did not affect surface roughness dramatically, Table 10.

Table 10. *Influence of Ti/TiO_2 layer thickness on surface roughness (Ra)*

Al alloy	Surface roughness *Ra*, μm	
	1050	6082
Before anodization	0.99 ± 0.09	1.28 ± 0.08
Anodized	0.86 ± 0.09	1.49 ± 0.14
5 nm TiO_2 (ALD)	0.80 ± 0.08	1.52 ± 0.22
10 nm TiO_2 (ALD)	0.87 ± 0.14	1.41 ± 0.25
15 nm TiO_2 (ALD)	0.99 ± 0.16	1.28 ± 0.20
16 nm Ti (sputtering)	0.82 ± 0.08	1.39 ± 0.14

When compared roughness of TiO_2 and Ti layers with similar thicknesses deposited either by ALD or sputtering, *Ra* values appear quite similar by adding error values. Therefore surface roughness should not be a major factor with respect to friction or cell adhesion presented in later paragraphs.

Nanostructured coatings were studied in detail by optical microscopy and SEM at microscale and nanoscale levels. Surface cracking of anodized coatings with TiO_2 layers was shown on both 1050 and 6082 alloys after ALD deposition, annex Fig. S4 and Fig. S5. The cracks with hundreds of nanometers to few microns of width was might appear due to high temperature of 250 °C in ALD deposition chamber. The sputtered anodized coatings did not show surface cracking, except 1050 alloy, which might have higher surface tension. As discussed above, surface homogeneity is much

lower on 6082 alloy rather than 1050 by showing visible grain boundaries present at the nanoscale level by SEM.

The effectiveness of Ti layers was investigated using wide range thickness scale. The influence of 16 nm, 75 nm and 2.3 μm Ti layers were evaluated on 1050 and 6082 Al surfaces before anodization using a magnetron sputtering device. Alloys were not mechanically grinded, except surface pre-treatment in an alkaline solution to remove surface oxides and impurities. The differences in surface characteristics before and after sputtering were not significant, see annex Fig. S6. The irregular surface topography was showed on both alloys with grain boundaries exceeding 100 μm on 6082 alloy. On 6082 grain boundaries remained visible even after depositing the 2.3 μm Ti layer. However, surface topography of both alloys could still be considered sufficiently similar.

For a better understanding of the Ti layer topography, anodized coatings with 75 nm Ti layer were thoroughly inspected by SEM, in some cases using cross-sections obtained by focused Ga ion beaming after pre-depositing a Pt overcoat, Fig. 29.

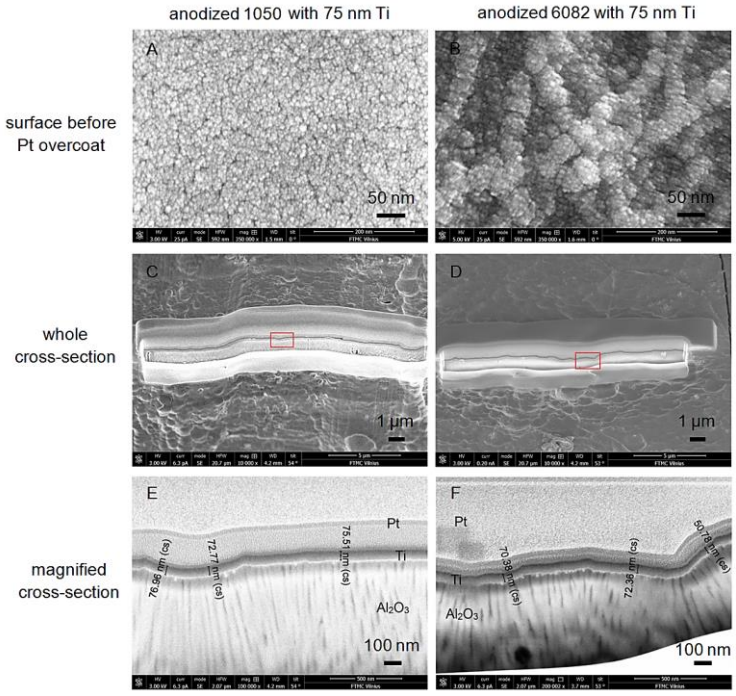

Fig. 29. *SEM images of surfaces (A, B) and cross-sections (C–F) of anodized 1050 and 6082 alloys with 75 nm Ti layers. Cross-sections obtained with focused Ga ion beaming after pre-depositing a Pt overcoat, copied from [150]*

At 350 000 × magnification 75 nm Ti layer differences between the alloys became more evident when compared to SEM images at lower magnification. 6082 alloy appeared much less homogeneous than 1050 by forming aggregates and elongated segments with 30–50 nm wide and hundreds of nanometers in length, Fig. 29 (A, B). This might suggest that sputtered 6082 had much higher roughness on the nano-scale level than 1050. However, on macroscale, as measured by contact profilometry, the increase in surface roughness was not so dramatic, see annex Fig. S7. Compared to anodized coatings before sputtering, the roughness changed only marginally. So it could not be stated that Ti layer deposition resulted in a substantial increase of roughness on 6082 compared to that on 1050. However, homogeneity of the Ti layer on 6082 appeared much lower than that on 1050 only on nano-scale.

In order to study the quality and thickness of Ti layers on anodized 1050 and 6082 alloys, Ga-ion beaming was used to form cross-sections of surfaces with a protective Pt overcoat. SEM images, also showed that Ti layer has higher uniformity on 1050 alloy than 6082, Fig. 29 (E, F). The layer thickness on 1050 fluctuated around 75 nm by less than ± 3nm error, whereas the thickness variations on 6082 alloy were much greater. In fact, Ti layer thickness on 6082 was calculated to average at 65 nm, rather than 75 nm, as determined by cross-sectional measurements. The amounts of Ti, deposited onto the surfaces, should be very similar since 1050 and 6082 specimens were coated in a rotary holder during the same runs of sputtering. Therefore, the lower measured thickness in 6082 could be an outcome of more Ti penetrating into the pores. In addition, significant roughness and surface irregularities could also lower the measured thickness of Ti layers.

While nanothin Ti layers of 16 nm and 75 nm thicknesses were determined by quartz crystal microgravimetry or cross-section of discs using Ga-ion beaming, the thickness of 2.3 μm Ti layers was confirmed using contact profilometry, see annex Fig. S8. Calculations of the average elevation corresponded well to changes in height, with an average thickness of 2.3 μm. The surface roughness of the specimens was too high for the GIXRD method to be effective for 75 nm and 2.3 μm Ti layers, so the presence of Ti and possibly its partial oxides was evident only with some uncertainty. The low intensity peaks of TiO were assessed on nanostructured coatings with 2.3 μm Ti layers, annex Fig. S9. It must also be pointed out that several peaks of Al and Ti have similar 2-theta values, so a good spectral resolution is necessary. Traces of air, present in the instrument chamber as well as within the anodized coating, made the formation of non-

stoichiometric oxides (and possibly nitrides) of Ti very likely, which further impeded the resolution and peak identification. Overall GIXRD method was effective only on smooth surfaces i.e. silicon plate for determining the thickness of nanothin layers.

Deposition quality and thickness of Ti/TiO_2 layers also were evaluated by XPS. Ti peaks which were found by XPS on nanostructured surfaces of 6082 alloy, confirm that Ti and TiO_2 layers were deposited on anodized coatings, Fig. 30. The notations of titanium $L_3M_{23}M_{23}$ and oxygen KVV indicates electron transitions of different core levels, V indicates valence band electrons.

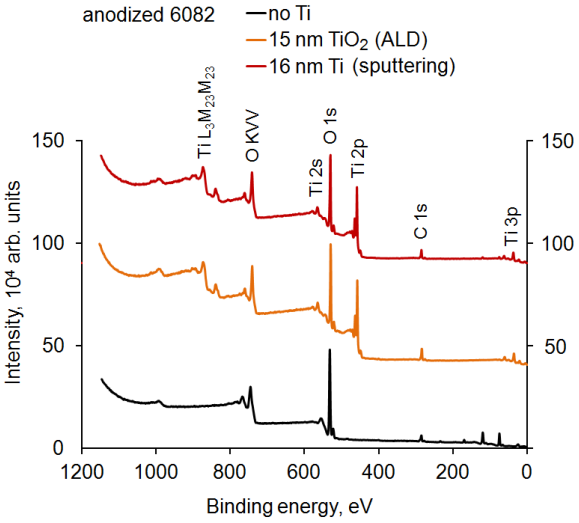

Fig. 30. *XPS survey spectrum of 6082 alloys with or without Ti/TiO₂ layers*

The deposition of Ti/TiO_2 layers was determined by XPS using etching time of ~3 nm/min by Ar^+ ions. The thickness of Ti/TiO_2 layers corresponds to the highest content of Ti measured after 360 s of etching (~18 nm in depth) and when beginning to decrease by increasing of Al content, Fig. 31. This shows that sputtering and ALD produces uniform Ti/TiO_2 layers on both 1050 and 6082 alloys. The decrease of Ti is much lower by ALD deposition suggesting that TDMAT penetration into the pores is higher than sputtering, as shown previously by EDS studies. It must be mentioned, that XPS also showed a high content of C at the surface due to the adsorption of CO_2 molecules from air atmosphere. Some traces of C found after etching suggests the formation of oxalates in hard anodized coatings which came from the electrolyte. Moreover, XPS also detected traces of nitrogen on ALD

deposited specimens of 6082 alloys, most likely due to unreacted TDMAT precursor left inside the pores.

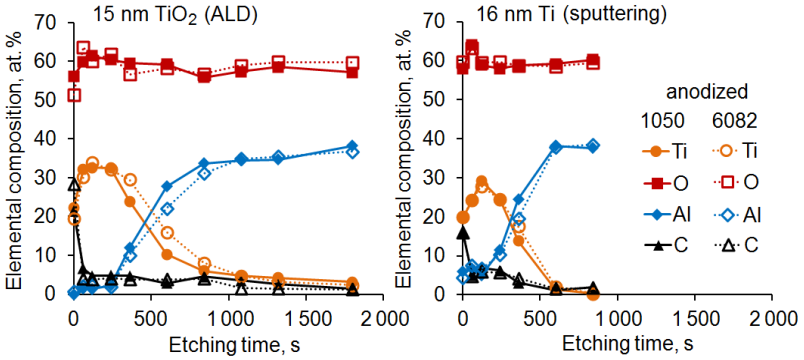

Fig. 31. *Elemental composition of anodized 1050 and 6082 alloys with 15 nm TiO_2 (left) and 16 nm Ti (right) layers by XPS using etching time of approximately 3 nm/min by Ar^+ ions. The Ti layers were deposited by sputtering, while those of TiO_2 were produced by ALD*

The chemical states of Ti 2*p*, O 1*s*, and Al 2*p* were showed by XPS after the deposition of TiO_2 layers on anodized coatings. High intensity peaks of 458.4 eV [177] and 458.7 ± 0.1 eV [178] are associated with TiO_2, annex Fig. S10. Ti 2*p* consists of two main peaks of $2p_{3/2}$ with higher peak intensity and $2p_{1/2}$ with lower peak intensity core levels. Each peak is accompanied by a satellite ~13 eV above the main peak, which is caused by the charge transfer effect due to the strong covalency hybridization. Peak intensity corresponds to a TiO_2 content deposited on the surface by showing a gradual decrease of intensity on both 1050 and 6082 alloys after surface etching. XPS spectra of O 1*s* revealed that oxygen could be related to TiO_2 or Al_2O_3 depending on binding energy. O 1*s* peak of 530.0 ± 0.1 eV was assigned to TiO_2 [179], while peak shifts of 530.6 eV and 531.1–531.6 eV were corresponding to Al_2O_3 [180] and γ-Al_2O_3 [177] respectively. No peaks of Al were observed at the surface suggesting that uniform layers of TiO_2 were effectively deposited on porous anodized coatings. Surface etching for 360 s and 1320 s showed a gradual increase of Al content with high intensity XPS peaks. The peaks of 74.3-74.6 eV and 74.3–75.9 eV were assigned to γ-Al_2O_3 or $Al(OH)_3$ according to previous studies [177, 181] and suggest that pores possibly are filled with hydroxides.

XPS spectra of sputtered specimens revealed that nanothin Ti layers are completely oxidized into TiO_2, annex Fig. S11. Moreover, the peak intensity

of Ti was decreased more rapidly when compared to Ti peak by ALD deposition. Gradual etching of the surfaces showed the phase of γ-Al_2O_3 or $Al(OH)_3$ by O 1*s* and Al 2*p* scans. Curve-fitting analysis of the Ti 2*p* and O 1*s* spectra on sputtered 6082 alloys also revealed the presence of TiO_2 and the possibility of formation of Ti oxysulfides (i.e. $TiO_{0.3}S_{1.5}$) according to peak of 456.3 eV [182], annex Fig. S12. Additionally, the analysis of O 1*s* spectra revealed three peaks of different intensities. The most intensive peak of 530.4 eV was ascribed to O^{2-} species of the TiO_2 [183], whereas peaks of 531.6 eV and 532.6 eV were assigned to γ-Al_2O_3 and hydroxyl groups [177, 184].

Some attempts were made to analyze the structural features of nanothin Ti layers. However, GIXRD, XPS or Raman spectroscopy did not lead to any conclusive characterization of crystalline arrangements. Significant roughness, presence of alloying elements and compounds from anodization made the analysis overly complex, in addition, there was no reason to reject an assumption that nanothin Ti layers could be amorphous or polycrystalline.

The effect of Ti/TiO_2 layers also was showed on phospho-anodized coatings. SEM images revealed that Ti/TiO_2 layers slightly reduce pore openings although pores are still visible with a diameter over 100 nm, see Fig. 32.

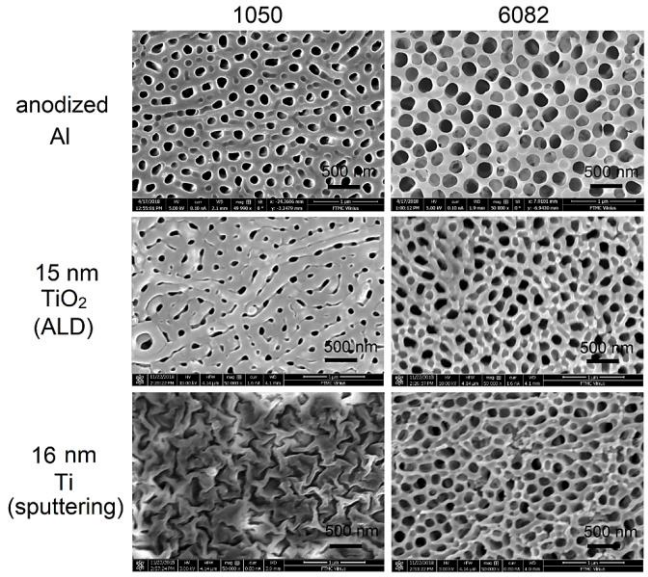

Fig. 32. *SEM images of phospho-anodized coatings produced in phosphoric a. electrolyte with nanothin TiO_2 or Ti layers, deposited by ALD or sputtering respectively*

EDS studies confirmed the presence of Ti with a much higher concentration after ALD deposition of TiO_2 layers, especially on 6082 alloys with pores over 200 nm diameter, Table 11.

Table 11. *Elemental analysis of deposited Ti/TiO_2 layers before and after anodization in phosphoric a. electrolyte*

Anodization and deposition	Alloy	Layer thickness, nm	Elemental composition at.%				
			Al	O	Ti	Si	P
Anodized	1050	0	32.16	66.03	0	0.05	1.76
	6082	0	32.84	65.69	0	0.62	0.85
Anodized + ALD	1050	15	30.59	63.99	3.52	0	1.89
	6082	15	24.30	63.62	10.77	0.40	0.92
Anodized + sputtered	1050	16	34.72	62.64	0.44	0	2.20
	6082	16	35.12	62.53	0.45	0.47	1.43

This was not surprising since similar results were obtained with hard anodized coatings produced in H_2SO_4/oxalic a. electrolyte. The content of phosphorus in phospho-anodized coatings is slightly lower when compared to the content of sulfur mostly due to wider pores which leads to faster washing off processes.

For comparison nanothin layers of group IVB transitional metals including ~15 nm HfO_2 and ~16 nm Zr were deposited on hard anodized coatings by ALD or sputtering respectively, Fig. 33.

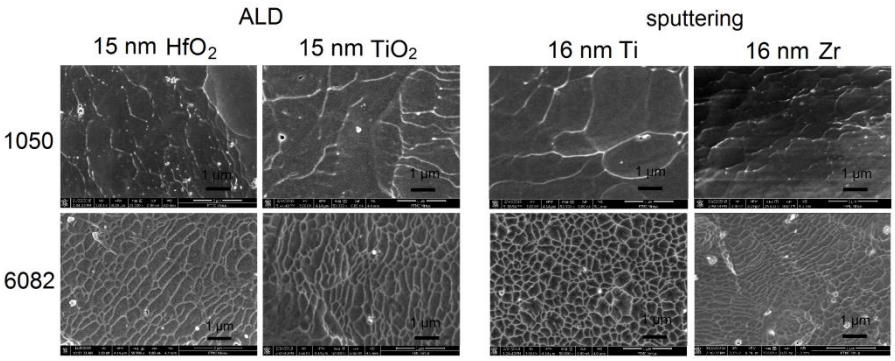

Fig. 33. *SEM images of hard anodized coatings with nanothin layers of group IVB transitional metals, deposited by ALD or sputtering*

The surface structure of HfO_2 and Zr layers were quite similar to Ti and its oxides with higher homogeneity on 1050 alloy. Many grain boundaries were observed on 6082 alloys of various sizes mostly from a few hundred nanometers.

Detail studies of nanothin layers of group IVB transitional metals (Ti, Zr, Hf) and other metals including Cr, Cu and Nb were showed in Fig. 34.

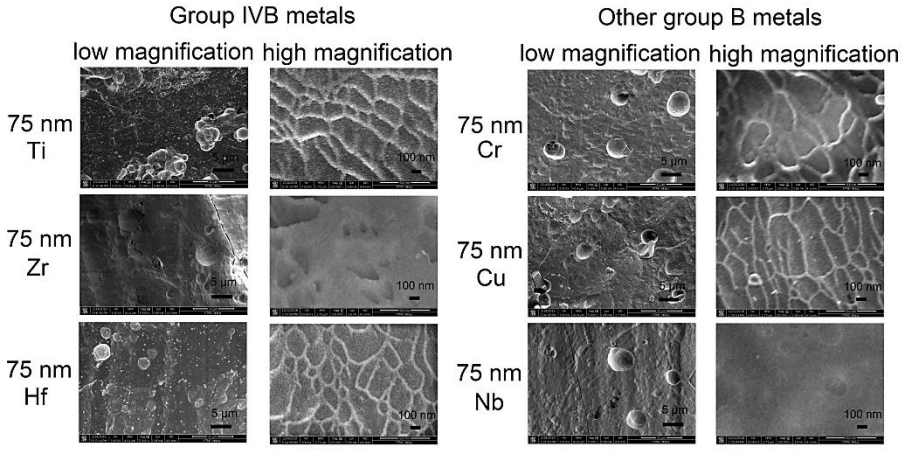

Fig. 34. *SEM images of hard anodized 6082 alloys with nanothin layers of 75 nm thickness at low and high magnifications, deposited by sputtering*

Surface defects or cracks were present on all sputtered specimens of anodized 6082 alloys at low magnification. High magnification revealed surface structure with visible grain boundaries after deposition of Ti, Hf, Cr and Nb layers, while plain surfaces obtained with Zr and Nb layers of 75 nm thicknesses. However, morphological differences are not very pronounced and the influence of these differences on both tribological and biomedical processes is much smaller than the chemical effect of coatings.

Overall, nanothin layers completely cover pore openings of hard anodized coatings while the pores of phospho-anodized coatings are still remained open. Such differences might affect surface tribology including the chemistry of different metallic layers.

3.1.6 Post-treatment of anodized coatings

It is expected that anodized Al should have a long service life in respect of anodization quality requirements. However, environmental conditions (i.e. humidity, temperature, etc.) and atmospheric pollution (i.e. CO_2, CO, NO_2, etc.) might shorten the life of anodized coatings by changing surface

properties, increasing degradation, cracking and corrosion. Previous studies showed that the aging of anodized Al specimens affects surface roughness and wettability [185].

In this study, the influence of aging of anodized coatings obtained in H_2SO_4/oxalic a. electrolyte was tested tribologically. Both static friction between initially stagnant surfaces and dynamic friction between continuously moving surfaces are important parameters of tribology. The friction was tested against chemically inert corundum (i.e. Al_2O_3) ball to eliminate the influence of unnecessary reactions. Results showed that the aging of anodized Al does not appear to affect dynamic friction or appearance significantly under dry conditions or humid atmosphere, Fig. 35.

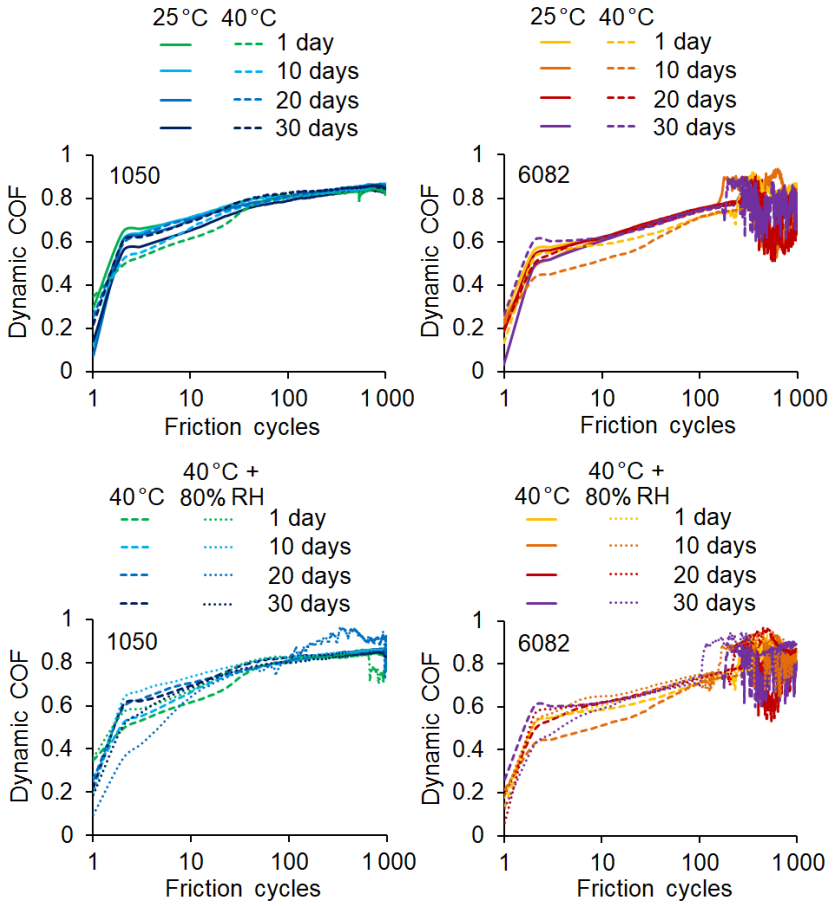

Fig. 35. *Influence on temperature (top) and humidity (bottom) of dynamic friction of anodized 1050 and 6082 alloys on aging time, tribotests against an Al_2O_3 ball under 10 N load*

Moreover, optical microscopy also could not confirm any structural changes of anodized coatings after heating at 25 °C or 40 °C with or without 80% RH humidity. Aging of anodized Al slightly reduced the mass of specimens mostly due to evaporation of bound water present in the pores of anodized coating at 40 °C, Fig. 36.

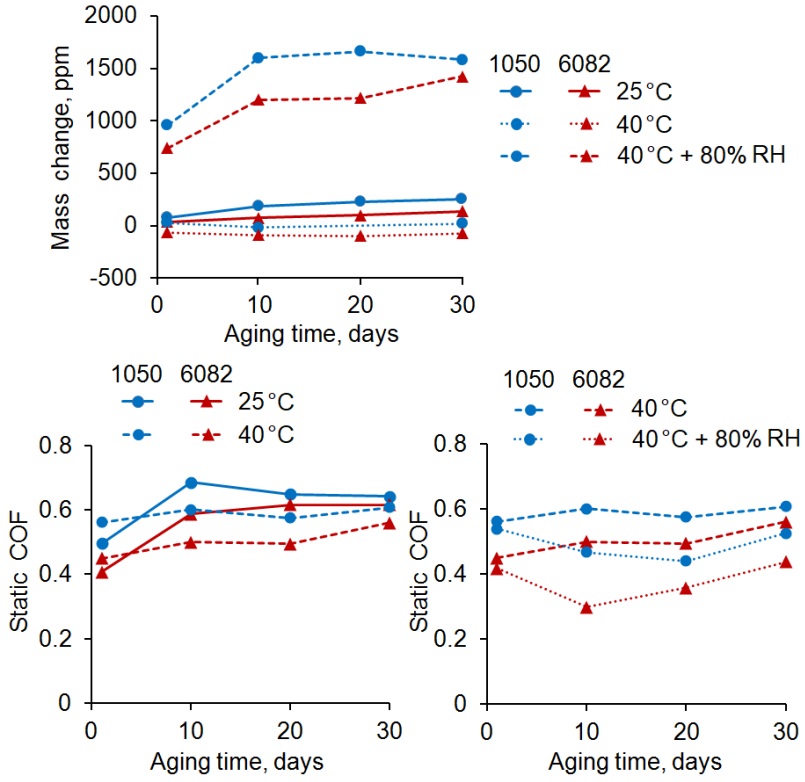

Fig. 36. *Influence on temperature and humidity of mass change and static friction of anodized 1050 and 6082 alloys on aging time, tribotests against an Al_2O_3 ball under 10 N load*

Meanwhile, aging in a humid atmosphere led to slight weight gain due to formation of Al hydroxides, Al hydrates, oxalate hydrates and possibly other compounds. Formation of new compounds due to reactions with humidity seems to slightly reduce static COF but bears a little effect on dynamic COF. Nevertheless, any tribological benefits of reactions with humidity seem to disappear after 20 to 30 days of aging.

The adsorption of water molecules on anodized coating leads to a surface hydroxylation and the formation of Al hydroxides in a humid atmosphere.

According to studies, high humidity (RH>70%) showed disordered adsorption of water molecules with the formation of a liquid-like water layer [186]. In atmospheric conditions which contain ~0.25wt.% water vapor anodized coating immediately forms hydroxyl groups due to chemisorbed water layer, see Fig. 37.

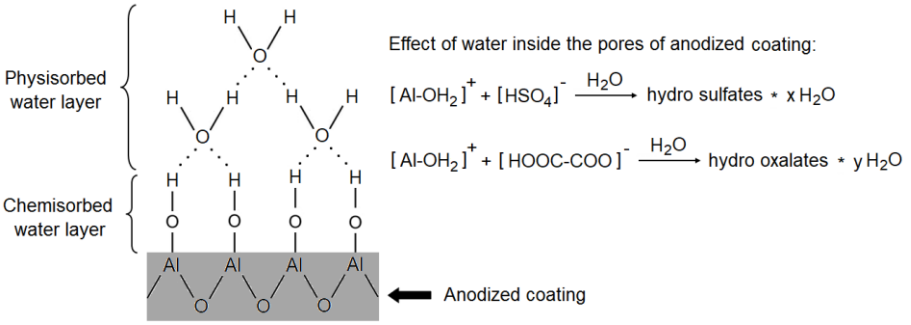

Fig. 37. *Adsorption of water on anodized Al (left) and reactions inside the pores of hard anodized coating (right)*

Physisorbed water, which interacts with the surface due to van der Waals forces has very low bonding energy than chemisorbed water (10–100 meV vs 1–10 eV) and contain three layers: I) stabilized water, removable at 100–160 °C; II) relative mobile water, removable at 80–100 °C; III) mobile water, removable at 50 °C [187]. Moreover, water molecules can interact with H_2SO_4/oxalic a. electrolyte leading to complexes and soaps with various hydration and ligand arrangements in the pores of the anodized coatings. Formation of various levels of hydrated salts also is possible. Adsorption of water molecules and high amount of hydrates might close off the surface pores which influence the reduction of static COF.

After anodization, it is often necessary to apply subsequent sealing. A hydrothermal sealing not only retains dyes and lubricants if any are applied but also increase the corrosion resistance. The hydrothermal method of sealing blocks the pores of anodized coating by dipping anodized Al in boiling water. Hydrothermal sealing of anodized coatings at 90 °C or similar temperatures led to significant COF reduction during early stages of friction, Fig. 38. COF reduced to 0.2 and sustained for at least 30 friction cycles under 10 N load. The formation of Al hydroxides, hydrated Al salts and various other structures of lower density blocks the pores and make an impermeable layer that is stable under various environmental conditions [188].

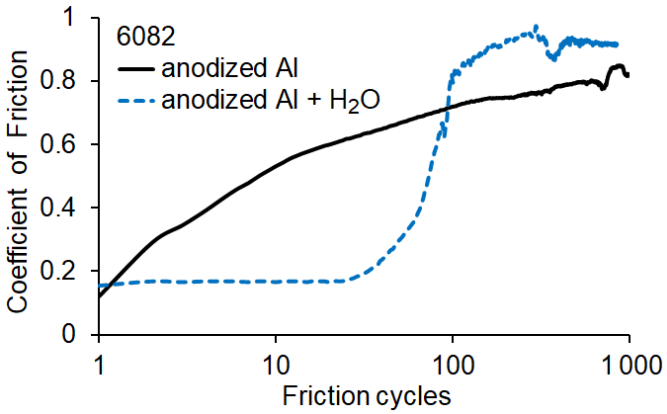

Fig. 38. *Influence of friction of 6082 alloy on the hydrothermal sealing, tribotests against an Al_2O_3 ball under 10 N load*

As mentioned before, the hydrothermal sealing also improves corrosion resistance. The corrosion rate of the anodized coating was 3 times lower after pore sealing, as established in previous studies [189]. Much higher corrosion resistance can be obtained on impregnated anodized coatings [189, 190]. However, this study mostly focuses on tribological as well as biological aspects of anodized coatings. Therefore, corrosion effects expected to be negligible by using chemically inert corundum balls for friction studies.

3.1.7 Selection of most promising nanostructured coatings

Preliminary tribological screening of hard anodized coatings, which were produced in H_2SO_4/oxalic a. electrolyte by varying current density, anodizing duration, temperature and other parameters, demonstrated that anodized coatings of 60 ± 10 μm thickness, obtained at 15 °C after 70 min under 2 A/dm² (~20 V) generally had better overall properties, including resistance to friction, see Fig. 39. Despite possible performance improvements under other anodizing parameters, further experiments with hard anodized coatings focused on the former set of anodizing conditions. Phospho-anodized coatings showed significant variation in morphology and thickness, depending on methanol, glycerol and other electrolyte additives. However, none of them led to appreciably better tribological properties, therefore plain aqueous 4% H_3PO_4 solution was selected for further phospho-anodization studies using a constant voltage of 120 V (~0,5 A/dm²) or 150 V (~1,5 A/dm²). Moreover, higher anodization

potential (150 V vs 120 V) led to a higher thickness of phospho-anodized coating and much shorter durations.

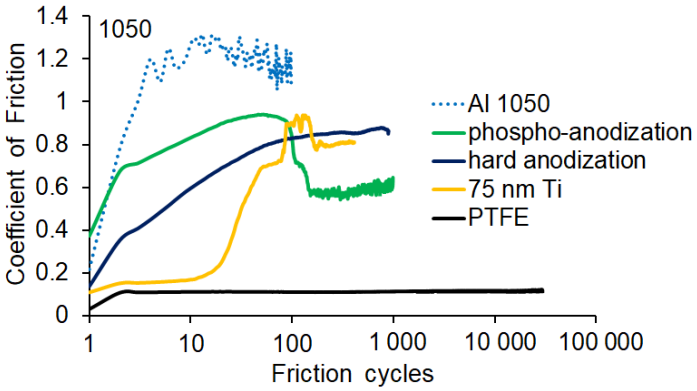

Fig. 39. *Friction tendencies of anodized 1050 alloys without or with solid fillers, tribotests against an Al_2O_3 ball under 10 N load*

For nanostructured coatings deposition by ALD was limited to 15 nm due to excessively long durations, required for thicker layers while deposition using sputtering was prioritized for nanothin layers of 16 nm and 75 nm thicknesses. The actual thickness of 16 nm sputtered layer was similar to a layer of 15 nm thickness of ALD specimens. In order to differentiate ALD specimens from the sputtered ones, the layer thickness was denominated as 15 nm and 16 nm respectively. Sputtering to form the layers of 75 nm thickness was prioritized, because preliminary tribological screening showed dramatic improvements after the deposition of layers of similar thickness. Preliminary screening showed that nanothin Ti layers appear more effective tribologically than Zr or other elements, therefore, detailed evaluations were performed only on nanostructured coatings with Ti layers of 75 nm thickness.

Antifrictional properties of anodized coatings significantly increase using barrier type lubricants, PTFE in particular. Low friction sustains at least 30 000 cycles with COF of 0.1 value. Therefore, PTFE coating was selected as a basis for tribological comparison among impregnated coatings.

3.2 Interactions between biological media and developed coatings

The inertness, porosity and relatively high roughness of nanostructured coatings can be useful in developing biocompatible surfaces. The ability of

nanothin Ti/TiO_2 layers ability to form a barrier layer can have a positive impact on cell adhesion and proliferation by protecting from impurities and residual electrolyte left in the pores of anodized coating.

3.2.1 Influence of cell type of developed coatings

Different cell types showed distinct cellular responses to biomaterials, which can affect cell adhesion, spreading, migration and differentiation [65, 111, 191]. Therefore, four cell lines of adherent growth mode including human cervix carcinoma Hep-2C (HeLa derivative) cells, murine fibroblast L929 cells, Chinese hamster ovary CHO-K1 cells and human PDLS cells were tested for adhesion on Ti alloy BT1 of 96.32% purity, which was chosen as the control specimen. Wide accessibility and high proliferation rate of epithelial cancer Hep-2C and CHO-K1 cells allow to use them for scientific research. L929 and PDLS cells of connective tissue synthesize the extracellular matrix components (i.e. collagen, glycoproteins) and play a critical role in wound healing that is especially important after implantation and surgery. Moreover, their preparation and high growth rate also resulted in a choice of selected cells, which was tested under laboratory conditions.

The optical study revealed different morphology of four cell lines. L929 and PDLS cells showed bipolar or multipolar structure with elongated shape, while Hep-2C and CHO-K1 cells had a more flattened structure in a polygonal shape, Fig. 40.

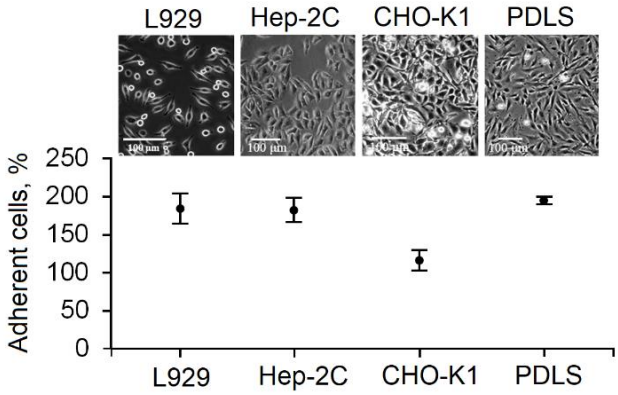

Fig. 40. *Morphology of L929 [192], Hep-2C [193], CHO-K1 [194], PDLS [*195*] cells and their adhesion on Ti alloy BT1*

The size of the cells is quite similar and has a length of ~50–100 μm. After testing four adherent cell lines, L929 and PDLS cells showed the best

growth results and the highest viability after seeding on Ti alloy BT1. L929 and PDLS cells which are isolated from connective tissue were chosen for further experiments.

The morphology of L929 cells was evaluated to identify the cell suspension interaction with control substrates and anodized coatings. No differences were observed on Ti BT1 or 1050 and 6082 alloys used for positive or negative controls respectively, Fig. 41.

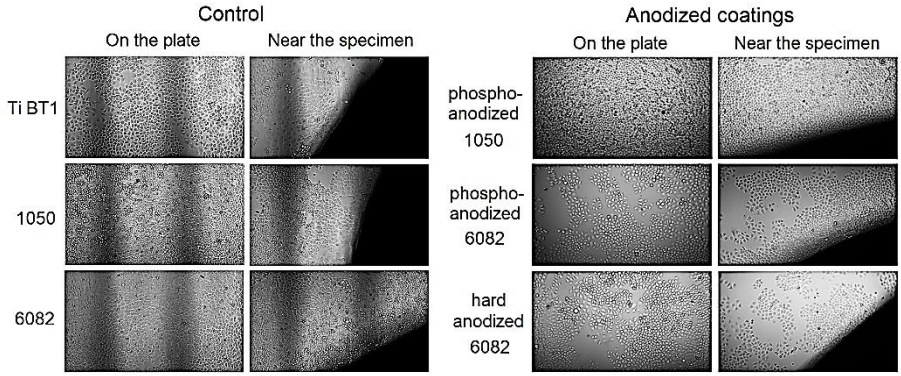

Fig. 41. *Morphological appearance of L929 cells on the plate and near the control specimens (left) and anodized coatings (right) after 48 h under 10× magnification*

The cells were growing on all plates with control specimens. Cell growth was similar either in culture plates with hard anodized coatings with pores of ~15 nm or phospho-anodized coatings with pores of ~200 nm of low purity 6082 alloy. However, cell density in culture plates with phospho-anodized coatings was higher on high purity 1050 alloy. This suggests that the purity of Al alloy might play a more important role rather than sulfates or phosphates. However, more detailed studies are required to confirm this hypothesis.

3.2.2 Adhesion of periodontal ligament cells

Since both biological and tribological aspects are important for dental implants and dental braces, PDLS cells were selected for biocompatibility studies. Fibroblasts of connective tissue producing extracellular matrix components and collagen are the main cells found in the periodontal ligament, which are widespread in all human organism tissues and organs.

In this study, PDLS cells adhesion and proliferation was demonstrated on hard anodized and phospho-anodized coatings of 6082 alloy. Results

showed a significant reduction of adherent cells on phospho-anodized coatings after 24 h and 72 h of incubation, Fig. 42.

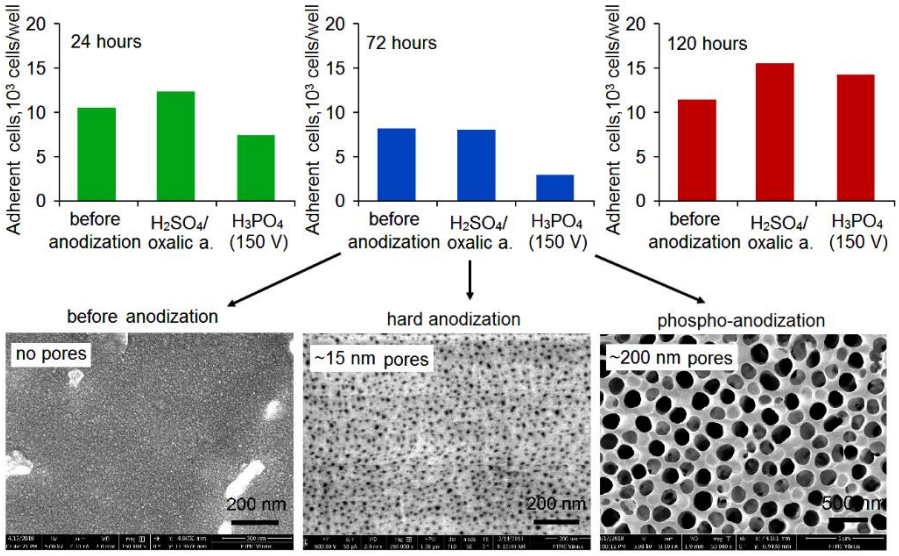

Fig. 42. *Adhesion and proliferation of PDLS cells on anodized and untreated 6082 alloys after 24 h, 72 h and 120 h (top) and nanotopograpghy of Al surfaces before and after anodization, evaluated by SEM (bottom)*

However, cell proliferation on phospho-anodized coatings became similar to those of hard anodized specimens after 120 h of incubation. As presented in the previous study, cell adhesion and proliferation were significantly faster on anodized coatings with higher pore densities than that on porous coatings of larger sizes due to enhanced cell-surface interaction through the integrin mediated focal adhesions [5]. Overall, porous coatings showed improved biocompatibility of PDLS cells when compared to flat Al surfaces after 120 h of incubation.

For a detailed investigation of biocompatibility studies, cell adhesion and proliferation was shown on both anodized 1050 and 6082 Al alloys. After 24 hours of incubation, anodized 6082 alloys of low purity demonstrated better adhesion properties than anodized 1050 alloy, Fig. 43. This effect could be related to a higher surface roughness of anodized 6082 alloys required for cell attachment and adaptation. The submicro-scale and micro-scale features promote cell adhesion, spreading and growth behavior by increasing surface area [87, 196]. Moreover, the response of cells to roughness and topographical features (i.e. grooves, ridges, pores, wells) is different

depending on the cell type and could be used for the selectivity of cells [197].

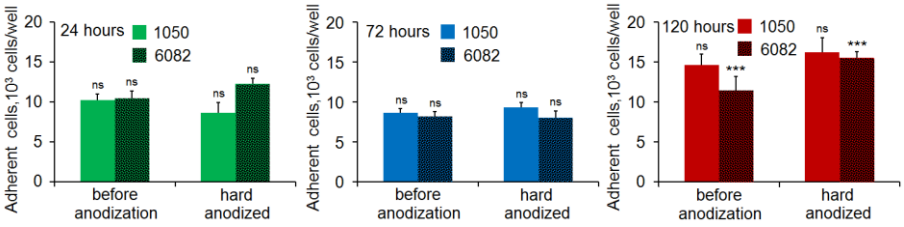

Fig. 43. *Adhesion and proliferation of PDLS cells on hard anodized and untreated alloys after 24 h, 72 h and 120 h. Data from three runs: ns - p>0.05 (not significant), *** p<0.001 (extremely significant)*

After 72 and 120 hours, cells proliferated faster on the 1050 alloy surfaces. This could be related to the lower purity of 6082 alloys, especially because of the toxicity of Fe and Mn alloying elements [198]. However, the statistical analysis showed there was no significant difference between the number of PDLS cells on untreated 1050 alloys in comparison to anodized alloys. Other researchers also had observed slight increase in biocompatibility of periodontal ligament progenitor cells on anodized 1050A alloy with coating thicknesses of 10 μm and 20 μm [199]. Anodization of 6082 alloys significantly increased cell adhesion by 36% after 120 hours ($p < 0.001$) by suggesting that the composition of alloys is important for cell growth. In summary, anodization has a positive effect on biocompatibility especially of anodized 6082 alloys.

Biocompatibility of nanostructured coatings also was evaluated by PDLS cells. Nanothin TiO_2 layers of 10 nm and 15 nm thicknesses inhibited cell adhesion by ~20% on nanostructured 6082 alloys when compared to anodized 6082 before ALD after 24 hours of incubation ($p<0.05$), Fig. 44.

In contrast, the deposition of TiO_2 layers of 10 nm and 15 nm thicknesses only slightly inhibited PDLS adhesion or showed a positive effect on anodized 1050 alloys respectively. Incubation for 120 h only slightly increased PDLS cell adhesion only on anodized 6082 with 15 nm TiO_2 layers. These results demonstrate that alloy composition and thickness of TiO_2 layers are important for adhesion and proliferation of PDLS cells. It can be hypothesized that observed differences may be due to the partially reacted TDMAT precursor or its hydrolysis products left inside the pores of anodized 6082 alloy. Importantly, diameters of pores in anodized 6082 alloy

are two times larger than those of 1050 alloy. This factor may be important for the retention of unreacted TDMAT precursors.

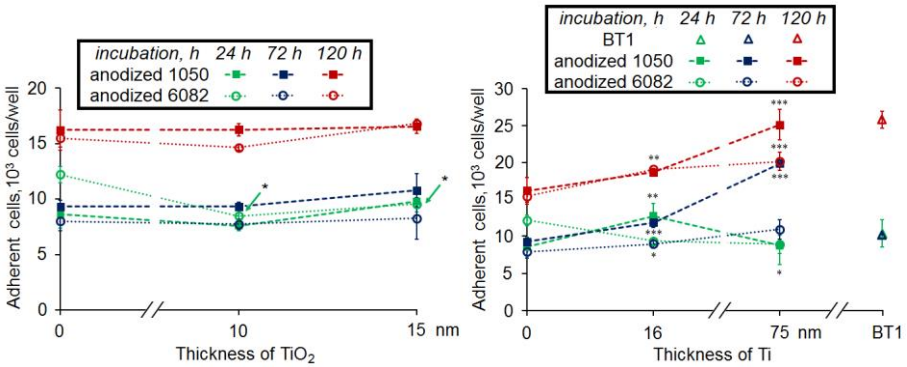

Fig. 44. *Adhesion and proliferation of PDLS cells on Ti alloy (BT1) and anodized 1050 and 6082 alloys with or without nanothin layers of Ti or its oxides. Left: TiO_2 layers of 10 nm and 15 nm thickness, produced by ALD. Right: BT1 alloy (96% Ti) and anodized Al alloys with nanothin Ti layers, produced by sputtering. Data from three runs: ns - p>0.05 (not significant), *p<0.05 (significant), ***p<0.001 (extremely significant)*

Anodized coatings with nanothin Ti layers of 16 nm and 75 nm thicknesses were studied for biocompatibility with PDLS cells as well. Initial cell adhesion decreased by 23% and 26% on anodized 6082 with nanothin layers of 16 nm and 75 nm thicknesses respectively after 24 hours of incubation. Nanothin layers of Ti completely cover the pores of anodized coating therefore cell adhesion to the surface might be more complicated especially during the initial incubation. In contrast, the adhesion of PDLS cells on anodized 1050 alloy with 16 nm Ti layer increased by 48% but did not change on 75 nm Ti layer when compared to anodized 1050 alloy before sputtering. Such differences might influence the purity of Al alloys. After 72 and 120 hours, cell adhesion improved on all sputtered specimens, especially on anodized 1050 alloys. At the same time, only a slight increase was registered in the case of nanostructured coatings of 6082 alloys. Ti layers of 16 nm and 75 nm thicknesses increased cell adhesion by 15% and 55% respectively on sputtered 1050 alloys after 120 hours of incubation. Higher thickness of nanothin Ti layers are beneficial for biocompatibility but it is important to maintain a rough surface topography during their formation. The adhesion on nanostructured coatings was quite comparable to Ti alloy BT1.

A comparison of morphological appearance by fluorescence imaging revealed some differences between PDLS cells on anodized 1050 and 6082 alloys, Fig. 45.

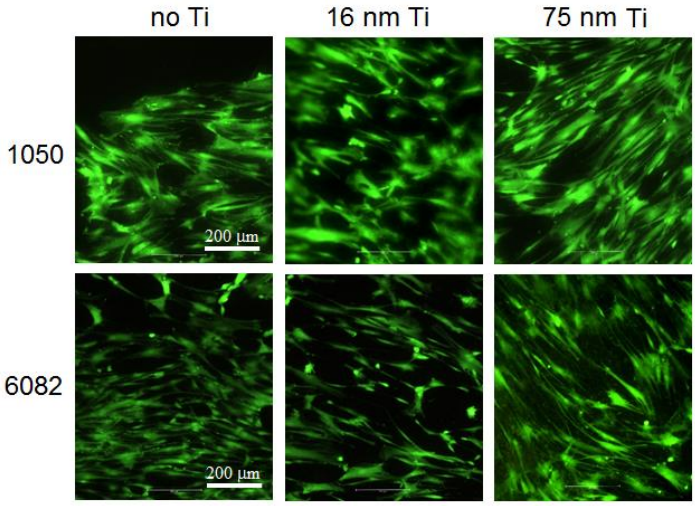

Fig. 45. *Morphological appearance of PDLS cells on the anodized 1050 and 6082 alloys with or without Ti layers of 16 nm and 75 nm thicknesses, deposited by sputtering. Fluorescence imaging performed after 48 h incubation, staining with 1 µM CellTrace™ Calcein Green*

Cells growing on the anodized 1050 alloy displayed more flattened morphology than those growing on 6082. Quite oppositely, PDLS cells on the anodized 6082 alloys were reduced in size and had long thin longitudinal profiles. Importantly, sputtered 16 nm and 75 nm Ti layers did not significantly affect the morphological appearance of PDLS cells.

Overall, nanostructured coatings with nanothin layers of Ti and its oxides are biocompatible with human PDLS cells. However, several important factors that must be taken into account. First, the composition of Al alloy can affect adhesion, morphology and growth of PDLS cells. Anodization increased cell adhesion only on lower purity 6082 alloys, while higher purity anodized 1050 alloys had similar adhesion when compared to untreated alloys. Second, the thickness Ti/TiO_2 layers is also an important factor, because thicker layers demonstrated better biocompatibility to PDLS cells. 16 nm and 75 nm Ti layers sputtered with magnetron significantly increased cell adhesion and proliferation, especially on 1050 alloys. TiO_2 layers of 10 nm and 15 nm thicknesses (deposited by ALD) did not show any significant improvement on cell adhesion. Additional parameters (i.e. surface

roughness) were not considered since nanothin Ti/TiO_2 layers should not affect surface roughness dramatically. However, anodized 6082 alloys are not as smooth as 1050 with *Ra* values of 1.5 µm and 0.85 µm respectively. Although, higher surface roughness might improve cell attachment, the release of metal ions and wear particles might intensify, if materials are not chemically pure [62].

3.3 Tribology of anodized coatings with or without deposited nanothin layers

It is important to consider the tribological properties when designing different products, especially for better durability. The importance of tribological research in biomedical products such as dental braces [200, 201] and mandibular implants [202] had been highlighted by using loads of 1 N to 10 N. The latter load was selected for friction tests on anodized and nanostructured coatings. Despite the importance of dynamic friction which acts between moving surfaces, static friction also should be considered. Static friction is relevant not only in industry but also for biomedical devices where surfaces might undergo intermittent movements. Only freshly anodized Al discs were tested for a better understanding of friction phenomena.

3.3.1 Tribology of anodized alumina coatings

The influence of Al alloys on friction firstly was demonstrated on specimens before anodization. As showed in Fig. 46, COF depends on alloy type very significantly.

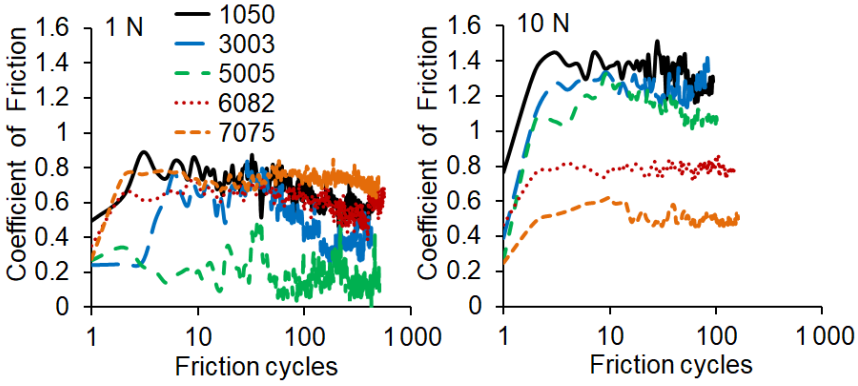

Fig. 46. *Influence of Al alloys on friction under 1 N (left) and 10 N (right) loads, against a steel ball*

Lower COF of 5005 alloy under 1N load might be caused by the involvement of Mg and other alloy elements into friction zone reactions. Despite low COF of 5005 alloy, wear rate was four times faster than wear of 7075 alloy, see Table 12.

Table 12. *Wear of Al alloys after 500 friction cycles under 2 cm/s and 1 N load*

Alloy	Wear track depth, μm	Cross-section area of wear track, μm²	Wear rate, $\mu m^3/(N \cdot mm_{wear})$	Scar diameter on ball, μm
1050	46 ± 1	16 800 ± 600	16 800 ± 600	2910
3003	44 ± 4	11 800 ± 1 300	11 800 ± 1 300	2430
5005	55 ± 1	24 200 ± 1 000	24 200 ± 1 000	2600
6082	54 ± 3	23 300 ± 1 700	23 300 ± 1 700	2230
7075	17 ± 1	6 200 ± 200	6 200 ± 200	1590

This suggests that high contents of Mg unable to withstand even low loads and lead to initial surface damage. Low wear of 7075 alloy might be related to the servovitic film formation influenced by Cu additives [203, 204]. Higher loads had a positive effect only for 6082 and 7075 alloys which led to COF reduction below 0.8 most likely due to increased surface hardness. The rest of the specimens resulted in COF above 1.0 under 10 N load.

The testing of anodized coatings showed quite similar COF curves independently on alloy type, Fig. 47.

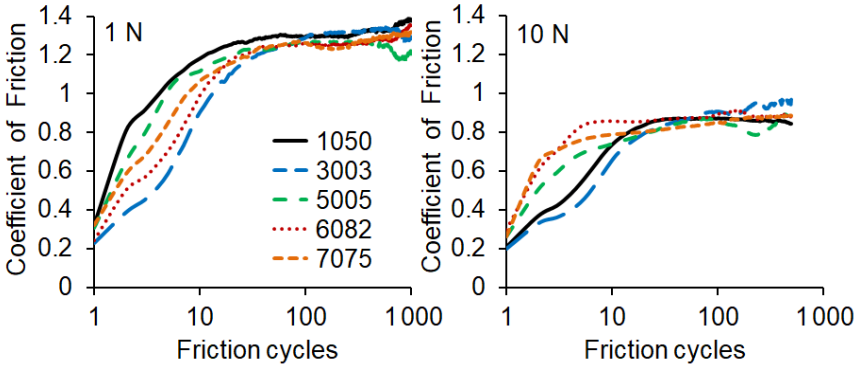

Fig. 47. *Influence of Al alloys after anodization in sulfuric/oxalic a. electrolyte on friction under 1 N (left) and 10 N (right) loads, against a steel ball*

However, friction significantly depends on the load. Increasing the load from 1 N to 10 N led to COF reduction from 1.2 to 0.8 due to increased

surface contact area. It must be mentioned that the wear of anodized alloys was 100–1000 times slower when compared to untreated alloys, Table 13.

Table 13. *Wear of hard anodized Al alloys after 500 friction cycles under 2 cm/s and 10 N load*

Alloy	Wear track depth, μm	Cross-section area of wear track, μm²	Wear rate, $\mu m^3/(N \cdot mm_{wear})$	Scar diameter on ball, μm
1050	3.2 ± 0.2	555 ± 39	56 ± 4	1417
3003	4.9 ± 0.2	996 ± 71	100 ± 7	1701
5005	2.5 ± 0.2	314 ± 40	31 ± 4	1055
6082	3.6 ± 0.2	516 ± 194	52 ± 19	1152
7075	2.2 ± 0.3	418 ± 65	42 ± 7	1018

Lower wear rate was observed on anodized 7075 alloys possibly due to the high content of Cu (2.1 wt.%) and Zn (7.7 wt.%) intermetallic compounds, responsible for surface hardness as well as formation of Cu servovitic film, annex Fig. S13. Surprisingly, anodized 5005 alloys also showed reduced wear rates. 3003 alloys had the highest wear rate suggesting increased surface deformation and faster destruction under tribological exposure. Fast destruction of disposed Al alloys (Al waste) from beverage cans to transport or construction items are beneficial since they can cause environmental problems if not disposed properly [205].

Among all Al specimens, 1050 and 6082 alloys represent distinct materials according to their physical and mechanical properties. Therefore, they were selected for further experiments using chemically inert corundum balls. The friction of hard anodized and phospho-anodized coatings of 1050 and 6082 alloys was described further.

Hard anodized coatings significantly reduced static COF from nearly 1.0 to about 0.4 on 6082 alloys under 1 N load, Fig. 48. No significant differences in static friction observed by changing the anodizing duration from 30 min to 70 min. Phospho-anodized coatings with much higher surface porosity resulted in static COF of 0.7, which is lower than static friction of surfaces before anodization. It could be expected that friction reduction of phospho-anodized coatings would be more significant, because many phosphates act as anti-wear additives in various coatings and lubricants. Nevertheless, surface porosity and other morphological properties most likely play a more important role in tribology under dry friction conditions.

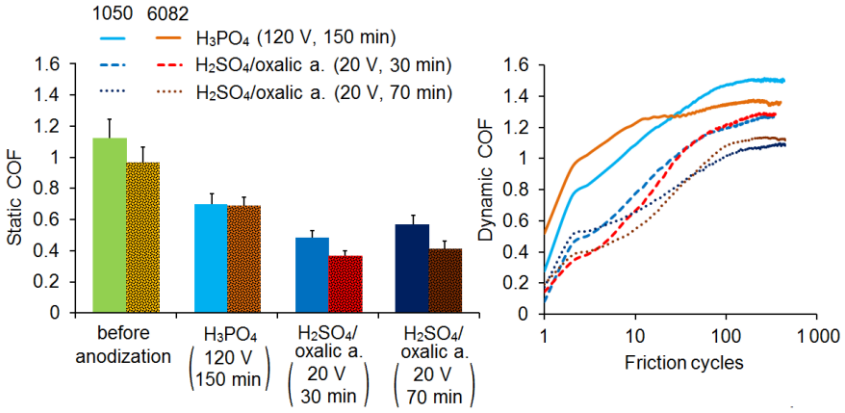

Fig. 48. *Influence of hard anodization (30 –70 min at 20 V) and phospho-anodization (150 min at 120 V) at 15 °C on static and dynamic friction under 1 N load (left bars – 1050, right bars – 6082), adapted from [151]*

The initial dynamic COF value is often lower than static COF and do not equal to the static COF since it is calculated from ~100 data points for one friction cycle at 2 cm/s velocity. Dynamic friction of hard anodized coatings was lower than that of phospho-anodized coatings, in agreement with static COF trends. Despite that anodization reduces COF, friction and wear of anodized coatings is still quite high in general, leading to abrasion and wear debris formation after just 100 friction cycles under 1 N load.

Friction properties of hard anodized coatings were also varied by setting different electrolyte temperatures for anodization. Changing anodization temperature from 10 °C to 20 °C did not significantly affect surface friction, Fig. 49.

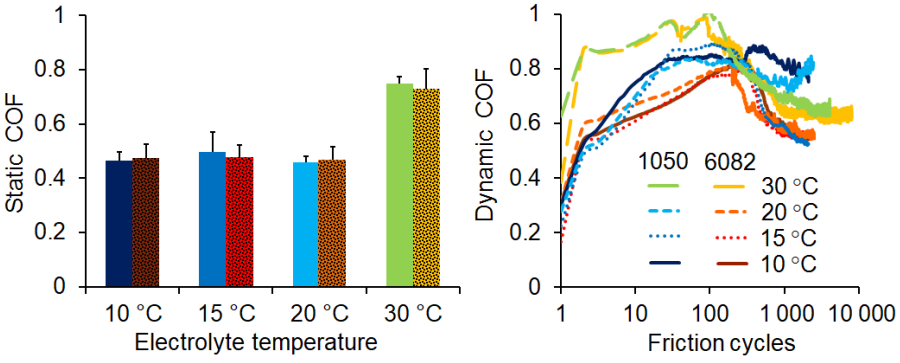

Fig. 49. *Influence of electrolyte temperature on static (left bars – 1050, right bars – 6082) and dynamic friction of hard anodized alloys under 10 N load, adapted from [151]*

However, anodization at 30 °C produced coatings with much higher friction under 10 N load. Most likely this can be explained by the fact that coating, anodized at 30 °C, was much softer than in case of 10–20 °C due to high surface porosity. Both static and dynamic COF exceeded over 0.7 at 30 °C under dry friction conditions. It can also be observed that static and dynamic COF remain quite similar between the alloys under 10 N load, while static friction differences were more pronounced under 1 N load. This is in agreement with the expectation that surface hardness affects friction more significantly under lower loads.

Phospho-anodized coatings obtained in the H_3PO_4 electrolyte with methanol and glycerol additives also were tested for friction, Fig. 50.

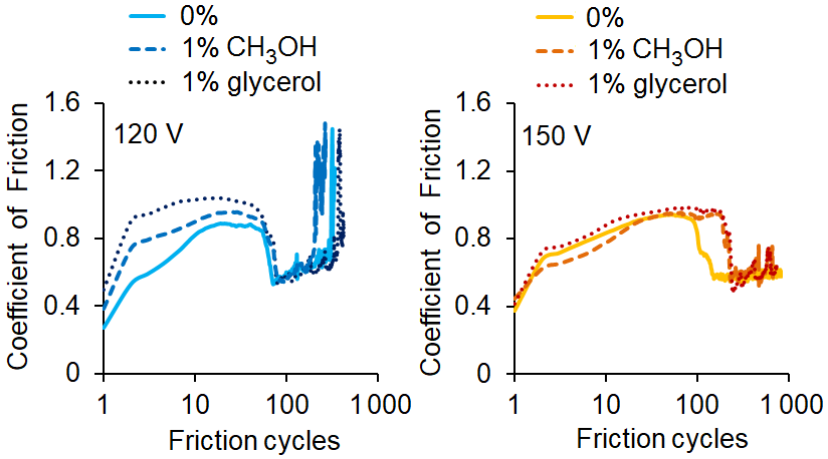

Fig. 50. *Influence of additives on friction after phospho-anodization for 150 min at 120 V (left) or 150 V (right) under 10 N load*

Despite increased coatings thickness, additives showed no improvement in friction either at 120 V or 150 V. Moreover, additives might have a negative effect on the initial friction stages of phospho-anodized coatings obtained at 120 V. The COF leap also represents that anodized coatings were totally removed after a few hundred cycles at 120 V under 10 N load.

Since static COF depends on material and surface properties, tribological conditions also should affect static friction as well. The influence of sliding velocity and load were evaluated on hard anodized coatings of 6082 alloy. Static COF decreased with increase in normal load using loads of 1 N and 10 N, Fig. 51.

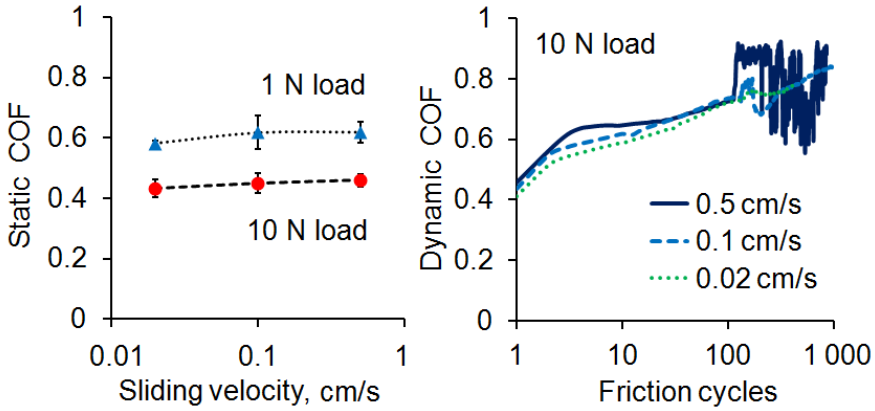

Fig. 51. *Influence of sliding velocity and load on friction of hard anodization of 6082 alloy at 15 °C, adapted from [151]*

In addition to the surface hardness effects, this might also be related to increased surface contact area [206]. As the normal load increases, the contact area changes slowly and reaches maximum, thus the friction force remains relatively constant and the COF decreases as load increases [207]. In contrast to load, sliding velocity had no influence on static or dynamic friction. However, under higher sliding velocity heat is dissipated less effectively, which increases surface wear and abrasion as expressed by fluctuations in COF curve in later friction stages.

The influence of surface roughness on static and dynamic friction also was evaluated. Surface roughness with <0.5 μm was named as "low *Ra*", ~1 μm - "medium *Ra*" and ~7 μm - "high *Ra*." Both static and dynamic friction showed high COF reaching over 0.8 of untreated 1050 alloys, Fig. 52.

On 6082 alloy COF not exceeded 0.8. After hard anodization static COF was dropped below 0.4 independently of surface roughness. This effect was more pronounced on anodized 1050 alloys when compared to untreated ones. According to studies static friction increases by increasing roughness values [208]. However, this effect was observed only on alloys before anodization. Hard anodized coatings had stable static COF below 0.4 while dynamic COF was markedly reduced on rough surfaces probably due to low contact area. In summary, surface roughness does not affect friction dramatically, while mechanical and morphological properties of porous Al_2O_3 coating is much more important for friction tendencies.

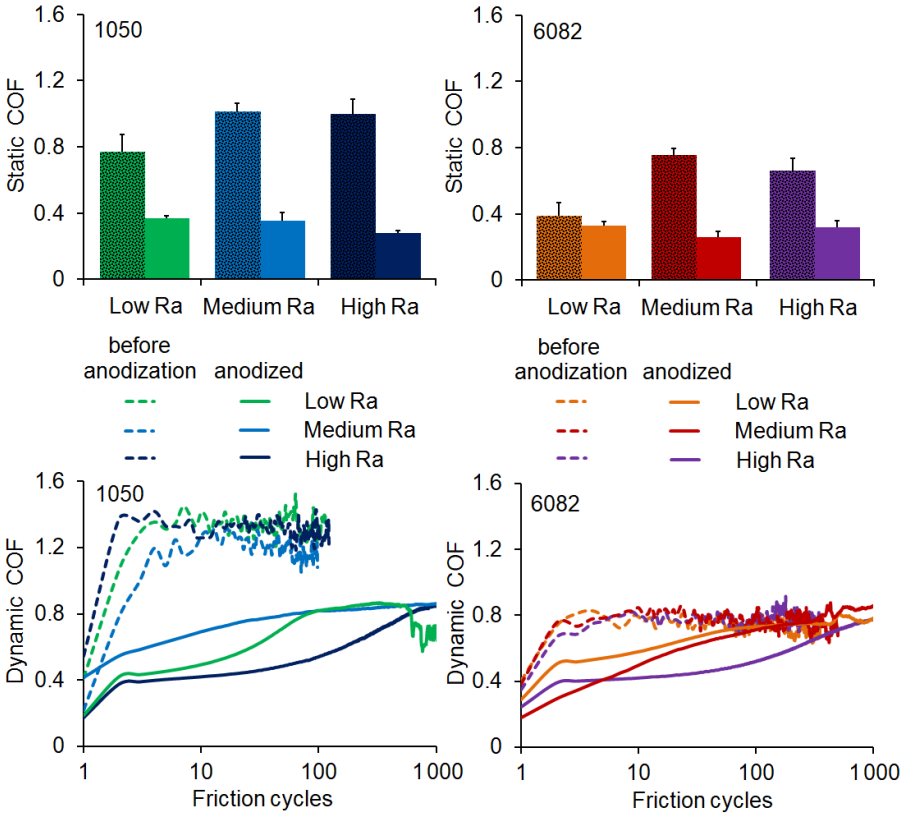

Fig. 52. *Influence of surface roughness on static (top) and dynamic (bottom) friction of 1050 and 6082 alloys before and after hard anodization (left bars – before anodization, right bars – hard anodized) under 10 N load*

For a more detail investigation of friction properties of Al, surfaces were treated with alkali/HNO_3 solution, Ar plasma or using a combined treatment. The combined treatment method has the most negative effect and increases static friction for both 1050 and 6082 alloys, Fig. 53. Surface treatment in alkali/HNO_3 solution significantly reduced static friction, especially on 6082 alloys despite less homogeneity and higher surface roughness. Static COF reduced to ~0.4 with alkali/HNO_3 and Ar plasma while combined treatment was less effective on hard anodized coatings. Moreover, surface treatment had almost no influence on dynamic friction despite slightly higher friction curves at initial stages obtained after combined treatment either on 1050 or 6082 alloys.

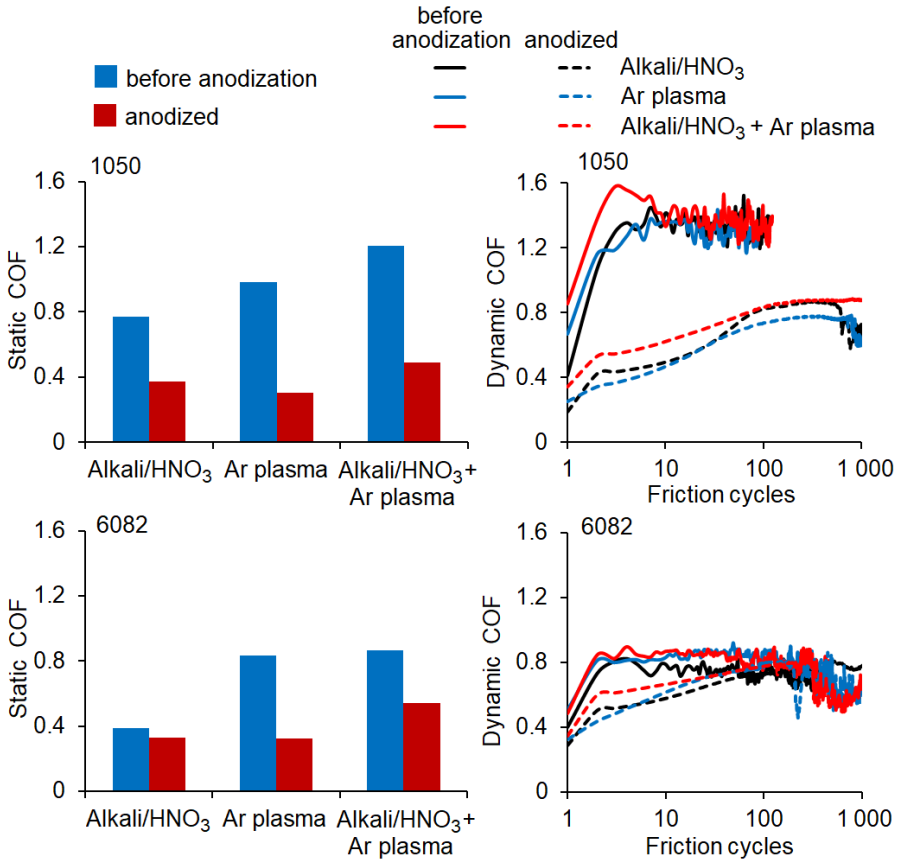

Fig. 53. *Static (left) and dynamic (right) friction of 1050 and 6082 alloys before and after hard anodization using different surface treatment methods under10 N load*

In summary, surface treatment and roughness are important for untreated specimens but have little relevance to anodized coatings. Therefore 1050 and 6082 alloys were not polished or mechanically abraded, except treatment in alkali/HNO_3 solution for removal of surface oxides and activation before anodization. Anodizing conditions for hard-anodized coatings (15 °C for 70 min under 2 A/dm²) and phospho-anodized coatings (15 °C for 150 min under 150 V) are most suitable both tribologically and morphologically. Hard anodized coatings significantly reduced both static and dynamic friction especially using 6082 alloys of low purity while the anti-frictional effect of phospho-anodized coatings is less relevant. The load of 10 N was prioritized for anodized coatings due to reduced COF. Sliding velocity has no influence on static or dynamic friction.

3.3.2 Effects of layer thickness of Ti and its oxides on friction and wear

From a tribological perspective, it is important to protect surface from any damage and accidental wear. Al alloys have poor mechanical properties producing rapid wear debris formation after just several friction cycles, which should be avoided under dry friction conditions. Although hard anodized coatings reduce COF to ~0.4, friction is still considered as high. In order to improve the resistance to friction and wear in anodized coatings, deposition of several metals and their oxides was performed. Reports by other researchers suggest that various metal-mediated mechanisms might be activated to improve tribological performance. First of all, the deposition of soft metals might induce a barrier effect, where a softer top layer acts sacrificially until it wears down to protect the anodized coating. Metal cladding effects might also be induced from the deposited oxides, possibly leading to wear reduction. In case of Cu, Sn, Pb, Ag and several other metals so called servovitic effect might be achieved. It might be expected that these metals tend to remain in the friction zone, while other metals wear down, which might eventually lead to low wear regime [203]. Other mechanisms might also be available. In this study, the best tribological effectiveness was demonstrated by Ti/TiO_2 nanolayers. However, the role of Ti in friction reduction remain unclear. No further study to investigate the causes of the tribological improvement was made available.

Several metals and their oxide layers have been tested to protect the anodized coatings against friction and abrasion by producing the barrier, metal cladding, servovitic or other tribological effects described in the literature. Nanothin layers of Ti/TiO_2 were most distinguished by considering their effect of layer thickness on surface friction. Nanothin TiO_2 layers of 5–15 nm thicknesses were formed by ALD method, while thicknesses of Ti layers varied from 16 nm to 2.3 μm using sputtering.

At first, Ti layers of 16 nm, 75 nm and 2.3 μm thicknesses were sputtered on untreated alloys using wide range thickness scale. Their friction was tested against chemically inert corundum ball, which is more applicable to studying biomaterials than other counter-bodies [209, 2010] using 10 N load. Friction was so severe on 1050 specimens that COF even exceeded 1.0, forming clearly visible wear tracks after few friction cycles, Fig. 54.

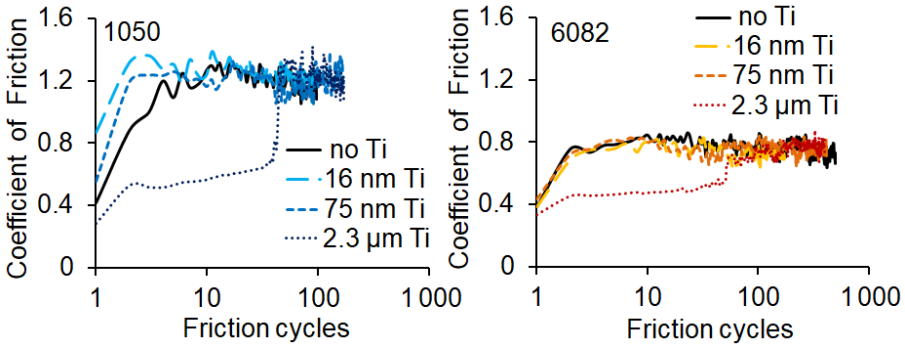

Fig. 54. *Influence of Ti layer thickness on friction tendencies of untreated 1050 (left) and 6082 (right) alloys under 10 N load, adapted from [150]*

6082 alloys had lower friction with COF ~0.8 primary due to mechanical properties. HV of 6082 alloy was more than 4 times higher than 1050 alloy, 139 HV for 6082 and 31 HV for 1050 respectively. The differences in other substrate properties, such as elasticity, compressibility, etc., might also be important, rather than any effects of Ti layers or surface topography. Ti layers of 16 and 75 nm thickness were not able to reduce dry friction on Al alloys, while thickest Ti layer of 2.3 µm reduced COF only to ~0.4. The hardness of Ti layers was expected to be much higher than that of Al substrate and this would not be beneficial to tribological properties. Ti is ~1.7 denser than Al with their densities of 4.51 g/cm^3 for Ti and 2.70 g/cm^3 for Al. As discussed by other researchers [211–213], hard top layers could easily fracture due to rapid deformation of the softer substrate, which instantly produce abrasion. Although thick Ti layers of 2.3 µm could withstand higher interfacial pressure and resist fracture or delamination, COF was still higher than 0.4, indicating rapid wear. This suggests that the arrangement of "hard layer/soft substrate" could not be considered favorable tribologically to any technological application due to high wear and surface delamination.

TiO_2 layers of 10 nm thickness also were deposited on Al alloys by ALD. As expected both 1050 and 6082 alloys showed high friction from the beginning with initial COF ~1.0, annex Fig. S14. Poor adhesion of TiO_2 layers led to rapid delamination and deformation of the softer Al substrate when engaged into mechanical contact even at 1 N load. COF values also demonstrated large fluctuations during friction tests.

Surface porosity and higher roughness of anodized coatings might increase surface contact area by allowing Ti to penetrate more deeply into

substrate and to disseminate delamination related stresses. Therefore, ALD was used to deposit 5, 10 and 15 nm TiO_2 layers on hard anodized coatings, Fig. 55.

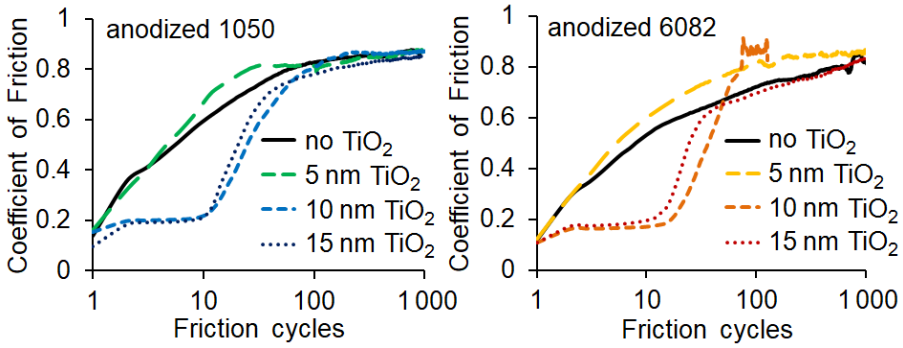

Fig. 55. *Influence of TiO_2 layer thickness on friction tendencies of hard anodized 1050 (left) and 6082 (right) alloys under 10 N load. Nanothin TiO_2 layers were produced by ALD*

The deposition of 5 nm TiO_2 layer did not have much influence on friction trends of anodized coatings, COF reaches 0.4 within just several friction cycles, similar to surfaces obtained after anodization. Anodization gives some slight tribological advantages with respect to untreated alloys, because anodizing increases surface hardness and therefore reduces wear rates. Although, anodized coatings with or without 5 nm TiO_2 layers never reached COF of 1.0 and never showed as much friction fluctuations as did 1050 or 6082 specimens without anodization, COF values were high, exceeding 0.4 within just several friction cycles. Gradual increase of COF showed higher surface friction and wear, which should generally be avoided, especially for *in-vivo* applications.

Differently than 5 nm TiO_2 layer, layers of 10 nm and 15 nm showed dramatic changes in tribology by reducing COF below to 0.2 for more than 10 initial friction cycles under 10 N load. Low COF values during initial stages of friction are important, since many organism functions are subjected to intermittent rather than continuous friction after engaging into mechanical contact with moving surfaces within an organism or during transportation and implantation. It should be noted that in both anodized alloys the difference in tribological performance between 10 nm and 15 nm TiO_2 layers is very minor, while that between 5 nm and 10 nm is much more dramatic. Comparing 1050 alloy with 6082, which has at least twice as wide pore diameter (7 nm vs 15 nm), both alloys show notable tribological

improvements after deposition of 10 or 15 nm layers, in contrast to 5 nm layers, which are not effective in that regard at all.

TiO_2 layers of 15 nm thickness, obtained by ALD, are quite comparable to Ti layers of 16 nm thickness, obtained by sputtering since error bars can exceed up to ± 2 nm. A good tribological performance of nanothin TiO_2 layers had been reported on both anodized 1050 and 6082 alloys, therefore their friction curves were compared with sputtered specimens. The same conditions: 10 N load and 2 cm/s reciprocal motion along 4 mm wear track were selected for friction tests. As mentioned above, deposition of Ti layers had no positive effect on 1050 and 6082 alloys without anodization. On hard anodized coatings, Ti layers led to a significant reduction of friction. The similarity of friction trends between 15 nm TiO_2 and 16 nm Ti layers (ALD and sputtering respectively) was remarkable, see Fig. 56.

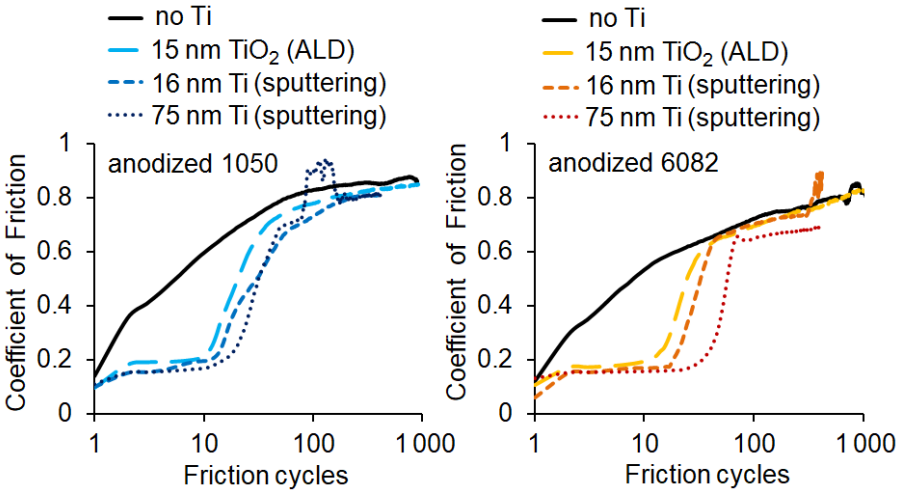

Fig. 56. *Influence of nanothin layers of Ti and its oxides on friction tendencies of hard anodized 1050 (left) and 6082 (right) alloys under 10 N load. The Ti layers were deposited by sputtering, while those of TiO_2 were produced by ALD*

Ti layers of 75 nm thickness and maybe a little thicker showed even higher effectiveness, maintaining COF below 0.2 for 20 and 60 friction cycles on anodized 1050 and 6082 alloys respectively. Since these specimens were exposed to ambient conditions for several days before tribotesting, large portion of nanothin Ti layers, which were obtained by magnetron sputtering, oxidized into TiO_2 in the presence of atmospheric oxygen and humidity as showed by XPS. Therefore, similarities of friction

trends between ALD and sputtered specimens should not be overly surprising.

Aqueous environment which predominates around biomaterials under biological conditions should also eventually lead to conversion of Ti into TiO_2. It would be reasonable to assume that layers of Ti and its oxides with thicknesses between 10 nm to 75 nm, obtained by ALD or sputtering, should demonstrate improved tribological performance under *in vivo* environment. Following this trend it might appear that thicker layers should demonstrate similar tribological performance as Ti layers of 75 nm or similar thickness, obtained by sputtering. Surprisingly, Ti layer of 515 nm thickness were much less effective, while layer of 2.3 μm thickness were not effective tribologically at all, succumbing to high friction in a very similar manner as the anodized coatings before sputtering, Fig. 57.

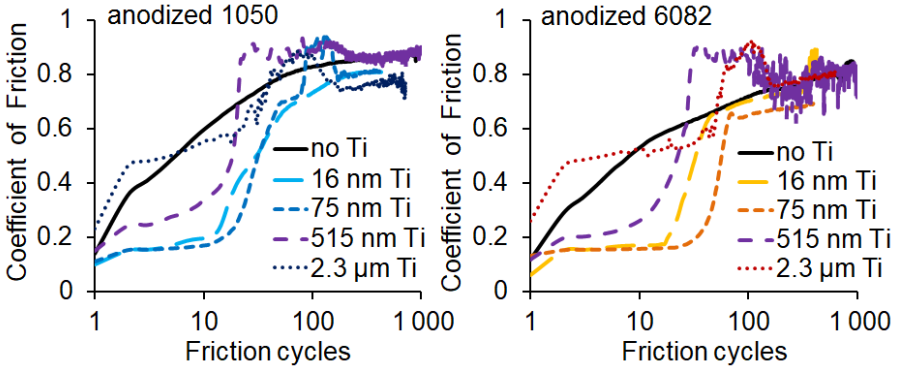

Fig. 57. *Influence of Ti layer thickness on dynamic friction tendencies of hard anodized 1050 (left) and 6082 (right) alloys under 10 N load, adapted from [150]*

In contrast to thick Ti layers, nanothin Ti layers were showed positive effect on friction reduction of anodized coatings by reducing COF below 0.2 for more than 20 friction cycles. The effectiveness of nanothin Ti or TiO_2 layers was independent of deposition method, ALD or sputtering. Although, Ti layer of 75 nm thickness was more effective and sustained more friction cycles on anodized 6082 alloys.

Nanothin Ti/TiO_2 layers have a positive effect on static friction as well. Fig. 58 shows that static COF was reduced below 0.2 using nanothin Ti/TiO_2 layers on both 1050 and 6082 anodized Al alloys. Thinner than 10 nm and thicker than 0.5 μm layers were less beneficial tribologically. Moreover, Ti layer of 2.3 μm thickness has much higher static friction when compared to anodized coatings before sputtering, especially of 6082 alloy. In contrast to

anodized coatings with thick Ti layers, nanostructured coatings are much more durable.

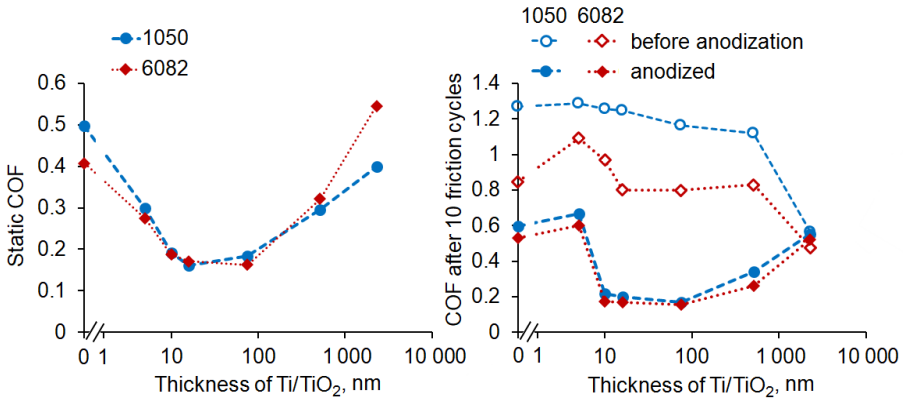

Fig. 58. *Influence of Ti/TiO₂ layer thickness on static friction (left) and after 10 friction cycles (right) of hard anodized 1050 and 6082 alloys under 10 N load, adapted from [150, 151]*

For a more detailed investigation of Ti/TiO₂ layers COF values were demonstrated after 10 friction cycles. The ability of nanostructured coatings to sustain low COF for at least several friction cycles would be beneficial in many cases including transportation or installation of anodized Al items to prevent surfaces from any incedintal damage or wear. Progressively higher thickness of Ti/TiO₂ layers almost had no possitive impact on untreated Al alloys. It is clearly evident from the graph that 6082 has much lower COF than 1050 alloy due to much higher surface hardness. The anodized alloys showed significant friction reduction with COF ~0.2 after deposition of nanothin Ti/TiO₂ layers with thickness from 10 nm to 75 nm. Surprisingly, very thin and very thick (5 nm TiO₂ and 2.3 μm Ti) layers were unable protect anodized coatings from friction and wear maintaining COF over 0.4.

For comparison the tests were performed using a steel ball, since friction against steel surfaces is quite widespread technologically. The whole sequence of untreated, anodized and sputtered specimens was screened using the same load, wear track length and velocity, i.e. 10 N, 4 mm and 2 cm/s respectively. However, no dramatical friction changes were observed on specimens against a steel or corrundum balls, despite that the difference between nanothin and 2.3 μm Ti layers was not as extreme as in case of a corundum ball [150].

When friction of Ti alloy BT1 was tested, the first 20 cycles showed very similar friction to that of 2.3 μm layers of sputtered Ti on both anodized Al alloys, Fig. 59.

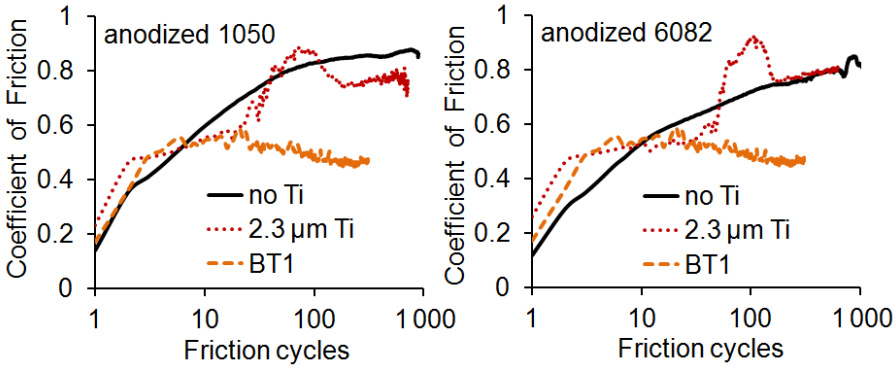

Fig. 59. *Comparison of friction tendencies of BT1 alloy (96% Ti) and anodized 1050 (left) and 6082 (right) Al alloys without or with Ti layers of 2.3 μm thickness under 10 N load*

BT1 approached steady-state COF ~0.5, while friction continued intensifying for anodized coatings without or with thick Ti layer under 10 N load. The friction stability of Ti alloys might be related to its mechanical properties including higher tensile strength and Brinell hardness when compared to Al alloys. Per technical specifications, tensile strength and Brinell hardness approximately compare as 150 MPa and 30 HB for 1050 alloy to 310 MPa and 95 HB for 6082 alloy respectively [214, 215]. Ti alloy BT1 was expected to have a tensile strength of 400–550 MPa and Brinell hardness of 380–467 HB [216]. Intensive friction of anodized coatings might be related to their disintegration, but more accurate explanation might be complex due to their nanostructured nature. In the current investigation no attempt was made to obtain much thicker layers of TiO_2 by ALD, because such approach would be impractical. Much longer durations are needed to produce ALD layers of the same thickness as those by sputtering.

Phospho-anodized coatings showed high surface friction with initial COF over 0.4 suggesting rapid surface deformation and damage after few friction cycles under 10 N load, Fig. 60. Nanothin Ti/TiO_2 layers of similar thicknesses produced either by ALD or sputtering even increased initial COF to ~0.7. However, friction was decreased to the primary value after 10 cycles. According to studies, effect of Ti and its oxides were less beneficial

on phospho-anodized coatings. Therefore, the friction and wear of nanothin Ti layers were studied in detail only on hard anodized coatings.

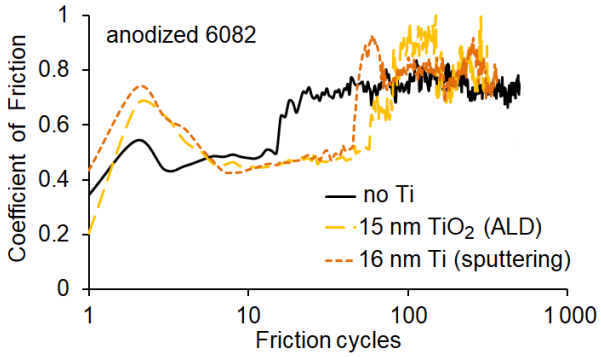

Fig. 60. *Influence of nanothin layers of Ti and its oxides on friction tendencies of phospho-anodized coatings of 6082 alloy against an Al_2O_3 ball under 10 N load*

Many applications are required long service time and durability, therefore any surface damage such as abrasion, pitting, scuffing, etc., should be avoided especially for biomedical applications. The surface wear of nanostructured coatings were evaluated using several methods, which includes optical microscopy, SEM and profilometry. Available AFM techniques could not be used because of excessive surface roughness.

The first 10 friction cycles were selected to show wear tendencies of 75 nm Ti layers before the significant abrasion were started. When Ti layers were deposited on hard anodized 1050, their wear was clearly noticeable visually just after 10 friction cycles. Before friction, the appearance of Ti layers of 75 nm thickness was bluish without significant discolorations, but after 10 friction cycles the surface with grey tones were observed, Fig. 61.

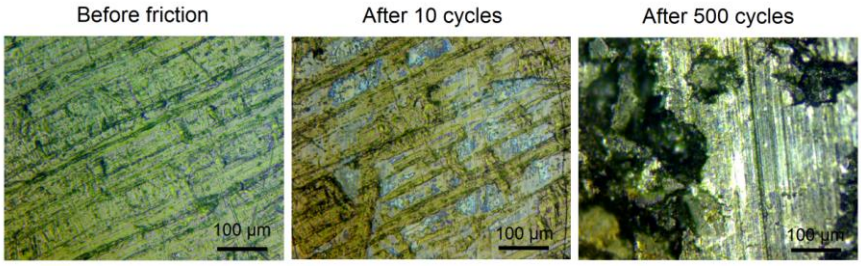

Fig. 61. *Optical microscope images of tribotest wear scars of 75 nm Ti layers on hard anodized coatings of 1050 alloy before and after 10 and 500 friction cycles under 10 N load, copied from [150]*

The grey color might be related to anodized coatings without any Ti on the top. Nevertheless, it could not be stated that the 75 nm Ti layer was completely removed from the discolored segments, because the grey protrusions might also appear as a consequence of optical effects at lower Ti layer thickness. However, at least partial delamination of the Ti layer seemed likely. The cracks were seen along the both sides of trace suggesting that the load of 10 N is sufficient for surface damage of anodized coating on a relatively soft substrate of 1050 alloy.

When the tribotester stopped automatically due to excessive friction force after 500 friction cycles, much more damage to the surface could be observed. The sharp color change from the original image implies that Ti layer is totally destroyed after 500 cycles. The black zones indicate surface decomposition and break down producing many wear debris. Very similar trends were observed on 6082 alloy as well.

The comparison between highly worn specimens is too complicated, because many specimens could not even last 500 friction cycles due to excessive friction force, which leads to an automatic tribotester shutdown. Moreover, after attaining high COF the whole Ti layer of 75 nm thickness could be removed within just several friction cycles, making it unreasonable to look for any influence of Ti on wear rates. Therefore, wear tracks was evaluated after 10 and 30 friction cycles indicating COF values below 0.2 or ~0.4 on anodized 1050 alloy, Fig. 62.

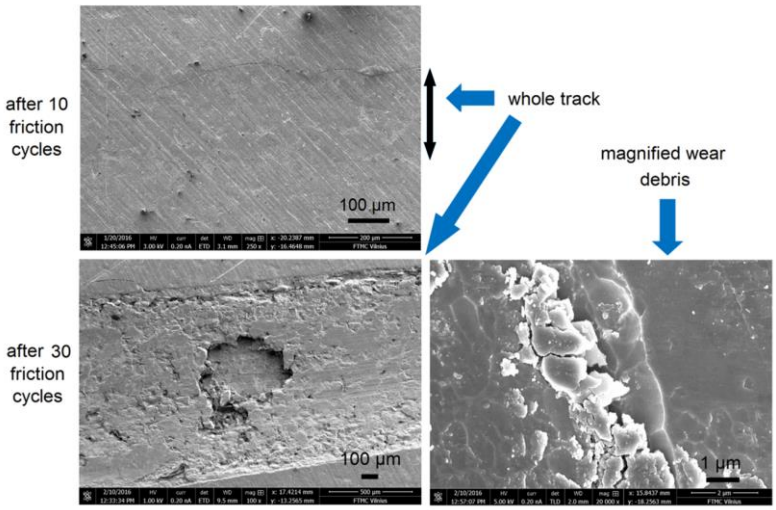

Fig. 62. *SEM images of wear tracks on hard anodized coatings of 1050 alloy with 75 nm Ti layers after 10 and 30 friction cycles under 10 N load, copied from [150]*

SEM was employed for better understanding of friction-induced Ti layer transformations on micro- and nanoscale. After 10 friction cycles the trace was barely visible despite of surface cracks formed along wear zone on anodized 1050 alloy, in agreement with optical photomicrographs. The formed trace of the friction zone still cannot be considered as a wear track after 10 cycles. According to contact mechanics theory, deformation occurs in elastic bodies under the load. For this tribotest, the theory of spherical/hemispherical deformation is most appropriate, which states that the indentation diameter is determined by the geometry, hardness, and elasticity of the interacting bodies [39]. However, the latter two parameters have not been determined for anodized coatings. Therefore, it is impossible to assess if the trace of the friction zone is greater than Hertzian elastic indentation, which would indicate that the wear had already begun. In addition, a relatively thin and porous anodized coating of ~60 μm in thickness when compared to the Al substrate might complicate the calculation.

After further impact on friction, wear resistance of nanostructured coatings was poor on 1050 alloy. A clearly visible pit was formed in the middle of the wear track after 30 friction cycles. Many smaller scars were also produced around the central part and near the edges of the track, where interfacial pressures were expected to be the highest. A large pit appeared after 30 friction cycles suggest that 75 nm Ti layer was removed with whole anodized coating of ~60 μm thickness. Calculation shows that under 10 N load the interfacial pressure exceeds 150 MPa when the contact zone diameter is less than 0.4 mm, which is the case in most tests, at least during the initial friction stages. If the high interfacial pressure is not compensated by favorable surface topography and tribofilm formation, it gradually destroys not only the Ti layers but also damages the anodized coating. It appears that such pressure is already sufficient to crack the anodized coating of ~60 μm thickness on 1050. Deterioration of the whole anodized coating gave a proof that the abrasion began sooner than 30 friction cycles producing large amounts of wear debris. Sizes of the abrasive debris particles might vary over a broad range both on microscale and nanoscale level as shown in magnified area. It might be pointed out that no cracks could be observed after 10 or 30 friction cycles on 6082, whose COF was still below 0.4 after that much of tribotesting.

Although, SEM images did not showed any surface changes on 1050 after 10 friction cycles at high magnification, surface flattening with a larger number of dark protrusions were present at microscale level when

compared to those before tribotesting, annex Fig. S15. After 30 friction cycles the surface underwent significant transformation. Different surface texture suggests that most of the 75 nm Ti layer was removed with original roughness. The abundance of small particles of ~ 0.1 μm in diameter was much higher, implying the presence of fine debris particles. The shapes and sizes of those particles showed some uniformity, which suggested that they might actually represent the remains of the delaminated Ti layer of 75 μm thickness with some tendency to aggregate.

Ti elemental mapping was performed on the zone without cracking after 30 friction cycles. EDS measurements without tribotesting showed that 75 nm Ti layers were effectively deposited on anodized 1050 and 6082 alloys, recording the average values of 1.77 at.% and 1.89 at.% of Ti respectively. Since EDS consumed the material from about 1 μm depth of the anodized coating, the contribution of Al_2O_3 coatings was much higher than that of 75 nm Ti layers which can give some error distribution then compared two different specimens. EDS showed different elemental distribution of Ti concentrations on anodized 1050 after 30 friction cycles, Fig. 63.

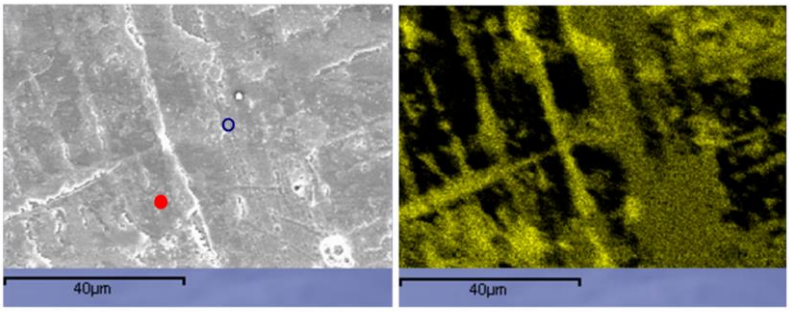

Fig. 63. *Wear track SEM (left) and EDS with elemental distribution (right) of Ti (light color) on anodized 1050 after 30 friction cycles under 10 N load. Filled and empty circles in SEM (left) represent lowest and highest Ti contents within the area, with 0.77 wt.% and 8.73 wt.% respectively, copied from [150]*

Ti concentration gradient was very high ranging from 0.77 wt.% to 8.73 wt.%, but no visible pits or major surface damage could be observed. It could be considered that Ti concentration might change more than 10 times within different areas of wear track. This suggested that Ti layer might undergo a quasi-fluid type of material transfer [162, 217, 218] from one location to another within the wear track, assuring significantly lower friction and wear, but losing the ability to withstand high interfacial pressures when friction is continuing. More complex tribological

mechanisms, such as selective transfer [203, 219] as in Cu on steel or possibly others might also be involved, but a much more extensive study would be needed to identify the most probable pathways.

Four stages of the friction curve could be excluded according to surface wear under dry friction conditions. In most cases, COF starts rising due to high interfacial pressures when the load is applied in “run-in” stage. However, COF also might decrease during surface polishing if the rough surfaces are used. The formation of quasi-fluid film using Ti layers lead to constant COF in steady state regime where no wear is present as shown by SEM after 10 friction cycles. Once Ti layer breaks down COF start rising leading to a change in interfacial pressures and a wear scar. The COF of anodized coatings also gradually increases until it reaches a plateau by suggesting the removal of adsorbed layers including hydroxides, sulfates, carbonates and other molecules. In the latest stage, many wear particles were generated and entrapped in the wear track zone during sliding leading to surface abrasion, major wear increase and COF fluctuations which are related to stick-slip phenomenon. It represents the movement of two surfaces that proceeds a series of jerks caused by alternate sticking and sliding. Stick-slip behavior could occur with both unlubricated and lubricated surfaces under high normal loads depending on the surface finish [220].

According to SEM images with noticeable surface damage of nanostructured coatings, profilometry was used to identify surface changes with or without Ti layers of 75 nm thickness. Contact profilometer showed that nanothin Ti layers did not increase wear resistance either on anodized 1050 or 6082 alloys after 30 friction cycles, annex Fig. S16. Nevertheless, COF of nanostructured coatings remains much lower when compared to anodized coatings. It must be mentioned that wear track depth was overlapped with surface roughness after 10 friction cycles by confirm the fact that Ti layers will resist to abrasion and incidental friction at least 10 friction cycles using 10 N load or less under dry friction conditions.

In conclusion, Ti/TiO_2 layers are beneficial only on hard anodized coatings while antifrictional effect of Ti on phospho-anodized coatings and specimens without anodization are less effective. Independently of the deposition method ALD or sputtering, Ti/TiO_2 layers of 10 nm to 75 nm in thicknesses or maybe a little thicker layers significantly reduce COF below 0.2 while layers thinner than 10 nm or thicker than 0.5 μm have much lower effect on friction reduction of hard anodized coatings. Despite low friction, wear of nanostructured coatings is still high in general.

As with dynamic friction, very thin or thick Ti/TiO_2 layers were less effective in reducing static friction. Such behavior is not consistent with the metal deposition hypothesis since both ALD and sputtered nanothin layers exhibit nearly identical trends. This is not consistent with the barrier layer hypothesis since thicker layers increase friction. Servovitic effects with Ti have not yet been described and due to its hardness are unlikely. Therefore, it was intended to evaluate the relationship with other metal oxides.

3.3.3 Tribological benefits of nanothin layers of group IVB elements and their oxides

Materials like ZrO_2 gain recognition in many areas including medicine for dental implants and prosthetic devices due to its biocompatibility, good mechanical stability, hardness and high resistance to scratching and corrosion [221, 222]. The potential of Hf based layers for biomedical applications also was studied earlier [223, 224]. Therefore, the friction of group IVB metals including Ti, Zr and Hf also were tested on anodized coatings. Results showed that nanothin layers of IVB group metals and its oxides reduced static friction mostly below 0.2, but dynamic friction was less effective when compared to Ti/TiO_2 layers of similar thicknesses deposited either by ALD or sputtering, Fig. 64.

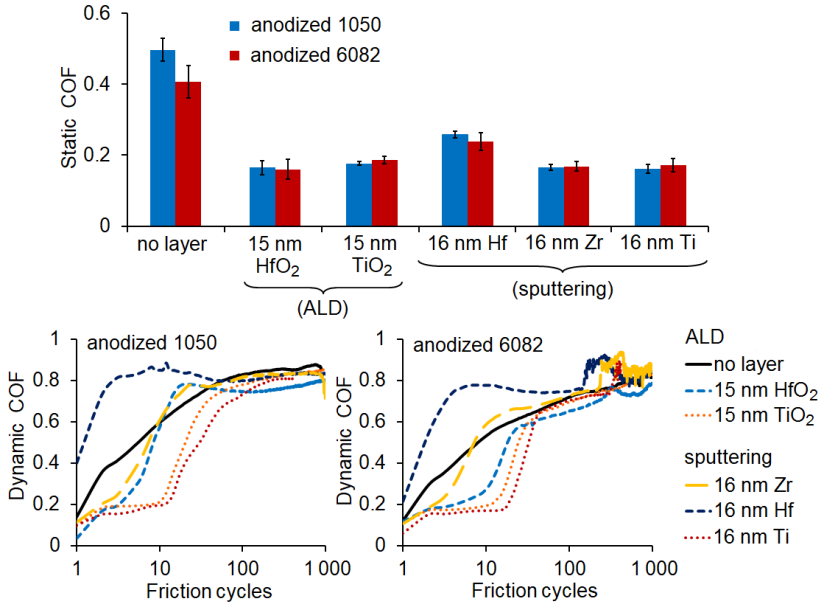

Fig. 64. *Influence of nanothin layers of group IVB transitional metals on static (top) and dynamic (bottom) friction of hard anodized alloys under 10 N load*

In contrast to HfO_2 layers deposited by ALD, sputtered layers of Hf static increased friction and wear leading to surface abrasion and damage after few friction cycles under 10 N load. The friction of Hf nanothin layers was much higher than of the other two IVB elements Ti and Zr. Such tribological differences might be influenced by the incomplete conversion of Hf layers to HfO_2 under a humid atmosphere. Another explanation might be related to the hardness of nanothin layers. HfO_2 is much harder and denser than ZrO_2 or TiO_2. Their hardness and density are 8.3–14.4 GPa and 9.68 g/cm^3 [225], 6.4–10.5 GPa and 5.68 g/cm^3 [226], 2–13 GPa and 3.78–4.23 g/cm^3 for TiO_2 [227] respectively. High hardness of Hf layers led to wear debris formation and abrasion of softer porous Al_2O_3 coatings. Overall, sputtered Hf layers have a negative effect only on dynamic friction while static COF reduced two times when compared to anodized coatings. ALD deposited HfO_2 layers reduce initial friction, especially on anodized 6082 alloys mostly due to higher TDMAH penetration into pores. Nanothin Ti/TiO_2 layers are most effective on friction reduction and reduce both static and dynamic friction below 0.2 for at least 10 friction cycles. Sputtered Zr layers reduce static COF, bus unable to assure low friction in later friction stages. It is expected that hardness of oxidized Zr might act as abrasive and initiate surface abrasion in later friction stages.

For comparison, other metal layers including Cr, Nb and Cu which do not belong to the group IVB also were tested for the friction. Although electrochemical coatings of Cr can have a positive effect on friction and wear on steel substrate [96, 228], nanothin Cr and Hf layers of 75 nm thicknesses showed rapid decomposition of anodized coatings under 10 N load, Fig. 65.

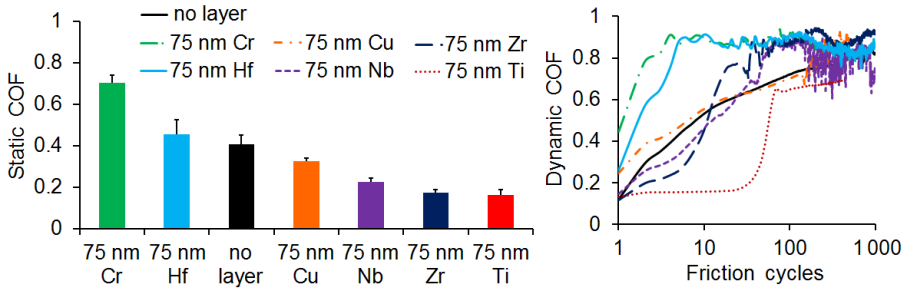

Fig. 65. *Influence of nanothin layers of 75 nm thickness on static (left) and dynamic (right) friction of hard anodized coatings of 6082 alloy under 10 N load*

A similar effect of nanothin layers was shown on untreated alloys leading to the high static and dynamic COF of ~0.8 with clearly visible surface damage after a few cycles, annex Fig. S17. The low friction of Cu was demonstrated on steel and a copper alloy i.e. bronze due to formation of a servovitic film created by the selective transfer mechanism. Servovitic film is porous and forms a microisland pattern with a size of 1 μm rather than a uniform film of constant thickness, which protects the surfaces in the contact zone by regenerating itself constantly [203, 204, 229]. However, nanothin layers of Cu or Nb do not showed a significant effect on friction reduction, although the static friction was lower compared to anodized coatings without nanostructurization. The elements of group IVB including Zr and Ti had the best tribological performance. Despite the higher dynamic COF of Zr layers, static COF reduced below 0.2 for both Zr and Ti.

The antifrictional effect of nanothin layers on phopsho-anodized coatings was less relevant. Although, Ti layers of 75 nm thickness reduced static friction for at least two times, see Fig. 66.

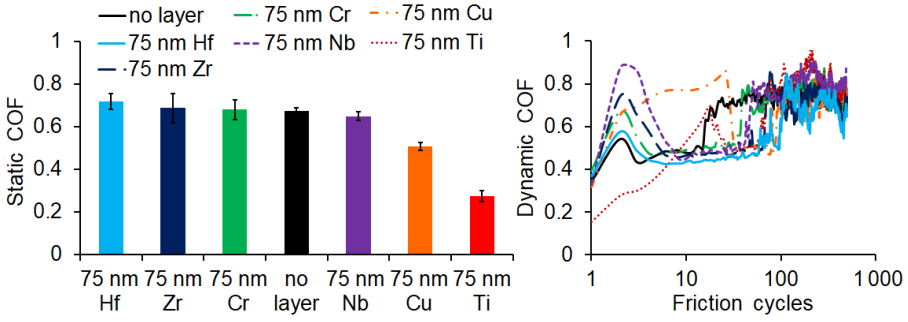

Fig. 66. *Influence of nanothin layers of 75 nm thickness on static (left) and dynamic (right) friction of phospho-anodized coatings of 6082 alloy under 10 N load*

Cu layers also showed some effectiveness on static friction reduction but in general not able to sustain friction and led to surface destruction after few cycles. Other layers showed no improvement on friction when compared to phopsho-anodized coatings before sputtering.

To sum up, nanothin layers of Zr and Ti provide the best anti-frictional effect, especially using hard anodized coatings. Although, the reasons for their remarkably high tribological efficiency has not been clarified yet, it is likely that Ti acquires quasi-fluid type of material transfer within the friction zone by assuring low friction [162, 217]. For technical, biomedical and other applications of anodized coatings, the findings of this study

provide that nanothin layers reduce static friction below 0.2, and in the case of Ti, decrease dynamic friction during initial cycles of dry friction.

According to the best tribological performance of sputtered Ti layers of 75 nm thickness, their stability also was evaluated on hard anodized and phospho-anodized coatings. Results showed that nanostructured coatings have more stable static friction rather than hard anodized coatings after 100 days of aging especially of 6082 alloys, Fig. 67.

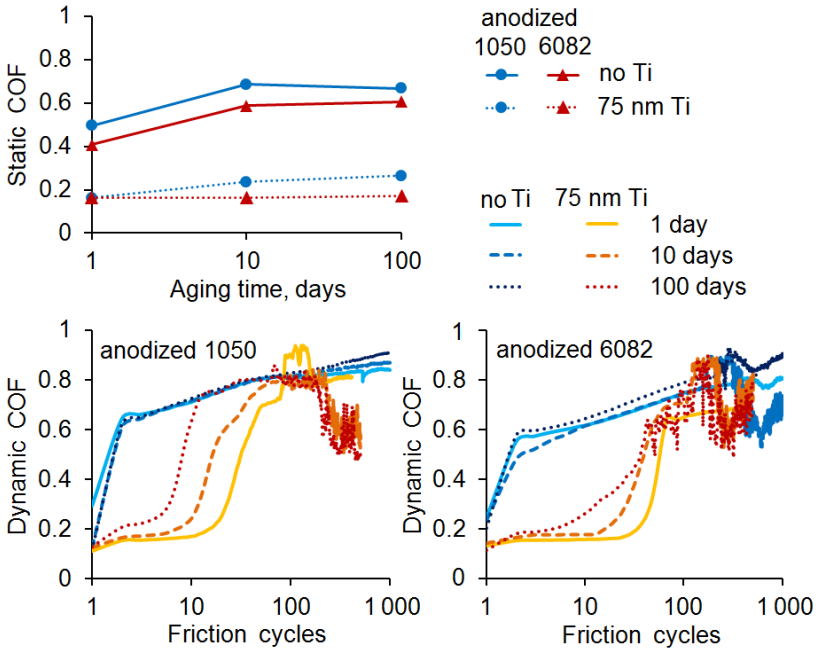

Fig. 67. *Stability of static (top) and dynamic(bottom) friction of hard anodized coatings of 1050 and 6082 alloys on aging time under 10 N load*

Oppositely of static friction evaluations, dynamic friction revealed poor sustainability of nanostructured coatings after surface aging. The highest deterioration of nanothin Ti layers was observed on 1050 alloy after 100 days of aging maintaining low COF for less than 10 friction cycles. Nevertheless, nanostructured coatings should be effective for incidental friction when surfaces are influenced by intermittent rather than continuous movements.

Similar findings were observed on phospho-anodized coatings of 6082 alloy. Surface aging had no influence on static friction of nanostructured coatings when compared to phospho-anodized coatings without Ti layer, Fig. 68.

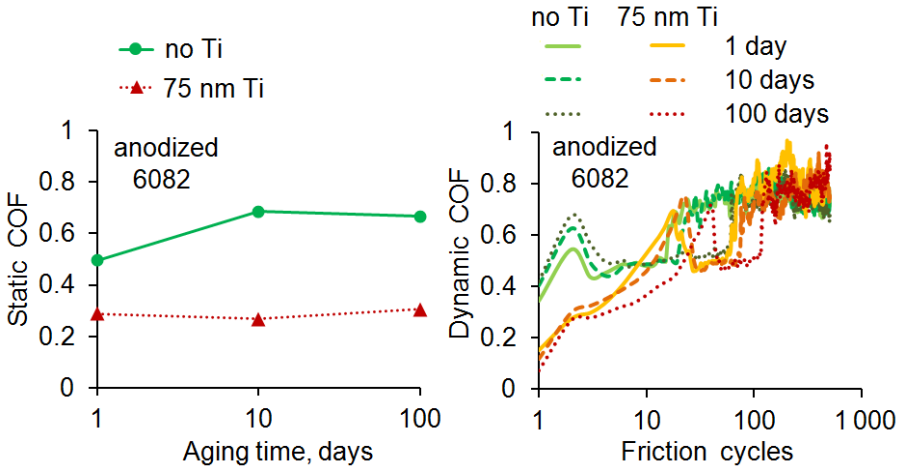

Fig. 68. *Stability of static (left) and dynamic(right) friction of phospho-anodized coatings of 6082 alloy on aging time under 10 N load*

In contrast to nanostructured coatings of hard anodization, phospho-anodized coatings with nanothin layers of Ti did not show any negative tribological effect on aging time. Although, friction reduction of Ti layers were less relevant on phospho-anodized coatings under 10 N load.

3.4 Migration of impregnated compounds into anodized coating

Lubricants, dyes, anti-corrosive fillers and other functional materials are often used to improve various properties of porous coatings. Therefore, it is important to monitor their migration into the coating in order to reduce surface friction and wear, transmitting forces, reducing heat generation, wear debris formation and ensuring control of other processes. The migration of organic compounds into the pores of anodized coating is also important in biological systems when coatings are in contact with body fluids. Therefore, friction occurs not under dry conditions but under lubricated conditions. Korean tribologists [230] tried to lubricate anodized coating with pentadecane paraffinic oil. Their anodization, impregnation and tribotesting approach was very similar to this investigation. They produced 60 μm thick coatings with ID pores in oxalic a. electrolyte saturated them with oil and performed ball-on-plate reciprocal tribotests. Only limited improvement in friction reduction and wear resistance was achieved. Significant wear was detected under 0.5 N load already with significant increase in friction just after 15 reciprocal cycles. Major wear of steel ball was also observed. This shows that traditional lubricants perform very poorly on anodized Al. In

addition, oxalates are known to decompose into CO_2 easily. Friction zone conditions also could facilitate CO_2 evolution and accelerate wear. The penetration of the organic compounds into the pores of anodized coating are questionable and requiring shaking, heating, long-term exposure and other techniques to accelerate migration for better tribological performance. Therefore migration of the most important biological compounds and tribologically effective fillers into the pores of the anodized coating has been investigated in detail.

In this study the term "migration" is used to describe the transfer of azodyes, fillers and other target materials from the outside into the inner portions of nanopores. The exact mechanism of the material transfer is often unknown, because electrostatic, colloidal, osmotic and other forces might take part during the process. It cannot be stated that the term "migration" is better than "diffusion", "impregnation", "penetration" or other possible terms. The term "migration" is used solely only in order to avoid confusion.

3.4.1 Penetration of hydrophobic fillers into the pores of anodized coating

At first, investigated materials including lipids (95% stearic a., 70% and 99% oleic a.), esters (60% and 99% methyl oleate), polymers (25% PTFE in IPA), lipid filler and biobased filler 18Z were identified by Raman spectroscopy. Lipids and esters are very differ from PTFE fluoropolymer, which is characterized by the highest intensity peak of CF_2 symmetric stretching at ~735 cm^{-1} and other lower vibrational modes of CF_x group as showed in Fig. 69 [231].

The high content of triglycerides (i.e. tristearin) found in adipose tissue [232] and fatty a. in blood plasma [233] suggest that bioceramic surfaces able to interact with lipids and components of a cell membrane, which might determine different tribological properties of anodized coatings after adsorption. Differently from stearic a., oleic a. is defined by C=C double bond stretching at ~1656 cm^{-1} in the aliphatic chain [234]. The stearic a. showed slightly different Raman spectrum and vibrational modes mostly due to its solid state under environmental conditions. The Raman spectra of esters based on oleates also showed some differences. Methyl oleate ester had low intensity peak of C=O stretching at 1740 cm^{-1}. A single peak of C=O vibration related to esters rather than fatty a. those showed no peak in the region of 1677–1711 cm^{-1} [235]. Other peaks are mostly related to the molecular vibrations of the aliphatic chain [236]. The concentration of fatty a. or esters had no influence on Raman spectra and their vibrational modes.

For lipid filler and biobased filler 18Z the Raman spectra were quite similar to fatty a. despite of higher intensity of C=C stretching groups.

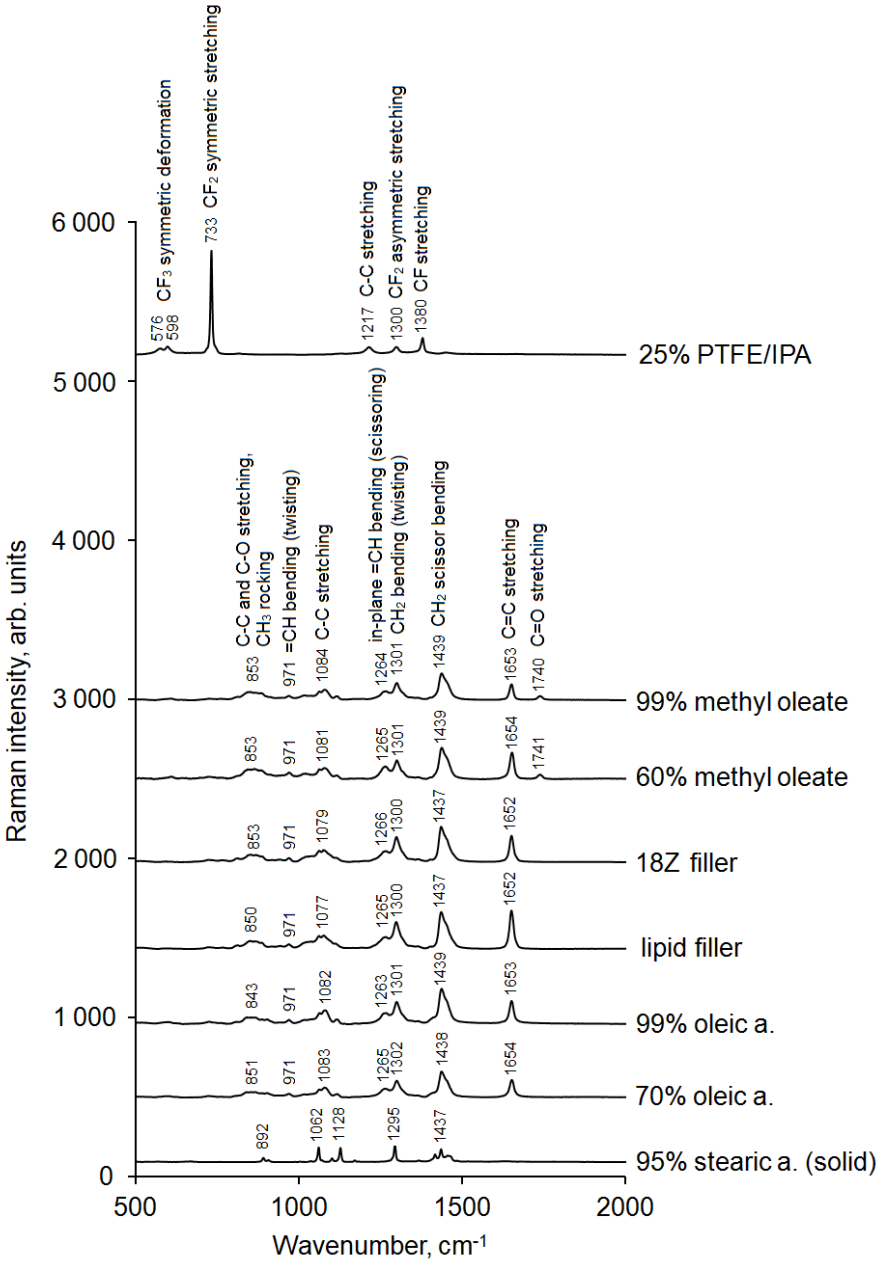

Fig. 69. *Raman spectra of investigated materials including lipids, esters, alcohols and polymers*

For the migration of organic compounds, the Raman spectroscopy method was developed using a fully anodized Al foil of 70 μm thickness with an average pore diameter of ~13 nm obtained after anodization in H_2SO_4/oxalic a. electrolyte at 15 °C.

For Raman scattering, which is the basis of Raman spectroscopy, photoluminescence (PL) is not beneficial. PL intensity of anodized coatings depends on alloy composition, type of electrolyte, temperature, anodization voltage, current density, pore diameter and other processing parameters [237–239]. As showed previously, PL of anodized coatings was much higher when prepared in the oxalic a. electrolyte rather than sulfuric a. or phosphoric a. [237]. It this study, high PL values was observed on both partially anodized foil and hard anodized Al alloys of 1050 and 6082 by focusing the laser beam of 785 nm according to PL maximum for the anodized coating, Fig. 70.

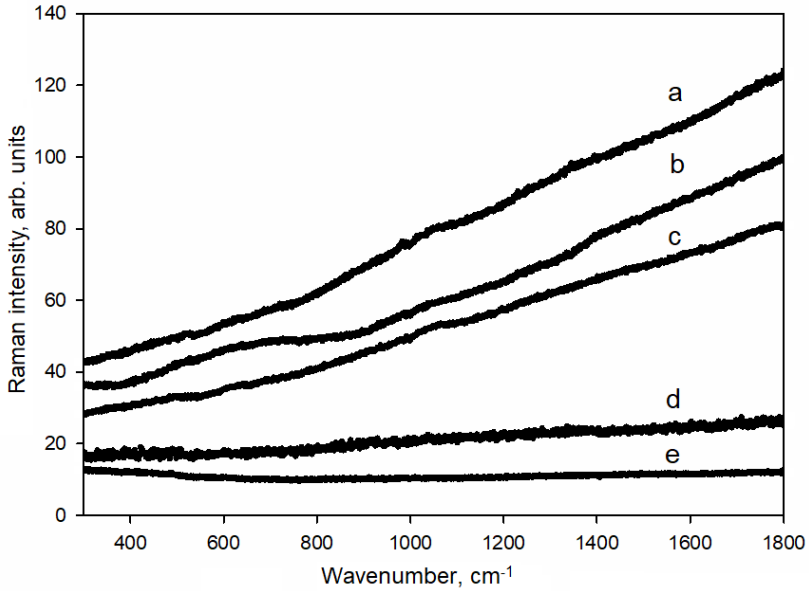

Fig. 70. *Raman spectra in "finger print" region of anodized Al: (a) partially anodized 1050 discs; (b) partially anodized 6082 discs; (c) partially anodized foil; (d) fully anodized foil; (e) plain Al foil before anodization, adapted from [152]*

PL phenomena was negligible for fully anodized Al foil as well as for non-anodized foil. Therefore, fully anodized Al foil was selected for further studies since the Raman responses of migrating compounds could be properly recorded.

FAMEs derived from renewable lipid feedstocks, such as vegetable oils or animal fats often used for biofuel additives and as sustainable lubricants. They comprised of monoalkyl esters of long-chain fatty a. mostly of methyl oleate (~60%), methyl linoleate, methyl palmitate and other esters which has anti-wear properties on both steel and anodized Al substrates. Their ability to reduce friction was much more effective than fatty a. [240]. These esters hereinafter referred to methyl oleate. Higher migration of lubricants into the pores of anodized coating might provide better resistance to friction and wear [140].

The penetration of methyl oleate was evaluated on the fully anodized Al foil by focusing the laser beam from the top of the surface to the coating of 54 μm in depth. Raman spectra of fully anodized Al foil with or without methyl oleate showed two intensive peaks at 980 cm^{-1} and 1060 cm^{-1} which corresponds to SO_4^{2-} group [241] and C-C stretching [242] vibrational modes respectively, Fig. 71.

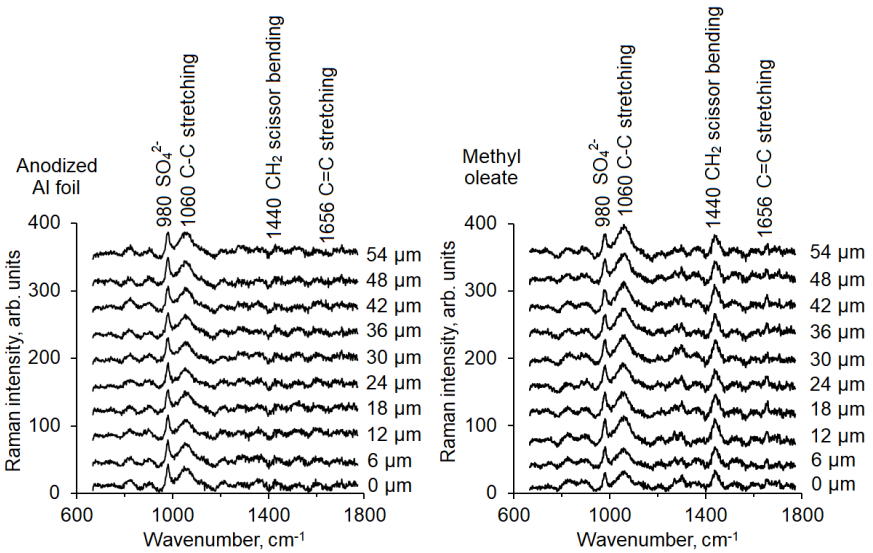

Fig. 71. *Raman spectra variations on depth before (left) and after (right) deposition of methyl oleate on the fully anodized Al foil surface*

The peaks exclusively represent additives (i.e. sulfates and oxalates) of anodized coating that appeared from H_2SO_4/oxalic a. electrolyte across the whole Al foil. Other peaks of lower intensity should be eliminated due to the high background signal. Although, some pollution of organic compounds is possible by not using high purity reagents for anodization electrolyte. After

one hour of methyl oleate deposition, high intensity mode of CH_2 scissor bending at 1440 cm^{-1} [235] and low intensity mode of C=C stretching at 1656 cm^{-1} were observed indicating vibrations of the unsaturated oleyl chain. Meanwhile, the intensities of the anodized Al foil without methyl oleate overlap with background signal at 1440 cm^{-1} and 1656 cm^{-1}.

Two anodized foils were selected for methyl oleate penetration by testing three different places under the same spot for Raman spectroscopy. The penetration depth of methyl oleate was calculated according to the area of Raman spectra of CH_2 vibrational mode at 1440 cm^{-1}, Fig. 72.

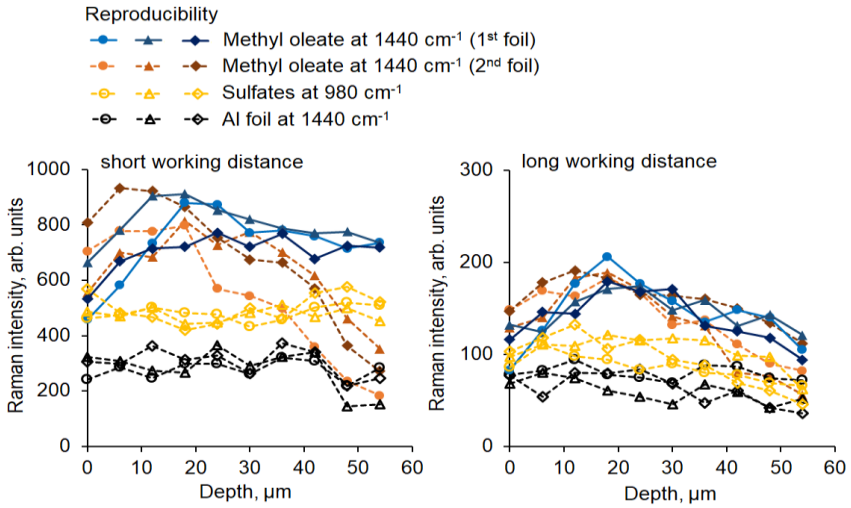

Fig. 72. *The penetration depth of methyl oleate throughout fully anodized Al foil using an objective lens with short working distance (left) and long working distance (right). The area of Raman spectra was calculated at 980 cm^{-1} for sulfates group and 1440 cm^{-1} for methyl oleate and fully anodized Al foil*

Raman intensity and peak area is much higher on lubricated conditions rather than anodized Al foil without lubrication. The peak of sulfates at 980 cm^{-1} is quite stable suggesting that distribution of sulfates possibly are uniform across all anodized coating. It was observed that the intensity of CH_2 peak was lower from 0 to 10 μm of depth rather than inside the pores of anodized coating. However the peak intensity might be reduced after removing the excess of methyl oleate from the surface after 1 hour exposure before analysis. The ability to penetrate is correlating to the highest peak intensity observed from depth of 10–20 μm with average reproducibility. This shows that lubricant able to penetrate into the pores of anodized Al foil due to capillary action or other related effects. The penetration of methyl

oleate was obtained using an objective lens with a short working distance of 0.3 mm and a long working distance of 8 mm by adjusting the Z axis for laser excitation. Although objective with a long working distance have lower efficiency of laser illumination and collection of the Raman scattered light, the diameter of the spot for methyl oleate detection is higher than 1 μm. Raman intensity reduced about three times using long working distance. Depending on the laser working distance, the measured intensity values change, but the penetration maximum of methyl oleate remains at 10–20 μm. Since the Raman with a lens of short working distance generates a stronger signal, it able to separate the differences between two anodized Al foils. The drop of Raman intensity of the second foil with methyl oleate was clearly evident when compared to the first foil, especially of 50–60 μm in depth. This can be explained by a significant decrease in the content of methyl oleate. Decreased pore integrity, increased content of hydrates and reduced collection efficiency from the deeper area of anodized coating might also contribute to the lower intensity of Raman signal.

The penetration studies of methyl oleate evaluated by Raman spectroscopy well corresponded to the migration of fluorophore rhodamine B dissolved in methyl oleate using confocal fluorescence microscopy. Their penetration depth was ~15 μm after impregnation into the anodized coating under submersive conditions [140]. However, only fluorophore concentrations were determined. Meanwhile, Raman spectroscopy detects the methyl oleate itself. In this study, it was unable to use fluorophore rhodamine B for penetration studies due to detector saturation and high background fluorescence with concentrations either of 10 ppm and 1 mM. Both methyl oleate measurements on anodized Al foil and fluorophore measurements on anodized coating showed a similar distribution of concentrations. This confirms the suitability of both methods and the penetration tendencies of methyl oleate into the pores of the anodized coating.

3.4.2 Migration of hydrophilic dyes through the anodized coating

Most dyes are designed so that the dyeing is performed by saturation of the pores by adsorption on Al_2O_3 in the region closest to the coating surface. Uniformity of coating thickness and pore structure are very important to obtain correct color and stability. To achieve this, anodization conditions including temperature, pH, concentration and duration must be controlled. The newly developed methodology was used to evaluate the migration of hydrophilic compounds into the pores of the anodized coating. Two types of

commercially available chromium-complexed anionic azo dyes (black and green) were chosen for the detection of penetration rates through fully anodized Al foil using Raman spectroscopy. These dyes are widespread commercially because they provide rich colors and hide gray irregularities obtained after anodization.

The migration of azo dyes was evaluated by directing the laser beam to Al foils anodized at 15 °C and 30 °C. The laser beam was focused to the center of the anodized Al foil according to the maximum of the background PL, although the exact position of the focused area in the 70 μm thick anodized foil is not known. In the case of methyl oleate, Raman intensity was recorded after 1 h of sample application. Raman spectra were recorded at various depths of foil by changing working distance of objective for laser illumination.

For the penetration studies, 5 μL of black and green azo dyes were deposited onto the fully anodized Al foil to avoid excessive overfilling of the pores of Al_2O_3 coating. After detection with Raman spectroscopy, the most intensive vibrational modes of each dye were selected for detail investigation to reduce the error values in spectra analysis. Vibrational modes of 1285 cm^{-1} for black dye and 1264 cm^{-1} for green dye were assigned to endocyclic or exocyclic C-N functional groups respectively [243]. It was observed that after 25 min the most intensive vibrational modes of each dye showed a small but distinct shift to lower frequencies. For black dye the shift registered was from 1285 to 1282 cm^{-1} and for the green dye it was from 1265 to 1263.6 cm^{-1}, Fig. 73.

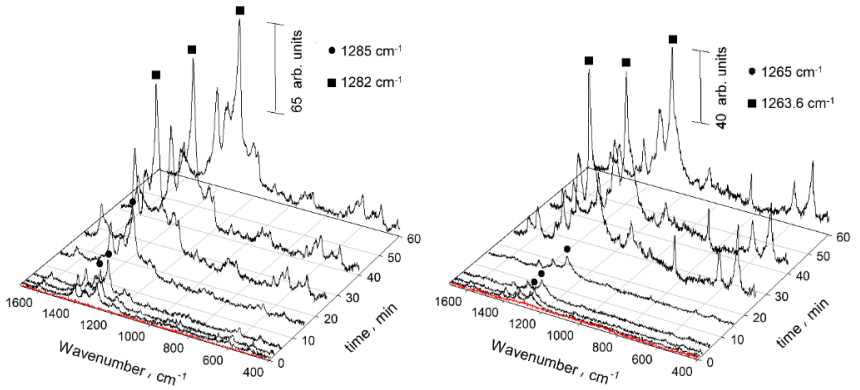

Fig. 73. *Raman spectra variations in time after 5 μL of each dye were dropped onto the fully anodized at 15 °C temperature Al foil surface: (a) black dye; (b) green dye, adapted from [152]*

Larger shifts suggest stronger interactions indicating that the interaction of the black dye with the anodized Al foil is much stronger than that of the green dye. Both dyes achieved the maximum Raman peak intensity within 25 minutes of drop deposition at 15 ºC, Fig. 74.

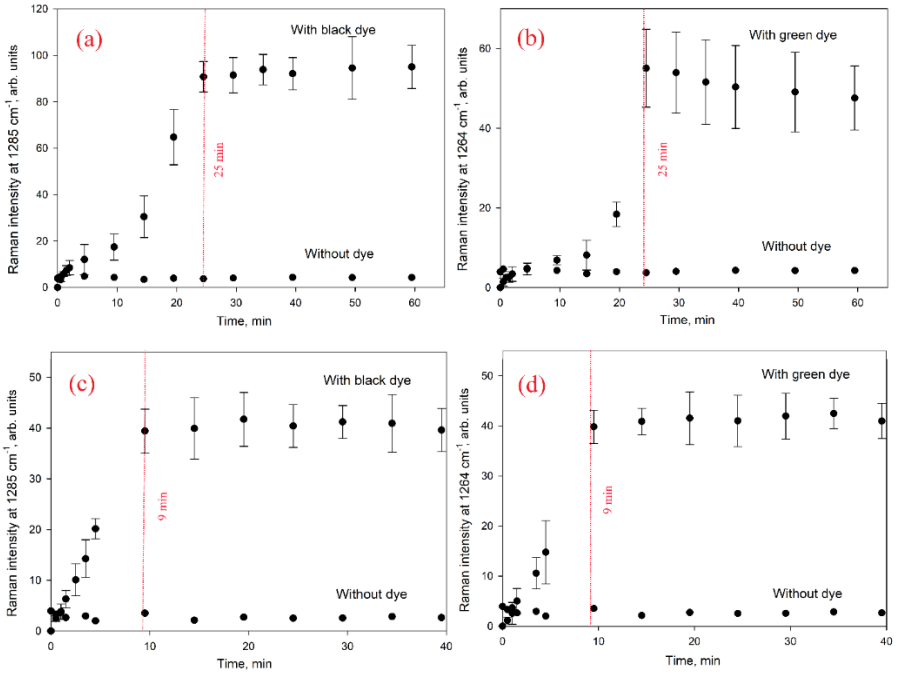

Fig. 74. *Penetration rate of two different dyes throughout fully anodized Al foil: (a) black dye and (b) green dye when Al foil was anodized at 15 °C temperature; (c) black dye and (d) green dye when Al foil was anodized at 30 °C, adapted from [152]*

The green dye curve has a sharper growth with some delay period at the beginning. This indicates that the initial migration of the azo dyes was uneven and migration of the green dye was slightly slower when compared to the black dye. However, both dyes later equalized and reached a uniform depth after 25 min of penetration. Once green dye reaches its maximum value after 25 min it shows a slight tendency to decline, although this is not statistically significant. The decrease of intensity might be related to the dye degradation processes or its interaction with residual electrolyte in the anodized foil. In addition, the green dye was partly washed out from the pores of anodized Al during the dyeing procedure. Raman intensity is related to the amount and nature of the functional groups and their ability to interact

with anodized Al foil. Results showed that the intensity of black dye was about two times higher than a green dye indicating stronger interaction with Al_2O_3. Migration of azo dyes depends on capillary action, diffusion, adsorption, colloidal and other effects. In the case of capillary action, dye penetration occurs when the adhesion to the pore walls is stronger than the cohesive forces between the dye molecules. When comparing dye migration studies with methyl oleate, it is likely that penetration of the dye into the pores of anodized Al foil is faster than methyl oleate. According to Raman intensity, the penetration depth of methyl oleate was 10–20 μm after 1 h of application, while the maximum intensity of the azo dye was reached just after 25 min probably of depth greater than 10 μm. In addition, dye molecules with hydrophilic properties may interact with hydrates more easily, which are remained in the anodized Al foil. When Al foil was anodized at 30 °C, larger pore sizes were obtained. It was showed that the temperature from 15 ºC to 30 ºC increases surface porosity (7.8% vs 18.0%) which led to 2.8 times higher dye penetration rates. The migration trends of both dyes were similar using anodized Al foil with higher porosity.

The utilization of Raman spectroscopy with anodized Al foil can be a valuable tool for assessing dye or lubricant behavior and its efficiency. A method based on Raman spectroscopy can be applied for evaluating the suitability of newly synthesized or formulated organic dyes and lubricants for porous Al_2O_3 surfaces. For a better understanding of the migration processes, dye structure and possible interaction with anodized Al foil were studied in detail.

3.4.3 Interactions with residual electrolyte

The composition of commercially available chromium-complexed anionic azo dyes is confidential. However, it might be reasonable to assume that they contain chromium-complexed azo moiety in commercial dyestuffs, Fig. 75.

Spectroscopic studies [244] detected that vibrations of Cr organometallic bonds and aromatic rings are dominated in dye molecules. As is evident from the molecular structure, anionic azo dyes contain a lot of aromatic rings and some double bonds, which result in vibrational modes of high intensity in Raman spectra. Far-field Raman spectra from 2000 cm^{-1} were not exposed any relevant information about the chemical structure of anionic azo dyes, annex Fig. S18. Therefore, only near-field Raman spectra were studied in detail.

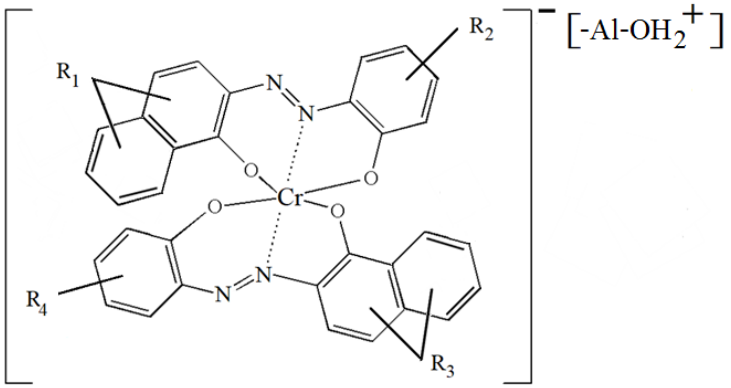

Fig. 75. *Molecular structure of the one of the most prevalent chromium-complexed azo moieties in commercial dyestuffs after adsorption within the pore of anodized Al. R_1 to R_4 represent a variety of substituents, ranging from anionic functional groups (-Cl^-, -COO^-, -SO_3^-), alkyls and other types of hydrophobic or hydrophilic chains, adapted from [152]*

Although C-N group of most intensive vibrational modes also could belong to amides, in this case, no signal was detected at 1646 cm^{-1} indicating that C-N functional groups are not amidic [243]. Other vibrational modes are mostly related to moieties of aromatic ring compounds, which are predominant in Raman spectra. The abundance of π electrons is very favorable for Raman spectroscopy due to the sensitivity of such compounds. Most relevant peaks also should be pointed out by revealing the possible structure of the most prevalent chromium-complexed azo compounds in commercial dyestuffs. It was shown that the phenyl group at ~1000 cm^{-1} are most intensive in Raman spectra [245]. However, the intensity of vibrational mode at 1001 cm^{-1} was very low for green dye while no band was found for black dye. This suggests that aromatic ring has at least 2–3 substituents for green dye or more substituents for black dye, which disassemble its symmetry and breathing mode. Low intensity vibrational modes of 408 cm^{-1} and 423 cm^{-1} might represent Cr-O and ring out of plane bending [246]. Fourier-transform infrared spectroscopy (FTIR) analysis confirmed that dye molecules are characterized by vibrations of aromatic rings of which the diazenil functional group N=N at 1541 cm^{-1}, the deformation vibration of C-N group at 1271 cm^{-1}, vibration of C-O stretching at 1120 cm^{-1} and the vibrations of sulfo functional group at 1026 cm^{-1} were found. XPS results also revealed sulfonate R-SO_3^- (sulfonic acid salts and esters, 168.2 eV) and a twice lower concentration of sulfate SO_4^{2-} (169.4 eV) in the structure of azo dyes. Organometallic bonds of Cr with oxidation state +3 (576.4 eV)

were also detected. Tridentate ligands form complexes with Cr (III) through 1:2 metal and ligand ratio, where lone pairs of electrons are donated by two oxygen atoms and one nitrogen atom of the diazo linkage [247, 248].

The substituents in the moiety are crucial for defining the color, adsorption, hydrophilicity, degradation stability and the variety of other properties, which are important for commercial dyes. They define not only the molecular structure but also packing shape and size which are different of various dyes. Furthermore, additives often include in dye formulations to enhance their lightfastness, glossiness, adsorption, penetration properties, degradation stability, curing durations, wetting, spreading, shelf life, antibacterial and antifungal performance and possibly other characteristics. Therefore, the exact chemical mechanisms describing the dye adsorption on anodized Al might be complex and diverse.

During impregnation of anodized coatings on substrates it is important to account for the influence of the residual electrolyte. Interaction between azodyes and anodized foil, which was described in the previous subchapter, was not affected by the residual electrolyte to any appreciable extent. Essentially all electrolyte was washed out from the foil after anodization due to near-hollow nature of the anodized foil. However, when anodized coatings are formed on the top portion of Al substrates, the electrolyte cannot be washed out easily at all. Therefore, the interaction with impregnated fillers becomes more complex and the importance of the residual electrolyte must be taken into consideration. Sulfuric, oxalic, phosphoric and other acids, which might be used during anodization, have low volatility. Furthermore, they form sulfates, oxalates, phosphates and other salts, when residing in the pores. Consequently, impregnated fillers might react not only with Al_2O_3 or Al hydroxides, but also with various salts and even free acids.

In case of azo dye impregnation into anodized coatings on Al substrates, the residual electrolyte will have additional effect. If water is still present in the pores, cations can be released from the impregnated molecules, which have ammonium or azo-moieties. Partial Al hydroxides can also act as cations. Anions can be generated from sulfonic, carboxylic and other functional groups within azo dye molecules as well as from sulfuric, oxalic, phosphoric and other acids in the residual electrolyte. In the pores water might be eventually consumed during formation of hydroxides and hydrates. But these processes might be slower than ionic reactions between the residual electrolyte and impregnated fillers. Molecules of chromium-complexed anionic azo dyes with an expected size of 3 nm easily migrate

into the pores of anodized coating. Through electrostatic interactions between oppositely charged ions, dye molecules can form ionic bonds into the pores of the anodized coating at acidic pH [249]. By streaming potential measurements, the zero point of charge (zpc) of or-Al_2O_3 having a fully hydroxylated surface was found to occur at pH 9.2 ± 0.2. It is able to reduce zpc by calcining the alumina at temperatures above 1000 °C [250]. In case of azo dyes pH values is lower to zpc, 4.5 and 5–6 for black dye and green dye respectively.

Anodized coatings may contain a considerable number of impurities, whose quantity depends on the nature of the electrolyte. For example, hard anodized coatings formed in H_2SO_4 contain up to 17% sulfates [108]. Phospho-anodized coatings might contain 6% phosphates, while those formed in oxalic a. electrolyte might contain up to 3% oxalates [251]. By contrast, the content of chromate in the coating obtained in chromic a. constitutes only 0.2%. In case of anodized foil produced in H_2SO_4/oxalic a. electrolyte the sulfate concentration was ~4%. The behavior of the Raman spectra may be explained by the dye interactions with the sulfates and oxalates remaining in the pores of anodized coating. However, a high concentration of electrolyte compounds present inside the pores might have a negative effect and reduce the penetration rates of the dyes. The reactivity of anionic functional groups within the dye molecule towards the cations can be too high, which would result in blockage of the pore openings. Furthermore, the abundance of residual electrolyte and its acidic media, UV exposure, biocontamination and possibly other factors may affect stability and induce chemical degradation of anionic azo dyes. In the case of azo dyes, these processes have not been studied in detail since their exact chemical composition is unknown.

The reactions between hydrophobic fillers (i.e. fatty a.) and anodized Al were explained in detail. Deprotonation of carboxylic a. (i.e. fatty a.) gives carboxylate anions when a proton is removed according to Brønsted-Lowry acid-base theory. The carboxylate anions have the resonance structure because the negative charge is delocalized over the two oxygen atoms, which allows making various types of interaction. Amphiphilic molecules of fatty a. which provide hydrophobic hydrocarbon tail and hydrophilic (polar) head group form a chemical bond with anodized coating. The deprotonation of fatty a. leads to coordinative adsorption of carboxylate group on the porous anodized coating, which can be either monodentate, bidentate or chelating [252], Fig. 76(a).

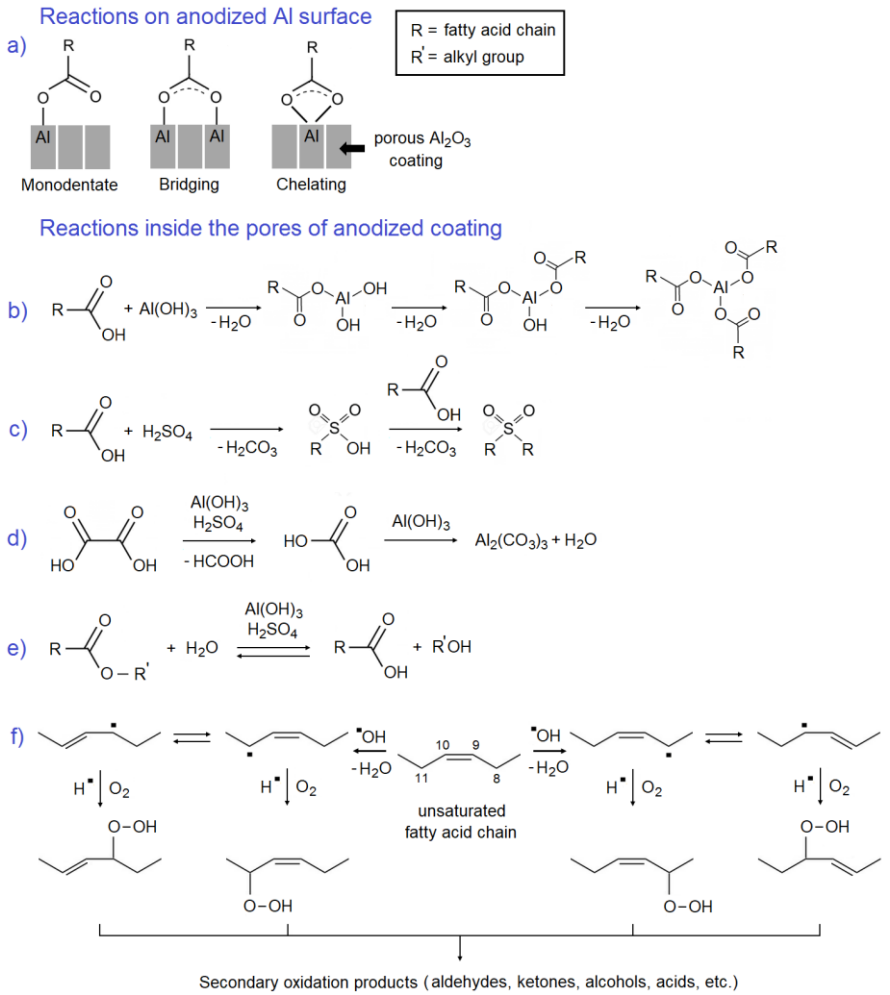

Fig. 76. *Possible reactions of fatty acids or esters at anodized Al surface (a) and inside the pores of anodized coating (b-f)*

A chemical reaction with the anodized coating and cohesive interactions between the alkyl chains able to maintain stable monolayer. With chemisorption, which can be either symmetric (through the two oxygens) or asymmetric (through one oxygen), the binding energy is much higher than for physisorption. For multilayer films, the first layer is chemisorbed and other layers are physisorbed by weak intermolecular forces like Van der Waals. It has been shown that the chemisorbed amount of matter on the surface is not influenced by the saturated or unsaturated alkyl chain of the fatty a. but is only dependent on the interactions between the head group of fatty a. and the substrate. While the physisorbed amount of matter increases

with the number of unsaturation in fatty a. [253]. Acid-base properties of anodized coatings play an important role in the binding mechanism of fatty a. As shown previously, γ-Al_2O_3 exhibits a variety of surface OH groups some of which are strongly acidic, while boehmite (AlOOH) has mostly basic reactivity [254]. In addition, the binding geometry and strength, number of adsorption sites and other possible factors determine binding affinity, which might influence the penetration of hydrophobic lubricants.

It is reasonable to assume that pores of anodized coating are filled with hydroxides that able to react with fatty a. The saponification reaction of fatty a. and $Al(OH)_3$ produces Al soaps (i.e. Al stearate, Al oleate), which have good oxidation and water resistance, Fig. 76(b). Such compounds play an important role as additives in lubricating greases, thickeners and protective films due to the ability to sustain low friction and reduce wear [255]. Long-chain fatty a. and metal soaps have the ability to reduce friction not only by adsorption of multimolecular films under boundary or near boundary friction conditions but also by reaction of residual electrolyte compounds entrapped inside the pores of anodized coating. It is able to obtain mono-, di- and tri-functional Al soaps. The stability of Al soaps are inversely proportional to the swelling ability, i.e. low-swelling tri-functional Al soaps are more stable than those of the high-swelling mono-functional Al soaps [256]. However, the formation of tri-functional Al soaps is hardly possible and requires much higher durations or utilization of catalysts for the reaction to occur.

The residual electrolyte compounds including H_2SO_4 and oxalic a. left in the pores of the anodized coating can significantly influence the migration and tribological properties of fatty a. and other lubricants, Fig. 76(c, d). It is expected that the reaction between H_2SO_4 and Al hydroxides is incomplete and not all the reactants are converted into hydroxy sulfates. H_2SO_4 might react with fatty a. by producing sulfonic a. or sulfonates and carbonic a. (H_2CO_3) at elevated temperatures. Decomposition mechanism of oxalic a. depends on temperature. Oxalic a. decomposes to formic a. (HCOOH) and CO_2 while upon further heating it transforms into CO and H_2O at ~130–160 °C. The formation of CO_2, CO, and H_2O from oxalic a. was detected in the pyrolysis process, which typically occurs at temperatures above 430 °C. However, none of these reactions of decomposition of oxalic a. are possible since the temperature was never reacher over 100 °C in this study. This suggests that oxalic a. might decompose to formic a. by generating dihydroxylcarbene as an intermediate species after decarboxylation mechanism [257]. According to scientists, the reaction is obtained at lower temperatures using H_2SO_4 and $Al(OH)_3$ as a catalyst in the presence of

water. Furthermore, the carbonic a. also might react with $Al(OH)_3$ producing carboxylic salts. However, the formation of these compounds in the pores of the anodized coating has not yet been proven. It could be stated that the formation of Al carbonates are hypothetical and not well characterized. Due to their basic nature and instability, Al carbonates can decompose to $Al(OH)_3$ and CO_2.

Esters (i.e. methyl oleate) are not very stable compounds in the aqueous environment. Therefore, part of the molecules is hydrolyzed to fatty a. and alcohol in the acidic medium, Fig. 76(e). The hydrolysis reaction is catalyzed by both acids and bases. This reaction is reversible and does not go to completion. Fatty a. obtained after hydrolysis able to react with $Al(OH)_3$ and residual electrolyte compounds as discussed previously.

The stability of unsaturated esters and lipids is also significantly influenced by peroxidation (autoxidation) reactions. It is a free radical initiated oxygen binding to the double bonds of unsaturated fatty a. and in case of increased oxygen concentration, autoxidation of saturated fatty a. occurs. By the way, not only in anodic coatings but also in biological systems oxidative stress results in irreversible cellular changes that damage cell membranes in the presence of free radicals. A free radical chain process often affects mono- or polyunsaturated fatty a. because they contain double bonds and methylene bridges (-CH_2-) that possess especially reactive hydrogen atoms. Free radicals have a tendency to gain or lose electrons (reduction or oxidation) and obtain a more stable state when electrons are paired due to extremely high chemical reactivity and instability. Most radicals have very short half-life 10^{-6} s or less [258]. One of the most important parameters that influence the mechanism of the radical reaction is redox potential, which describes the ability to acquire electrons and therefore to be reduced. Hydroxyl radical (•OH) have the highest electron reduction potential of 2310 mV and is considered the strongest oxidizing radical in biological systems [259]. It affects all types of biological molecules and contributes to a major part of oxidative damage. Free radical mediated chain reaction mechanism consists of three major steps: initiation, propagation and termination. At the initiation reaction, reactive oxygen species (hydroxyl radical, peroxides, superoxide) combines with a H atom to form water and a fatty a. radical. Once the free radical has formed, it react with O_2 to give a peroxyl radical (ROO•) intermediate. Since the radical is unstable it reacts with another free fatty a. by removing an H atom from a weak C-H bond and producing another fatty a. radical and lipid hydroperoxide (ROOH). When a radical reacts with a free fatty a., it always produces another radical and the

cycle continues by chain reaction mechanism. Oleic a. which has 18 carbon atoms and one double bond in the 9 C position can be oxidized with hydroperoxyl radical at 8 C and 11 C atoms directly or at 9 C and 10 C atoms after double bond displacement, see Fig. 76(f). The peroxidation reaction stops when two radicals react and their odd electrons form a new bond. Primary oxidation products, i.e. hydroperoxides, are formed through different chemical mechanisms. In the next step the hydroperoxides break down into secondary oxidation products including aldehydes, ketones, alkenals, short chain fatty a. and other compounds. Several of them possess toxic properties [260]. Peroxidation reaction of lipids also may be accelerated by the presence of metals and by exposure to heat and light.

Therefore, the penetration of organic fillers depends not only on the properties of the anodized coatings and residual electrolyte but also on the hydrolysis, autoxidation and other chemical transformations of the migrating compounds. During impregnation, new compounds with novel characteristics might be formed in the pores of anodized coating including different color, anti-friction properties, etc.

3.5 Severely starved or lubricated friction on developed coatings

In contrast to dry friction, in biological systems, surface friction occurs in the presence of body fluids (lymph, water, blood, saliva, etc.) and the substances they contain, including lipids [233]. Saturated stearic a. and monounsaturated oleic a. is found in human and animal adipose tissue as well as included in phospholipids and triglycerides composition with concentrations up to 30% [126] and up to 50%, respectively [127]. Because it is one of the most common types of lipids both free acids (oleic a., stearic a.) and triglycerides (tristearin) can interact with anodized and nanostructured coatings.

When lubricants are applied on the anodized coating it is able to obtain severely starved or lubricated friction which depends on the thickness of lubricant film. In lubricated friction conditions, fluid completely separates two solid surfaces and ensures that the contact zone is fully flooded with lubricant. Differently from lubricated friction, severely starved friction is attributed to the insufficiency of fluid replenishment on the friction zone. The onset of starvation depends on lubrication parameters (i.e. viscosity), amount of oil and operating conditions (i.e. load, speed). In this study tribological properties of lubricants were tested mostly on severely starved

conditions with greater regard to the properties of the coatings rather than of lubricant itself.

3.5.1 Friction in physiological media

Both lipophilic and hydrophilic environments were considered in order to approach frictional conditions in the body. For the latter, Hanks balanced salt solution was used, which is similar to blood plasma by its osmotic pressure, the content of salts and buffering properties required to maintain optimal pH by the acid-base homeostatic mechanism. The friction was tested with chemically inert corundum balls in order to avoid corrosion and other chemical or electrochemical reactions, which could have a negative effect on friction results. As showed in Fig. 77 the antifrictional properties of salt solution were poor leading to an initial COF of ~0.4 on hard anodized coatings.

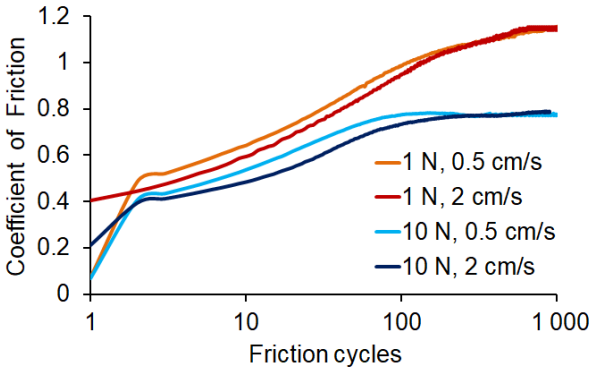

Fig. 77. *Influence of load and velocity on friction of hard anodized 1050 alloy in Hanks solution*

Tribological parameters i.e. sliding velocity and load also were analyzed in simulated biological fluids. The load of 10 N led to COF reduction from 1.0 to 0.8 while sliding velocity had no influence on friction on later friction stages.

Hanks solution was applied on nanostructured coatings with Ti layers of 75 nm thicknesses to simulate the conditions of the biological environment. The lubricating properties of Hanks solution was poor by showing the gradual COF increase on both 1050 and 6082 anodized Al alloys, Fig. 78.

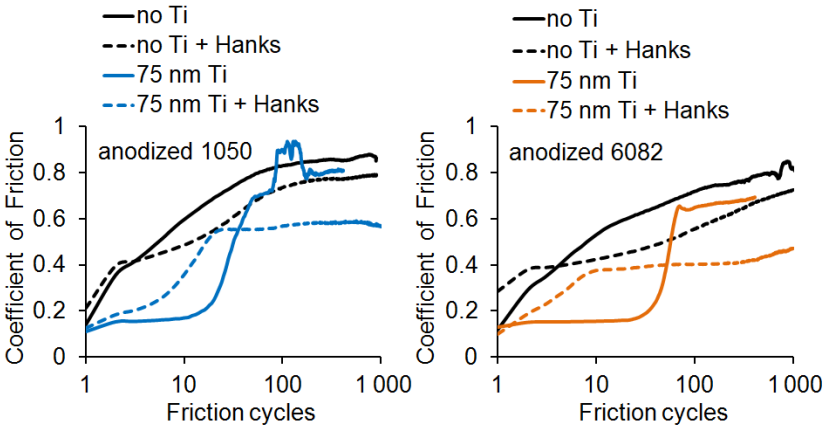

Fig. 78. *Friction tendencies of hard anodized and nanostructured coatings with 75 nm Ti layers of 1050 (left) and 6082 (right) alloys before and after lubrication under 10 N load*

For nanostructured coatings, COF showed friction stabilization after 10 (for 6082 alloy) or 20 (for 1050 alloy) friction cycles. According to previous studies Ti/TiO_2 layers able to promote the formation of apatite including hydroxyapatite when it is immersed in simulated biological fluids [261]. Precipitates of calcium phosphate have positive effect on friction reduction by stabilizing COF for about 1000 friction cycles. Nevertheless, the initial COF values are about two times higher when compared to nanostructured coatings under dry friction conditions. Additionally, surface wear measurements were evaluated by profilometry. Anodized and nanostructured coatings with Ti layers of 75 nm thickness showed high wear rates after 100 friction cycles under dry friction conditions, Fig. 79.

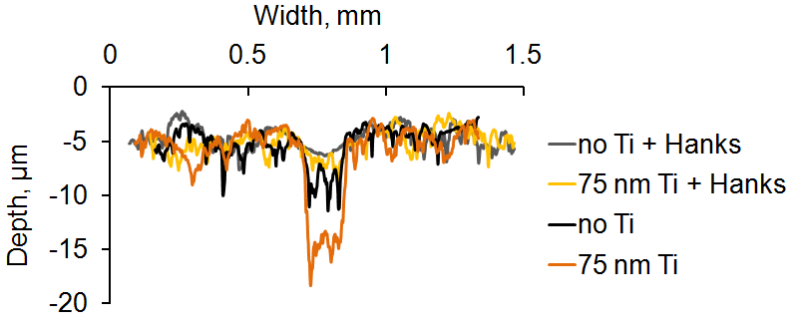

Fig. 79. *Wear profiles of hard anodized and nanostructured coatings before and after lubrication after 100 friction cycles under 10 N load*

In dry friction, wear rate was at least two times higher on the nanostructured coating when compared to hard anodized coating without any layer, Table 14.

Table 14. *Wear of hard anodized and nanostructured coatings of 6082 alloy before and after lubrication after 100 friction cycles under 10 N load*

	Wear track depth, μm	Cross-section area of wear track, μm²	Wear rate, $\mu m^3/(N \cdot mm_{wear})$
No Ti	6.5 ± 0.7	545 ± 29	273 ± 14
No Ti + Hanks	2.0 ± 0.2	362 ± 80	181 ± 40
75 nm Ti	13.3 ± 2.1	1513 ± 85	757 ± 42
75 nm Ti + Hanks	2.9 ± 0.5	429 ± 60	215 ± 30

Anodized coatings show progressive COF growth under sliding against inert corundum ball. This represents the removal of adsorbed layers of hydroxides, sulfates, carbonates or other molecules from the surface. In case of nanothin Ti layers, COF rises suddenly and reaches over 0.6 after 20 to 60 friction cycles. Once the COF reaches a plateau it might fluctuate which are related to stick-slip phenomenon. This represents abrasive friction regime when too much wear debris particles accumulate in the wear track zone. Wear increases dramatically by the formation of large debris particles, which act as abrasives. Intensive abrasion begins and the wear rate is mostly dictated by the properties of the dry coating and the substrat. High COF leads to anodized coating failure and major temperature increase. This suggests that abrasive particles of Ti and Al_2O_3 could produce more debris accumulation in friction zone, which increases surfaces wear and degradation more rapidly.

Surface wear of Al_2O_3 coatings without or with Ti layers was significantly reduced in Hanks solution. The wear rate of lubricated Ti layers was ~3.5 times lower when compared to dry friction. Despite high initial COF of nanostructured coatings, the friction was still lower after 100 friction cycles in simulated biological fluids. A wear rate of Al_2O_3 and Ti was quite similar with respect to error values in Hanks solution. Lower wear of nanostructured coatings might depend not only on apatite formation but also on tribofilm reaction to sulfates, hydrates, hydroxides and other molecules incorporated in pores. Overall, lubricated friction conditions by using simulated biological fluids significantly reduce wear of nanostructured coatings, but has no positive effect on friction reduction.

Three common lipids (stearic a., oleic a. and tristearin) found in the human organism were chosen to evaluate the possible friction conditions of the biomaterials in the body. The substrates were coated with biolubricants by immersive method in order to produce uniform layers across the substrate surface and possibly reduce the influence of oxidation during impregnation. According to gravimetric analysis, the thickness was 40–60 μm for solid lubricants (i.e. stearic a., tristearin) and 15–30 μm for oleic a. of a liquid phase. Despite of small variations on thickness of the lubricating materials, the lipids (i.e. stearic a.) showed good reproducibility on hard anodized coating, Fig. 80.

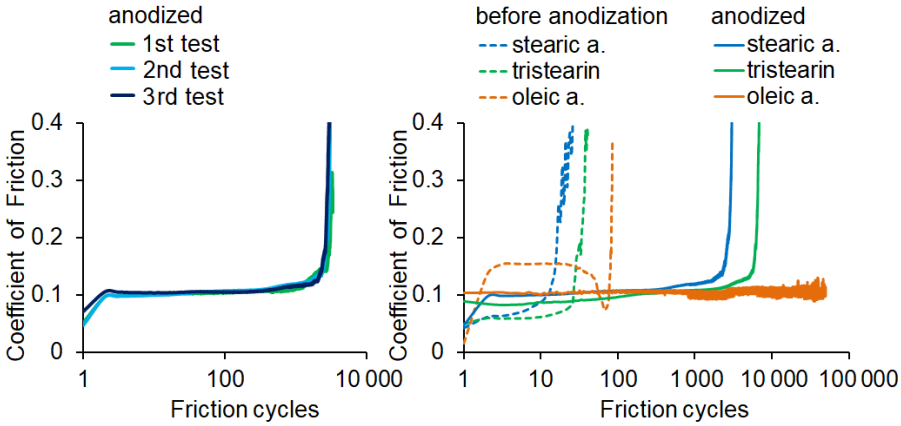

Fig. 80. *Reproducibility of friction tests in the presence of stearic a. (left) and influence of lipid layers on friction tendencies of 1050 alloys before and after hard anodization (right). Tribotests against a steel ball under 10 N load*

As expected lubricated coatings were over a hundred times effective tribologically when compared to anodized or nanostructured coatings. It is known that lubricants are able to improve tribological properties and reduce surface friction. Porous anodized coatings able to increase the adsorption of lipids, which leads to higher resistance against friction and wear after tribofilm formation. The adsorbed film is formed by weak intermolecular forces between lipid and metal surface, while tribofilm formation is influenced by tribochemical reactions which are characterized by different chemical properties and tribological behavior. Liquid phase lubricants able to penetrate more deeply into the pores of anodized coating and provide better lubrication rather than solid lubricants. Oleic a. reduced friction to 0.1 and sustained for at least 50 000 friction cycles (400 m), although the friction could be continued more than 6 hours. Low friction sustained only

for 2 000 (16 m) or 6 000 (48 m) friction cycles for stearic a. and tristearin respectively.

Lubricating layers of oleic a. able to suppress friction of anodized coatings under 10 N load. Therefore friction was tested using different tribological conditions. It was showed that friction significantly depends on load and velocity. Impregnated coatings are less resistant to friction by increasing the load and reducing velocity, Fig. 81.

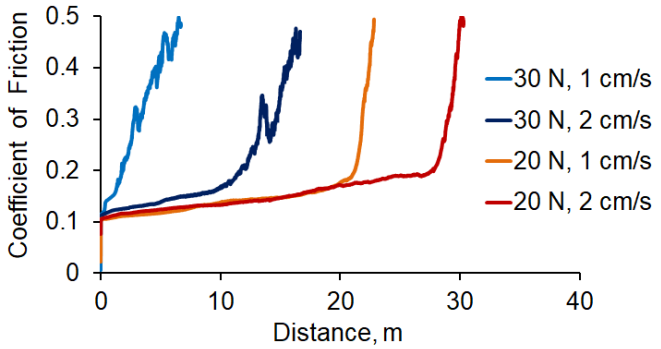

Fig. 81. *Influence of load and velocity on friction tendencies of hard anodized 1050 alloys with oleic a.*

In contrast to severely starved friction, dry friction mostly influences on load rather than velocity, especially at initial friction stages. The wear of anodized coatings is not beneficial either tribologically or biologically. High loads and cyclical rubbing influence plastic deformation and detachment of wear particles which leads to surface cracking, wear debris formation and increased damage. Therefore wear of anodized coatings must be avoided in the organism.

According to the tendencies of the friction curve, four distinct stages can be identified in regard to progressing wear: “run-in”, steady state, fatigue and abrasion [140]. During initial “run-in” stage, COF starts rising due to high interfacial pressures and temperature at asperities after the exerted load is applied. Oppositely, rough surfaces might decrease COF during surface polishing at initial friction stages. Steady state regime begins when COF stabilizes and lubricating materials from the pores of anodized coating ensure a partial surface separation by formation of tribofilm or interfacial layer. In this stage COF mostly decreases to ~0.1 either on severely starved or lubricated conditions. Once lubricant starvation starts, the film thickness decreases and interfacial pressures are change, leading to transformations of

the wear scar and increase of COF. Lubricant depletion and other factors including oxidation, hydrolysis, tribofilm breakdown increase friction fluctuations and accumulation of wear debris suggesting to more pronounced surface damage. Severe plastic deformation and crack propagation show visible changes in surface topography and morphology in fatigue wear regime. Eventually, too much of the wear debris accumulates in the friction zone which acts as abrasives. The abrasion leads to sharp COF and wear increase due to lubrication failure and high temperature in the friction zone. In this case, wear rate is mostly dictated not by the lubricant availability, but by the properties of the dry coating and the substrate.

Wear of impregnated coatings was tested initially after 1000 friction cycles using profilometry and optical microscopy. As expected stearic a. showed the highest wear rate of the anodized coating and a steel ball while wear rate of oleic a. was 1.7 times slower under 10 N load, Table 15.

Table 15. *Wear of anodized 1050 alloys after 1000 friction cycles*

Lipid	Load, N	Wear track depth, μm	Cross-section area of wear track, μm²	Wear rate, $\mu m^3/(N \cdot mm_{wear})$	Steel ball wear diameter, μm
Stearic a.	10	2.5	800	40	235
Tristearin	10	2.5	635	32	198
Oleic a.	10	2	465	23	178
Oleic a.	20	5	2175	54	320
Oleic a.	30	45	27470	458	432

Solid phase stearic a. and tristearin have limited ability to penetrate into pores and mostly adsorb on the surface of the anodized coating, while the penetration of oleic a. is deeper leading to the formation of new compounds. Higher loads significantly increased wear rate and depth of wear track with almost total destruction of anodized coating with oleic a. lubricant using 30 N load. Both stearic and oleic a. likely react with Al hydroxides in the friction zone, forming soaps. These soaps could also participate in the formation of tribofilm, along with fatty acids. In addition, the reaction of fatty a. and residual electrolyte compounds including H_2SO_4 is also possible by formation of sulfonates or similar compounds. Unlike the penetration studies of anodized foil, anodized coatings with lubricants were heated to 90 °C in order to accelerate the chemical reactions before tribotesting. Despite

higher melting point and frequently impressive solitary tribological performance, stearic acid was not as effective as oleic acid. The latter is more reactive due to unsaturation. Apparently, double-bond driven reactions could lead to formation of tribologically effective compounds, such as oxidized matter and oxypolymers. Oxygen is able to react with C=C double bond groups in the fatty a. chain to initiate the formation of peroxides (RCOOH). The newly formed peroxides degrade through a free radical process and form hydroperoxides, which able to form high molecular weight polymers through a condensation polymerization process. The presence of metal salts acts as a catalyst to further increase the rate of this reaction. After a significant degree of oxy-polymerization the fatty a. will have a substantial increase of viscosity. Therefore, tribofilms produced by oleic a. and oleate soaps were more effective than those of stearic a. or tristearin. Free fatty acids were not likely to interact much with the residual electrolyte. Tristearin could undergo hydrolysis or transesterification, producing glyceryl derivatives with sulfate and oxalate. The chemical reaction between glycerol and oxalic a. occurs at 100–110 °C by producing glyceryl mono-oxalate. In the next step, it could transform into the glycerol and formic a. after decarboxylation and hydrolysis. The formation of glyceryl dioxalate requires higher temperatures from 260 °C to 280 °C [262]. The ability to form fatty a. monoglyceride sulfates might also possible through sulfation and transesterification reactions [263]. However, these reactions did not appear to contribute to major tribological effectiveness, although tristearin performed a bit better than stearic a.

Nanostructured coatings with Ti layers of 75 nm thicknesses which showed high tribological resistance under dry friction conditions were selected for testing of lubricated friction. However, solid lubricants of stearic a. and tristearin had no positive effect on friction reduction and disintegrated more rapidly on nanostructured coatings under 10 N load, Fig. 82.

Higher loads from 20 N and 30 N were selected for oleic a. to reduce the duration of friction tests. Results showed that oleic a. reduce COF to 0.1 and sustain up to 10 000 (80 m) friction cycles under 20 N load. The wear rates of hard anodized coatings before and after nanostructurization was similar 54 $\mu m^3/(N \cdot mm_{wear})$ and 52 $\mu m^3/(N \cdot mm_{wear})$ respectively using oleic a. lubricant. However, the load of 30 N did not led to any tribological improvements. It is expected that sputtered Ti layers of 75 nm thickness completely fills pore openings and block lubricant penetration. Although, oleic a. able to maintain low friction under 20 N load, a synergistic effect between Ti layer and oleic a. was not observed.

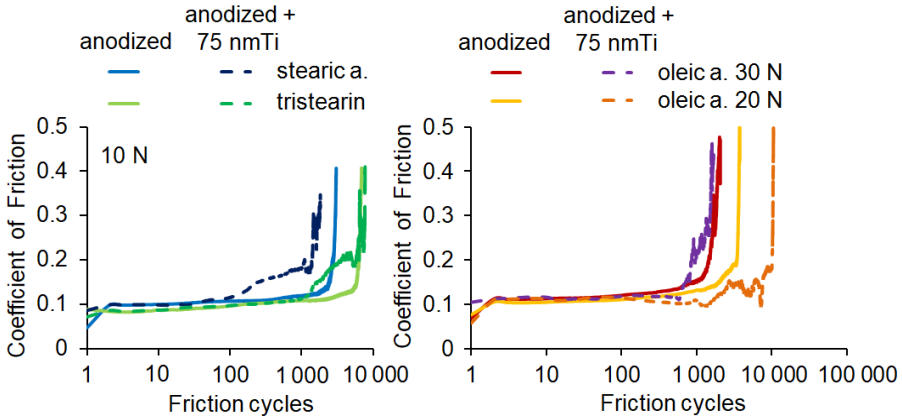

Fig. 82. *Influence of lipid layers of stearic a., tristearin (left) and oleic a. (right) on friction tendencies of anodized 1050 alloys without or with 75 nm Ti layer*

Dip coating is not a very effective method to control the thickness of lipid layer since the pores with less than 20 nm in diameter might be blocked using Ti layers of 75 nm thicknesses. To solve this problem, the gravimetric method was applied for oleic a. films that allow controlling its thickness directly. At initial friction cycles, COF went down until it reached a plateau at ~0.1 by suggesting that asperities of coating surface became polished in contact with extremely hard corundum balls under 20 N load. Relatively thin layers of oleic a. with thicknesses of ~15 μm and ~30 μm showed very similar friction results with the ability to sustain low friction up to 10 000 cycles, Fig. 83.

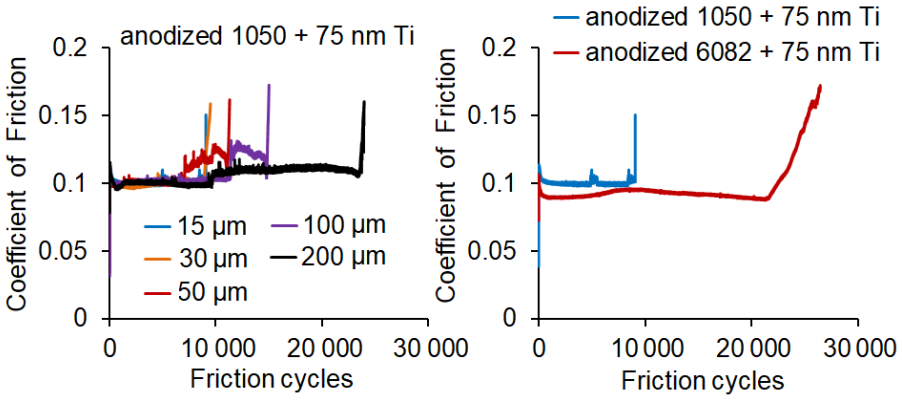

Fig. 83. *Influence of friction tendencies on thickness of oleic a. of nanostructured 1050 alloy with 75 nm Ti layer (left) and friction tendencies of oleic a. of 15 μm thickness coated on nanostructured 1050 and 6082 alloys (right) under 20 N load*

In addition, thicker layers of oleic a. has an only small advantage on friction sustainability. Nevertheless, thick layers of 200 μm thickness increased friction resistance up to 2.5 times and maintained low COF for about 25 000 friction cycles. The friction showed dependence not only on layer thickness, but also on properties of Al alloys. Two times wider pores and up to four times higher surface porosity of 6082 alloy improved lubrication properties and led to COF reduction of ~0.08. Nanostructured coatings of 6082 alloy increase friction resistance more than twice when compared to 1050 alloys.

Biological lubricants based on oleic a. significantly reduce surface friction and wear with COF ~0.1 and protect anodized and nanostructured coatings from severe damage in biological systems. Al alloy properties and tribological conditions, as well as the content of lubricating materials, affect friction by simulating biological environment conditions.

3.5.2 Tribological performance in fuels and lubricants

Lubricated systems are very favorable for various applications when surfaces undergo high stresses under tribological exposure. In the case of anodized coatings, the most widespread method for lubrication is still based on PTFE coatings. It is expected that solid lubricants form a barrier layer because PTFE molecules are usually too large to penetrate inside the pores of hard anodized coating of less than 20 nm in diameter. The pores of hard anodized coatings are too narrow for a linear molecule of 300 carbon atoms, while PTFE polymers are often as large as 10 000 C atoms. In addition, the low wetting capability of PTFE molecules even reduces the penetration into the pores of anodized coating. In the case of organic fillers the ability to migrate in the pores should be more pronounced since the lubricants i.e. methyl oleate able to penetrate for ~15 μm in depth as detected by Raman spectroscopy. The better penetration of organic lubricants are beneficial for both biomedical and industrial applications where low friction is required.

Isopropanol-based PTFE coatings showed high tribological resistance and ability to maintain low friction of 0.1 for at least 30 000 cycles that make PTFE coatings useful for various industrial and commercial applications, Fig. 84.

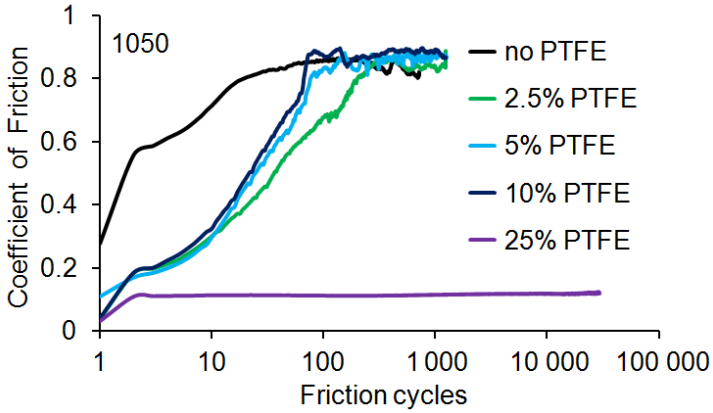

Fig. 84. *Influence of PTFE concentration on friction of anodized 1050 alloy against a steel ball under 10 N load*

The anti-frictional properties of PTFE fillers depend not only on deposition conditions but also on additives and its concentration. Only dispersion of 25% PTFE in IPA improved tribological performance, while concentrations of 2.5% to 10% showed high friction and surface damage after just 100 friction cycles under 10 N load. Nevertheless, even the low concentrations of PTFE able to reduce initial COF when compared to anodized coating without PTFE.

The tribological performance of PTFE and organic fillers were tested under 30 N loads. PTFE polymers form barrier coatings on anodized Al which reduce COF to ~0.1 and sustain up to 10 000 cycles under 30 N load, Fig. 85.

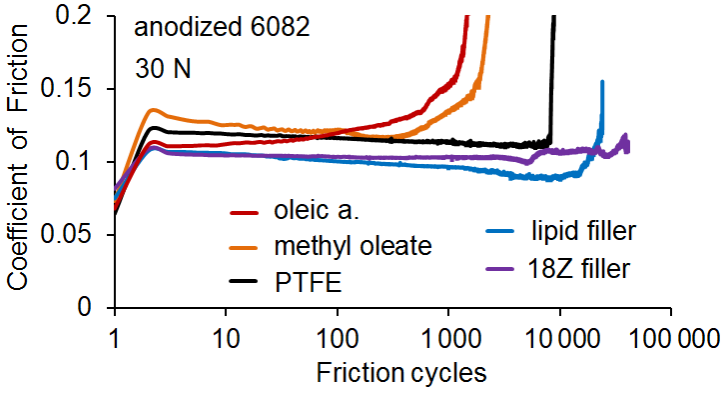

Fig. 85. *Influence of solid and organic fillers on friction of hard anodized 6082 alloys, under 30 N load*

Although oleic a. and methyl oleate were not as effective as PTFE they showed positive tribological effect at lower loads. Biobased lipid and 18Z fillers exhibited lower COF and sustained over 10 000 friction cycles at 30 N load. These fillers were more effective tribologically than fatty a., esters or barrier coatings. PTFE coatings work as a mechanical barrier and perform well only until the anodized coating is exposed. It has a limited ability to penetrate into the pores of less than 20 nm in diameter due to high molecular weight. Liquid fillers, i.e. fatty a. or esters have the ability to penetrate inside the pores and provide better lubrication, see Fig. 86. Moreover, tribofilm formation initiated by the tribochemical reaction between lubricant and electrolyte compounds left inside the pores of the anodized coating could lead to a large improvement in tribological properties.

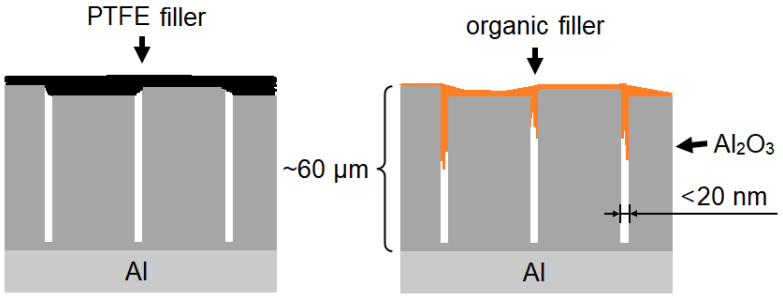

Fig. 86. *The penetration of solid (left) and organic(right) tribofillers into the pores of anodized coating*

Lipid and 18Z fillers could have more interaction with the residual electrolyte. Despite their lower viscosity, they were able to produce more durable tribofilms in the friction zone. Low COF was retained many times longer than in the case of free fatty a. and significantly longer than PTFE. Being a widespread lubricant for anodic coatings, PTFE is nevertheless just a barrier lubricant, which gradually wears out. In contrast, 18Z and lipid fillers can rely on the residual electrolyte, which contributes to the tribofilm formation and such synergy leads to better anti-wear performance. This suggests that ability to produce tribofilm depends not only on the chemical and physical properties of lubricating materials but also on interaction with residual electrolyte.

The structure of anodized coating is very important for better tribological performance. The friction of hard anodized coatings obtained at different temperatures was tested before and after methyl oleate deposition, Fig. 87.

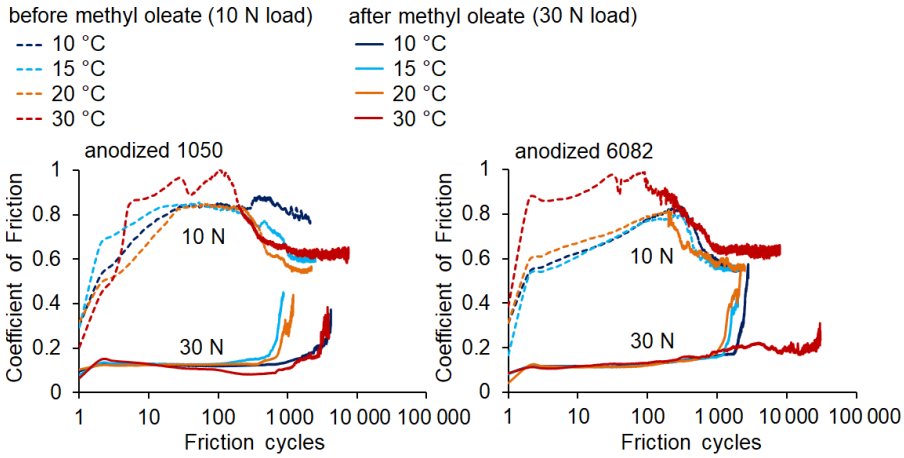

Fig. 87. *Influence of anodization temperature on friction tendencies of anodized 1050 (left) and 6082 (right) alloys with or without methyl oleate under 10 and 30 N loads*

It is known that higher temperature leads to faster dissolution rate and increase porosity of the anodized coating. Porous coatings produced at 30 °C showed the fastest surface destruction under 10 N load using dry friction conditions. However, the deposition of methyl oleate significantly improved friction maintaining low COF over 1 000 or 10 000 friction cycles for 1050 or 6082 alloys respectively under 30 N load. The penetration of methyl oleate in the pores was much noticeable when porosity increased to ~40% for 6082 alloy at 30 °C.

In addition, the antifriction effect of hard anodized coatings with or without methyl oleate was showed by changing anodizing duration from 30 min to 150 min. As expected, non-lubricated friction of hard anodized coatings unable to withstand elevated loads either on thin or thick porous Al_2O_3 coatings, Fig. 88.

When methyl oleate was applied on the surface, COF was quite similar for anodization duration of 30 min or 70 min under 30 N load. However, the ability to sustain low friction was dramatically improved more than ten times after hard anodization for 150 min at 15 °C. This could be explained by higher surface tension which led to crack formation on anodized coatings. The cracks of several hundreds of width might increase penetration of methyl oleate by allowing sustain low friction more than 10 000 cycles under 30 N load, annex Fig. S19. Anodized coatings with methyl oleate undergo mild surface destruction at some level as expressed by fluctuations in the friction curve.

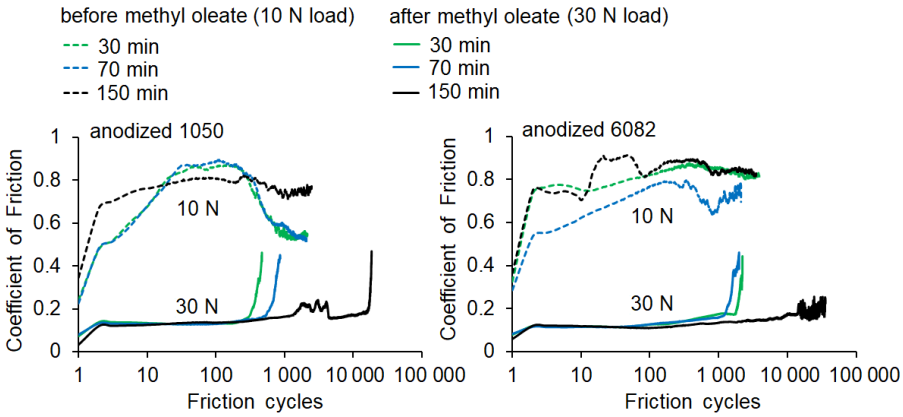

Fig. 88. *Influence of anodizing duration on friction tendencies of anodized 1050 (left) and 6082 (right) alloys with or without methyl oleate under 10 and 30 N loads*

Evidently, tribological performance of anodized coatings on industrial Al alloys can be dramatically improved by capitalizing on the synergistic interaction between the residual electrolyte and impregnated fillers. Both the structure of anodized coatings and the chemical and physical properties of the lubricants are important to ensure low surface friction and wear. Fundamental studies that allow to evaluate the relationship between electrolyte and lubricants provide a better understanding of friction mechanisms that occur on the surface of the anodized coating and its pores. These studies provide yet another avenue to commercial advancement and various applications of anodized Al in biomedicine, high-tech industry and many other scientific fields.

CONCLUSIONS

1. The layers of Ti and its oxides significantly improve the biocompatibility of anodized coatings. Nanostructured coatings with a Ti layer of about 75 nm thickness are most appropriate.
2. Anodization in sulfuric/oxalic a. electrolyte significantly reduces not only dynamic but also static friction. Anodization in phosphoric a. electrolyte produce much softer and more porous coatings which have much lower resistance to friction and wear.
3. Independently of the method (ALD or magnetron) used to form nanothin layers of Ti or its oxides on a solid anodized coating, nanothin Ti/TiO_2 layers of 10 to 75 nm thickness reduce COF below 0.2 which remain from 20 to 60 friction cycles under 1–10 N. The COF exceed 0.5for both Ti alloys and anodized coatings without Ti layers just after several friction cycles.
4. Nanothin layers of Zr and Hf oxides reduce static COF below 0.2, although they were less effective tribologically than Ti and its oxides. Nanothin layers of other transition metals do not have a positive effect on the tribological properties of anodized coatings.
5. Raman spectroscopy is able to quantify the penetration of hydrophilic azo compounds into the pores of the anodized coating. It is also possible to determine the intensity of interaction of azo compounds with the pores of the anodized coating.
6. The penetration of monofunctional esters and other hydrophobic compounds to the anodized coating is determined not only by the geometric parameters of the pores but also by the residual electrolyte. Significant amounts of material accumulate deeper into the pores, e.g. coatings with a thickness of 60–70 μm, the average penetration depth of methyl oleate is 10–20 μm.
7. The formation of tribofilms on the anodized coating is determined not only due to tribochemical reactions of the lubricants in the friction zone but also due to their chemical interaction with compounds left in pores of anodized coating.
8. COF of the anodized coatings can be reduced to ~0.1 and wear rate can be suppressed by more than 3 orders of dry friction conditions by combining the lubricant and the anodizing electrolyte.

1. ĮVADAS

Trinties ir dilimo problemų sukelti nuostoliai dažnai viršija 2 % BVP, todėl siekiama kurti paviršius, kurie būtų atsparūs dilimui, o tepamųjų medžiagų panaudojimas būtų minimalus. Trintis tarp judančių paviršių priklauso nuo daugybės parametrų: apkrovos, greičio, šiurkštumo, kietumo, elastiškumo, tepalo klampos ir pan. Tačiau vieni svarbiausių yra cheminiai virsmai, ypač dilimo procesams. Tribologija nagrinėja visų šių parametrų ir procesų visumą, todėl detalūs cheminių aspektų tyrimai yra itin svarbūs ne tik transporto ir kituose techniniuose sektoriuose, bet ir biomedicinoje. Dantų, kaulų, sąnarių pažeidimai ir ligos tampa vis labiau aktualia problema pasaulyje. Kasmet pasaulyje atliekama virš 2 mln. kaulinio audinio gydymo operacijų [1], o dantų implantavimo rinka pasaulyje sudaro 12–18 milijonų [2]. Iki 10 % implantų yra atmetami per pirmąsias dienas ar kelis metus, tačiau priklausomai nuo sąlygų šis skaičius gali siekti 20 % ir daugiau [3, 4].

Biokeraminės medžiagos (Al_2O_3, ZrO_2) dažnai naudojamos medicinoje, dantų, kaulų bei sąnarių implantams, nes yra chemiškai inertiškos, biosuderinamos, pasižymi dideliu kietumu bei mechaniniu atsparumu. Visgi, nepaisant plataus panaudojimo biokeramika pasižymi bioinertiškumu, todėl ląstelių adhezija ir sąveika su biologiniais audiniais gali būti nepakankama. Siekiant padidinti ląstelių ir biomedžiagų sąveiką naudinga naudoti poringus bei šiurkščius paviršius.

Vienas iš dažniausiai naudojamų būdų siekiant suformuoti poringą biokeraminę Al_2O_3 dangą yra aliuminio anodavimas (elektrocheminis oksidavimas), kuris padidina paviršiaus kietumą, korozinį atsparumą, užtikrina dažų adsorbciją, adheziją bei kitas savybes. Titano, cirkonio, plieno ir kitų lydinių panaudojimą medicinoje riboja ne tik aukšta kaina, bet ir sudėtingas mechaninis apdorojimas. Al tankis yra daug mažesnis negu Ti ar Zr ir sudaro atitinkamai 2,70 g/cm³, 4,51 g/cm³ ir 6,52 g/cm³, todėl Al lengvumas ir mažesnis svoris gali turėti didesnę paklausą kuriant tiek medicininius įtaisus, pvz. implantus, tiek kitas detales. Itin grynas Al (>99,999 %) yra brangus ir turi prastesnes mechanines savybes, nes jo kietumas 2–3 kartus mažesnis už Al lydinius. Poringos struktūros anodinės dangos, turinčios didelį paviršiaus plotą padidina ląstelių adheziją ir biosuderinamumą [5, 6]. Be to, į paviršines anodinės dangos skylutes gali įaugti pažeisto kaulo audiniai, kurių metu padidinamas mechaninis stabilumas bei apkrovimo pasiskirstymas.

Kietasis (III tipo) anodavimas, kuris atliekamas sieros/oksalo r. elektrolituose esant žemoms temperatūroms leidžia suformuoti kietas anodines dangas, kurių storis siekia virš 100 μm [7]. Terminas „anodinės dangos“ nėra tikslus elektrochemine prasme. Kadangi Al paviršius pakyla po anodavimo, todėl topografine prasme tai gali būti vadinama danga. Šis terminas paliekamas tekste ir dėl jo populiarumo. Kietasis anodavimas įprastai atliekamas sieros/oksalo r. elektrolite žemose temperatūrose, pavyzdžiui, 0 °C, tačiau šiame darbe terminas „kietasis anodavimas“ buvo naudojamas ir Al anodavimui prie 15 °C. Nepaisant didelio kietumo, anodinių dangų dilimas išlieka viena iš pagrindinių problemų daugelyje pramonės sričių. Biologinėse sistemose dilimo turi būti išvengta. Santykinis judėjimas tarp implanto ir aplinkinių audinių gali lemti sankabumo problemas ir organizmo atmetimo reakcijas. Jonų migracija į aplinkinius audinius ir organus gali sukelti uždegimą implantacijos vietoje, kaulo eroziją. Al^{3+} jonai didelėmis koncentracijomis yra toksiški žmogaus organizmui [8, 9], todėl Al^{3+} jonų koncentracija neturi viršyti 1 mg/kg kūno svorio per dieną [10]. Be to, didelis legiruojančių priedų (Mn, Cu, Fe, Zn, kt.) kiekis, esantis pramoniniuose Al lydiniuose gali turėti neigiamą poveikį ląstelių adhezijai ir proliferacijai.

Vienas labiausiai paplitusių metodų anoduotų paviršių apsaugai nuo dilimo remiasi politetrafluoretileno (PTFE) barjerinių dangų susidarymu, kuris sumažina trinties koeficientą žemiau 0,2. Visgi, PTFE dangų panaudojimą biomedicinoje riboja keletas faktorių. Poringi ir šiurkštūs anoduoti paviršiai tampa lygūs ir nepasižymi drėkinimu dėl PTFE molekulių prigimties, todėl ląstelių adhezija dar labiau apsunkinama. Viena iš alternatyvų yra biosuderinamų Ti sluoksnių formavimas ant anodinių dangų.

Ti oksidai ir nitridai pasižymi apsauginėmis, trintį ir dilimą slopinančiomis savybėms ant įvairių paviršių [11, 12], tarp jų ir anodinių dangų [13]. Kelios tyrėjų grupės nustatė, kad Ti pagrindu suformuoti sluoksniai efektyviai slopina dilimą ir sumažina trinties koeficientą iki 0,15 [12, 14]. Ti ir TiO_2 sluoksnių efektyvumas užfiksuotas implantuose [15], tvirtinimo detalėse [16], aviacijos bei laivyno pramonėje [17], turbinų varikliuose [18]. Įvairiems technologiniams tikslams šie sluoksniai buvo suformuoti ant anoduoto Al, naudojant zolių-gelių [19], magnetroninio nusodinimo [20], atominio sluoksnio nusodinimo (ALD) [21], hidroterminio apdorojimo [22] bei kitus metodus. TiO_2 yra chemiškai stabilus, netirpus, netoksiškas, todėl nereaguoja su dauguma rūgščių, šarmų ir organinių junginių. Ti paviršiai pasižymi cheminiu inertiškumu [23], koroziniu atsparumu [24] ir biosuderinamumu [25], todėl dažnai naudojami jutikliuose,

implantuose bei kituose biomedicininiuose gaminiuose. Ti oksidų sluoksnių formavimas padidina tiesioginę implanto-kaulinio audinio sąveiką (osteointegraciją), padeda išvengti imuninių atmetimo reakcijų ir sudaro apsaugą nuo organizmo terpės poveikio. Nors trinties bei dilimo režimai organizmuose dar nėra aiškiai identifikuoti, tačiau akivaizdu, jog biomedicininiai gaminiai gali susidurti su judančiais paviršiais ir pačiame organizme, o taip pat transportavimo bei įdiegimo į organizmą metu. Aktualu ištirti biosuderinamų dangų svarbiausias tribologines savybes. Anodinių dangų ir Ti sluoksnių sinerginis poveikis, užtikrinantis žemą paviršių trintį ir aukštą biosuderinamumą yra perspektyvus kuriant naujos kartos biomedicininius įrenginius. Nanostruktūrinių dangų panaudojimas gali būti naudingas ekonomiškai keičiant šiuo metu paplitusias ir brangias Ti osteosintezės sistemas odontologijoje bei ortopedijoje.

Siekiant priartėti prie trinties sąlygų biologinėse sistemose tikslinga tirti lipidais ir kitais organiniais junginiais padengtus paviršius, kadangi didžioji dalis junginių esančių kraujo plazmoje bei įeinančių į ląstelės sudėtį gali sąveikauti su nanostruktūrinėmis dangomis [26]. Organinių junginių adsorbcija ir migracija į anodinės dangos skylutes cheminių reakcijų dėka lemia triboplėvelių formavimąsi, kurios gali užtikrinti žemą paviršių trintį bei dilimą. Šių junginių migracija įvairiose dangose dažnai tiriama nedestrukcine Ramano spektroskopija, kuri teikia informaciją ne tik apie molekulių struktūrą bei kiekius, bet ir sąveiką su danga.

Darbo tikslas

Darbo tikslas yra įvertinti nanostruktūrinių anodinių dangų ant pramoninių aliuminio lydinių aktualiausias chemines, fizines, tribologines ir biosuderinamumo savybes bei jų sąveiką su svarbiausiomis biologinėmis tepamosiomis medžiagomis.

Uždaviniai

- Įvertinti elektrolito ir anodavimo parametrų poveikį formuojamų anodinių Al_2O_3 dangų topografijai ir trinčiai.
- Atrinkti tyrimams tinkamiausias ląstelių linijas bei įvertinti anodinių ir nanostruktūrinių dangų biosuderinamumo savybes.
- Įvertinti paviršinio Ti/TiO_2 sluoksnio poveikį anodinių dangų statinei ir dinaminei trinčiai.
- Palyginti IVB grupės elementų bei kitų pereinamųjų metalų nanosluoksnių ant anodinių dangų tribologines savybes.

- Įvertinti Ramano spektroskopijos tinkamumą organinių junginių migracijai į anodinės dangos skylutes tirti.
- Įvertinti svarbiausių biologinių tepamųjų medžiagų poveikį anodinių bei nanostruktūrinių dangų tribologinėms savybėms.

Mokslinis naujumas

- Tiek Ti lydinių, tiek Al_2O_3 biosuderinamumas jau yra plačiai ištirtas. Tačiau nėra tinkamai atsižvelgiama į tai, jog pramoniniai Al lydiniai turi legiruojančius priedus (Cu, Mn, Si ir pan.), o juos anodavus dangose lieka ženklūs kiekiai elektrolito komponentų. Disertacijoje parodoma, jog cheminiu inertiškumu pasižymintys Ti/TiO_2 nanosluoksniai pagerina anodinių dangų biosuderinamumą suformuojant barjerinę apsaugą.
- Kelios tyrėjų grupės yra nagrinėję Ti ir TiO_2 sluoksnių įtaką tribologinėms savybėms, tačiau šie sluoksniai ant anodinių Al dangų beveik nebuvo tirti. Kol kas buvo užfiksuotas tik nežymus tribologinių savybių pagerėjimas. Nepriklausomai nuo dengimo metodo, pvz. ALD ar magnetroninio nusodinimo, Ti/TiO_2 nanosluoksniai itin reikšmingai pagerina anodinių dangų tribologines savybes ir sumažina trinties koeficientą iki 0,2. Įvertinus ir kitų elementų sluoksnius, paaiškėjo, jog IVB grupės metalai suteikia geresnes tribologines savybes už kitus pereinamuosius metalus, tačiau Ti efektyvumas yra nepalyginamai aukštesnis.
- Dar nebuvo pasiūlyta, jog nanostruktūrinės dangos suformuotos ant anoduoto Al bei pasižyminčios geru biosuderinamumu ir atsparumu trinčiai gali būti sėkmingai panaudotos biomedicininiuose gaminiuose siekiant pakeisti šiuo metu naudojamus titano lydinius.
- Organinių junginių migracija į anodinės dangos skylutes dar nebuvo stebima Ramano spektroskopijos metodu. Ši metodika buvo sėkmingai pritaikyta nagrinėjant dažų skverbimąsi į anoduotą sluoksnį, o taip pat siekiant atrinkti tribologiškai efektyviausius dangos užpildus.

Ginamieji teiginiai

- Ti nanosluoksniai ir jų oksidai pagerina anoduoto Al biosuderinamumą ne tik dėl Ti bioinertiškumo, bet ir dėl barjerinio sluoksnio, apsaugančio nuo elektrolito komponentų, esančių skylutėse. Mažas sluoksnio storis leidžia išlaikyti šiurkščią paviršiaus topografiją, kuri naudinga ląstelių adhezijai.

- Anodavimo sieros/oksalo r. metu suformuotų anodinių dangų tribologinės savybės gali būti ženkliai pagerintos nusodinant IVB grupės elementų nanosluoksnius arba jų oksidus. Maždaug 10–100 nm storio Ti nanosluoksniai ir jų oksidai ženkliai sumažina trintį lyginant su Al, anodinėmis dangomis ar Ti substratais. Sluoksniai plonesni nei 10 nm ir storesni nei 0,5 µm turi panašią arba prastesnę trintį lyginant su minėtais substratais. Trinties sumažėjimas yra būdingas Zr ir Hf oksido nanosluoksniams. Metalų, nepriklausančių IVB grupei, pavyzdžiui, Cr, Cu ar Nb nanosluoksniai neturi teigiamo poveikio tribologinėms savybėms.
- Sausoji ir iš dalies tepamoji trintis gali būti reikšmingai pagerinta vykstant reakcijoms tarp impregnuojamo užpildo ir elektrolito komponentų, esančių dangos skylutėse. Užpildo trinties charakteristikos turi mažai reikšmės tribologinėms savybėms, nes skylutėse ir trinties zonoje susidaro nauji junginiai, kurie lemia triboplėvelių formavimąsi. Barjerinis sluoksnis, esantis anodinės dangos paviršiuje, nėra būtinas dilimo mažinimui, kadangi tribologines savybes nulemia gilesnis užpildo įsiskverbimas, kuris gali būti stebimas Ramano spektroskopija.

Autoriaus indėlis

1. Al lydinių ir elektrolito paruošimo, anodavimo bei impregnavimo tepamosiomis medžiagomis procedūras, taip pat trinties ir dilimo testus atliko autorius.
2. Autorius didžiąja dalimi prisidėjo prie anodinių ir nanostruktūrinių dangų paviršių analizės bei jų paruošimo publikacijoms, naudojant optinę mikroskopiją (dalį atliko L. Staišiūnas), skenuojančią elektroninę mikroskopiją (atliko G. Stalnionis ir A. Selskis), profilometriją (dalį atliko L. Staišiūnas), rentgeno spindulių energijos dispersijos spektroskopiją (atliko G. Stalnionis), rentgeno spindulių difrakciją (atliko V. Pakštas), kietumo matavimus (atliko G. Bikulčius), rentgeno fotoelektronų spektroskopiją (atliko V. Jasulaitienė). Taip pat tiesiogiai prisidėjo prie biosuderinamumo tyrimų (atliko A. Stirkė, J. Kavaliauskaitė bei IMC tyrėjai G. Pivoriūnas ir A. Čebatariūnienė) rezultatų analizės ir apdorojimo.
3. Užpildų įsiskverbimo į anodinės dangos skylutes matavimus, panaudojant Ramano spektroskopiją, atliko autorius ir I. Ignatiev. Disertacijos ir jos santraukos tekstus bei grafinę dalį suruošė autorius.

2. EKSPERIMENTINĖ DALIS

Dauguma bandinių buvo suruošti anoduojant Al lydinius ir ant jų nusodinant Ti/TiO_2 bei kitų elementų nanosluoksnius. Oksidų nanosluoksniai buvo formuojami ALD metodu, o Ti, Zr, Cu, Cr ir Nb nanosluoksniai – magnetroniniu dulkinimu. Bendra eksperimentų koncepcija pateikta 1 pav.

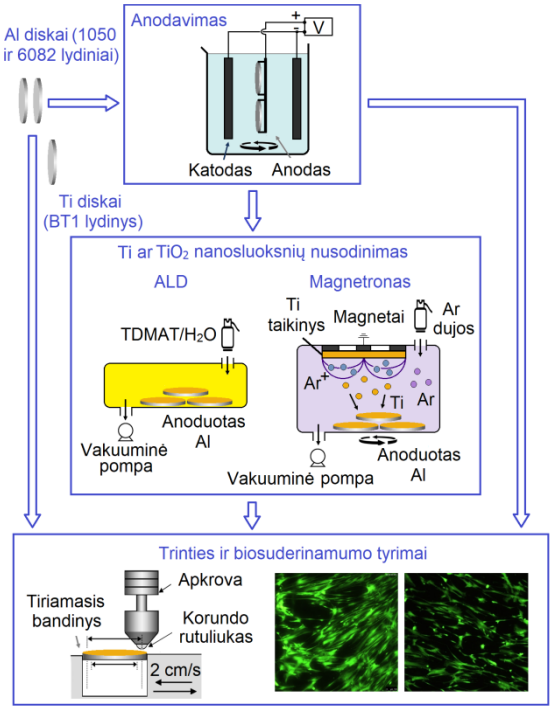

1 pav. *Al anodavimo, nanostruktūrizavimo Ti sluoksniais bei paviršių trinties ir biosuderinamumo tyrimų schema*

Anodinių ir nanostruktūrinių dangų statinė ir dinaminė trintis ištirta tribotesteriu bei įvertintas šių paviršių biosuderinamumas.

2.1 Medžiagos ir ląstelės

Diskeliai (16 mm OD) iš pramoninių Al lydinių: 99,67 % 1050 (0,25 % Fe; 0,08 % Si) ir 96,72 % 6082 (1,10 % Si; 1,02 % Mg; 0,61 % Mn; 0,54 % Fe) iš UAB „FXB-Niemet“ (Lietuva) buvo naudojami kaip substratai. 96,32 % Ti lydinys BT1 (1,76 % Mn; 1,75 % Al; 0,11 % Fe; 0,06 % Si) iš UAB „SP MET“ (Lietuva) buvo naudojamas biosuderinamumo ir trinties

tyrimams. 50 μm storio ir 99,95 % Al folija (Rusija) buvo naudojama organinių junginių migracijos tyrimams.

99,99 % Ti, 99,20 % Zr, 99,90 % Hf, 99,95 % Cr, 99,99 % Cu ir 99,80 % Nb taikinai buvo naudojami nanosluoksnių nusodinimui magnetronu. Tetrakis (dimetilamino) titano (TDMAT) ir Tetrakis (dimetilamino) hafnio (TDMAH) dujos buvo atitinkamai naudojamos TiO_2 or HfO_2 nanosluoksnių formavimui ALD metodu.

Dažymui buvo naudojami komerciniai Sanodal Deep Black MLW ir Sanodure Green LWN (Clariant, Šveicarija) anijoniniai Cr-kompleksų azo dažai atitinkamai pavadinti „juodas dažas“ ir „žalias dažas.“ Dažai buvo ištirpinti dejonizuotame (DI) vandenyje, pasiekiant koncentraciją 2 g/L.

Hankso subalansuotas druskų tirpalas (0,185 g/L $CaCl_2 \cdot 2H_2O$ + 0,09767 g/L $MgSO_4$ + 0,4 g/L KCl + 0,06 g/L KH_2PO_4 + 0,35 g/L $NaHCO_3$; 8,0 g/L NaCl + 0,04788 g/L Na_2HPO_4; 1,0 g/L D-gliukozė + 0,011 g/L fenolio raudonoji Na druska; pH 7,2–7,6) iš Carl Roth GmbH (Vokietija) bei tepamosios medžiagos: 70 % oleino r. (StanChem, Lenkija), 95 % stearino r. (Sigma, JAV), 80 % tristearinas (TCI, Japonija) buvo naudojamos trinties tyrimams. 25 % PTFE (DuPont, JAV) dispersija praskiesta izopropanolyje.

Žmogaus gimdos kaklelio vėžio Hep-2C ląstelės, pelės fibroblastų L929 ląstelės ir kinų žiurkėno kiaušidžių vėžio CHO-K1 ląstelės buvo augintos Dulbecco modifikuotoje Eagle terpėje (DMEM) su 10 % jaučio vaisiaus serumu, o PDLS ląstelės – DMEM terpėje su 10 % fetaliniu veršelių serumu ir antibiotikais prie 37 °C, esant 5 % CO_2. Plaunama fosfatiniu buferiniu tirpalu (PBS) ir surenkama, naudojant tripsino ir EDTA tirpalą.

2.2 Paviršių paruošimas ir nanosluoksnių formavimas

Al anodavimas. Al diskų anodavimo metodika detaliai aprašyta [150, 151] ir kt. Apibendrinant trumpai, diskai buvo ėsdinami šarminiame tirpale, plaunami ir patalpinami į elektrolitą. Kietasis anodavimas atliktas H_2SO_4/oksalo r. elektrolite (175 g/L H_2SO_4 + 30 g/L $(COOH)_2 \cdot 2H_2O$ + 55.5 g/L $Al_2(SO_4)_3 \cdot 18H_2O$) esant 2 A/dm^2 anodiniam srovės tankiui prie 15 °C, 70 min., siekiant suformuoti 60 ± 10 μm storio dangas. Anodavimas 40 g/L H_3PO_4 elektrolite atliktas prie 15 °C, esant 120 V ar 150 V įtampai ir 150 min. trukmei. Al folija buvo anoduota H_2SO_4/oksalo r. elektrolite, paliekant tik barjerinį sluoksnį vientisumui išlaikyti. Anodinės dangos storis buvo įvertintas dangos storio matuokliu CM-8825FN (Guangzhou Landtek Instruments Co., Kinija). Anoduoti lydiniai buvo džiovinami 30–60 min. prie 50–60 °C.

Atominio sluoksnio nusodinimas (ALD). TiO_2 bei HfO_2 nanosluoksniai buvo formuojami ALD metodu, naudojant „Fiji F200“ (Cambridge NanoTech) įrenginį, vykstant THMAT/THMAH pirmtako chemisorbcijai bei jo oksidacijai H_2O garais prie 250 °C ir 30–35 Pa darbinio slėgio.

Magnetroninis nusodinimas. Ti, Zr, Hf, Cr, Cu ir Nb sluoksniai buvo formuojami magnetronu naudojant „Univex 350“ (Leybold Vacuum Systems, Vokietija) įrenginį, esant 12 °C ir 250 mPa darbiniam slėgiui.

2.3 Biosuderinamumo tyrimai

Ti BT1 ir Al lydiniai (prieš ir po anodavimo bei nanostruktūrizavimo) buvo autoklavuojami 15 min. prie 121 °C. L929, Hep-2C, CHO-K1 ląstelių adhezijos ir gyvybingumo tyrimams buvo užsėta 0,53 x $10^6/cm^2$ ląstelių suspensijos ir inkubuota 48 val. (37 ˚C; 5 % CO_2). PDLS ląstelės užsėtos prie skirtingų tankių 15000/1,9 cm^2, 10000/1,9 cm^2 ir 8000/1,9 cm^2 ir inkubuotos atitinkamai 24 val., 72 val. ir 120 val. (37 ˚C; 5 % CO_2). Ląstelės atkabintos ir hemocitometru suskaičiuotas gyvybingų ląstelių skaičius, naudojant tripano mėlio testą. Fluorescenciniam vaizdavimui PDLS ląstelės dažytos 1 μM kalceino fluorescentiniais dažais (Invitrogen, JAV) po 48 val. ir įvertintos TCS SP8 DMI6000B mikroskopu (Leica Microsystems).

Statistinė analizė atlikta naudojant vienpusę ANOVA dispersijos analizę ir Bonferroni testą su „MaxStat Pro Statistics“ programine įranga (3.6 versija). Statistinis reikšmingumo lygmuo buvo $p < 0,05$. Atlikti trys nepriklausomi eksperimentai su 2–4 bandiniais, siekiant gauti statistiškai patikimus rezultatus.

2.4 Tribologiniai tyrimai

Anodinių ir nanostruktūrinių dangų tribologinės charakteristikos buvo tiriamos tribotesteriu (Anton Paar TriTec SA, Šveicarija), kaip detaliai aprašyta [150, 151] ir kt. Apibendrinant trumpai, buvo taikoma „rutulys ant plokštumos“ konfigūracija, naudojant 6 mm skersmens 99,8 % korundo (G16; ~2900 HV; *Ra* 0,025 μm) rutuliukus (RGP International Srl, Italija), įtvirtintus laikiklyje ir judančius tiesine grįžtamąja trajektorija bandinio paviršiumi stacionarioje fazėje. Matavimams pasirinkta 1 N arba 10 N apkrova bei 2 cm/s judesio greitis. Trinties koeficiento matavimams beveik visada buvo naudojami korundo rutuliukai, todėl aprašant rezultatus šios sąlygos nėra papildomai paminimos. Tais atvejais, kai buvo naudojami plieno rutuliukai, tai yra nurodoma aprašant rezultatus.

2.5 Paviršių analizė

Skenuojanti elektroninė mikroskopija (SEM). SEM atlikta naudojant „Helios NanoLab 650“ (FEI, Olandija) įrangą. Prieš analizę ant paviršių buvo užgarintas 2–3 nm Cr sluoksnis, naudojat magnetroną Quorum Q150T ES (Judges Scientific Plc, JK) dėl didesnio elektrinio laidumo.

Rentgeno spindulių energijos dispersijos spektroskopija (EDS). INCA spektrometru (Oxford Instruments, JK) įvertinta anodinių ir nanostruktūrinių dangų elementinė sudėtis bei Ti elementinis pasiskirstymas.

Rentgeno fotoelektronų spektroskopija (XPS). ESCALAB-MKII spektrometras (VG Scientific, JK) pritaikytas nanostruktūrinių dangų tyrimams, esant ~3 nm/min ėsdinimo greičiui su Ar^+ jonais.

2.6 Organinių junginių migracija

Metiloleato ir dažų migracija į visiškai anoduotą Al foliją ištirta Ramano spektroskopijos metodu. ~10 µL metiloleato buvo užlašinta ant anoduotos folijos ir po 1 val. buvo užrašyti Ramano spektrai pašalinus perteklių nuo paviršiaus mikropluošto popieriumi. Spektrų registravimui panaudotas spektrometras su konfokaliniu mikroskopu inVia (Renishaw, JK), sufokusavus 785 nm bangos ilgio lazerio spindulį į anoduotos folijos paviršių. Metiloleato įsiskverbimo gylis įvertintas, keičiant lazerio fokusavimo atstumą nuo 0 µm iki 54 µm, esant 6 µm intervalo žingsniui.

Dažų migracijos tyrimams panaudotas spektrometras „RamanFlex 400“ (PerkinElmer, Inc.). 785 nm lazerio spindulys iš apačios buvo sufokusuotas į anoduotos folijos vidų, naudojant 30 mW lazerio galią ir 7 mm darbinį atstumą pagal anodinės dangos fotoliuminescencijos maksimumą. 5 µL dažo užlašinta ant anoduotos Al folijos ir 1 val. bėgyje buvo registruojami Ramano spektrai.

2.7 Tepamųjų medžiagų impregnavimas

Kietos fazės lipidai (stearino r. ir tristearinas) buvo formuojami ant anodinių dangų pamerkus substratus į išlydytus lipidus 1 val. prie 90 °C. Po valandos substratai buvo ištraukti iš lydalų ir laikomi krosnyje mažiausiai 1 val., siekiant užtikrinti tolygų lipido pasiskirstymą. 15 µm storio skystos fazės oleino r., metiloleato, lipidinio užpildo ir 18 Z užpildo sluoksniai buvo formuojami gravimetriniu būdu ir laikomi krosnyje 1 val., esant 90°C temperatūrai. PTFE dangų formavimui anoduoti lydiniai buvo laikomi 25 % PTFE/IPA dispersijoje 15 min., džiovinami ore 30 min. ir kaitinami 10 min. prie 310 °C, atvėsinama iki kambario temperatūros.

3. REZULTATAI IR JŲ APTARIMAS

Šis skyrius sudarytas iš keturių dalių. Trijose dalyse išdėstyti rezultatai pagrindžia atitinkamą ginamąjį teiginį. Pirmoji dalis skirta tyrimo objektų parinkimui ir apibūdinimui.

3.1 Nanostruktūrinių anodinių dangų formavimas ir jų charakterizavimas

Tiriant cheminius, tribologinius, biomedicininius ir daugelį kitų procesų ant anodinių dangų yra svarbu nuodugniai įvertinti struktūrines, morfologines ir topografines paviršių savybes. Nors chemiškai gryno Al anodavimas bei gaunami paviršiai yra gana plačiai aprašyti, anodinės dangos ant pramoninių Al lydinių moksliniais principais nagrinėjamos nepalyginamai rečiau. Pramoninio Al anodavimo metu suformuojamos kietos, korozijai atsparios oksidų dangos, turinčios didelį potencialą ne tik aukštųjų technologijų (robotikos, aviacijos ir kt.), bet ir biomedicinos taikymuose. Visgi, nepaisant jų kietumo, apsauginės anodinių dangų savybės yra nepakankamos ir veikiant didelėms apkrovoms sparčiai dyla. Kiti tyrėjai [13] bandė įterpti TiO_2 nanodaleles į anodines dangas suformuotas H_3PO_4 elektrolite, kurių storis siekė 6 μm. TiO_2 galėjo visiškai užpildyti 125 nm ID skylutes. Gautų dangų trinties koeficientas sudarė 0,1–0,2 bei pasižymėjo geru atsparumu dilimui. Nors tribologinės savybės buvo tik šiek tiek geresnės nei supresuoto TiO_2, tai gana gerai atitiko lūkesčius, nes kompozicinėje dangoje buvo daug TiO_2. Be to pabrėžtina, jog nanostruktūrinių dangų panaudojimas biomedicinoje dar yra mažai ištirtas. Svarbu ir tai, jog dilimo procesų mechanizmai, vykstantys ant poringų dangų, ženkliai skiriasi nuo vykstančių klasikinėse trinties zonose, todėl triboplėvelių formavimo ir dilimo slopinimo metodai dar nėra aiškiai identifikuoti. Todėl būtina detaliai išnagrinėti įvairias anodavimo sąlygas ir nanostruktūrinių dangų morfologiją.

3.1.1 Anodavimo parametrų poveikis anodinėms dangoms

Kadangi pramoniniai Al lydiniai yra labai įvairūs, juos apibendrinti yra sudėtinga ir tyrimams buvo parinkti du lydiniai 1050 ir 6082 bei Al folija, kadangi aukšto grynumo Al (>99,999 %) pasižymi nepakankamomis mechaninėmis savybėmis ir turi du kartus mažesnį kietumą bei atsparumą tempimui [165]. Komercinė 99,95 % grynumo Al folija ir 99,67 % grynumo 1050 lydinys dažnai naudojami maisto ir chemijos pramonėje, o 96,72 % grynumo 6082 lydinys taikomas techniniuose įrenginiuose, kur paviršius

veikia dideli įtempimai bei didelės apkrovos [166]. Abu lydiniai pasižymi antikorozinėmis savybėmis, tačiau 1050 lydiniams būdingas didesnis plastiškumas ir lengvesnis apdirbimas, o 6082 lydiniams – tvirtumas ir mechaninis atsparumas dėl Mn, Mg bei Si priemaišų. Morfologiniai tyrimai parodė, kad 1050 lydiniai turi lygią, vienodą paviršiaus struktūrą, tuo tarpu 6082 lydinių paviršiuje stebimi mikroįtrūkimai, kurie lemia didesnį šiurkštumą (1,28 μm prieš 0,99 μm). Be to 6082 lydinių kietumas pagal Vikersą yra 4,5 karto didesnis lyginant su 1050.

Anodinės dangos formavimui buvo pasirinktas plačiai paplitęs kietasis (III tipo) anodavimas sieros/oksalo r. elektrolite [93], kurio metu galima gauti virš 100 μm storio Al_2O_3 dangas. Palyginimui pasirinktas anodavimas fosforo r. elektrolite, kadangi fosfatai dažnai įeina į dilimą slopinančių junginių sudėtį [167] ir jų anijonai yra nekenksmingi organizmui [168].

SEM parodė, kad H_2SO_4/oksalo r. elektrolite formuojasi kietos 60 μm storio anodinės dangos su siauromis skylutėmis (<20 nm) , o plonos dangos su plačiomis skylutėmis (>100 nm) formuojasi H_3PO_4 elektrolite (2 pav.).

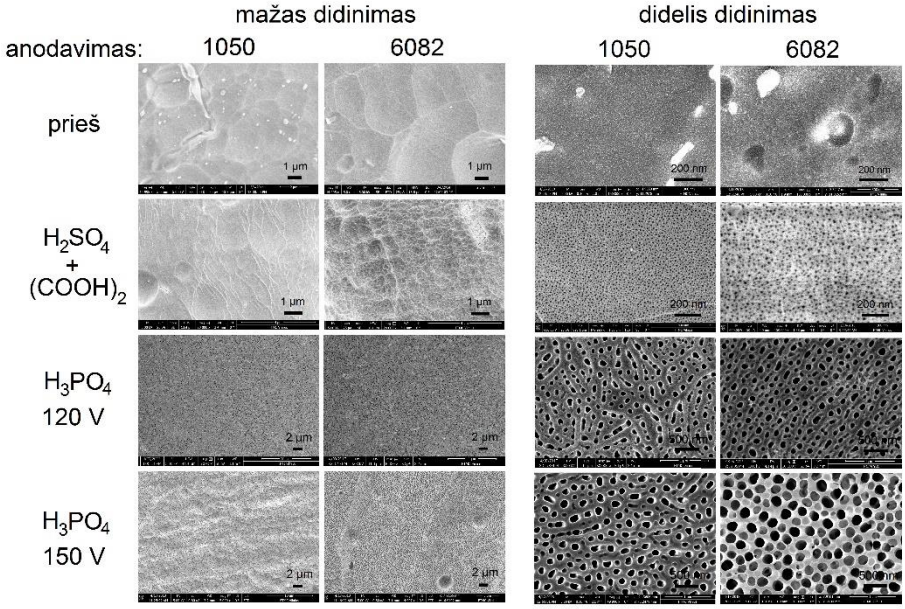

2 pav. *Al paviršių SEM topografija prieš ir po anodavimo, esant mažam (kairėje) ir dideliam (dešinėje) didinimams*

Sieros/oksalo r. elektrolite anoduoti 6082 lydiniai turi du kartus didesnį skylučių diametrą ir apie keturis kartus didesnį poringumą lyginant su 1050 (1 lentelė).

1 lentelė. *Paviršiaus skylučių charakteristikos, gautų anoduojant 15 °C; pritaikyta pagal [151]*

Elektrolitas	Al lydinys	Dangos storis, μm	Skylučių diametras, nm	Skylučių tankis, skylutės/ μm^2	Poringumas, %
H_2SO_4/ oksalo r.	1050	59 ± 2	7 ±1	1560 ± 110	6
	6082	56 ± 2	15 ± 2	1040 ± 121	23
	folija	70 ± 1	13 ± 2	530 ± 34	8
H_3PO_4 (120 V)	1050	7 ± 1	110 ± 23	22 ± 2	27
	6082	6 ± 1	119 ±14	25 ± 2	39
H_3PO_4 (150 V)	1050	15 ± 2	144 ± 11	19 ± 2	44
	6082	11 ± 1	203 ± 19	14 ± 2	83

Visiškai anoduotos Al folijos poringumas yra panašus į 1050 lydinį. Buvo pastebėta, kad skylučių diametras ir dangos storis priklauso nuo anodavimo įtampos. Keliant įtampą iki 150 V skylučių diametras siekia apie 200 nm, o poringumas ir dangos storis padidėja apie du kartus, naudojant H_3PO_4 elektrolitą.

SEM paviršių analizė taip pat atskleidė, kad Al lydiniai formuoja kristalitus (grūdelių ribas), kurių dydis siekia iki 10 μm, nors 6082 lydiniams būdingi kristalitai viršijantys net 100 μm [172]. Po anodavimo kristalitų dydis ženkliai sumažėja, tačiau išlieka įžvelgiamas. Anodavimas mažai keičia paviršiaus šiurkštumo savybes, tačiau kietumas yra apie 1,5 kartus didesnis 1050 lydinyje lyginant su 6082 po anodavimo H_2SO_4/oksalo r. elektrolite.

Optimalios anodavimo sąlygos buvo atrinktos, keičiant srovės tankį, anodavimo trukmę, elektrolito temperatūrą bei kitus parametrus. Morfologiniais bei tribologiniais tyrimais nustatyta, kad 60 ± 10 μm storio anodinės dangos, suformuotos H_2SO_4/oksalo r. elektrolite prie 15 °C temperatūros, 2 A/dm² srovės tankio (~20 V), esant 70 min. anodavimo trukmei pasižymi geriausiu atsparumu sausajai trinčiai ir tolygia paviršiaus struktūra. Anodavimas H_3PO_4 priklausomai nuo elektrolite esančių priedų, pavyzdžiui, metanolio, glicerolio, padidino anodinės dangos storį iki 1,5 karto, tačiau geresnio tribologinio efekto nebuvo pasiekta. Todėl tyrimams buvo naudojamos dangos, suformuotos 4 % H_3PO_4 elektrolite esant pastoviai 120 V (~0,5 A/dm²) arba 150 V (~1,5 A/dm²) įtampoms be papildomų

priedų. Didesnė įtampa (150 V vietoje 120 V) leido suformuoti storesnes anodines dangas per trumpesnį laiką.

3.1.2 Nanosluoksnių formavimas ALD ir magnetronu

Ti ir kitų metalų bei jų oksidų nanosluoksnių formavimui ant anodinių dangų atitinkamai buvo panaudoti magnetroninio nusodinimo ir ALD metodai. 5 nm, 10 nm ir 15 nm TiO_2 nanosluoksniai buvo formuojami ALD vykstant TDMAT chemisorbcijai ir jo oksidacijai į TiO_2 vandens garais. SEM parodė, kad 5 nm TiO_2 sluoksniai visiškai uždengia anodinės dangos skylutes, todėl storesnių sluoksnių formavimas vyksta susidarant ištisinei plėvelei ant paviršiaus anoduoto H_2SO_4/oksalo r. elektrolite (3 pav.). TiO_2 sluoksniams ant anoduoto 1050 lydinio būdinga smulkiadispersinė ir tolygi struktūra, o 6082 lydinių paviršiuje TiO_2 sluoksniai išsidėsto mažiau tolygiomis sankaupomis ir sudaro skirtingo dydžio saleles, kurių ilgis siekia kelis šimtus nanometrų ir daugiau. Nanostruktūrinių 6082 dangų paviršiuje taip pat užfiksuoti defektai pavaizduoti kaip tamsios tuštumos galimai dėl netolygiai pasiskirsčiusių legiruojančių priedų.

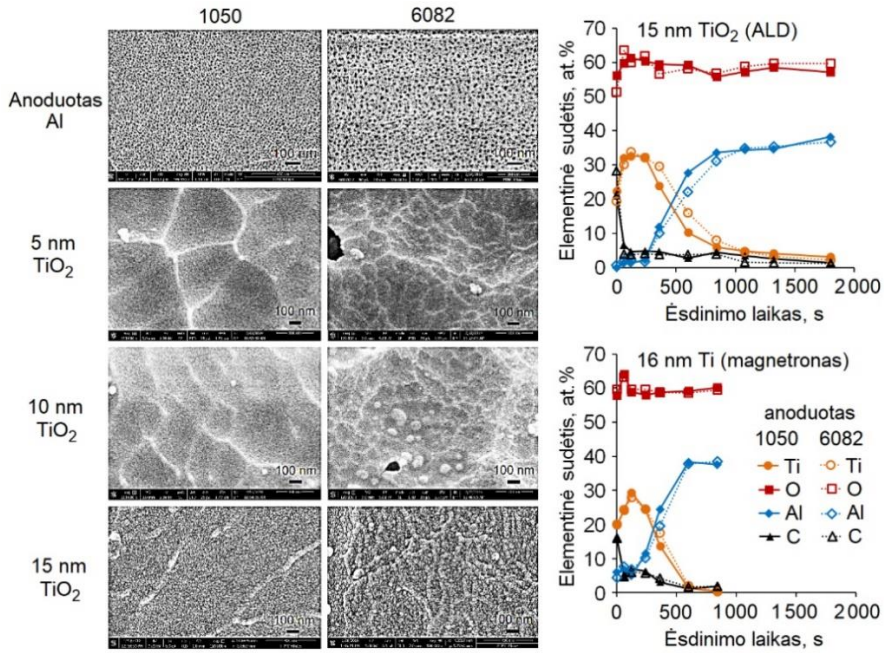

3 pav. *Sieros/oksalo r. elektrolite anoduotų 1050 ir 6082 lydinių SEM vaizdai prieš ir po TiO_2 nanosluoksnių nusodinimo su ALD (kairėje) bei 15 nm TiO_2 (ALD) ir 16 nm Ti (magnetronu) nanosluoksnių elementinė sudėtis, nustatyta XPS metodu (dešinėje)*

Panašaus storio 15 nm TiO_2 (ALD) ir 16 nm Ti (magnetroninis) nanosluoksniai ant anodinių dangų buvo ištirti XPS metodu, naudojant 3 nm/min. ėsdinimo greitį su Ar^+ jonais. Didžiausias Ti kiekis užfiksuotas po 360 s ėsdinimo (pasiekiant ~18 nm gylį) tiek su magnetronu, tiek su ALD. Nustatyta, kad TiO_2 nanosluoksniai daug giliau įsiskverbia į skylutes naudojant ALD, negu Ti nusodintą magnetronu. Šie tyrimai taip pat patvirtina EDS rezultatus, kurių metu buvo gautas virš keturių kartų didesnis Ti kiekis ALD metodu. XPS tyrimų metu taip pat nustatyta, kad Ti sluoksniai nusodinti magnetronu yra visiškai oksidavęsi į TiO_2. Terminas „Ti/TiO_2 nanosluoksniai“ šiame tyrime apima visus galimus oksidus pvz. TiO_2, TiO, Ti_2O_3 ir kt., o taip pat ir Ti nitridus dėl sąveikos su atmosferine aplinka. Nėra žinoma ar Ti/TiO_2 nanosluoksniai formuoja amorfines ar polikristalines dangas, kadangi GIXRD, XPS ir Ramano spektroskopijos tyrimai nerodė metalams būdingos kristalinės tvarkos signalų.

Nepaisant nevienodo priemaišų išsidėstymo anoduotuose lydiniuose, Ti pasiskirstymas buvo pakankamai tolygus po ALD nusodinimo (4 pav.).

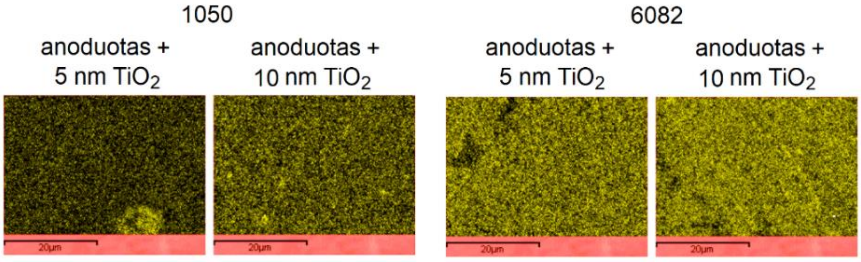

4 pav. *Ti (šviesi spalva) pasiskirstymas ant anodinių dangų po ALD nanosluoksnių nusodinimo, įvertintas EDS analize*

Iki 1,5 karto didesnis Ti kiekis EDS metodu buvo užfiksuotas ant anoduoto 6082 lydinio dėl du kartus platesnių skylučių, lemiančių geresnį TiO_2 nanosluoksnių įsiskverbimą lyginant su anoduotu 1050 lydiniu. Anodinėse dangose taip pat buvo rasta virš 4 % sieros. Sulfatai gali ženkliai slopinti Ti migraciją į anodinės dangos skylutes, kadangi $Al_2(SO_4)_3$ suriša iki 18 molių H_2O molekulių ir sudaro oktadekahidratus. Nors oktadekahidratų formavimasis yra mažai tikėtinas dėl mažo skylučių diametro, tačiau sulfatai gali turėti įtakos tribologijai bei ląstelių adhezijai. Nepaisant to, tikėtina jog Ti nanosluoksniai gali apsaugoti nuo neigiamo elektrolito ir druskų poveikio likusio anodinės dangos skylutėse.

Siekiant palyginti Ti/TiO_2 nanosluoksnių efektyvumą, buvo ištirtos IVB grupės pereinamųjų metalų sluoksnių, tarp jų Zr ir HfO_2, savybės. 15 nm

HfO_2 ir 16 nm Zr sluoksniai suformuoti atitinkamai ALD ir magnetronu ant anodinių dangų turėjo pakankamai panašią morfologiją į Ti ir jo oksidus. SEM tyrimai parodė, kad 1050 paviršiams būdinga kiek lygesnė struktūra, tuo tarpu 6082 paviršiuje stebimi įvairaus dydžio kristalitai (5 pav.).

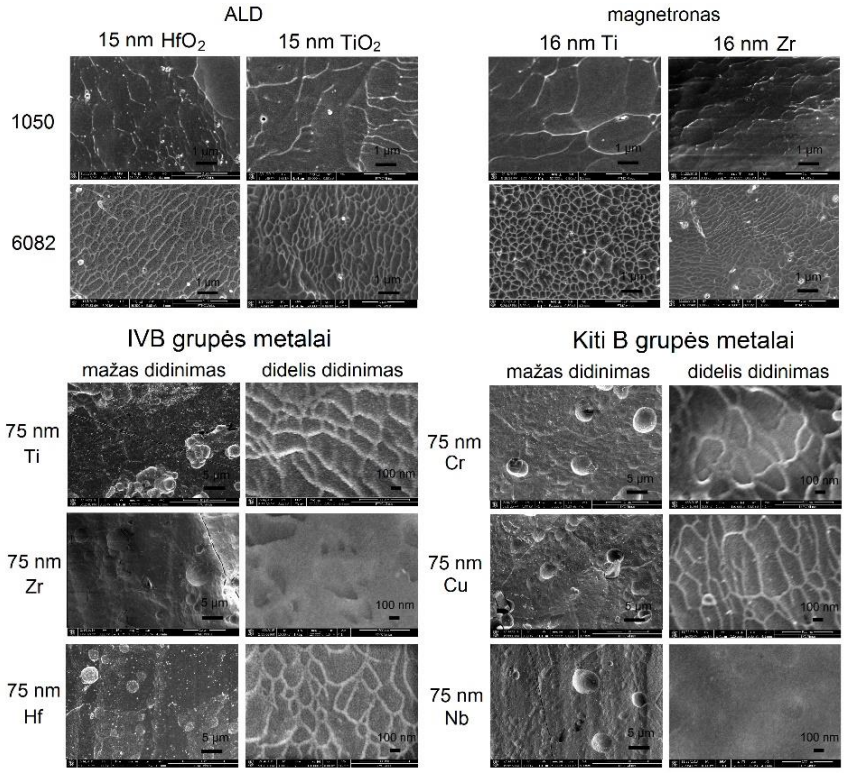

5 pav. *Sieros/oksalo r. elektrolite suformuotų anodinių dangų su metalų nanosluoksniais, nusodintais ALD arba magnetronu, SEM vaizdai*

Detalesni paviršių morfologiniai tyrimai buvo išnagrinėti naudojant IVB ir kitų B grupės (Cr, Cu, Nb) metalų 75 nm storio nanosluoksnius, suformuotus magnetronu. Nanostruktūrinių 6082 dangų paviršiuje buvo aptikta defektų bei įtrūkimų, o SEM nanotopografiniai tyrimai parodė, kad Zr ir Nb nanosluoksniams būdinga lygi struktūra.

Kiti nanosluoksniai turi netolygią struktūrą su aiškiai išsidėsčiusiais kristalitais, kaip ir Ti atveju. Visgi, užfiksuoti paviršių morfologiniai skirtumai nėra itin ryškūs ir šių skirtumų įtaka tiek tribologiniams, tiek biomedicininiams procesams yra daug mažesnė už cheminių dangų savybių poveikį.

3.2 Biologinės terpės ir nanostruktūrinių dangų sąveika

Nanostruktūrinių dangų inertiškumas, poringumas ir gana didelis šiurkštumas gali būti naudingi kuriant biosuderinamus paviršius. Ti/TiO_2 nanosluoksnių gebėjimas formuoti barjerinius sluoksnius gali turėti teigiamą įtaką ląstelių adhezijai ir proliferacijai, apsaugant nuo neigiamo priemaišų poveikio bei elektrolito komponentų, esančių anodinės dangos skylutėse.

Apžvalginiams tyrimams pasirinktos keturios adhezinio tipo ląstelės: žmogaus gimdos kaklelio vėžio Hep-2C ląstelių linija, pelės fibroblastų L929 ląstelių linija, kinų žiurkėno kiaušidžių vėžio CHO-K1 ląstelių linija ir žmogaus periodonto raiščio stromos PDLS ląstelių linija. Šios ląstelės yra lengvai prieinamos, paruošiamos bei pasižymi aukštu proliferacijos greičiu. Jungiamojo audinio L929 ir PDLS ląstelės pasižymi bipoline ir daugiapole morfologija, tuo tarpu epitelinėms Hep-2C ir CHO-K1 ląstelėms būdinga plokštesnė daugiapolė struktūra (6 pav.). Nustatyta, kad L929 ir PDLS ląstelės pasižymi didžiausiu proliferacijos greičiu ir gyvybingumu ant BT1 lydinio (96,32 % Ti). Atsižvelgus į rezultatų atsikartojamumą, detaliems tyrimams buvo naudojamos PDLS ląstelės, gaminančios tarpląstelinio užpildo komponentus (kolageną, glikoproteinus, kt.) ir atliekančios svarbų vaidmenį žaizdų gijime.

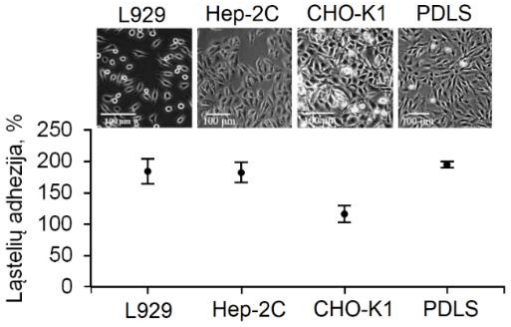

6 pav. *L929 [192], Hep-2C [193], CHO-K1 [194], PDLS [*195*] ląstelių morfologija ir jų adhezija ant Ti lydinio BT1*

Ištirtas anodinių dangų, suformuotų skirtinguose elektrolituose, poveikis biosuderinamumui ant 6082 lydinio. Nustatyta, kad anodavimas padidina PDLS ląstelių adheziją ir proliferaciją po 120 val. inkubacijos (7 pav.).

Visgi, ląstelių adhezija ir gyvybingumas yra kiek mažesnis ant H_3PO_4 elektrolite suformuotų anodinių dangų pirmosiomis auginimo dienomis galimai dėl plačių skylučių, siekiančių ~200 nm. Ankstesni tyrimai

patvirtina, kad didesniu skylučių tankiu pasižymintys paviršiai užtikrina geresnę ląstelių adheziją bei sąveiką su anodinėmis dangomis [5].

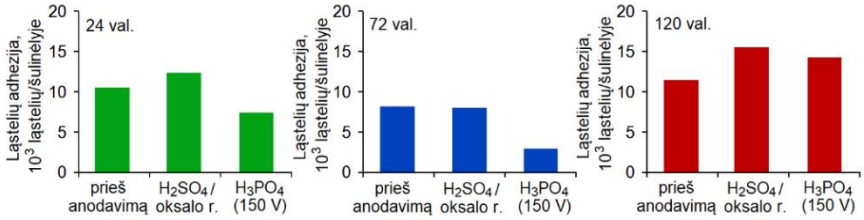

7 pav. *PDLS ląstelių adhezija ir proliferacija ant anoduotų ir neanoduotų 6082 lydinio paviršių po 24 val., 72 val. ir 120 val. inkubacijos*

Taip pat buvo ištirtas anodinių dangų, suformuotų kietojo anodavimo metodu, biosuderinamumas po TiO_2 ir Ti nanosluoksnių nusodinimo atitinkamai ALD ir magnetronu. Tyrimai parodė, kad 10 nm ir 15 nm TiO_2 nanosluoksniai 20 % slopino PDLS ląstelių adheziją ant anoduoto 6082 lydinio po 24 val. inkubacijos (8 pav.).

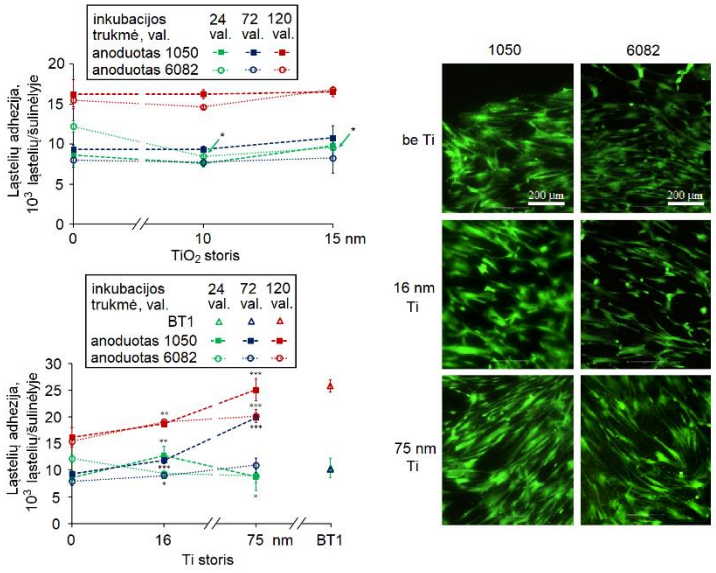

8 pav. *PDLS ląstelių adhezija ir proliferacija ant Ti BT1 bei kietojo anodavimo dangų su skirtingo storio Ti nanosluoksniais po 24 val., 72 val. ir 120 val. inkubacijos (kairėje). Ląstelių morfologija su skirtingo storio Ti nanosluoksniais po 48 val. inkubacijos (dešinėje). Viršuje: TiO_2 nanosluoksniai suformuoti ALD metodu. Apačioje: Ti nanosluoksniai suformuoti magnetronu ir Ti BT1 lydinys. Trijų tyrimų duomenys: ns - p> 0,05 (nereikšmingas), *p <0,05 (reikšmingas), ***p <0,001 (labai reikšmingas)*

Tačiau net po 120 val. inkubacijos nebuvo pasiekta ryškaus teigiamo efekto nei ant 1050, nei ant 6082 lydinių po paviršių nanostruktūrizavimo. Tikėtina, kad iš dalies sureagavęs TDMAT pirmtakas ar jo produktai likę anodinės dangos skylutėse galėjo slopinti PDLS ląstelių adheziją ir proliferaciją, ypač 6082 lydiniuose dėl platesnių skylučių.

Pradinės inkubacijos metu 16 nm ir 75 nm Ti nanosluoksniai suformuoti ant anoduoto 6082 lydinio magnetronu turėjo neigiamą poveikį PDLS ląstelėms ir slopino pradinę adheziją atitinkamai 23 % ir 26 %. Priešingai, anoduoti 1050 lydiniai su 16 nm Ti sluoksniu padidino ląstelių adheziją, tačiau nerodė teigiamo poveikio su 75 nm Ti po 24 val. inkubacijos. Kadangi Ti nanosluoksniai visiškai uždengia anodinių dangų skylutes, ląstelių sukibimas su paviršiumi gali būti dar labiau apsunkinamas ypač pradinės inkubacijos metu. Nepaisant to, nanostruktūrinės dangos ženkliai pagerino paviršių biosuderinamumą, ypatingai naudojant didesnio grynumo 1050 lydinius po 72 val. ir 120 val. inkubacijos. Didesnis Ti storis yra naudingas PDLS ląstelėms ir padidina ląstelių adheziją 15 % ir 55 %, naudojant atitinkamai 16 nm ir 75 nm Ti sluoksnius po 120 val. inkubacijos.

Mikroskopijos tyrimai atskleidė, kad PDLS ląstelės yra didesnės ir pasižymi plokštesne morfologija ant anoduoto 1050 lydinio lyginant su 6082, tačiau Ti nanosluoksniai neturi didelės reikšmės ląstelių morfologijai.

Apibendrinus, nanostruktūrinės dangos pasižymi geru biosuderinamumu su žmogaus PDLS ląstelėmis, tačiau būtina atsižvelgti į keletą faktorių: Al grynumą, Ti/TiO_2 sluoksnio storį, nusodinimo metodą. 10 nm ir 15 nm TiO_2 nanosluoksniai, suformuoti ALD metodu, neturėjo teigiamo poveikio ląstelių adhezijai. Visgi, panašaus storio 16 nm ir storesni 75 nm Ti nanosluoksniai reikšmingai pagerino PDLS ląstelių adheziją, ypač ant anoduotų 1050 lydinių. Mažesnio grynumo anoduoti 6082 lydiniai galėjo slopinti ląstelių adheziją dėl jame esančių Fe ir Mn priemaišų, turinčių neigiamą poveikį ląstelių gyvybingumui [198], nors ir pasižymi didesniu paviršiaus šiurkštumu nei 1050 (1,5 µm ir 0,85 µm). Didesniu šiurkštumu pasižymintys paviršiai yra naudingi ląstelių adhezijai, tačiau būtina atsižvelgti į lydinių grynumą, kadangi vyksta intensyvesnis metalo jonų išsilaisvinimas bei dilimo nuolaužų formavimasis trinties metu [62].

3.3 Tribologinės anodinių ir nanostruktūrinių dangų savybės

Kuriant įvairius gaminius svarbu atsižvelgti į tribologines paviršių savybes, ypač siekiant ilgaamžiškumo. Tribologinių tyrimų svarba naudojant 1–10 N apkrovas buvo nagrinėta ir biomedicininiuose gaminiuose, įskaitant

breketus [200, 201], dantų bei žandikaulio implantus [202]. 10 N apkrova pasirinkta tiriant anodines ir nanostruktūrines dangas. Dinaminė trintis, vykstanti tarp dviejų judančių paviršių ir statinė trintis, kuri apibūdinama kaip didžiausia pasipriešinimo (trinties) jėga, kurią reikia įveikti paviršių judėjimo pradžioje, buvo išnagrinėta detaliau. Statinės trinties nustatymas svarbus ne tik pramonėje, bet ir medicinoje, nes santykinis judėjimas tarp paviršių nėra nuolatinis ir dažnai vyksta su pertraukiamais judesiais. Trintis buvo tiriama, naudojant chemiškai inertiškus korundo (Al_2O_3) rutuliukus, siekiant išvengti šalutinių reakcijų trinties zonoje. Matavimams buvo naudojami tik šviežiai anoduoti Al lydiniai.

3.3.1 Ti ir jo oksidų nanosluoksnių poveikis trinčiai ir dilimui

Daugeliui gaminių reikalingas ilgas eksploatavimo laikas ir ilgaamžiškumas, todėl dilimo, įbrėžimų bei kitų pažeidimų turi būti išvengta, ypač biomedicininiuose pritaikymuose. Anodinių dangų su 75 nm Ti sluoksniu dilimo tyrimai buvo įvertinti SEM. Po 10 trinties ciklų trinties zonos paliktas pėdsakas buvo vos matomas, tačiau išilgai judėjimo krypčiai buvo stebimi įtrūkimai ant anoduoto 1050 lydinio (9 pav.)

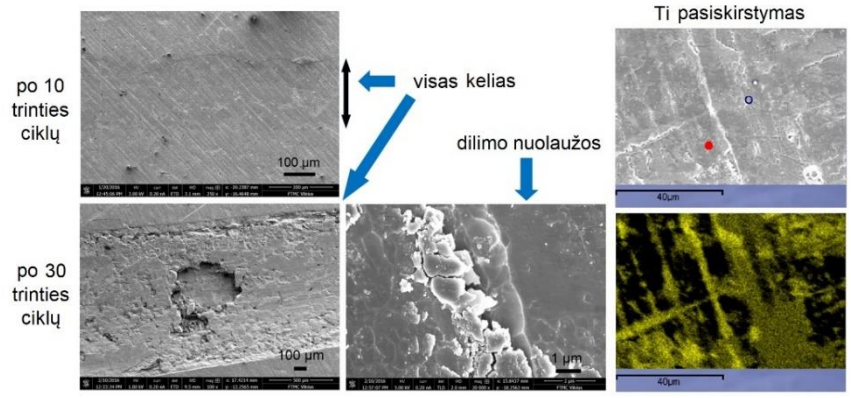

9 pav. *Kietojo anodavimo dangų su 75 nm Ti nanosluoksniu, suformuotų ant 1050 lydinio, SEM vaizdai po 10 ir 30 trinties ciklų (kairėje) ir Ti elementinis pasiskirstymas (dešinėje) esant 10 N apkrovai. Užpildyti ir tušti apskritimai atitinka Ti kiekį 0,77 masės% ir 8,73 masės%, pritaikyta pagal [150]*

Suformuoto trinties zonos pėdsako po 10 ciklų dar negalima traktuoti kaip dilimo žymės. Pagal kontaktinės mechanikos teoriją, elastiškuose kūnuose dėl apkrovos atsiranda deformacijos. Šio tribotesto atveju labiausiai tinka sferos/pusplokštumės deformacijos teorija, nurodanti jog indentacijos skersmenį apsprendžia sąveikaujančių kūnų geometrija, kietumas ir

elastiškumas. Tačiau pastarieji du parametrai anodinėms dangoms nebuvo nustatyti. Todėl neįmanoma įvertinti, ar užfiksuotas trinties zonos pėdsakas didesnis už Herco elastinę indentaciją, kas įrodytų, jog dilimas jau buvo prasidėjęs.

Nanostruktūrinės dangos ant 1050 lydinio nepasižymėjo dideliu atsparumu dilimui. Jau po 30 ciklų buvo užfiksuotas aiškiai matomas dilimo griovelis, o dalis anodinės dangos, kurios storis siekė apie 60 μm, buvo atskilusi, atsirandant giliai duobei centrinėje dalyje. Priešingai, ant 6082 lydinio įtrūkimų nebuvo pastebėta nei po 10, nei po 30 trinties ciklų. Įvairaus dydžio dilimo nuolaužos stebimos griovelio centre ir kraštuose, kur tarpfazinis slėgis yra didžiausias. Nustatyta, kad esant 10 N apkrovai tarpfazinis slėgis viršija 150 MPa, kai kontaktinės zonos diametras yra mažesnis negu 0,4 mm. Tai būdinga daugumai trinties testų, ypač pradinėse stadijose. Jeigu aukštas tarpfazinis slėgis nėra kompensuojamas palankios paviršiaus topografijos ir triboplėvelės poveikiu, jis palaipsniui suardo ne tik Ti sluoksnius, bet ir pažeidžia anodinę dangą.

Ti elementinis pasiskirstymas parodė, kad po 30 trinties ciklų Ti kiekis skiriasi daugiau nei 10 kartų skirtingose trinties zonose. Ti koncentracijos gradientas varijuoja nuo 0,77 masės% iki 8,73 masės%. Tai rodo, kad gali vykti kvazi-skysto Ti pernešimas [162, 217, 218] iš vienos trinties zonos į kitą, užtikrinant žemą paviršių trintį ir dilimą pradiniuose trinties cikluose, tačiau prarandant gebėjimą priešintis aukštiems tarpfaziniams slėgiams trinčiai tęsiantis.

Visų pirma buvo įvertintos anodinių dangų trinties savybės. Pastebėta, kad kietasis anodavimas H_2SO_4/oksalo r. elektrolite ženkliai sumažino paviršių statinės trinties koeficientą nuo ~1,0 iki ~0,4, ypač naudojant 6082 lydinius (10 pav.).

Anodavimo trukmė nuo 30 min. iki 70 min. neturėjo didelės reikšmės statinei trinčiai. Anodinės dangos, suformuotos H_3PO_4 elektrolite, pasižymėjo aukštu trinties koeficientu, kuris siekė 0,7. Nors fosfatai dažnai naudojami dangose ir tepaluose kaip dilimą slopinantys priedai, tačiau paviršių morfologija ir mechaninės savybės atlieka svarbesnį vaidmenį sausosios trinties sąlygomis. Dinaminės trinties koeficientas taip pat buvo aukštesnis ir viršijo 1,2 po anodavimo H_3PO_4 elektrolite. Nepaisant teigiamo anodavimo poveikio statinės trinties mažinimui, anodinių dangų dilimas buvo aiškiai matomas, stebint paviršių abraziją ir nuolaužų susidarymą jau po 100 trinties ciklų prie 1 N apkrovos. Atsižvelgus į aukštą H_3PO_4 elektrolite suformuotų anodinių dangų trintį, daugiausia dėmesio buvo skiriama anodinėms dangoms, gautoms kietojo anodavimo metu.

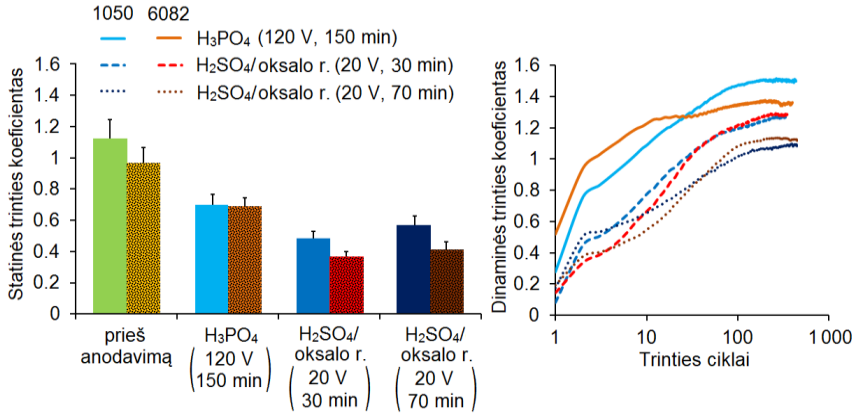

10 pav. *Sieros/oksalo r. (30–70 min. prie 20 V) ir fosforo r. (150 min. prie 120 V) elektrolituose suformuotų anodinių dangų poveikis statinei (kairėje) ir dinaminei (dešinėje) trinčiai, esant 1 N apkrovai (stulpelinės diagramos kairėje – 1050, dešinėje – 6082), pritaikyta pagal [151]*

Anodinių dangų apsaugai nuo trinties ir dilimo buvo išbandyti keleto metalų ir jų oksidų sluoksniai, tikintis barjerinio, metalą išsluoksniuojančio, servovitinio [203] ar kitų literatūroje aprašytų tribologinių efektų. Tuo labiausiai išsiskyrė Ti/TiO_2 nanosluoksniai, ypač įvertinus jų sluoksnio storio poveikį dangų trinčiai. ALD metodu buvo suformuoti 5–15 nm TiO_2 nanosluoksniai, o Ti sluoksnių storis varijavo nuo 16 nm iki 2,3 µm, suformavimui naudojant magnetroną (11 pav.).

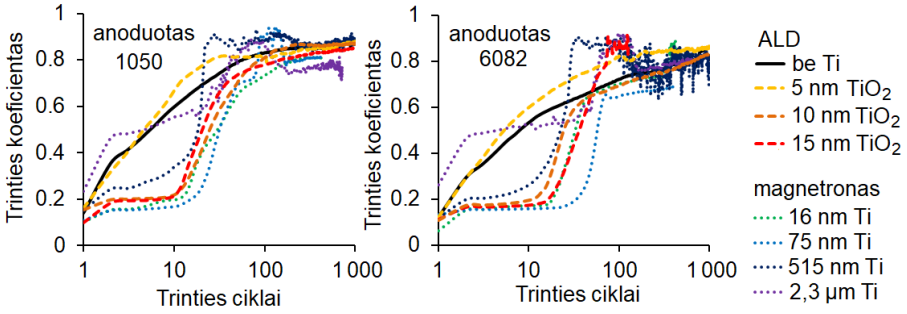

11 pav. *Ti sluoksnio storio poveikis anodinių dangų, suformuotų sieros/oksalo r. elektrolite, dinaminei trinčiai esant 10N apkrovai ant 1050 (kairėje) ir 6082 (dešinėje) lydinių, pritaikyta pagal [150]*

Nepriklausomai nuo nusodinimo metodo 10–75 nm ir galbūt kiek storesni Ti/TiO_2 nanosluoksniai užtikrina žemą anodinių dangų trintį ir sumažina trinties koeficientą žemiau 0,2. Efektyviausiai trintį slopina 75 nm Ti

nanosluoksniai, kurie išsilaiko nuo 20 iki 60 trinties ciklų atitinkamai ant 1050 ir 6082 lydinių. Priešingai, ploni 5 nm TiO_2 ir stori 2,3 µm Ti sluoksniai nėra efektyvūs tribologiškai ir pasižymi aukšta trintimi, panašia į anodines dangas be Ti sluoksnio. 515 nm Ti sluoksniai turėjo teigiamą poveikį trinčiai, tačiau ne tokį ryškų lyginant su 75 nm nanosluoksniais, be to, jie neišlaikė savo vientisumo ir jų atsparumas buvo daug prastesnis trinčiai tęsiantis. Tuo tarpu 10–75 nm Ti/TiO_2 nanosluoksniai sumažino statinę trintį ir išlaikė bent 10 trinties ciklų, esant žemesniam nei 0,2 trinties koeficientui (12 pav.).

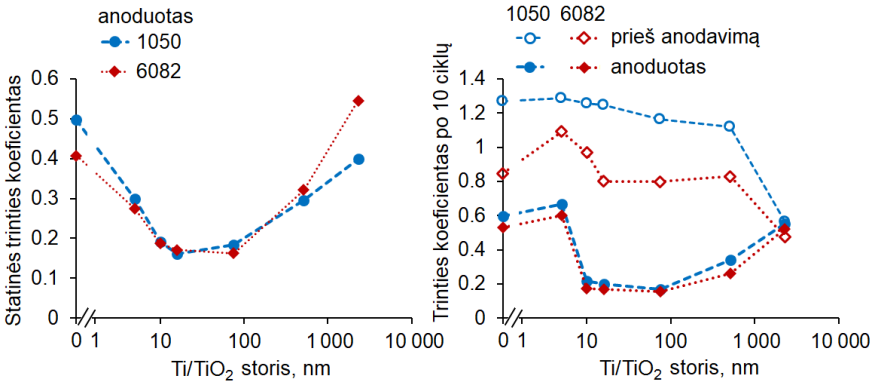

12 pav. *Ti sluoksnio storio poveikis anodinių dangų, suformuotų sieros/oksalo r. elektrolite, statinei trinčiai bei trinties koef. po 10 ciklų esant 10 N apkrovai, pritaikyta pagal [150, 151]*

Kaip ir dinaminės trinties metu, plonesnių arba storesnių Ti/TiO_2 sluoksnių efektyvumas mažinant statinę trintį buvo prastesnis. Tokia elgsena neatitinka metalo išsodinimo hipotezės, nes tiek magnetroniniai nanosluoksniai, tiek ALD nanosluoksniai demonstruoja beveik vienodas tendencijas. Tai neatitinka ir barjerinio sluoksnio hipotezės, nes storesni sluoksniai didina trintį. Servovitiniai efektai su Ti dar nebuvo aprašyti ir dėl jo kietumo yra mažai tikėtini. Todėl buvo siekiama įvertinti sąsają su kitų metalų oksidais.

3.3.2 IVB grupės elementų bei kitų pereinamųjų metalų nanosluoksnių tribologinės savybės

Ištirtos IVB grupės elementų, tarp jų Ti, Zr ir Hf, nanosluoksnių tribologinės savybės. ZrO_2 keramika dėl biosuderinamumo ir mechaninių savybių plačiai naudojama medicinoje, pavyzdžiui, dantų implantams [221, 222], tuo tarpu Hf taip pat parodė teigiamą poveikį biomedicininiuose

gaminiuose [223, 224]. IVB grupės metalų nanosluoksniai daugumoje atvejų sumažino statinės trinties koeficientą žemiau 0,2, tačiau dinaminė trintis buvo kiek prastesnė lyginant su Ti/TiO_2 nanosluoksniais (2 lentelė ir 13 pav.).

2 lentelė. *IVB grupės metalų nanosluoksnių poveikis statinei trinčiai, ant anoduotų lydinių, esant 10 N apkrovai*

Statinis COF	Be sluoksnio	15 nm HfO_2	15 nm TiO_2	16 nm Hf	16 nm Zr	16 nm Ti
1050	0,50±0,03	0,16±0,02	0,18±0,01	0,26±0,01	0,17±0,01	0,16±0,01
6082	0,41±0,05	0,16±0,03	0,19±0,01	0,24±0,02	0,17±0,01	0,17±0,02

Skirtingai negu HfO_2 po ALD nusodinimo, Hf nanosluoksniai suformuoti magnetronu padidino trintį ir dilimą jau pirmųjų ciklų metu. Taip pat Hf nanosluoksnių trintis buvo daug didesnė nei kitų dviejų IVB elementų Ti ir Zr atveju. Aukštą trintį galėjo lemti nepilna Hf oksidacija. Be to, HfO_2 yra tankesnis negu ZrO_2 ar TiO_2, jų tankiai atitinkamai sudaro 9,68 g/cm^3, 5,68 g/cm^3 ir 3,78–4,23 g/cm^3 ir galimai veikia kaip abrazyvas bei sąlygoja minkštesnių poringų anodinių dangų irimą.

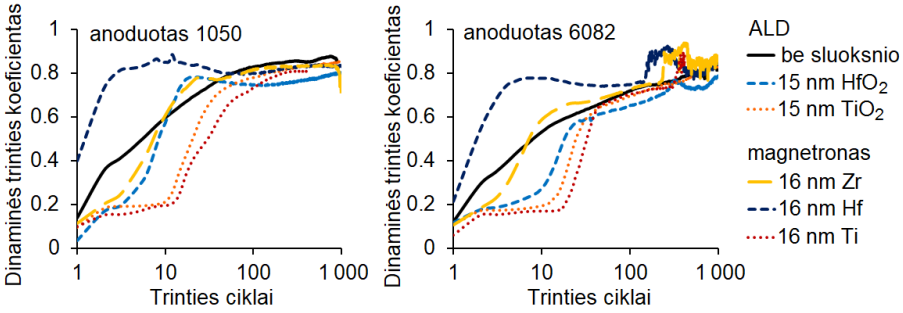

13 pav. *IVB grupės metalų nanosluoksnių poveikis dinaminei trinčiai ant anoduotų lydinių, esant 10 N apkrovai*

Ištirtos kitų B grupės pereinamųjų metalų (Cr, Cu, Nb) nanosluoksnių tribologinės savybės. Nors elektrocheminės Cr dangos gali turėti teigiamą poveikį trinčiai ir dilimui ant plieno [96, 228], tačiau magnetronu suformuoti 75 nm Cr ir Hf nanosluoksniai skatino spartų anodinių dangų irimą prie 10 N apkrovos (14 pav.).

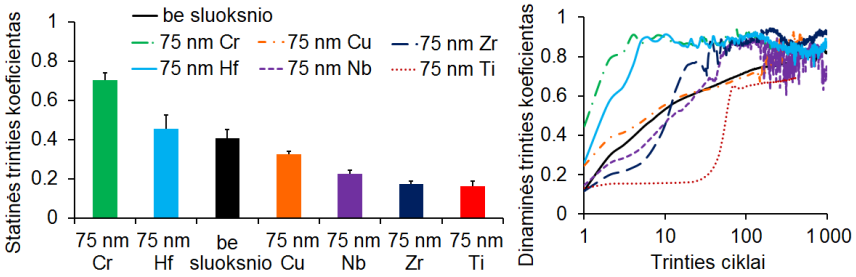

14 pav. *75 nm storio sluoksnių poveikis statinei (kairėje) ir dinaminei (dešinėje) trinčiai ant sieros/oksalo r. elektrolite anoduoto 6082 lydinio, esant 10 N apkrovai*

Servovitinius sluoksnius galintis formuoti varis ant plieno ir bronzos kartais ženkliai slopina paviršių dilimą, veikiant selektyvios pernašos mechanizmui [203, 204, 229]. Visgi, nei Cu, nei Nb nanosluoksniai nerodė ženklaus teigiamo poveikio trinčiai, nors statinis trinties koeficientas buvo mažesnis lyginant su anodinėmis dangomis be nanostruktūrinio sluoksnio. Geriausiomis tribologinėmis savybėmis pasižymėjo IVB grupės elementai – Zr ir Ti. Jų neįtikėtinai ženklaus tribologinio efektyvumo priežasčių visgi nepavyko išsiaiškinti nors galima spėti, kad trinties metu Ti/TiO_2 įgauna kvazi-skysčio savybių ir yra pernešamas iš vienos trinties zonos vietos į kitą taip sąlygodamas žemą paviršių trintį [162, 217]. Techniniams, biomedicininiams ir kitiems anodinių dangų pritaikymams gali būti plačiai panaudotos šio tyrimo išvados, jog nanosluoksniai sumažina statinę trintį žemiau 0,2, o Ti atveju stebimas ir dinaminės trinties sumažėjimas pradiniuose sausosios trinties cikluose.

3.4 Organinių junginių migracija anodinėse dangose

Tepalai, dažai, antikoroziniai užpildai ir kitos funkcinės medžiagos dažnai naudojamos pagerinti įvairias poringų dangų savybes. Todėl yra svarbu stebėti jų migraciją į dangos gylį siekiant sumažinti paviršių trintį bei dilimą, paskirstant jėgas, mažinant šilumos susidarymą, nuolaužų formavimąsi trinties metu ir užtikrinant kitų procesų kontrolę. Organinių junginių migracija į dangos skylutes svarbi ir biologinėse sistemose, kai dangos kontaktuoja su organizmo skysčiais, todėl trintis vyksta ne sausosiomis, o tepamosiomis sąlygomis. Kitos grupės [230] tyrė pentadekano parafininės alyvos trintį ant anodinių dangų suformuotų oksalo r. elektrolite, kurių dangos storis siekė 60 µm, o skylučių ID 45 nm. Visgi, ženkli anodinių dangų trintis ir didelis plieno rutuliuko nusidėvėjimas buvo užfiksuotas jau po 15 trinties ciklų prie 0,5 N apkrovos. Tai rodo, kad

tradiciniai tepalai pasižymi prastomis tepamosiomis savybėmis ant anoduoto Al. Be to, tribologinės sąlygos gali palengvinti oksalatų skilimą ir CO_2 išsiskyrimą trinties zonoje bei pagreitinti dėvėjimąsi. Užpildų migracija yra reikšminga trinties slopinimui, todėl svarbiausių biologinių junginių ir tribologiškai efektyvių užpildų migracija į anodinės dangos skylutes buvo išnagrinėta detaliau.

3.4.1 Hidrofobinių medžiagų migracija į anodinės dangos skylutes

Organinių junginių migracijos tyrimams buvo sukurta Ramano spektroskopija pagrįstas metodas, panaudojant 70 µm storio visiškai anoduotą Al foliją, kurios vidutinis skylučių diametras sudaro ~13 nm po anodavimo H_2SO_4/oksalo r. elektrolite esant 15 °C (15 pav.).

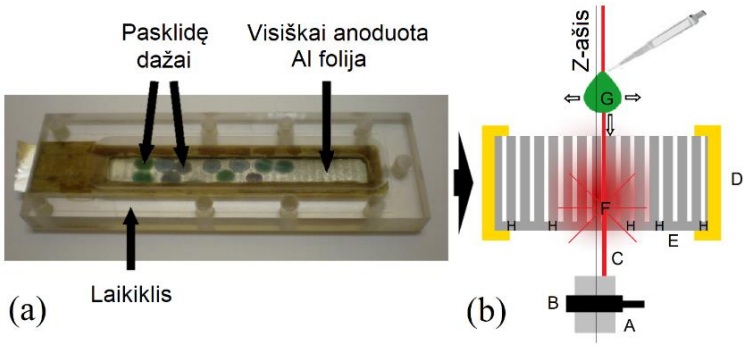

15 pav. *Visiškai anoduota Al folija po organinių junginių užlašinimo (a) ir Ramano spektroskopijos matavimų tyrimo schema (b): A = optinis kabelis 7 mm darbiniam atstumui; B = laikiklis Z-ašies reguliavimui; C = 785 nm bangos ilgio lazerio spindulys; D = bandinio laikiklis; E = 70 µm storio visiškai anoduota Al folija; F = apytikslė lazerio spindulio fokusavimo padėtis; G = bandinio lašas ir jo sklidimo kryptys; H = anodinės dangos barjerinis sluoksnis (~10–20 nm). Neatitinka mastelio, pritaikyta pagal [152]*

Anodinės dangos ant Al lydinių substratų negalėjo būti tiriamos dėl fotoliuminescencijos trukdžių. Jie smarkiai sumažėjo anoduotoje Al folijoje, todėl buvo galima fiksuoti migruojančių junginių Ramano atsakus. Metodikos kūrimas detaliai aprašytas [152].

Toliau tobulinant metodiką, buvo tiriami riebalų rūgščių metilo esteriai. Jie sudaryti iš metiloleato, kuris yra gausiausias komponentas (apie 60 %), metillinoleato, metilpalmitato ir kitų esterių bei pasižymi dilimą slopinančiomis savybėmis tiek ant plieno, tiek ant anoduoto Al. Jų gebėjimas mažinti trintį buvo daug efektyvesnis lyginant su riebalų r. [240]. Šie esteriai

toliau vadinami metiloleatu. Intensyvesnė tepamųjų medžiagų migracija į anodinės dangos skylutes gali užtikrinti efektyvesnes tribologines savybes [140].

Tyrimų metu buvo įvertintas Ramano spinduliuotės intensyvumas prieš ir po metiloleato užlašinimo ant visiškai anoduotuos Al folijos 0–54 µm gylyje naudojant du skirtingus objektyvo darbinius atstumus lazeriniam sužadinimui (16 pav.).

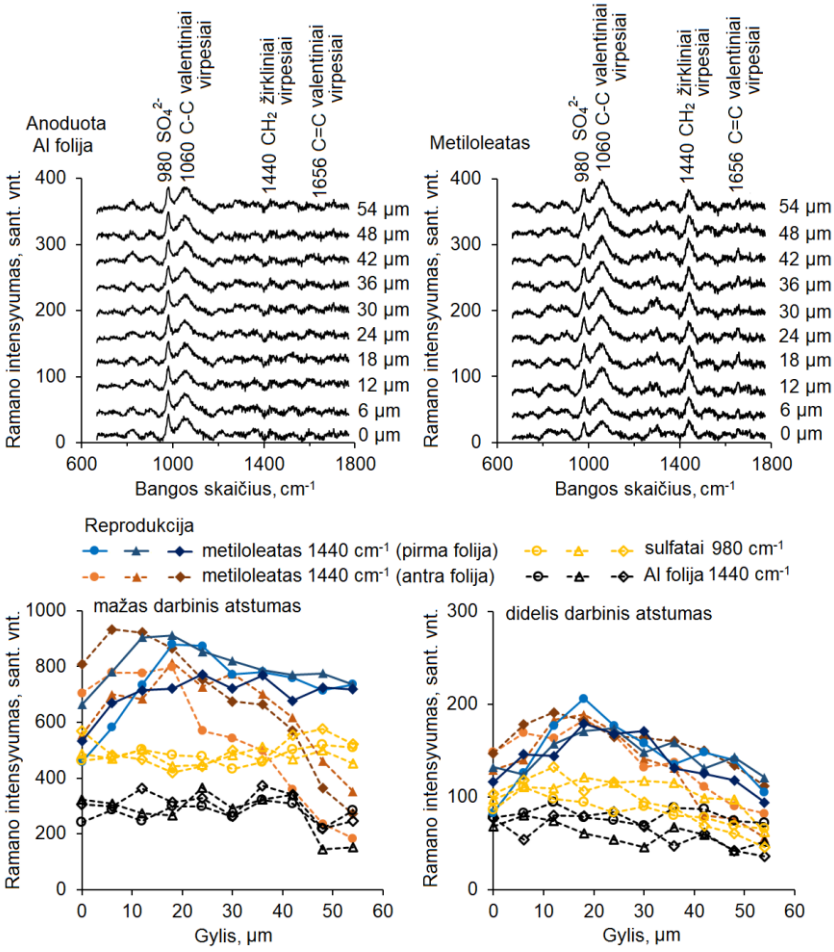

16 pav. *Ramano spektrai prieš ir po metiloleato užlašinimo ant anoduotuos Al folijos (viršuje) ir metiloleato įsiskverbimo gylis, esant mažam ir dideliam darbiniams atstumams (apačioje)*

Anoduotos Al folijos Ramano spektre stebimos intensyvios 980 cm^{-1} ir 1060 cm^{-1} smailės, kurios atitinka SO_4^{2-} grupes ir C-C valentinius virpesius

dėl anodinės dangos skylutėse esančių sulfatų ir oksalatų. Praėjus 1 valandai po metiloleato užlašinimo buvo stebima aukšto intensyvumo CH_2 grupės žirklinių virpesių moda prie 1440 cm^{-1} ir žemo intensyvumo C=C valentinių virpesių moda prie 1656 cm^{-1}, kurios susijusios su mononesočiosios oleato anglies grandinės vibracijomis. Tuo tarpu anoduotos Al folijos be metiloleato smailių intensyvumai prie 1440 cm^{-1} ir 1656 cm^{-1} sutampa su fono signalu.

Metiloleato migracijos tyrimams buvo apskaičiuotas smailės plotas prie 1440 cm^{-1}, atitinkantis CH_2 grupės virpesių modą. Didžiausias virpesių intensyvumas buvo užfiksuotas 10–20 μm gylyje, kuris patenkinamai atsikartojo naudojant abu darbinius atstumus lazeriniam sužadinimui. Tai rodo, kad metiloleatas linkęs migruoti į anodinės dangos skylučių vidų, o ne likti jų išorėje prie paviršiaus. Anoduotos folijos smailių intensyvumas prie 980 cm^{-1} ir 1440 cm^{-1} buvo pakankamai stabilus visame dangos gylyje. Priklausomai nuo lazerio darbinio atstumo kinta išmatuotos intensyvumo vertės, tačiau metiloteato įsiskverbimo maksimumas išlieka ties 10–20 μm. Esant mažam darbiniam atstumui yra generuojamas stipresnis Ramano signalas, todėl galima užfiksuoti skirtumus tarp anoduotų Al folijų. 50–60 μm anodinės dangos gylyje stebimas ženklus Ramano intensyvumo kritimas, greičiausiai dėl ženkliai sumažėjusio metiloleato kiekio. Iš dalies signalo silpnėjimą galėjo lemti ir mažėjantis skylučių vientisumas, didėjantis hidratų kiekis ir prastėjanti signalo detekcija iš gilesnės anodinės dangos zonos.

Gauti rezultatai gerai koreliuoja su metiloleate ištirpinto fluoroforo rodamino B migracijos tyrimais naudojant fluorescencinę konfokalinę mikroskopiją. Jų įsiskverbimo gylis po impregnavimo į anodinę dangą siekė ~15 μm [140], tačiau buvo nustatoma tik fluoroforo koncentracija. Tuo tarpu Ramano spektroskopija fiksuoja patį metiloleatą. Tiek metiloleato matavimai anoduotoje Al folijoje, tiek fluoroforo matavimai anodinėje dangoje nustatė panašius koncentracijų pasiskirstymus. Tai patvirtina ir abiejų metodų tinkamumą, ir metiloleato migracijos tendencijas anodinės dangos skylutėse.

3.4.2 Hidrofilinių dažų migracija į anodinės dangos skylutes

Naujai sukurta metodika taip pat buvo naudojama siekiant įvertinti hidrofilinių junginių migraciją į anodinės dangos skylutes. Tam buvo pasirinkti komerciniai chromo kompleksiniai anijoniniai azo dažai (juodi ir žali), kurie yra paplitę pramonėje, nes suteikia sodrias spalvas ir maskuoja po anodavimo susidariusių pilkų atspalvių netolygumus.

Tiksli šių komercinių azo dažų sudėtis nėra žinoma, tačiau spektroskopiniais tyrimais [244] buvo nustatyta, kad dažų molekulėse dominuoja Cr organometalinių jungčių ir aromatinių žiedų virpesiai. Junginiai greičiausiai turi įvairių pakaitų: halogenų, anijoninių funkcinių grupių, alkilo grupių bei kitų hidrofilinių ar hidrofobinių grandinių, kurie nulemia dažo spalvą, adsorbciją, stabilumą, vilgumą bei kitas savybes. Pačios intensyviausios 1285 cm^{-1} (juodas dažas) ir 1264 cm^{-1} (žalias dažas) Ramano vibracinės modos buvo atitinkamai priskirtos endociklinei arba egzociklinei C-N jungtims [243]. Ramano spektuose vyrauja aromatinių žiedų vibracinės modos, turinčios mažiausiai 2–3 (žalias dažas) ir daugiau (juodas dažas) pakaitų. Mažo intensyvumo juostos prie 408 cm^{-1} ir 423 cm^{-1} būdingos Cr-O bei aromatinių žiedų vibracijoms. FTIR spektrometrija atskleidė, kad dažų molekulėms būdingi aromatinių žiedų virpesiai iš jų diazenil N=N funkcinė grupė prie 1541 cm^{-1}, deformacinių virpesių C-N grupė prie 1271 cm^{-1}, C-O grupės virpesiai prie 1120 cm^{-1} bei sulfo funkcinių grupių virpesiai prie 1026 cm^{-1}. XPS rezultatai taip pat patvirtino sulfonatų R-SO_3^- (sulfonrūgščių druskų ir esterių, 168,2 eV) bei dvigubai mažesnę sulfato SO_4^{2-} (169,4 eV) funkcinių grupių koncentraciją azo dažų struktūroje. Taip pat užfiksuotos Cr, kurio oksidacijos laipsnis yra +3 (576,4 eV), organometalinės jungtys. Tridentatiniai ligandai sudaro kompleksus su Cr (III) esant 1: 2 metalo ir ligando santykiui, kai laisvoms elektronų poroms tenka du deguonies atomai ir vienas diazo grupės azoto atomas [247, 248].

Azo dažų migracija buvo įvertinta nukreipus lazerio spindulį į Al folijas, anoduotas esant 15 °C ir 30 °C. Lazerio spindulys buvo sufokusuotas į anoduotos Al folijos centrinę dalį pagal fotoliuminescencijos maksimumą, nors tiksli sufokusuotos zonos padėtis 70 μm storio anoduotoje folijoje nėra žinoma. Skirtingai nuo azodažų tyrimų, metiloleato atveju buvo fiksuojamas Ramano intensyvumas praėjus 1 val. po bandinio užlašinimo. Keičiant lazerio fokusavimo atstumą buvo užrašyti Ramano spektrai įvairiuose folijos gyliuose.

Remiantis intensyviausiais virpesiais nustatyta, kad abu azo dažai pasiekia didžiausią intensyvumą praėjus 25 min. po bandinio užlašinimo ant anoduotos folijos (17 pav.), nors žaliam dažui būdingas staigesnis intensyvumo didėjimas ir vėlavimo laikotarpis pradžioje. Tai rodo, kad pradinė azo dažų migracija buvo netolygi ir žalias dažas pradžioje migravo šiek tiek lėčiau nei juodas, tačiau vėliau susilygino ir abu dažai po 25 min. pasiekė vienodą įsiskverbimo gylį. Be to, dažymo metu žalias dažas buvo labiau pasklidęs ir iš dalies išplautas iš anoduoto Al skylučių. Azo dažai migruoja veikiant kapiliarinėms jėgoms, difuziniams, adsorbciniams,

koloidiniams ir kitiems efektams. Lyginant dažų migracijos tyrimus su metiloleatu tikėtina, kad dažai skverbiasi į anoduotos Al folijos skylutes greičiau nei metiloleatas. Pagal Ramano intensyvumą metiloleato įsiskverbimo gylis siekė 10–20 μm praėjus 1 val. po jo užlašinimo, o azo dažų intensyvumo maksimumas užfiksuotas jau po 25 min. greičiausiai didesniame nei10 μm gylyje. Be to, hidrofilinėmis savybėmis pasižyminčios dažų molekulės gali lengviau sąveikauti su hidratais, likusiais anoduotoje folijoje.

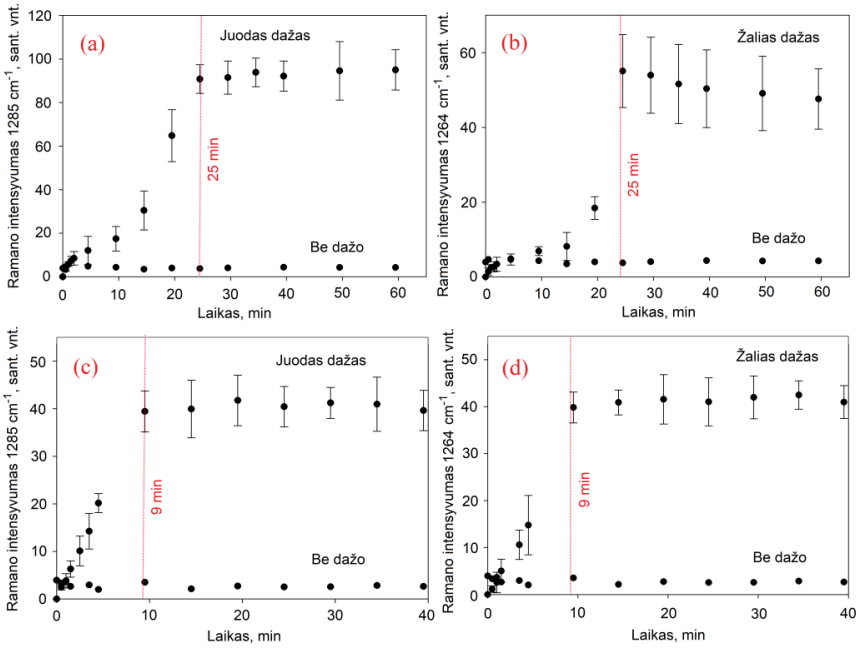

17 pav. *Dažų migracijos tendencijos į anoduotą Al foliją pagal Ramano spektrų intensyvumą: juodas (a) ir žalias (b) dažai po anodavimo prie 15 °C temperatūros; juodas (c) ir žalias (d) dažai po anodavimo prie 30 °C temperatūros, pritaikyta pagal [152]*

Po 25 min. užfiksuotas intensyviausios smailės poslinkis, kuris sudaro nuo 1285 cm^{-1} iki 1282 cm^{-1} juodam dažui bei nuo 1265 cm^{-1} iki 1263.6 cm^{-1} žaliam dažui. Atsižvelgus į dažnio poslinkį juodo dažo molekulės daug stipriau sąveikauja su anodine Al_2O_3 danga. Taip pat pastebėta, kad žalio dažo intensyvumas šiek tiek mažėja, nors tai ir nėra statistiškai patikima. Intensyvumo mažėjimas gali būti susijęs su dažo degradacijos procesais ar jo sąveika su elektrolito komponentais anoduotoje folijoje. Taip pat palygintos migracijos tendencijos labiau poringoje anoduotoje folijoje, kuri buvo

suformuota elektrolito temperatūrą padidinus nuo 15 °C iki 30 °C. Paviršiaus poringumas atitinkamai padidėjo nuo 7.8% iki 18.0%, o dažų migracija paspartėjo 2,8 karto. Poringoje anoduotoje Al folijoje abiejų dažų migracijos tendencijos skyrėsi mažiau.

3.4.3 Sąveika su elektrolito komponentais

Tiriant impregnavimą anodinėse dangose ant substratų, svarbu atsižvelgti ne tik į užpildų sąveiką ir su elektrolito komponentais. Azo dažų ir anoduotos folijos sąveikai likutinis elektrolitas faktiškai neturėjo poveikio, nes po anodavimo jo folijoje beveik neliko. Tačiau sulfonatai bei kitos anijoninės funkcinės grupės (-Cl, -COOH, kt.), esančios azo dažo molekulėse gali sąveikauti su Al katijonais hidroksidų formoje. Taip pat impregnuotos molekulės gali turėti amonio, azo ir kitų katijoninių funkcinių grupių. Chromo kompleksinių anijoninių azo dažų molekulės, kurių dydis gali siekti iki 3 nm, lengvai migruoja į anodinės dangos skylutes. Vykstant elektrostatinei sąveikai tarp priešingai įkrautų jonų dažo molekulės gali formuoti joninius ryšius anodinės dangos skylutėse. Sulfatai esantys anodinės dangos skylutėse, nes S koncentracija siekia ~4 %, gali formuoti kompleksinius junginius, muilus ar kitus darinius ir blokuoti dažų migraciją. Be to, elektrolito komponentai ir jo rūgštinė terpė, UV poveikis, biologinis užterštumas bei kiti faktoriai gali turėti įtakos dažo stabilumui ir cheminei degradacijai. Azo dažų atveju šie procesai nebuvo detaliai tiriami, nes nėra žinoma jų cheminė sudėtis.

Daug detaliau buvo įvertinta hidrofobinių tepamųjų medžiagų sąveika su anodine danga. Amfifilinės riebalų r. molekulės, turinčios hidrofobinę alifatinę uodegėlę ir hidrofilinę (polinę) karboksi grupės galvutę, gali sudaryti ir cheminį ryšį su anodine danga. Vykstant riebalų r. deprotonizacijai karboksigrupės adsorbuojasi ant anodinės dangos paviršiaus susidarant koordinacinei sąveikai, kuri gali būti monodentatinė, bidentatinė arba chelatinė [252] (18 pav.).

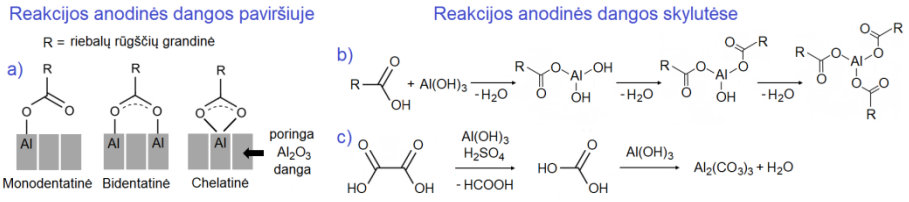

18 pav. *Galimos riebalų rūgščių reakcijos anodinės dangos paviršiuje (a) bei skylutėse (b, c remiantis [257])*

Chemisorbcija, kuri gali būti simetrinė (sąveika per du deguonies atomus) arba asimetrinė (sąveika per vieną deguonies atomą), turi daug didesnę rišančiąją energiją nei fizisorbcija. Formuojant daugiasluoksnes plėveles, pirmas sluoksnis sudaro chemisorbcinę sąveiką, o kitiems sluoksniams būdinga fizisorbcinė sąveika, veikiant silpnesnėms tarpmolekulinėms jėgoms, pavyzdžiui, Van der Valso. Taip pat svarbu atsižvelgti į dangų rūgštines-bazines savybes, ryšio stiprumą ir geometriją, adsorbcinių vietų skaičių bei kitus faktorius, kurie gali nulemti hidrofobinių medžiagų migraciją.

Kadangi anodinės dangos skylutės turi hidroksidų, tikėtina, kad riebalų r. gali sąveikauti su $Al(OH)_3$ ir saponifikacijos metu formuoti Al muilus, pavyzdžiui, Al stearatus ar Al oleatus. Šios medžiagos įeina į tepalų, tirštiklių ir apsauginių sluoksnių sudėtį, nes pasižymi antioksidacinėmis savybėmis bei gebėjimu mažinti trintį ir dilimą [255]. Sąveikos metu gali susidaryti mono-, di- arba tri-funkciniai Al muilai. Nors pastarieji muilai yra stabiliausi, tačiau jų formavimasis skylutėse yra sunkiai tikėtinas, nes reikalingas daug ilgesnis reakcijos laikas ar katalizatorių panaudojimas.

Elektrolito komponentai, esantys anodinės dangos skylutėse, gali ženkliai daryti įtaką ne tik riebalų r., bet ir kitų tepamųjų medžiagų migracijai ir tribologinėms savybėms. Oksalo r. gali skilti į skruzdžių (metano) r. ir anglies r., susidarant tarpiniam dihidroksikarbeno junginiui [257]. Šių mokslininkų teigimu, reakcija vyksta katalizuojant H_2SO_4 ir $Al(OH)_3$ vandens aplinkoje. Anglies r. taip pat gali sąveikauti su $Al(OH)_3$ bei formuoti karboksilo druskas, tačiau šių karbonatų susidarymas anodinės dangos skylutėse dar nėra pilnai įrodytas.

Esteriai, pavyzdžiui, metiloleatas, nėra labai stabilūs vandens aplinkoje, todėl dalis molekulių rūgštinėje terpėje hidrolizuojasi į riebalų r. ir alkoholį. Hidrolizės reakciją katalizuoja tiek rūgštys, tiek ir bazės (19 pav.).

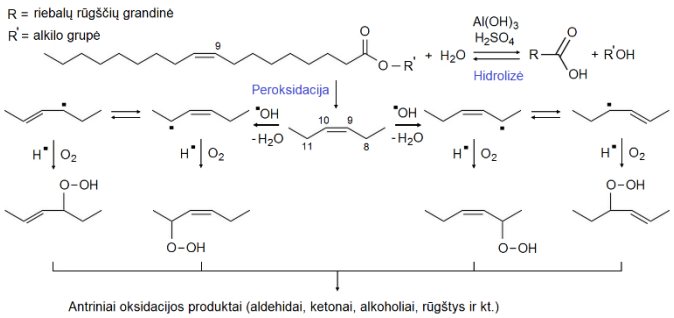

19 pav. *Į anodinę dangą impregnuojamų esterių hidrolizės ir peroksidacijos reakcijos*

Nesočiųjų esterių ir lipidų stabilumą reikšmingai sąlygoja ir peroksidacijos (autooksidacijos) procesai. Tai laisvųjų radikalų inicijuotas deguonies prisijungimas prie nesočiųjų lipidų dvigubųjų jungčių, o esant pakankamai deguonies koncentracijai vyksta ir sočiųjų riebalų peroksidacija. Tarp kitko, ne tik anodinėse dangose, bet ir biologinėse sistemose oksidacinio streso metu vyksta negrįžtami ląstelių pakitimai, kuomet pažeidžiama ląstelės membrana dalyvaujant laisviesiems radikalams. Vienas svarbiausių parametrų įtakojančių radikalo veikimo mechanizmą yra jo redokso potencialas, kuris apibūdina pajėgumą redukuoti kitą junginį. Iš žinomų laisvųjų radikalų hidroksilo radikalas (•OH) turi teigiamiausią standartinį redokso potencialą (2310 mV) ir yra laikomas stipriausiai oksiduojančiu radikalu biologinėse sistemose [259]. Radikalinės grandininės reakcijos metu, kurią sudaro pradžios, sklidimo ir baigties stadijos, laisvasis radikalas atima H atomą iš riebalų r. grandinės. Susidaręs lipidinis radikalas reaguoja su deguonimi ir sudaro peroksilo radikalą (ROO•), kuris yra nestabilus ir lengvai gali prisijungti H atomą iš kito lipido, o pats virsti hidroperoksidu (ROOH). Oleino r. turinti dvigubą jungtį prie 9 C atomo yra oksiduojama hidroperoksilu prie 8 C ir 11 C atomų arba prie 9 C ir 10 C atomų po dvigubos jungties poslinkio.

Peroksidacijos reakcija nutraukiama, kai susijungia du laisvieji radikalai ir sudaro produktus, kurie nėra radikalai. Pirminiai oksidacijos produktai yra hidroperoksidai arba peroksidai. Tolesniame peroksidacijos etape hidroperoksidai skyla ir susidaro daug antrinių produktų: aldehidų, ketonų, alkoholių, trumpos grandinės rūgščių, ketorūgščių bei kitų junginių.

Todėl organinių junginių migracija priklauso ne tik nuo anodinių dangų ar elektrolito komponentų, bet ir nuo migruojančių junginių hidrolizės, peroksidacijos ir kitų cheminių virsmų. Taigi, impregnavimo metu anodinės dangos skylutėse gali susiformuoti nauji junginiai, kurie pasižymi naujomis charakteristikomis, pvz. kita spalva, trintį mažinančiomis savybėmis ir pan.

3.5 Tepamųjų medžiagų poveikis anodinių ir nanostruktūrinių dangų tribologinėms savybėms

Skirtingai negu sausojoje trintyje, biologinėse sistemose paviršių trintis vyksta dalyvaujant organizmo skysčiams (limfa, vanduo, kraujas, seilės, kt.) bei juose esančioms medžiagoms, tarp jų ir lipidams [233]. Sočioji stearino r. ir mononesočioji oleino r. aptinkama žmogaus ir gyvūnų riebaliniame audinyje, taip pat įeina į fosfolipidų ir trigliceridų sudėtį, o jų koncentracijos atitinkamai siekia iki 30 % [126] ir iki 50 % [127]. Kadangi tai vienos

labiausiai paplitusių riebalų r., tiek laisvosios rūgštys (oleino r., stearino r.) tiek ir trigliceridai (tristearinas) gali sąveikauti su anodinėmis ir nanostruktūrinėmis dangomis. Tepamųjų medžiagų tribologinės savybės buvo tiriamos iš dalies tepamosios (angl. „lubricant starvation“) trinties sąlygomis daugiau atsižvelgiant į dangų savybes, nei pačio užpildo.

Siekiant priartėti prie organizme vykstančių trinties sąlygų buvo nagrinėjamos ir lipofilinės, ir hidrofilinės aplinkos. Pastarajai panaudotas Hankso subalansuotas druskų tirpalas, kuris osmosiniu slėgiu, druskų sudėtimi ir buferinėmis savybėmis panašus į kraujo serumą. Nors nanostruktūrinių dangų su 75 nm storio Ti sluoksnių dilimas sumažėjo apie 3,5 karto, tačiau trintis buvo du kartus aukštesnė lyginant su sausąja trintimi.

Taip pat ištirtas grynų lipidų poveikis trinčiai ant anodinių dangų, įvertinant ir 75 nm Ti sluoksnį (suformuotą magnetronu). Nustatyta, kad lipidai ženkliai slopina anodinių dangų trintį ir sumažina trinties koeficientą iki 0,1 (20 pav.)

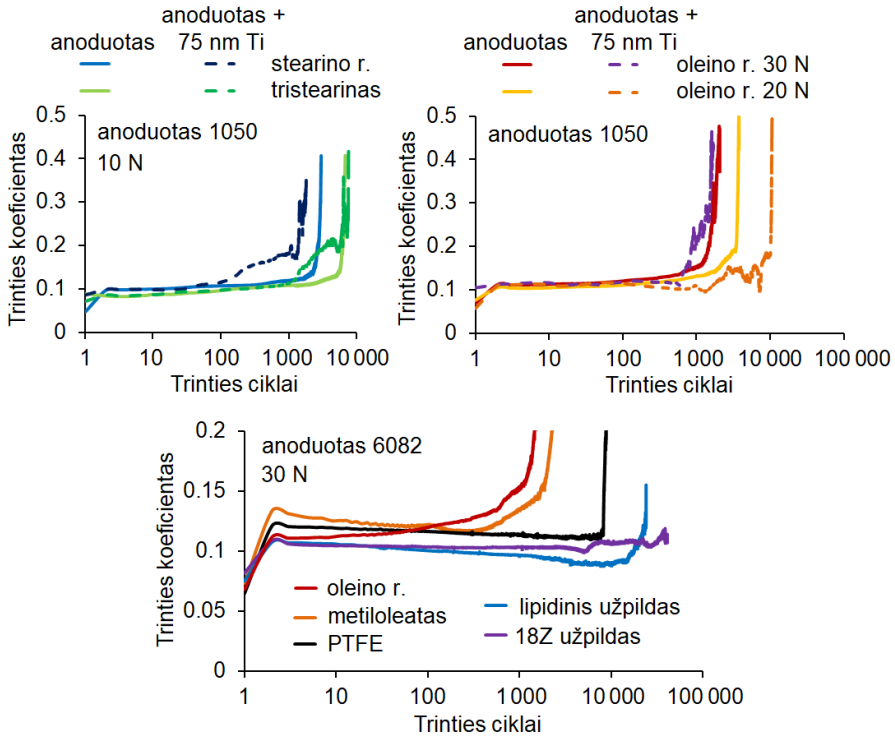

20 pav. *Tepamųjų medžiagų poveikis anodinių ir nanostruktūrinių dangų trinčiai, esant 10–30 N apkrovoms*

Tepamosios medžiagos gali įsiskverbti į anodinės dangos skylutes ir trinties metu formuoti triboplėveles, kurios mažina paviršių trintį bei dilimą. Skirtingai negu adsorbcinė plėvelė, kuri susiformuoja dėl tarpmolekulinės lipido ir metalo sąveikos, triboplėvelės susidaro tribocheminių reakcijų metu dėl trinties poveikio ir pasižymi skirtinga chemine sudėtimi, struktūra bei tribologine elgsena [134, 135]. Tiek stearino, tiek oleino r. trinties zonoje galėjo reaguoti su Al hidroksidais, suformuojant muilus, kurie pagerina tepamosios plėvelės efektyvumą. Oleino r. buvo daug efektyvesnė už stearino r. bei tristeariną dėl dvigubosios C=C jungties reaktyvumo. Be to, trinties zonoje esant deguonies oleino r. gali formuoti oksipolimerus vykstant kondensacinei grandininei polimerizacijai, kurios metu labai padidėja tepamosios medžiagos klampumas. Metalų druskos šiuo atveju veikia kaip katalizatoriai ir skatina aukštos molekulinės masės junginių formavimąsi. Tristearinas hidrolizės ir transesterifikacijos metu gali formuoti glicerilo junginius, kurie sąveikauja su sulfatais bei oksalatais. Pvz. vykstant cheminei reakcijai tarp glicerolio ir oksalo r. formuojasi glicerilo mono oksalatas prie 100–110 °C, o dioksalatų susidarymui reikalinga 260–280 °C [262]. Monogliceridо sulfatų susidarymas taip pat įmanomas vykstant sulfatinimo bei transesterifikacijos reakcijoms [263].

Paviršių nanostruktūrizavimas neturėjo teigiamo poveikio trinčiai tiriant kietos fazės lipidus (stearino r. ir tristeariną) prie 10 N apkrovos, nors žema trintis su tristearinu išsilaikė kiek ilgiau. Oleino r. tepamiesiems sluoksniams buvo pasirinktos 20–30 N apkrovos, kadangi prie 10 N apkrovos trintis išliko stabili net po 50 000 ciklų, nors trintį buvo galima tęsti ir toliau. Žema trintis skystos fazės ~15 μm storio oleino r. plėvelėje ant nanostruktūrinių dangų išsilaikė apie 10 000 trinties ciklų prie 20 N apkrovos. Tačiau akivaizdaus Ti nanosluoksnio sinerginio poveikio nebuvo pastebėta nei prie 20, nei 30 N apkrovos. Tikėtina, jog 75 nm Ti nanosluoksniai visiškai užpildo anodinių dangų skylutes ir blokuoja oleino r. įsiskverbimą. Visgi, buvo pastebėta, kad oleino r. yra dvigubai efektyvesnė ir išsilaiko du kartus ilgiau naudojant nanostruktūrines dangas, suformuotas ant 6082 lydinio, galimai dėl platesnių skylučių.

Kietų ir polimerinių tepamųjų medžiagų, pavyzdžiui, PTFE, panaudojimas anodinių dangų apsaugai nuo trinties ir dilimo yra ribotas, kadangi skylučių diametras siekiantis iki 20 nm yra per mažas PTFE molekulių įsiskverbimui. PTFE polimerai formuoja barjerines dangas ant anoduoto Al, kurie sumažina trinties koeficientą ~0,1 ir išsilaiko iki 10 000 ciklų prie 30 N apkrovos. Nors oleino r. ir metiloleato tepamieji sluoksniai nebuvo tokie efektyvūs, kaip PTFE, tačiau jie parodė teigiamą tribologinį

poveikį prie mažesnių apkrovų. Lipidinis ir 18Z užpildai pasižymėjo žemesniu trinties koeficientu ir išsilaikė virš 10 000 trinties ciklų prie 30 N apkrovos. Šie užpildai efektyviau slopino trintį nei riebalų r., esteriai ar barjerinės dangos.

Rezultatai rodo, kad sinerginė elektrolito komponentų ir impregnuotų užpildų sąveika ženkliai pagerina pramoninių Al lydinių anodinių dangų tribologines savybes. Siekiant geresnio tribologinio efektyvumo svarbu atsižvelgti tiek į anodinių dangų struktūrą, tiek į chemines bei fizikines tepamųjų medžiagų savybes, kurios užtikrintų žemą paviršių trintį bei dilimą. Fundamentalūs tyrimai, leidžiantys įvertinti ryšį tarp elektrolito ir tepamųjų medžiagų, gali padėti geriau suprasti trinties mechanizmus vykstančius anodinės dangos paviršiuje bei jos skylutėse. Šie tyrimai sudaro galimybę komercinei pažangai bei įvairiems anoduoto Al taikymams biomedicinoje, aukštųjų technologijų pramonėje bei daugelyje kitų mokslo sričių.

IŠVADOS

1. Ti ir jo oksidų nanosluoksniai ženkliai pagerina anodinių dangų biosuderinamumą, Nanostruktūrinės dangos su maždaug 75 nm Ti sluoksniu yra tinkamiausios.
2. Anodavimas sieros/oksalo r. elektrolite reikšmingai sumažina ne tik dinaminę, bet ir statinę trintį. Anodavimas fosforo r. elektrolite formuoja daug minkštesnes ir labiau poringas dangas, kurių atsparumas trinčiai ir dilimui yra daug prastesnis.
3. Nepriklausomai nuo Ti ar jo oksidų nanosluoksnių formavimo ant kietosios anodinės dangos metodo (ALD arba magnetroninio), 10–75 nm storio Ti/TiO_2 nanosluoksniai esant 1–10 N apkrovoms sumažina trinties koeficientą žemiau 0,2, kuris išsilaiko nuo 20 iki 60 sausosios trinties ciklų. Tiek Ti lydinių, tiek anodinių dangų be Ti sluoksnių trinties koeficientas viršija 0,5 jau po kelių sausosios trinties ciklų.
4. Zr ir Hf oksidų nanosluoksniai sumažina statinės trinties koeficientą žemiau 0,2, tačiau tribologiškai yra mažiau efektyvūs nei Ti ir jo oksidai. Kitų pereinamųjų metalų nanosluoksniai neturi teigiamo poveikio anodinių dangų tribologinėms savybėms.
5. Ramano spektroskopijos metodu galima kiekybiškai įvertinti hidrofilinių azo-junginių skverbimąsi į anoduotos folijos skylutes. Taip pat įmanoma nustatyti šių junginių sąveikos intensyvumą su anodinės dangos aplinka.
6. Monofunkcinių esterių ir kitų hidrofobinių junginių skverbimąsi į anodinę dangą nulemia ne tik skylučių geometriniai parametrai, bet ir elektrolito komponentų poveikis. Ženklūs medžiagų kiekiai gali susikaupti dangos gilumoje, pvz. 60–70 µm storio dangose vidutinis metiloleato įsiskverbimo gylis siekia 10–20 µm.
7. Triboplėvelių formavimasis ant anodinės dangos vyksta ne tik dėl tribocheminių tepamųjų medžiagų reakcijų trinties zonoje, bet ir dėl jų cheminės sąveikos su dangos skylutėse esančiais junginiais.
8. Suderinus tepamąją medžiagą ir anodavimo elektrolitą, anodinių dangų trinties koeficientą galima sumažinti iki ~0,1, o dilimo intensyvumą nuslopinti daugiau kaip 3 eilėmis sausosios trinties sąlygomis.

GYVENIMO APRAŠYMAS

Vardas: Tadas
Pavardė: Matijošius
Gimimo data: 1990-08-29
Gimimo vieta: Vilnius, Lietuva
E-paštas: tadas.matijosius@ftmc.lt

Išsilavinimas:

1997–2009 m.	Vilniaus Martyno Mažvydo vidurinė mokykla
2009–2013 m.	Vilniaus Gedimino technikos universitetas, Fundamentinių mokslų fakultetas, bioinžinerijos specialybė, bioinžinerijos bakalauro laipsnis
2013–2015 m.	Vilniaus Gedimino technikos universitetas, Fundamentinių mokslų fakultetas, nanobiotechnologijos specialybė, biotechnologijų magistro laipsnis
Nuo 2015 m.	Fizinių ir technologijos mokslų centras, Elektrocheminės medžiagotyros skyrius, chemijos krypties doktorantūros studijos

Profesinė veikla:

2011 m.	Praktikantas Vilniaus universiteto Biochemijos institutas
2012–2013 m.	Praktikantas UAB „Biocentras“
2014–2015 m.	Praktikantas Fizinių ir technologijos mokslų centras, Cheminės inžinerijos ir technologijų skyrius, Tribologijos lab.
2014–2017 m.	Inžinierius Fizinių ir technologijos mokslų centras, Cheminės inžinerijos ir technologijų skyrius, Tribologijos lab.
Nuo 2017 m.	Jaunesnysis mokslo darbuotojas Fizinių ir technologijos mokslų centras, Cheminės inžinerijos ir technologijų skyrius, Tribologijos lab.

REFERENCES

[1] Dinçel, Y.M. (2018). Bone Graft Types. In: R. Kummoona, ed., *Bone Grafting: Recent Advances with Special References to Cranio-Maxillofacial Surgery*, 1st ed. London: IntechOpen, pp.27-39.

[2] Klinge, B., Lundström, M., Rosén, M., Bertl, K., Klinge, A. and Stavropoulos, A. (2018). Dental Implant Quality Register—A possible tool to further improve implant treatment and outcome. *Clinical Oral Implants Research*, 29(S18), pp.145-151.

[3] Snauwaert, K., Duyck, J., van Steenberghe, D., Quirynen, M. and Naert, I. (2000). Time dependent failure rate and marginal bone loss of implant supported prostheses: a 15-year follow-up study. *Clinical Oral Investigations*, 4(1), pp.13-20.

[4] Hadi, S.A., Ashfaq, N., Bey, A. and Khan, S. (2011). Biological factors responsible for failure of osseointegration in oral implants. *Biology and Medicine*, 3(2), pp.164-170.

[5] Hu, J., Tian, J.H., Shi, J., Zhang, F., He, D.L., Liu, L., Jung, D.J., Bai, J.B. and Chen, Y. (2011). Cell culture on AAO nanoporous substrates with and without geometry constrains. *Microelectronic Engineering*, 88(8), pp.1714-1717.

[6] Pedimonte, B.J., Moest, T., Luxbacher, T., von Wilmowsky, C., Fey, T., Schlegel, K.A. and Greil, P. (2014). Morphological zeta-potential variation of nanoporous anodic alumina layers and cell adherence. *Acta Biomaterialia*, 10(2), pp.968-974.

[7] Buijnsters, J.G., Zhong, R., Tsyntsaru, N. and Celis, J.P. (2013). Surface wettability of macroporous anodized aluminum oxide. *ACS Applied Materials and Interfaces*, 5(8), pp.3224-3233.

[8] Becaria, A., Campbell, A. and Bondy, S.C. (2002). Aluminum as a toxicant. *Toxicology and Industrial Health*, 18(7), pp.309-320.

[9] Verstraeten, S.V., Aimo, L. and Oteiza, P.I. (2008). Aluminium and lead: molecular mechanisms of brain toxicity. *Archives of toxicology*, 82(11), pp.789-802.

[10] Bassioni, G., Mohammed, F.S., Al Zubaidy, E. and Kobrsi, I. (2012). Risk assessment of using aluminum foil in food preparation. *International Journal of Electrochemical Science*, 7(5), pp.4498-4509.

[11] Krishna, D.S.R. and Sun, Y. (2005). Thermally oxidised rutile-TiO_2 coating on stainless steel for tribological properties and corrosion resistance enhancement. *Applied Surface Science*, 252(4), pp.1107-1116.

[12] Goldbaum, D., Manimuda, P., Kamath, G., Descartes, S., Klemberg-Sapieha, J.E. and Chromik, R.R. (2016). Tribological behavior of TiN and Ti (Si, C) N coatings on cold sprayed Ti substrates. *Surface and Coatings Technology*, 291, pp.264-275.

[13] Anouar, K. and Mansour, B. (2018). Improving tribological behavior of porous anodic film by electrophoretic impregnation by a TiO_2 synthesized nanoparticle. In: O.-M. Boldura, C. Balta, ed., *Electrophoresis: Life Sciences Practical Applications*, 1st ed. London: IntechOpen, pp.125-143.

[14] Li, J., Zhang, H., Fan, A. and Tang, B. (2016). Tribological properties characterization of Ti/Cu/N Thin films prepared by DC magnetron sputtering on titanium alloy. *Surface and Coatings Technology*, 294, pp.30-35.

[15] Leng, Y.X., Chen, J.Y., Yang, P., Sun, H. and Huang, N. (2007). The microstructure and properties of titanium dioxide films synthesized by unbalanced magnetron sputtering. *Nuclear Instruments and Methods in Physics Research Section B: Beam Interactions with Materials and Atoms*, 257(1-2), pp.451-454.

[16] Stocchi, C., Robinson, P. and Pinho, S.T. (2013). A detailed finite element investigation of composite bolted joints with countersunk fasteners. *Composites Part A: Applied Science and Manufacturing*, 52, pp.143-150.

[17] Garsivaz jazi, M.R., Golozar, M.A., Raeissi, K. and Fazel, M. (2014). Evaluation of corrosion and tribocorrosion of plasma electrolytic oxidation treated Ti–6Al–4V alloy. *Surface and Coatings Technology*, 244, pp.29-36.

[18] Veiga, C., Davim, J.P. and Loureiro, A.J.R. (2012). Properties and applications of titanium alloys: a brief review. *Reviews on Advanced Materials Science*, 32(2), pp.133-148.

[19] Massard, C., Pairis, S., Raspal, V., Sibaud, Y. and Awitor, K.O. (2015). Fabrication of TiO_2 nanotanks embedded in a nanoporous alumina template. *Journal of Nanomaterials*, 16(1), p.216.

[20] Es-Souni, M. and Habouti, S. (2014). Ordered nanomaterial thin films via supported anodized alumina templates. *Frontiers in Materials*, 1, p.19.

[21] Liu, C.M., Chen, C. and Cheng, H.E. (2011). Growth mechanism of TiO_2 nanotube arrays in nanopores of anodic aluminum oxide on Si substrates by atomic layer deposition. *Journal of The Electrochemical Society*, 158(3), pp.K58-K63.

[22] Lee J.-J., Rahman M.M., Sarker S., Nath N.C.D., Ahammad A.J.S. and Lee J.K. (2011). Metal oxides and their composites for the photoelectrode of dye sensitized solar cells. In: B. Attaf, ed., *Advances in Composite Materials for Medicine and Nanotechnology*, 1st ed. Rijeka: IntechOpen, pp.181-210.

[23] Shi, J., Sun, C., Starr, M.B. and Wang, X. (2011). Growth of titanium dioxide nanorods in 3D-confined spaces. *Nano letters*, 11(2), pp.624-631.

[24] Abdulagatov, A.I., Yan, Y., Cooper, J.R., Zhang, Y., Gibbs, Z.M., Cavanagh, A.S., Yang, R.G., Lee, Y.C. and George, S.M. (2011). Al_2O_3 and TiO_2 atomic layer deposition on copper for water corrosion resistance. *ACS Applied Materials and Interfaces*, 3(12), pp.4593-4601.

[25] Niinomi, M., 2008. Mechanical biocompatibilities of titanium alloys for biomedical applications. *Journal of the Mechanical Behavior of Biomedical Materials*, 1(1), pp.30-42.

[26] Fetz, A.E., Fantaziu, C.A., Smith, R.A., Radic, M.Z. and Bowlin, G.L. (2019). Surface Area to Volume Ratio of Electrospun Polydioxanone Templates Regulates the Adsorption of Soluble Proteins from Human Serum. *Bioengineering*, 6(3), p.78.

[27] Zhou, Z.R. and Zheng, J. (2008). Tribology of dental materials: a review. *Journal of Physics D: Applied Physics*, 41(11), p.113001.

[28] Zheng, J. and Zhou, Z.R. (2006). Effect of age on the friction and wear behaviors of human teeth. *Tribology International*, 39(3), pp.266-273.

[29] Wang, Y., Fan, Y. and Zhang, M. (2014). Comparison of stress on knee cartilage during kneeling and standing using finite element models. *Medical Engineering and Physics*, 36(4), pp.439-447.

[30] Krishnan, R., Mariner, E.N. and Ateshian, G.A. (2005). Effect of dynamic loading on the frictional response of bovine articular cartilage. *Journal of Biomechanics*, 38(8), pp.1665-1673.

[31] Merkher, Y., Sivan, S., Etsion, I., Maroudas, A., Halperin, G. and Yosef, A. (2006). A rational human joint friction test using a human cartilage-on-cartilage arrangement. *Tribology Letters*, 22(1), pp.29-36.

[32] Ge, S., Wang, Q., Zhang, D., Zhu, H., Xiong, D., Huang, C. and Huang, X. (2003). Friction and wear behavior of nitrogen ion implanted UHMWPE against ZrO_2 ceramic. *Wear*, 255(7-12), pp.1069-1075.

[33] Shacham, S., Castel, D. and Gefen, A. (2010). Measurements of the static friction coefficient between bone and muscle tissues. *Journal of Biomechanical Engineering*, 132(8), p.084502.

[34] Dunn, A.C., Zaveri, T.D., Keselowsky, B.G. and Sawyer, W.G. (2007). Macroscopic friction coefficient measurements on living endothelial cells. *Tribology Letters*, 27(2), pp.233-238.

[35] Rennie, A.C., Dickrell, P.L. and Sawyer, W.G. (2005). Friction coefficient of soft contact lenses: measurements and modeling. *Tribology Letters*, 18(4), pp.499-504.

[36] Ivkovic, B., Djurdjanovic, M. and Stamenkovic, D. (2000). The influence of the contact surface roughness on the static friction coefficient. *Tribology in Industry*, 22(3-4), pp.41-44.

[37] Israelachvili, J.N. (2011). Adhesion and wetting phenomena. In: J.N. Israelachvili, ed., *Intermolecular and Surface Forces*, 3rd ed. California: Academic Press, pp.415-467.

[38] Pailler-Mattéi, C. and Zahouani, H. (2006). Analysis of adhesive behaviour of human skin in vivo by an indentation test. *Tribology International*, 39(1), pp.12-21.

[39] Zeng, K., Breder, K., Rowcliffe, D.J. and Herrström, C. (1992). Elastic modulus determined by Hertzian indentation. *Journal of Materials Science*, 27(14), pp.3789-3792.

[40] Sotres, J. and Arnebrant, T. (2013). Experimental investigations of biological lubrication at the nanoscale: the cases of synovial joints and the oral cavity. *Lubricants*, 1(4), pp.102-131.

[41] Davim, J.P. (2011). *Tribology for Engineers: A Practical Guide*. Philadelphia: Woodhead Publishing, p.69.

[42] Srivastava, S.P. (2014). *Developments in Lubricant Technology*. Hoboken: John Wiley and Sons, pp.7-21.

[43] Eisentraeger, A., Schmidt, M., Murrenhoff, H., Dott, W. and Hahn, S. (2002). Biodegradability testing of synthetic ester lubricants—effects of additives and usage. *Chemosphere*, 48(1), pp.89-96.

[44] Alves, S.M., Barros, B.S., Trajano, M.F., Ribeiro, K.S.B. and Moura, E. (2013). Tribological behavior of vegetable oil-based lubricants with nanoparticles of oxides in boundary lubrication conditions. *Tribology International*, 65, pp.28-36.

[45] Nicolenco, A., Tsyntsaru, N., Matijošius, T., Asadauskas, S. and Cesiulis, H. (2018). Wear resistance of electrodeposited Fe-W alloy coatings under dry conditions and in the presence of rapeseed oil. *Green Tribology*, 1(1), pp.16-23.

[46] Bart, J.C., Gucciardi, E. and Cavallaro, S. (2012). *Biolubricants: Science and Technology*. Philadelphia: Woodhead Publishing, p.42.

[47] Domínguez-Meister, S., Rojas, T.C., Brizuela, M. and Sánchez-López, J.C. (2017). Solid lubricant behavior of MoS_2 and WSe_2-based nanocomposite coatings. Sci*ence and Technology of Advanced Materials*, 18(1), pp.122-133.

[48] Bandaru, N., Kumar, R.S., Sneed, D., Tschauner, O., Baker, J., Antonio, D., Luo, S.N., Hartmann, T., Zhao, Y. and Venkat, R. (2014). Effect of pressure and temperature on structural stability of MoS_2. *The Journal of Physical Chemistry C*, 118(6), pp.3230-3235.

[49] Escobar, J., Arurault, L. and Turq, V. (2012). Improvement of the tribological behavior of PTFE-anodic film composites prepared on 1050 aluminum substrate. *Applied Surface Science*, 258(20), pp.8199-8208.

[50] Harris, K.L., Curry, J.F., Pitenis, A.A., Rowe, K.G., Sidebottom, M.A., Sawyer, W.G. and Krick, B.A. (2015). Wear debris mobility, aligned surface roughness, and the low wear behavior of filled polytetrafluoroethylene. *Tribology Letters*, 60(1), p.2.

[51] Kowandy, C., Richard, C., Chen, Y.M. and Tessier, J.J. (2007). Correlation between the tribological behaviour and wear particle morphology—case of grey cast iron 250 versus Graphite and PTFE. *Wear*, 262(7-8), pp.996-1006.

[52] Dekker, A., Reitsma, K., Beugeling, T., Bantjes, A., Feijen, J. and Van Aken, W.G. (1991). Adhesion of endothelial cells and adsorption of serum proteins on gas plasma-treated polytetrafluoroethylene. *Biomaterials*, 12(2), pp.130-138.

[53] Possart, W. ed. (2006). *Adhesion: Current Research and Applications*. Weinheim: John Wiley and Sons, p.159.

[54] Baragetti, S. (2007). Fatigue resistance of steel and titanium PVD coated spur gears. *International Journal of Fatigue*, 29(9-11), pp.1893-1903.

[55] She, D., Yue, W., Fu, Z., Wang, C., Yang, X. and Liu, J. (2015). Effects of nitriding temperature on microstructures and vacuum tribological properties of plasma-nitrided titanium. *Surface and Coatings Technology*, 264, pp.32-40.

[56] Kim, H.S., Kim, D.H., Lee, W., Cho, S.J., Hahn, J.H. and Ahn, H.S. (2010). Tribological properties of nanoporous anodic aluminum oxide film. *Surface and Coatings Technology*, 205(5), pp.1431-1437.

[57] Jäger, M., Jennissen, H., Dittrich, F., Fischer, A. and Köhling, H. (2017). Antimicrobial and osseointegration properties of nanostructured titanium orthopaedic implants. *Materials*, 10(11), p.1302.

[58] Karjalainen, P.P., Ylitalo, A., Airaksinen, J.K. and Nammas, W. (2010). Titanium-nitride-oxide-coated Titan-2 bioactive coronary stent: a new horizon for coronary intervention. *Expert Review of Medical Devices*, 7(5), pp.599-604.

[59] Gemelli, E. and Camargo, N.H.A. (2007). Oxidation kinetics of commercially pure titanium. *Matéria (Rio de Janeiro)*, 12(3), pp.525-531.

[60] Palmquist, A., Grandfield, K., Norlindh, B., Mattsson, T., Brånemark, R. and Thomsen, P. (2011). Bone–titanium oxide interface in humans revealed by transmission electron microscopy and electron tomography. *Journal of the Royal Society Interface*, 9(67), pp.396-400.

[61] Guo, C.Y., Tang, A.T.H., Tsoi, J.K.H. and Matinlinna, J.P. (2014). Effects of different blasting materials on charge generation and decay on titanium surface after sandblasting. *Journal of the Mechanical Behavior of Biomedical Materials*, 32, pp.145-154.

[62] Le Guéhennec, L., Soueidan, A., Layrolle, P. and Amouriq, Y. (2007). Surface treatments of titanium dental implants for rapid osseointegration. *Dental Materials*, 23(7), pp.844-854.

[63] Cho, S.A. and Park, K.T. (2003). The removal torque of titanium screw inserted in rabbit tibia treated by dual acid etching. *Biomaterials*, 24(20), pp.3611-3617.

[64] Minagar, S., Wang, J., Berndt, C.C., Ivanova, E.P. and Wen, C. (2013). Cell response of anodized nanotubes on titanium and titanium alloys. *Journal of Biomedical Materials Research Part A*, 101(9), pp.2726-2739.

[65] Brüggemann, D. (2013). Nanoporous aluminium oxide membranes as cell interfaces. *Journal of Nanomaterials*, 2013(32), pp.1-18.

[66] Sakkas, V.A., Calza, P., Medana, C., Villioti, A.E., Baiocchi, C., Pelizzetti, E. and Albanis, T. (2007). Heterogeneous photocatalytic degradation of the pharmaceutical agent salbutamol in aqueous titanium dioxide suspensions. *Applied Catalysis B: Environmental*, 77(1-2), pp.135-144.

[67] Haggerty, J.E., Schelhas, L.T., Kitchaev, D.A., Mangum, J.S., Garten, L.M., Sun, W., Stone, K.H., Perkins, J.D., Toney, M.F., Ceder, G. and

Ginley, D.S. (2017). High-fraction brookite films from amorphous precursors. *Scientific Reports*, 7(1), p.15232.

[68] Vera, M.L., Rosenberger, M.R., Schvezov, C.E. and Ares, A.E. (2015). Fabrication of TiO_2 crystalline coatings by combining Ti-6Al-4V anodic oxidation and heat treatments. *International Journal of Biomaterials*, 2015, pp.1-9.

[69] Beydoun, D. and Amal, R. (2002). Implications of heat treatment on the properties of a magnetic iron oxide–titanium dioxide photocatalyst. *Materials Science and Engineering: B*, 94(1), pp.71-81.

[70] Hanaor, D.A. and Sorrell, C.C. (2011). Review of the anatase to rutile phase transformation. *Journal of Materials Science*, 46(4), pp.855-874.

[71] Juma, A.O., Acik, I.O., Mikli, V., Mere, A. and Krunks, M. (2015). Effect of solution composition on anatase to rutile transformation of sprayed TiO_2 thin films. *Thin Solid Films*, 594, pp.287-292.

[72] Oh, S.M., Kim, S.S., Lee, J.E., Ishigaki, T. and Park, D.W. (2003). Effect of additives on photocatalytic activity of titanium dioxide powders synthesized by thermal plasma. *Thin Solid Films*, 435(1-2), pp.252-258.

[73] Archaapinun, K., Witit-Anun, N. and Visuttipitukul, P. (2013). Effect of heat treatment on phase transformation of TiO_2 and its reflectance properties. *Journal of Metals, Materials and Minerals*, 23(2), pp.43-49.

[74] Liu, X., Chu, P.K. and Ding, C. (2004). Surface modification of titanium, titanium alloys, and related materials for biomedical applications. *Materials Science and Engineering: R: Reports*, 47(3-4), pp.49-121.

[75] Forosh, M.K., Kajinebaf, V.T. and Sarpoolaky, H. (2014). Multi-step Coating of Monodisperse Silica Spheres by Titania Nanoparticles Base on Electrostatic Attraction Strategy. *Progress in Color, Colorants and Coatings*, 7(4), pp.259-268.

[76] Nine, M.D., Choudhury, D., Hee, A.Y., Mootanah, R. and Osman, N. (2014). Wear debris characterization and corresponding biological response: artificial hip and knee joints. *Materials*, 7(2), pp.980-1016.

[77] Bitar, D. and Parvizi, J. (2015). Biological response to prosthetic debris. *World Journal of Orthopedics*, 6(2), p.172-189.

[78] Kowandy, C., Mazouz, H. and Richard, C. (2006). Isolation and analysis of articular joints wear debris generated in vitro. *Wear*, 261(9), pp.966-970.

[79] Vieira, A.C., Ribeiro, A.R., Rocha, L.A. and Celis, J.P. (2006). Influence of pH and corrosion inhibitors on the tribocorrosion of titanium in artificial saliva. *Wear*, 261(9), pp.994-1001.

[80] Zieliński, A. and Sobieszczyk, S. (2008). Corrosion of titanium biomaterials, mechanisms, effects and modelisation. *Corrosion Reviews*, 26(1), pp.1-22.

[81] Rodrigues, D., Valderrama, P., Wilson, T., Palmer, K., Thomas, A., Sridhar, S., Adapalli, A., Burbano, M. and Wadhwani, C. (2013). Titanium corrosion mechanisms in the oral environment: a retrieval study. *Materials*, 6(11), pp.5258-5274.

[82] Cheng, Y., Cai, W., Zheng, Y.F., Li, H.T. and Zhao, L.C. (2005). Surface characterization and immersion tests of TiNi alloy coated with Ta. *Surface and Coatings Technology*, 190(2-3), pp.428-433.

[83] Joseph, L.A., Israel, O.K. and Edet, E.J. (2009). Comparative evaluation of metal ions release from titanium and Ti-6Al-7Nb into bio-fluids. *Dental Research Journal*, 6(1), p.7-11.

[84] Tagaya, M., Ikoma, T., Hanagata, N. and Tanaka, J. (2012). Analytical investigation of protein mediation between biomaterials and cells. *Materials Express*, 2(1), pp.1-22.

[85] Webb, K., Hlady, V. and Tresco, P.A. (1998). Relative importance of surface wettability and charged functional groups on NIH 3T3 fibroblast attachment, spreading, and cytoskeletal organization. *Journal of Biomedical Materials Research*, 41(3), pp.422-430.

[86] Arima, Y. and Iwata, H. (2007). Effects of surface functional groups on protein adsorption and subsequent cell adhesion using self-assembled monolayers. *Journal of Materials Chemistry*, 17(38), pp.4079-4087.

[87] Chang, H.I. and Wang, Y. (2011). Cell responses to surface and architecture of tissue engineering scaffolds. In: D. Eberli, ed., *Regenerative Medicine and Tissue Engineering: Cells and Biomaterials*, 1st ed. Rijeka: IntechOpen, pp.569-588.

[88] Gittens, R.A., Olivares-Navarrete, R., Schwartz, Z. and Boyan, B.D. (2014). Implant osseointegration and the role of microroughness and nanostructures: lessons for spine implants. *Acta Biomaterialia*, 10(8), pp.3363-3371.

[89] Cavalli, V., Arrais, C.A.G. and Giannini, M. (2009). Influence of low-concentrated bleaching agents on the human enamel roughness and

morphology. *Clínica e Pesquisa em Odontologia-UNITAU*, 1(1), pp.14-19.

[90] Ghosh, S., Bowen, J., Jiang, K., Espino, D.M. and Shepherd, D.E. (2013). Investigation of techniques for the measurement of articular cartilage surface roughness. *Micron*, 44, pp.179-184.

[91] Bellis, S.L. (2011). Advantages of RGD peptides for directing cell association with biomaterials. *Biomaterials*, 32(18), pp.4205-4210.

[92] Drnovšek, N., Rade, K., Milačič, R., Štrancar, J. and Novak, S. (2012). The properties of bioactive TiO_2 coatings on Ti-based implants. *Surface and Coatings Technology*, 209, pp.177-183.

[93] Bensalah, W., Elleuch, K., Feki, M., Wery, M. and Ayedi, H.F. (2007). Optimization of anodic layer properties on aluminium in mixed oxalic/sulphuric acid bath using statistical experimental methods. *Surface and Coatings Technology*, 201(18), pp.7855-7864.

[94] Goueffon, Y., Mabru, C., Labarrère, M., Arurault, L., Tonon, C. and Guigue, P. (2010). Investigations into the coefficient of thermal expansion of porous films prepared on AA7175 T7351 by anodization in sulphuric acid electrolyte. *Surface and Coatings Technology*, 205(7), pp.2643-2648.

[95] Saha, R., Nandi, R. and Saha, B. (2011). Sources and toxicity of hexavalent chromium. *Journal of Coordination Chemistry*, 64(10), pp.1782-1806.

[96] Bikulčius, G., Češunienė, A., Selskienė, A., Pakštas, V. and Matijošius, T. (2017). Dry sliding tribological behavior of Cr coatings electrodeposited in trivalent chromium sulphate baths. *Surface and Coatings Technology*, 315, pp.130-138.

[97] Wielage, B., Nickel, D., Alisch, G., Podlesak, H. and Lampke, T. (2007). Effects of pre-treatment on the growth rate and morphology of hard anodic films on aluminium (EN AW-6082). *Surface and Coatings Technology*, 202(3), pp.569-576.

[98] Liu, C., He, D., Yan, Q., Huang, Z., Liu, P., Li, D., Jiang, G., Ma, H., Nash, P. and Shen, D. (2015). An investigation of the coating/substrate interface of plasma electrolytic oxidation coated aluminum. *Surface and Coatings Technology*, 280, pp.86-91.

[99] Venugopal, A., Srinath, J., Krishna, L.R., Narayanan, P.R., Sharma, S.C. and Venkitakrishnan, P.V. (2016). Corrosion and nanomechanical behaviors of plasma electrolytic oxidation coated AA7020-T6 aluminum alloy. *Materials Science and Engineering: A*, 660, pp.39-46.

[100] Ahmadi, N.P., Khosroshahi, R.A. and Asi, B.B. (2009). Deposition of Oxide Layer on Aluminium Via Plasma Electrolysis Method in Alkali Solutions by Unipolar Pulsed Current System and Study of its Physical Properties. *Asian Journal of Applied Sciences*, 2(1), pp.74-82.

[101] Zhu, X.F., Li, D.D., Song, Y. and Xiao, Y.H. (2005). The study on oxygen bubbles of anodic alumina based on high purity aluminum. *Materials Letters*, 59(24-25), pp.3160-3163.

[102] Ali, H.O. (2017). Review of porous anodic aluminium oxide (AAO) applications for sensors, MEMS and biomedical devices. *Transactions of the IMF*, 95(6), pp.290-296.

[103] Sulka, G.D. (2008). Highly ordered anodic porous alumina formation by self-organized anodization. In: A. Eftekhari, ed., *Nanostructured Materials in Electrochemistry*, 1st ed. Weinheim: Wiley-VCH, pp.1-116.

[104] Jani, A.M.M., Losic, D. and Voelcker, N.H. (2013). Nanoporous anodic aluminium oxide: Advances in surface engineering and emerging applications. *Progress in Materials Science*, 58(5), pp.636-704.

[105] Konieczny, J., Labisz, K., Wieczorek, J. and Dobrzański, L.A. (2009). Stereometry specification of anodised and PVD coated surface of aluminium alloy. *Archives of Materials Science and Engineering*, 38(2), pp.85-92.

[106] Yao, M., Chen, J., Yang, P., Shan, W., Hu, B. and Yao, X. (2013). Preparation and breakdown property of aluminum oxide thin films deposited onto anodized aluminum substrate. *Ferroelectrics*, 455(1), pp.21-28.

[107] Eklund, P., Sridharan, M., Singh, G. and Bøttiger, J. (2009). Thermal Stability and Phase Transformations of γ-/Amorphous-Al_2O_3 Thin Films. *Plasma Processes and Polymers*, 6(S1), pp.S907-S911.

[108] Goueffon, Y., Arurault, L., Mabru, C., Tonon, C. and Guigue, P. (2009). Black anodic coatings for space applications: study of the process parameters, characteristics and mechanical properties. *Journal of Materials Processing Technology*, 209(11), pp.5145-5151.

[109] Masuda, H. and Fukuda, K. (1995). Ordered metal nanohole arrays made by a two-step replication of honeycomb structures of anodic alumina. *Science*, 268(5216), pp.1466-1468.

[110] Li, A.P., Müller, F., Birner, A., Nielsch, K. and Gösele, U. (1998). Hexagonal pore arrays with a 50–420 nm interpore distance formed by

self-organization in anodic alumina. *Journal of Applied Physics*, 84(11), pp.6023-6026.

[111] Poinern, G.E.J., Ali, N. and Fawcett, D. (2011). Progress in nano-engineered anodic aluminum oxide membrane development. *Materials*, 4(3), pp.487-526.

[112] Meng, G., Jung, Y.J., Cao, A., Vajtai, R. and Ajayan, P.M. (2005). Controlled fabrication of hierarchically branched nanopores, nanotubes, and nanowires. *Proceedings of the National Academy of Sciences*, 102(20), pp.7074-7078.

[113] Zaraska, L., Kurowska, E., Sulka, G.D. and Jaskuła, M. (2012). Porous alumina membranes with branched nanopores as templates for fabrication of Y-shaped nanowire arrays. *Journal of Solid State Electrochemistry*, 16(11), pp.3611-3619.

[114] Sulka, G.D. and Hnida, K. (2012). Distributed Bragg reflector based on porous anodic alumina fabricated by pulse anodization. *Nanotechnology*, 23(7), p.075303.

[115] Portan, D.V., Kroustalli, A.A., Deligianni, D.D. and Papanicolaou, G.C. (2012). On the biocompatibility between TiO_2 nanotubes layer and human osteoblasts. *Journal of Biomedical Materials Research Part A*, 100(10), pp.2546-2553.

[116] Wu, H., Zhang, X., Geng, Z., Yin, Y., Hang, R., Huang, X., Yao, X. and Tang, B. (2014). Preparation, antibacterial effects and corrosion resistant of porous Cu–TiO_2 coatings. *Applied Surface Science*, 308, pp.43-49.

[117] Oh, S.H., Finones, R.R., Daraio, C., Chen, L.H. and Jin, S. (2005). Growth of nano-scale hydroxyapatite using chemically treated titanium oxide nanotubes. *Biomaterials*, 26(24), pp.4938-4943.

[118] Kang, H.J., Kim, D.J., Park, S.J., Yoo, J.B. and Ryu, Y.S. (2007). Controlled drug release using nanoporous anodic aluminum oxide on stent. *Thin Solid Films*, 515(12), pp.5184-5187.

[119] Sabry, R.S., Ali Al-fouadi, A.H. and Habool, H.K. (2018). Enhanced antibacterial activity of anodic aluminum oxide membranes embedded with nano-silver-titanium dioxide. *Journal of Adhesion Science and Technology*, 32(8), pp.874-888.

[120] Altuntas, S. and Buyukserin, F. (2014). Fabrication and characterization of conductive anodic aluminum oxide substrates. *Applied Surface Science*, 318, pp.290-296.

[121] Vengatesh, P. and Kulandainathan, M.A. (2015). Hierarchically ordered self-lubricating superhydrophobic anodized aluminum

surfaces with enhanced corrosion resistance. *ACS Applied Materials and Interfaces*, 7(3), pp.1516-1526.

[122] Stoker H.S. (2012) *Organic and Biological Chemistry*. 6th ed. Ogden: Cengage Learning, p.580.

[123] Ratnayake, W.N. and Galli, C. (2009). Fat and fatty acid terminology, methods of analysis and fat digestion and metabolism: a background review paper. *Annals of Nutrition and Metabolism*, 55(1-3), p.8-43.

[124] Mukhopadhyay, M. (2000). *Natural Extracts Using Supercritical Carbon Dioxide*. Boca Raton: CRC Press, p.321.

[125] Ermilova, I. (2019). *Modeling of biomembranes: from computational toxicology to simulations of neurodegenerative diseases* (PhD dissertation). Department of Materials and Environmental Chemistry, Stockholm University, Stockholm.

[126] Narayanan, T.S., Park, I.S. and Lee, M.H. (2015). *Surface Modification of Magnesium and Its Alloys for Biomedical Applications: Modification and Coating Techniques*. Sawston: Woodhead Publishing, p.319.

[127] Sires, B.S., Lemke, B.N., Dortzbach, R.K. and Gonnering, R.S. (1998). Characterization of human orbital fat and connective tissue. *Ophthalmic Plastic and Reconstructive Surgery*, 14(6), pp.403-414.

[128] Mayama, H. (2009). Blooming theory of tristearin. *Soft Matter*, 5(4), pp.856-859.

[129] Stipanuk, M. H., Caudill, M. A. (2013). *Biochemical, Physiological, and Molecular Aspects of Human Nutrition*. 3rd ed. St. Louis: Elsevier/Saunders, pp.116-117.

[130] Siniawski, M.T., Saniei, N., Adhikari, B. and Doezema, L.A. (2007). Influence of fatty acid composition on the tribological performance of two vegetable-based lubricants. *Journal of Synthetic Lubrication*, 24(2), pp.101-110.

[131] Ručinskienė, A., Bikulčius, G., Jankauskas, S. and Asadauskas, S. (2013). Ball-on-plate testing of nanopore fillers for tribologically effective anodized alumina coatings. *Proceedings of the International Conference BALTTRIB'2013*, pp.73-78.

[132] Zainal, N.A., Zulkifli, N.W.M., Gulzar, M. and Masjuki, H.H. (2018). A review on the chemistry, production, and technological potential of bio-based lubricants. *Renewable and Sustainable Energy Reviews*, 82, pp.80-102.

[133] Fox, N.J., Tyrer, B. and Stachowiak, G.W. (2004). Boundary lubrication performance of free fatty acids in sunflower oil. *Tribology Letters*, 16(4), pp.275-281.
[134] Kato, K. and Adachi, K. (2002). Wear of advanced ceramics. *Wear*, 253(11-12), pp.1097-1104.
[135] Luo, Q. (2013). Tribofilms in solid lubricants. In: Q.J. Wang, and Y.-W. Chung, ed., *Encyclopedia of Tribology*, 1st ed. Sheffield: Springer, pp.1-12.
[136] Luo, Q. (2010). Origin of friction in running-in sliding wear of nitride coatings. *Tribology Letters*, 37(3), pp.529-539.
[137] Sun, W.C., Zhang, P., Zhao, K., Tian, M.M. and Wang, Y. (2015). Effect of graphite concentration on the friction and wear of Ni–Al_2O_3/graphite composite coatings by a combination of electrophoresis and electrodeposition. *Wear*, 342-343, pp.172-180.
[138] Sahoo, R.R. and Biswas, S.K. (2010). Microtribology and friction-induced material transfer in layered MoS_2 nanoparticles sprayed on a steel surface. *Tribology Letters*, 37(2), pp.313-326.
[139] Ronkainen, H. and Holmberg, K. (2008). Environmental and thermal effects on the tribological performance of DLC coatings. In: C. Donnet and A. Erdemir, ed., *Tribology of diamond-like carbon films*, 1st ed. Boston: Springer, pp.155-200.
[140] Bikulčius, G., Valius, M., Ručinskienė, A., Jankauskas, S. and Asadauskas, S.J. (2017). Measurement of lubricant layer thickness in anodised alumina using confocal fluorescence microscopy. *Transactions of the IMF*, 95(4), pp.226-232.
[141] Ismail, K. (2015). Fabrication and characterisation of SERS substrates through photo-deposition of Gold Nanoparticles (PhD dissertation). Department of Condensed Matter Physics, The Abdus Salam International Center for Theoretical Physics, Trieste Italy.
[142] Wang, W., Zhao, J., Short, M. and Zeng, H. (2015). Real-time in vivo cancer diagnosis using raman spectroscopy. *Journal of Biophotonics*, 8(7), pp.527-545.
[143] Durickovic, I. (2016). Using Raman spectroscopy for characterization of aqueous media and quantification of species in aqueous solution. In: M. Stauffer, ed., *Applications of Molecular Spectroscopy to Current Research in the Chemical and Biological Sciences*, 1st ed. Rijeka: IntechOpen, pp.405-427.

[144] Culha, M., Cullum, B., Lavrik, N. and Klutse, C.K.(2012). Surface-enhanced Raman scattering as an emerging characterization and detection technique. *Journal of Nanotechnology*, 2012, pp.1-15.
[145] Jiao, Y., Ryckman, J.D., Ciesielski, P.N., Escobar, C.A., Jennings, G.K. and Weiss, S.M. (2011). Patterned nanoporous gold as an effective SERS template. *Nanotechnology*, 22(29), p.295302.
[146] Fan, M. and Brolo, A.G. (2009). Silver nanoparticles self assembly as SERS substrates with near single molecule detection limit. *Physical Chemistry Chemical Physics*, 11(34), pp.7381-7389.
[147] Cejkova, J., Prokopec, V., Brazdova, S., Kokaislova, A., Matejka, P. and Stepanek, F. (2009). Characterization of copper SERS-active substrates prepared by electrochemical deposition. *Applied Surface Science*, 255(18), pp.7864-7870.
[148] Wong-Ek, K., Eiamchai, P., Horprathum, M., Patthanasettakul, V., Limnonthakul, P., Chindaudom, P. and Nuntawong, N. (2010). Silver nanoparticles deposited on anodic aluminum oxide template using magnetron sputtering for surface-enhanced Raman scattering substrate. *Thin Solid Films*, 518(23), pp.7128-7132.
[149] Bae, Y., Yu, J., Jung, Y., Lee, D. and Choi, D. (2019). Cost-Effective and High-Throughput Plasmonic Interference Coupled Nanostructures by Using Quasi-Uniform Anodic Aluminum Oxide. *Coatings*, 9(7), p.420.
[150] Matijošius, T., Ručinskienė, A., Selskis, A., Stalnionis, G., Leinartas, K. and Asadauskas, S.J. (2016). Friction reduction by nanothin titanium layers on anodized alumina. *Surface and Coatings Technology*, 307, pp.610-621.
[151] Matijošius, T., Gedvilas, M., Gečys, P., Vozgirdaitė, D. and Asadauskas, S. (2018). Effects of electrolyte and Ti layers on static and dynamic friction of anodized alumina. *Proceedings of the International Conference BALTTRIB'2017*, 1, pp.199-206.
[152] Matijošius, T., Asadauskas, S.J., Bikulčius, G., Selskis, A., Jankauskas, S., Višniakov, J. and Ignatjev, I. (2019). Determination of the dye penetration rate in porous aluminum oxide using Raman spectroscopy. *Coloration Technology*, 135(4), pp.275-282.
[153] Čebatariūnienė, A., Jarmalavičiūtė, A., Tunaitis, V., Pūrienė, A., Venalis, A. and Pivoriūnas, A. (2017). Microcarrier culture enhances osteogenic potential of human periodontal ligament stromal cells. *Journal of Cranio-Maxillofacial Surgery*, 45(6), pp.845-854.

[154] Evertsson, J., Vinogradov, N.A., Harlow, G.S., Carlà, F., McKibbin, S.R., Rullik, L., Linpé, W., Felici, R. and Lundgren, E. (2018). Self-organization of porous anodic alumina films studied in situ by grazing-incidence transmission small-angle X-ray scattering. *RSC advances*, 8(34), pp.18980-18991.

[155] Sheasby, P.G., Short, E.P. and Gupta, T.K. (1981). *Electrolytic coloring of anodized aluminium by means of optical interference effects*. US4251330A.

[156] Keshavarz, A., Parang, Z. and Nasseri, A. (2013). The effect of sulfuric acid, oxalic acid, and their combination on the size and regularity of the porous alumina by anodization. *Journal of Nanostructure in Chemistry*, 3(1), p.34.

[157] Bocchetta, P., Sunseri, C., Chiavarotti, G. and Di Quarto, F., 2003. Microporous alumina membranes electrochemically grown. *Electrochimica Acta*, 48(20-22), pp.3175-3183

[158] Nelson, J.H. and Kemp, K.C. (2006). *Laboratory Experiments*. 10th ed. Reno: Pearson Education, p.97.

[159] Smith, S.B. and Shute, J.M. (1955). Separation and detection of the aluminum ion in qualitative analysis. *Journal of Chemical Education*, 32(7), p.380-382.

[160] Houghton, R. (2009). *Field Confirmation Testing for Suspicious Substances*. Boca Raton: CRC Press, pp.142-143.

[161] Sauerbrey, G.Z. (1959). The use of quarts oscillators for weighing thin layers and for microweighing. *Zeitschrift für Physik*, 155, pp.206-222.

[162] Zmitrowicz, A. (2005). Wear debris: a review of properties and constitutive models. *Journal of Theoretical and Applied Mechanics*, 43(1), pp.3-35.

[163] Asadauskas, S.J., Kreivaitis, R., Bikulčius, G., Grigucevičienė, A. and Padgurskas, J. (2016). Tribological effects of Cu, Fe and Zn nano-particles, suspended in mineral and bio-based oils. *Lubrication Science*, 28(3), pp.157-176.

[164] Chen, X.Q., Niu, H., Li, D. and Li, Y. (2011). Modeling hardness of polycrystalline materials and bulk metallic glasses. *Intermetallics*, 19(9), pp.1275-1281.

[165] Totten, G.E. and MacKenzie, D.S. (2003). *Handbook of Aluminum: Vol. 1: Physical Metallurgy and Processes*. New York: CRC Press, p.67.

[166] Cabibbo, M., Evangelista, E. and Vedani, M. (2005). Influence of severe plastic deformations on secondary phase precipitation in a 6082

Al-Mg-Si alloy. *Metallurgical and Materials Transactions A*, 36(5), pp.1353-1364.

[167] Yazawa, S., Minami, I. and Prakash, B. (2014). Reducing friction and wear of tribological systems through hybrid tribofilm consisting of coating and lubricants. *Lubricants*, 2(2), pp.90-112.

[168] Gao, P., Zhang, X., Wang, H., Zhang, Q., Li, H., Li, Y. and Duan, Y. (2016). Biocompatible and colloidally stabilized mPEG-PE/calcium phosphate hybrid nanoparticles loaded with siRNAs targeting tumors. *Oncotarget*, 7(3), pp.2855-2866.

[169] Aerts, T., Dimogerontakis, T., De Graeve, I., Fransaer, J. and Terryn, H. (2007). Influence of the anodization temperature on the porosity and the mechanical properties of the porous anodic oxide film. *Surface and Coatings Technology*, 201(16-17), pp.7310-7317.

[170] Wu, Z., Richter, C. and Menon, L. (2007). A study of anodization process during pore formation in nanoporous alumina templates. *Journal of the Electrochemical Society*, 154(1), pp.E8-E12.

[171] Mahta, M., Emamy, M., Cao, X. and Campbell, J. (2008). Overview of β-Al_5FeSi phase in Al-Si alloys. *Materials Science Research Trends*, pp.251-271.

[172] Minoda, T. and Yoshida, H. (2002). Effect of grain boundary characteristics on intergranular corrosion resistance of 6061 aluminum alloy extrusion. *Metallurgical and Materials Transactions A*, 33(9), pp.2891-2898.

[173] Wang, H. and Wang, H. (2005). Thick and macroporous anodic alumina membranes for self-lubricating surface composites. *Applied Surface Science*, 249(1-4), pp.151-156.

[174] Kikuchi, T., Nishinaga, O., Nakajima, D., Kawashima, J., Natsui, S., Sakaguchi, N. and Suzuki, R.O. (2014). Ultra-high density single nanometer-scale anodic alumina nanofibers fabricated by pyrophosphoric acid anodizing. *Scientific Reports*, 4, p.7411.

[175] Zaraska, L., Sulka, G.D. and Jaskuła, M. (2009). Properties of nanostructures obtained by anodization of aluminum in phosphoric acid at moderate potentials. *Journal of Physics: Conference Series*, 146(1), p.012020.

[176] Bosund, M., Salmi, E.M. and Peltonen, R. (2016). Atomic layer deposition into ultra-high aspect ratio structures with a stop-flow ALD reactor. *Science letter*, pp.1-2.

[177] Harju, M., Areva, S., Rosenholm, J.B. and Mäntylä, T. (2008). Characterization of water exposed plasma sprayed oxide coating

materials using XPS. *Applied Surface Science*, 254(18), pp.5981-5989.

[178] Gołąbiewska, A., Checa-Suárez, M., Paszkiewicz-Gawron, M., Lisowski, W., Raczuk, E., Klimczuk, T., Polkowska, Ż., Grabowska, E., Zaleska-Medynska, A. and Łuczak, J. (2018). Highly active TiO_2 microspheres formation in the presence of ethylammonium nitrate ionic liquid. *Catalysts*, 8(7), p.279.

[179] Jackman, M.J., Thomas, A.G. and Muryn, C. (2015). Photoelectron spectroscopy study of stoichiometric and reduced anatase TiO_2 (101) surfaces: the effect of subsurface defects on water adsorption at near-ambient pressures. *The Journal of Physical Chemistry C*, 119(24), pp.13682-13690.

[180] Jagminas, A., Češūnienė, A., Vrublevsky, I., Jasulaitienė, V. and Ragalevičius, R. (2010). Behavior of alumina barrier layer in the supporting electrolytes for deposition of nanowired materials. *Electrochimica Acta*, 55(9), pp.3361-3367.

[181] Gougousi, T., Barua, D., Young, E.D. and Parsons, G.N. (2005). Metal oxide thin films deposited from metal organic precursors in supercritical CO_2 solutions. *Chemistry of Materials*, 17(20), pp.5093-5100.

[182] Gonbeau, D., Guimon, C., Pfister-Guillouzo, G., Levasseur, A., Meunier, G. and Dormoy, R., (1991). XPS study of thin films of titanium oxysulfides. *Surface Science*, 254(1-3), pp.81-89.

[183] Azeez, F., Al-Hetlani, E., Arafa, M., Abdelmonem, Y., Nazeer, A.A., Amin, M.O. and Madkour, M. (2018). The effect of surface charge on photocatalytic degradation of methylene blue dye using chargeable titania nanoparticles. *Scientific Reports*, 8(1), p.7104.

[184] Haeberle, J., Henkel, K., Gargouri, H., Naumann, F., Gruska, B., Arens, M., Tallarida, M. and Schmeißer, D. (2013). Ellipsometry and XPS comparative studies of thermal and plasma enhanced atomic layer deposited Al_2O_3-films. *Beilstein Journal of Nanotechnology*, 4(1), pp.732-742.

[185] Yoganandan, G., Bharathidasan, T., Sri, M.S., Vasumathy, D., Balaraju, J.N. and Basu, B.J.(2015). Effect of Anodized Oxide Layer Aging on Wettability of Alkyl Silane Coating Developed on Aerospace Aluminum Alloy. *Metallurgical and Materials Transactions A*, 46(1), pp.337-346.

[186] Al-Abadleh, H.A. and Grassian, V.H. (2003). FT-IR study of water adsorption on aluminum oxide surfaces. *Langmuir*, 19(2), pp.341-347.

[187] Wu, C.Y., Tu, K.J., Deng, J.P., Lo, Y.S. and Wu, C.H. (2017). Markedly enhanced surface hydroxyl groups of TiO_2 nanoparticles with superior water-dispersibility for photocatalysis. *Materials*, 10(5), p.566.

[188] Mathew, N. (2016). A Short Review on Aluminum Anodizing: An Eco-Friendly Metal Finishing Process. *Journal for Research*, 2(6), pp.5-9.

[189] Asadauskas, S., Bikulčius, G., Matijošius, T., Bučinskienė, D., Jankauskas, S. (2016). Improvement in Resistance to Wear and Corrosion of Anodized Alumina by Impregnation in Biobased Filler. *International Conference of Lithuanian Society of Chemistry*, p.188.

[190] Lee, J., Shin, S., Jiang, Y., Jeong, C., Stone, H.A. and Choi, C.H. (2017). Oil-Impregnated Nanoporous Oxide Layer for Corrosion Protection with Self-Healing. *Advanced Functional Materials*, 27(15), p.1606040.

[191] Jäger, M., Zilkens, C., Zanger, K. and Krauspe, R. (2007). Significance of nano-and microtopography for cell-surface interactions in orthopaedic implants. *BioMed Research International*, 2007(8), p.69036.

[192] Lasocka, I., Szulc-Dąbrowska, L., Skibniewski, M., Skibniewska, E., Strupinski, W., Pasternak, I., Kmieć, H. and Kowalczyk, P. (2018). Biocompatibility of pristine graphene monolayer: Scaffold for fibroblasts. *Toxicology in Vitro*, 48, pp.276-285.

[193] Guo, Y., Fu, W., Chen, H., Shang, C. and Zhong, M. (2012). miR-24 functions as a tumor suppressor in Hep2 laryngeal carcinoma cells partly through down-regulation of the S100A8 protein. *Oncology Reports*, 27(4), pp.1097-1103.

[194] Creative Biogene. CHO-K1 Cell Line. [online] Available at: https://www.creative-biogene.com/support/CHO-K1.html [Accessed Date 10 Dec. 2019].

[195] Hasegawa, T., Chosa, N., Asakawa, T., Yoshimura, Y., Asakawa, A., Ishisaki, A. and Tanaka, M. (2010). Effect of fibroblast growth factor-2 on periodontal ligament cells derived from human deciduous teeth in vitro. *Experimental and Therapeutic Medicine***,** 1(2), pp.337-341.

[196] Ranella, A., Barberoglou, M., Bakogianni, S., Fotakis, C. and Stratakis, E. (2010). Tuning cell adhesion by controlling the roughness and wettability of 3D micro/nano silicon structures. *Acta Biomaterialia*, 6(7), pp.2711-2720.

[197] Ferrari, M. and Cirisano, F. (2019). Mammalian Cell Behavior on Hydrophobic Substrates: Influence of Surface Properties. *Colloids and Interfaces*, 3(2), p.48.

[198] Fraga, C.G. (2005). Relevance, essentiality and toxicity of trace elements in human health. *Molecular Aspects of Medicine*, 26(4-5), pp.235-244.

[199] Kiradzhiyska, D.D., Feodorova, Y.N., Draganov, M.M., Girginov, C.A., Viraneva, A.P., Yovcheva, T.A. and Mantcheva, R.D. (2016). Influence of surface treatment on the biocompatibility of aluminum substrates promising for medical application. *AIP Conference Proceedings*, 1722(1), p.300003.

[200] Doshi, U.H. and Bhad-Patil, W.A. (2011). Static frictional force and surface roughness of various bracket and wire combinations. *American Journal of Orthodontics and Dentofacial Orthopedics*, 139(1), pp.74-79.

[201] Tominaga, J.Y., Ozaki, H., Chiang, P.C., Sumi, M., Tanaka, M., Koga, Y., Bourauel, C. and Yoshida, N. (2014). Effect of bracket slot and archwire dimensions on anterior tooth movement during space closure in sliding mechanics: a 3-dimensional finite element study. *American Journal of Orthodontics and Dentofacial Orthopedics*, 146(2), pp.166-174.

[202] Savadi, R.C. and Goyal, C. (2010). Study of biomechanics of porous coated root form implant using overdenture attachment: A 3D FEA. *The Journal of Indian Prosthodontic Society*, 10(3), pp.168-175.

[203] Garkunov, D.N. (1989). Self-organizing processes in tribological system under friction interaction. In: M. Hebda, A.V. Chichnadze, ed., *Handbook on tribology*, 1 st ed. Moscow: Machinostroenie, pp.288-323.

[204] Mortazavi, V. and Nosonovsky, M. (2011). Friction-induced pattern formation and Turing systems. *Langmuir*, 27(8), pp.4772-4779.

[205] Matijošius, T., Valsiūnas, I., Asadauskas, S. (2018). Tribological destruction of anodized al waste of different alloys in environment. *The International Conference Proceedings EcoBalt 2018*, p.31.

[206] Salem, A.M. (2005). Mechanism of Sliding Wear under Lubrication Conduction A1-Balqa Applied University. *Journal of Applied Sciences*, 5(5), pp.862-867.

[207] Hickman, J.A. (1997). *Polymeric Seals and Sealing Technology*. Shawbury: iSmithers Rapra Publishing, p.4.

[208] Sedlaček, M., Podgornik, B. and Vižintin, J. (2009). Influence of surface preparation on roughness parameters, friction and wear. *Wear*, 266(3-4), pp.482-487.
[209] Bakan, H.I. and Celis, J.P. (2012). Fretting behaviour of 316L stainless steel produced by powder injection moulding. *Kovove Materialy*, 50(1), pp.33-38.
[210] Beresnev, V.M., Smolyakova, M.Y., Pogrebnyak, A.D., Kaverina, A.S., Drobyshevskaya, A.A., Svetlichnyy, E.A. and Kolesnikov, D.A. (2014). Studying tribological characteristics of alumina-and zirconia-based ceramics. *Journal of Friction and Wear*, 35(2), pp.137-140.
[211] Staedler, T. and Schiffmann, K. (2001). Correlation of nanomechanical and nanotribological behavior of thin DLC coatings on different substrates. *Surface Science*, 482, pp.1125-1129.
[212] Holmberg, K., Laukkanen, A., Ronkainen, H., Wallin, K., Varjus, S. and Koskinen, J. (2006). Tribological contact analysis of a rigid ball sliding on a hard coated surface: Part II: Material deformations, influence of coating thickness and Young's modulus. *Surface and Coatings Technology*, 200(12-13), pp.3810-3823.
[213] Holmberg, K., Ronkainen, H., Laukkanen, A. and Wallin, K. (2007). Friction and wear of coated surfaces—scales, modelling and simulation of tribomechanisms. *Surface and Coatings Technology*, 202(4-7), pp.1034-1049.
[214] Ryall, M.J., Hewson, N., Parke, G.A.R. and Harding, J.E. (2000). *The manual of bridge engineering*. London: Thomas Telford, p.704.
[215] Liu, D., Atkinson, H.V., Kapranos, P., Jirattiticharoean, W. and Jones, H. (2003). Microstructural evolution and tensile mechanical properties of thixoformed high performance aluminium alloys. *Materials Science and Engineering: A*, 361(1-2), pp.213-224.
[216] Moiseyev, V.N. (2005). *Titanium alloys: Russian aircraft and aerospace applications*. Boca Raton: CRC press, p.50.
[217] Iordanoff, I. and Khonsari, M.M. (2004). Granular lubrication: toward an understanding of the transition between kinetic and quasi-fluid regime. *Journal of Tribology*, 126(1), pp.137-145.
[218] Dmitriev, A.I., Popov, V.L. and Psakhie, S.G. (2006). Simulation of surface topography with the method of movable cellular automata. *Tribology International*, 39(5), pp.444.
[219] Myshkin, N.K. (2000). Friction transfer film formation in boundary lubrication. *Wear*, 245(1-2), pp.116-124.

[220] Menezes, P., Kailas, S. and Lovell, M. (2012). Tribological response of materials during sliding against various surface textures. In: J.P. Davim, ed., *Materials and Surface Engineering*, 1st ed. Sawston: Woodhead Publishing, pp.207-242.

[221] Sollazzo, V., Pezzetti, F., Scarano, A., Piattelli, A., Bignozzi, C.A., Massari, L., Brunelli, G. and Carinci, F. (2008). Zirconium oxide coating improves implant osseointegration in vivo. *Dental Materials*, 24(3), pp.357-361.

[222] Guess, P.C., Att, W. and Strub, J.R. (2012). Zirconia in fixed implant prosthodontics. *Clinical Implant Dentistry and Related Research*, 14(5), pp.633-645.

[223] Zhao, T., Li, Y., Zhao, X., Chen, H. and Zhang, T. (2012). Ni ion release, osteoblast–material interactions, and hemocompatibility of hafnium-implanted NiTi alloy. *Journal of Biomedical Materials Research Part B: Applied Biomaterials*, 100(3), pp.646-659.

[224] Rituerto Sin, J., Neville, A. and Emami, N. (2014). Corrosion and tribocorrosion of hafnium in simulated body fluids. *Journal of Biomedical Materials Research Part B: Applied Biomaterials*, 102(6), pp.1157-1164.

[225] Berdova, M., Liu, X., Wiemer, C., Lamperti, A., Tallarida, G., Cianci, E., Fanciulli, M. and Franssila, S. (2016). Hardness, elastic modulus, and wear resistance of hafnium oxide-based films grown by atomic layer deposition. *Journal of Vacuum Science & Technology A: Vacuum Surfaces and Films*, 34(5), p.051510.

[226] Benouareth, K., Tristant, P., Jaoul, C., Le Niniven, C., Nouveau, C., Dublanche-Tixier, C. and Bouabellou, A. (2016). Study of the interaction between a Zirconium thin film and an EN C100 steel substrate: temperature effect. *Vacuum*, 125, pp.234-239.

[227] Wojcieszak, D., Mazur, M., Indyka, J., Jurkowska, A., Kalisz, M., Domanowski, P., Kaczmarek, D. and Domaradzki, J. (2015). Mechanical and structural properties of titanium dioxide deposited by innovative magnetron sputtering process. *Materials Science-Poland*, 33(3), pp.660-668.

[228] Bikulčius, G., Češūnienė, A., Matijošius, T., Selskienė, A. and Pakštas, V. (2019). Investigation of the properties of Cr coatings deposited in an improved Cr (III) electrolyte. *Chemija*, 30(2), pp.69-77.

[229] Padgurskas, J., Snitka, V., Jankauskas, V. and Andriušis, A. (2006). Selective transfer phenomenon in lubricated sliding surfaces with

copper and its alloy coatings made by electro-pulse spraying. *Wear*, 260(6), pp.652-661.

[230] Kim, H.S., Kim, D.H., Hahn, J.H. and Ahn, H.S. (2011). Friction Behavior of Oil-Enriched Nanoporous Anodic Aluminum Oxide Film. *Tribology and Lubricants*, 27(4), pp.193-197.

[231] Mihály, J., Sterkel, S., Ortner, H.M., Kocsis, L., Hajba, L., Furdyga, É. and Mink, J. (2006). FTIR and FT-Raman spectroscopic study on polymer based high pressure digestion vessels. *Croatica Chemica Acta*, 79(3), pp.497-501.

[232] Zimmermann, R., Strauss, J.G., Haemmerle, G., Schoiswohl, G., Birner-Gruenberger, R., Riederer, M., Lass, A., Neuberger, G., Eisenhaber, F., Hermetter, A. and Zechner, R. (2004). Fat mobilization in adipose tissue is promoted by adipose triglyceride lipase. *Science*, 306(5700), pp.1383-1386.

[233] Quehenberger, O., Armando, A.M., Brown, A.H., Milne, S.B., Myers, D.S., Merrill, A.H., Bandyopadhyay, S., Jones, K.N., Kelly, S., Shaner, R.L. and Sullards, C.M. (2010). Lipidomics reveals a remarkable diversity of lipids in human plasma. *Journal of Lipid Research*, 51(11), pp.3299-3305.

[234] Otero, V., Sanches, D., Montagner, C., Vilarigues, M., Carlyle, L., Lopes, J.A. and Melo, M.J. (2014). Characterisation of metal carboxylates by Raman and infrared spectroscopy in works of art. *Journal of Raman Spectroscopy*, 45(11-12), pp.1197-1206.

[235] Fei, G., Lujia, H. and Xian, L. (2017). Vibration spectroscopic technique for species identification based on lipid characteristics. *International Journal of Agricultural and Biological Engineering*, 10(3), pp.255-268.

[236] Miranda, A.M., Castilho-Almeida, E.W., Ferreira, E.H.M., Moreira, G.F., Achete, C.A., Armond, R.A., Dos Santos, H.F. and Jorio, A. (2014). Line shape analysis of the Raman spectra from pure and mixed biofuels esters compounds. *Fuel*, 115, pp.118-125.

[237] Mukhurov, N.I., Zhvavyi, S.P., Terekhov, S.N., Panarin, A.Y., Kotova, I.F., Pershukevich, P.P., Khodasevich, I.A., Gasenkova, I.V. and Orlovich, V.A. (2008). Influence of electrolyte composition on photoluminescent properties of anodic aluminum oxide. *Journal of Applied Spectroscopy*, 75(2), pp.214-218.

[238] Stojadinovic, S., Nedic, Z., Belca, I., Vasilic, R., Kasalica, B., Petkovic, M. and Zekovic, L. (2009). The effect of annealing on the photoluminescent and optical properties of porous anodic alumina

films formed in sulfamic acid. *Applied Surface Science*, 256(3), pp.763-767.

[239] Santos, A., Alba, M., Rahman, M.M., Formentín, P., Ferré-Borrull, J., Pallarès, J. and Marsal, L.F. (2012). Structural tuning of photoluminescence in nanoporous anodic alumina by hard anodization in oxalic and malonic acids. *Nanoscale Research Letters*, 7(1), p.228.

[240] Matijošius, T., Kalužina, A., Bikulčius, G., Valsiūnas, I., Asadauskas, S. (2018) Comparison of liquid friction trends between steel and several bioceramic surfaces. *Conference of PhD Students and Young Researchers FizTech2018*, p.42.

[241] Baillon, F., Provost, E. and Fürst, W. (2008). Study of titanium (IV) speciation in sulphuric acid solutions by FT-Raman spectrometry. *Journal of Molecular Liquids*, 143(1), pp.8-12.

[242] Meier, R.J., Csiszar, A. and Klumpp, E. (2006). On the Interpretation of the 1100 cm-1 Raman Band in Phospholipids and Other Alkyl-Containing Molecular Entities. *The* Journal of Physical Chemistry B, 110(12), pp.5842-5844.

[243] Mathlouthi, M., Seuvre, A.M. and Koenig, J.L. (1986). FT-IR and laser-Raman spectra of cytosine and cytidine. *Carbohydrate Research*, 146(1), pp.1-13.

[244] Zubrytė, E. (2019). Sorption of cationic and anionic pollutants by hybrid organic and inorganic phase adsorbents (preparing PhD dissertation). Department of Chemical Engineering and Technology, Center for Physical Sciences and Technology, Vilnius.

[245] Chowdhury, J. and Ghosh, M. (2004). Adsorption of 3- and 4-benzoylpyridine on colloidal silver particles: a surface-enhanced Raman scattering study. *Journal of Raman Spectroscopy*, 35(12), pp.1023-1033.

[246] Hardcastle, F.D. and Wachs, I.E. (1988). Raman spectroscopy of chromium oxide supported on Al_2O_3, TiO_2 and SiO_2: a comparative study. *Journal of Molecular Catalysis*, 46(1-3), pp.173-186.

[247] Wojciechowski, K. and Szuster, L. (2016). [Azo-Hyd] Tautomerism and Structure of Selected Metal Complex Dyes AM1 and ZINDO/1 Methods. *Computational Chemistry*, 4(4), p.97-118.

[248] Hussain, G., Ather, M., Khan, M.U.A., Saeed, A., Saleem, R., Shabir, G. and Channar, P.A. (2016). Synthesis and characterization of chromium (III), iron (II), copper (II) complexes of 4-amino-1-(p-sulphophenyl)-3-methyl-5-pyrazolone based acid dyes and their applications on leather. *Dyes and Pigments*, 130, pp.90-98.

[249] Banerjee, S., Dubey, S., Gautam, R.K., Chattopadhyaya, M.C. and Sharma, Y.C. (2019). Adsorption characteristics of alumina nanoparticles for the removal of hazardous dye, Orange G from aqueous solutions. *Arabian Journal of Chemistry*, *12*(8), pp.5339-5354.

[250] Robinson, M., Pask, J.A. and Fuerstenau, D.W. (1964). Surface charge of alumina and magnesia in aqueous media. *Journal of the American Ceramic Society*, *47*(10), pp.516-520.

[251] Tajima, S., Baba, N., Shimizu, K. and Mizuki, I. (1976). Photoluminescence of anodic oxide films on aluminium. *Active and Passive Electronic Components*, 3(2), pp.91-95.

[252] Sui, R., Lo, J.M., Lavery, C.B., Deering, C.E., Wynnyk, K.G., Chou, N. and Marriott, R.A. (2018). Sol–Gel-Derived 2D Nanostructures of Aluminum Hydroxide Acetate: Toward the Understanding of Nanostructure Formation. *The Journal of Physical Chemistry C*, 122(9), pp.5141-5150.

[253] Lundgren, S.M., Persson, K., Mueller, G., Kronberg, B., Clarke, J., Chtaib, M. and Claesson, P.M. (2007). Unsaturated fatty acids in alkane solution: adsorption to steel surfaces. *Langmuir*, 23(21), pp.10598-10602.

[254] Liascukiene, I., Aissaoui, N., Asadauskas, S.J., Landoulsi, J. and Lambert, J.F. (2012). Ordered nanostructures on a hydroxylated aluminum surface through the self-assembly of fatty acids. *Langmuir*, 28(11), pp.5116-5124.

[255] Glovnea, R.P., Olver, A.V. and Spikes, H.A. (2005). Effectiveness of boundary lubricant additives on some coated surfaces. *Tribology and Interface Engineering Series*, 48, pp.135-143.

[256] Parry, G.A., Roberts, J.E. and Taylor, A.J. (1950). Factors which affect the gelling characteristics of aluminium soaps. *Proceedings of the Royal Society of London. Series A. Mathematical and Physical Sciences*, 200(1061), pp.148-154.

[257] Moldoveanu, S.C. (2009). *Pyrolysis of organic molecules: applications to health and environmental issues*. Amsterdam: Elsevier, pp. 482-483.

[258] Young, I.S. and Woodside, J.V. (2001). Antioxidants in health and disease. *Journal of Clinical Pathology*, 54(3), pp.176-186.

[259] Choe, E. and Min, D.B. (2005). Chemistry and reactions of reactive oxygen species in foods. *Journal of Food Science*, 70(9), pp.R142-R159.

[260] Halvorsen, B.L. and Blomhoff, R. (2011). Determination of lipid oxidation products in vegetable oils and marine omega-3 supplements. *Food and Nutrition Research*, 55(1), p.5792.
[261] Yang, S., Lee, S., Bajpai, I. and Kim, S. (2015). Hydrothermal treatment of Ti surface to enhance the formation of low crystalline hydroxyl carbonate apatite. *Biomaterials Research*, 19(1), p.4.
[262] Bhasin, S.K., Khare, R. and Gupta, R. (2013). *Pharmaceutical Organic Chemistry*. New Delhi: Elsevier Health Sciences, p.470.
[263] Texter, J. (2001). *Reactions And Synthesis In Surfactant Systems*. New York: CRC Press, p.11.

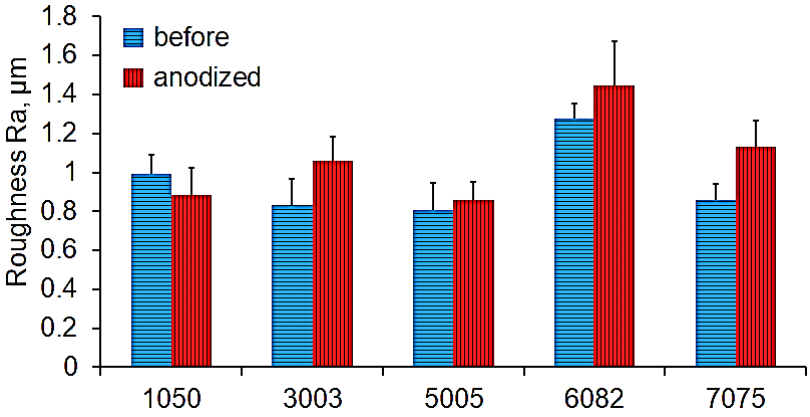

Fig. S1. *Influence of Al alloys on roughness before and after anodization*

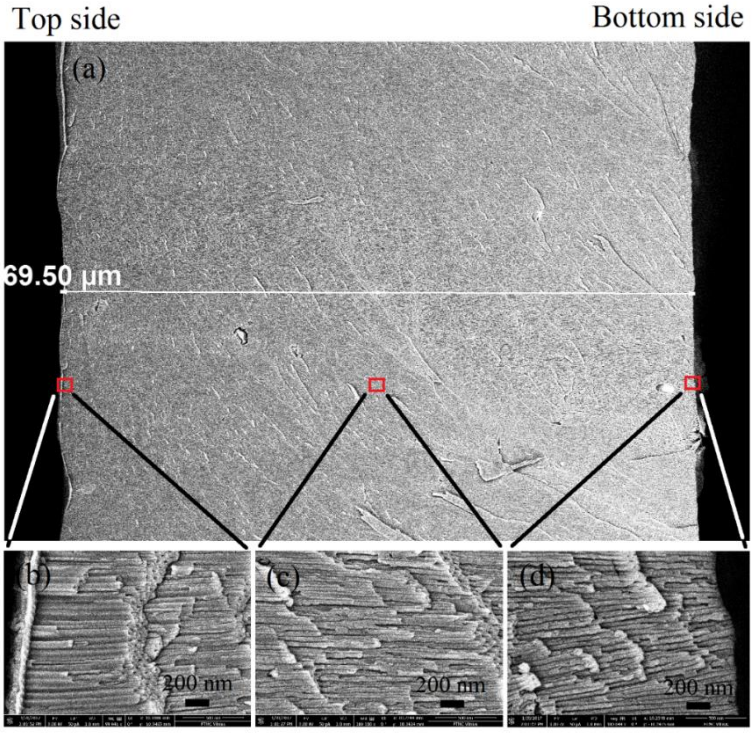

Fig. S2. *Scanning electron microscopy images of the cross-section of fully anodized foil at 15 °C: (a) the full cross-sectional view of the fully anodized foil; (b–d) magnified images of the pores in various cross-sectional spots, copied from [152]*

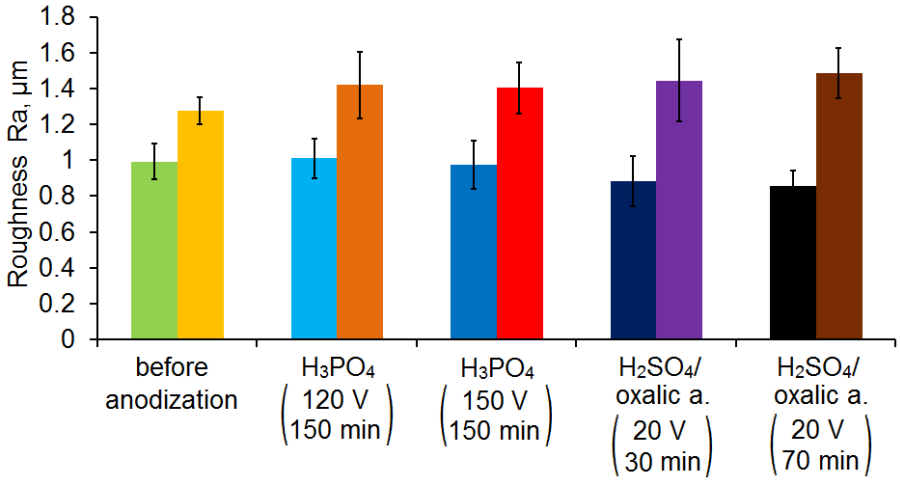

Fig. S3. *Influence of Al alloys on surface roughness before and after anodization (left bars – 1050, right bars – 6082)*

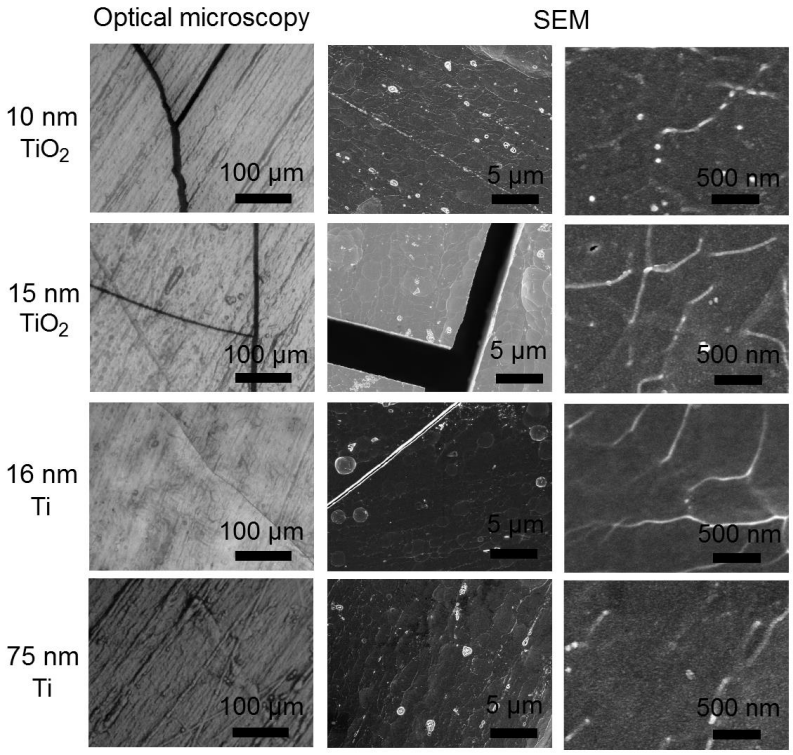

Fig. S4. *SEM and optical microscopy images of anodized 1050 alloys with nanothin TiO_2 and Ti layers, deposited either by ALD or sputtering*

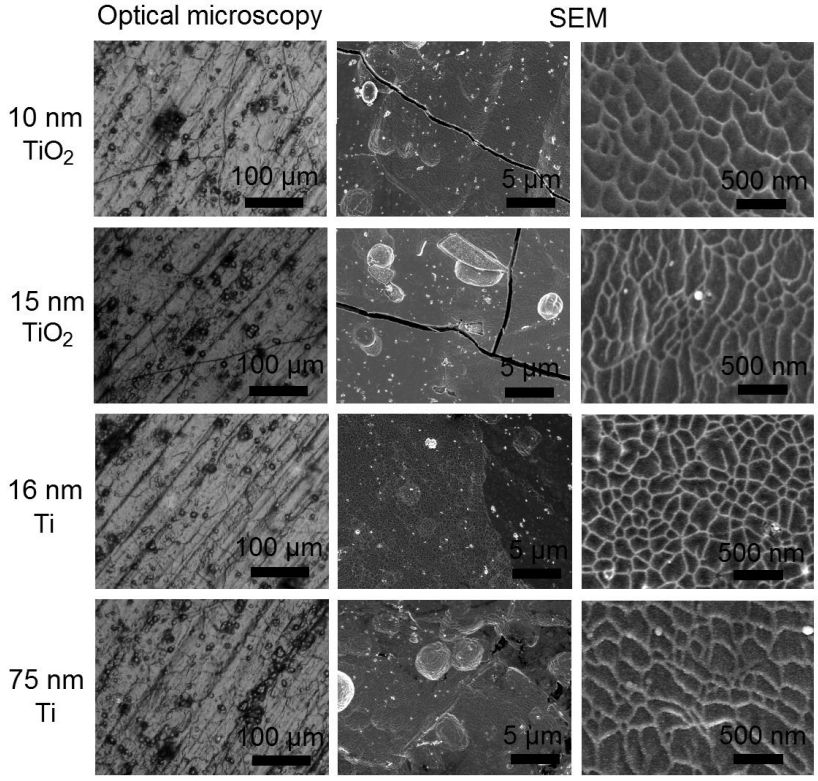

Fig. S5. *SEM and optical microscopy images of anodized 6082 alloys with nanothin TiO_2 and Ti layers, deposited either by ALD or sputtering*

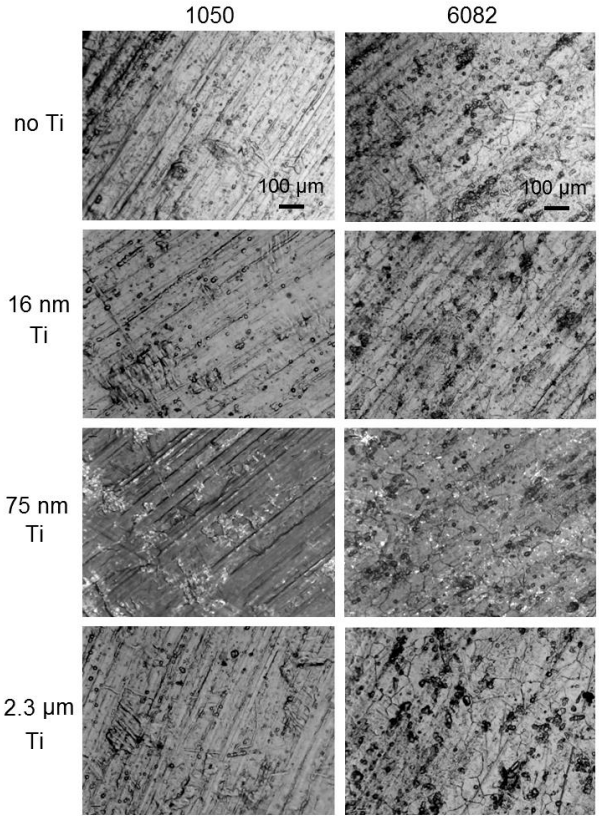

Fig. S6. *Optical images of Al alloys without anodization before and after sputtering, copied from [150]*

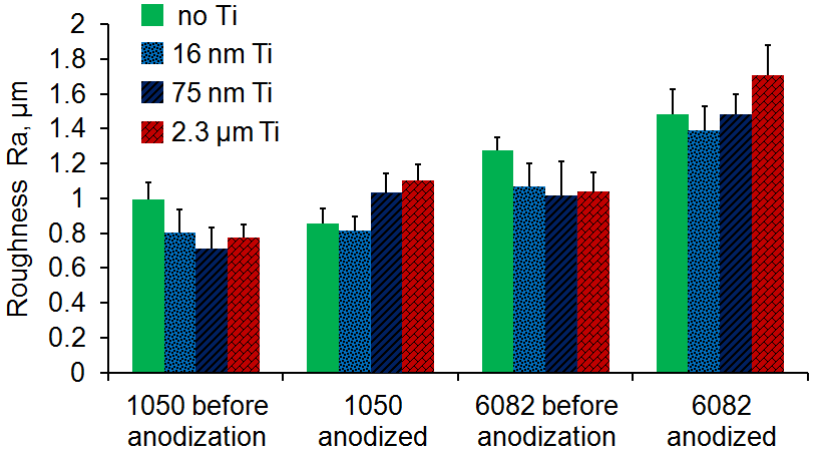

Fig. S7. *Average roughness Ra of untreated and anodized surfaces with and without Ti layers, deposited by sputtering, copied from [150]*

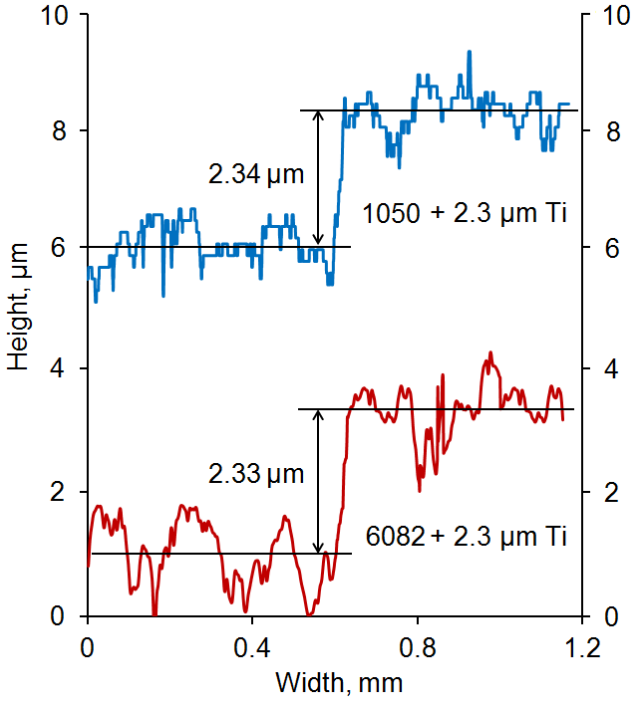

Fig. S8. *Height shift on the threshold between hard anodized Al alloys and sputtered Ti layers, adapted from [150]*

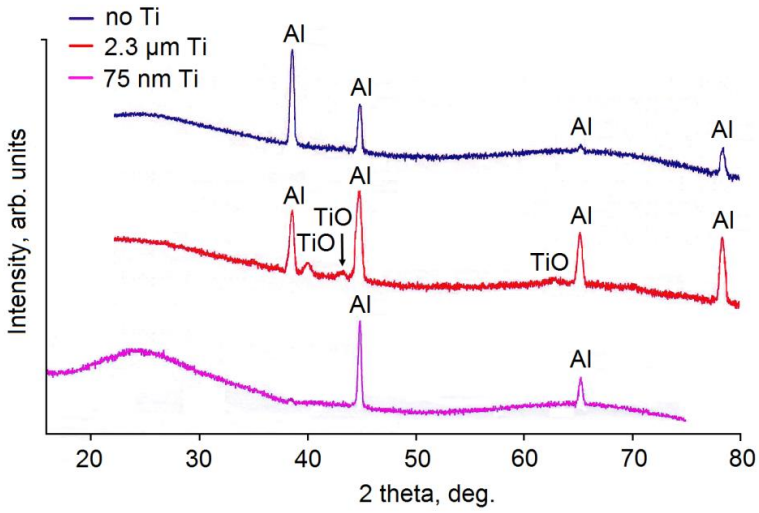

Fig. S9. *GIXRD spectra of anodized coatings with or without 75 nm and 2.3 µm Ti layers of 1050 alloy*

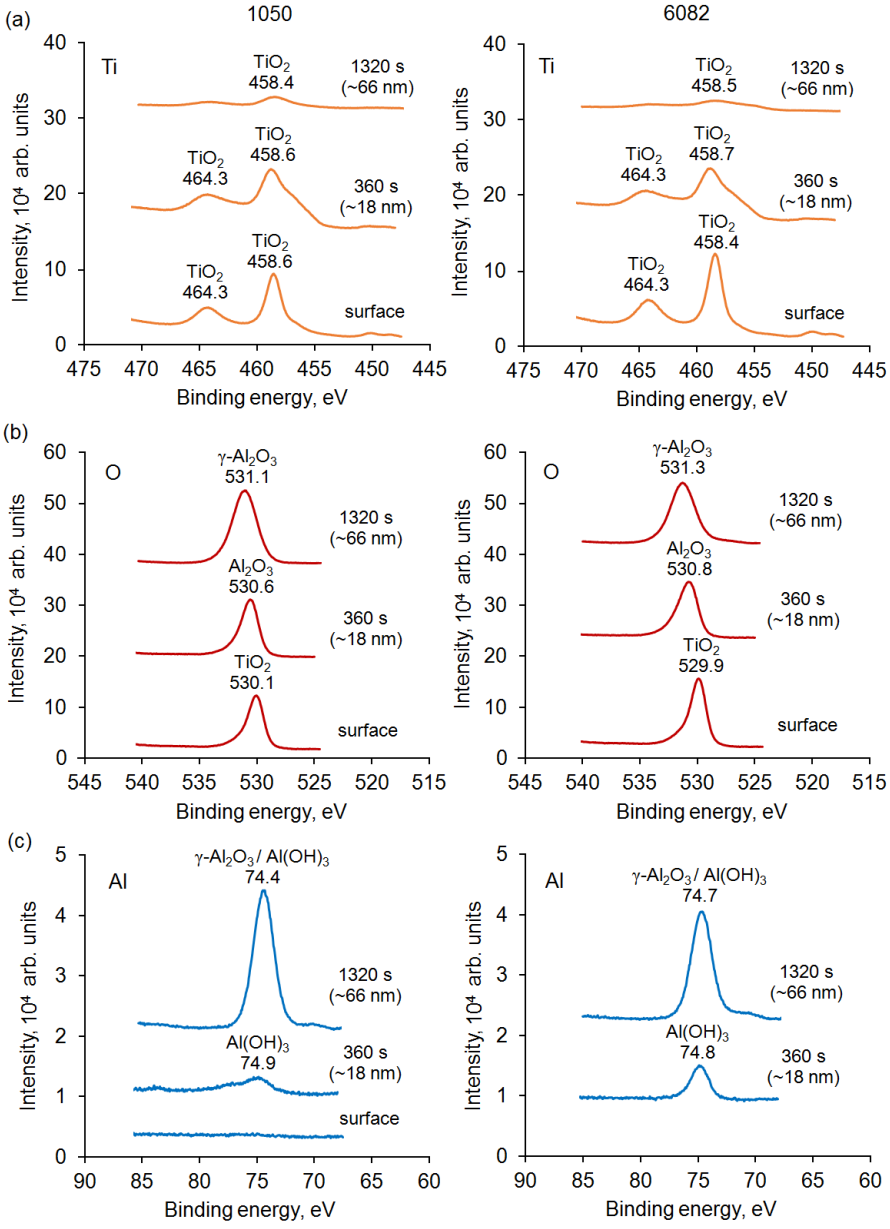

Fig. S10. *Titanium 2p (a), oxygen 1s (b) and aluminum 2p (c) XPS spectra of TiO_2 layers deposited on anodized 1050 (left) and 6082 (right) alloys by ALD before or after 360 s and 1320 s of etching with Ar^+ ions*

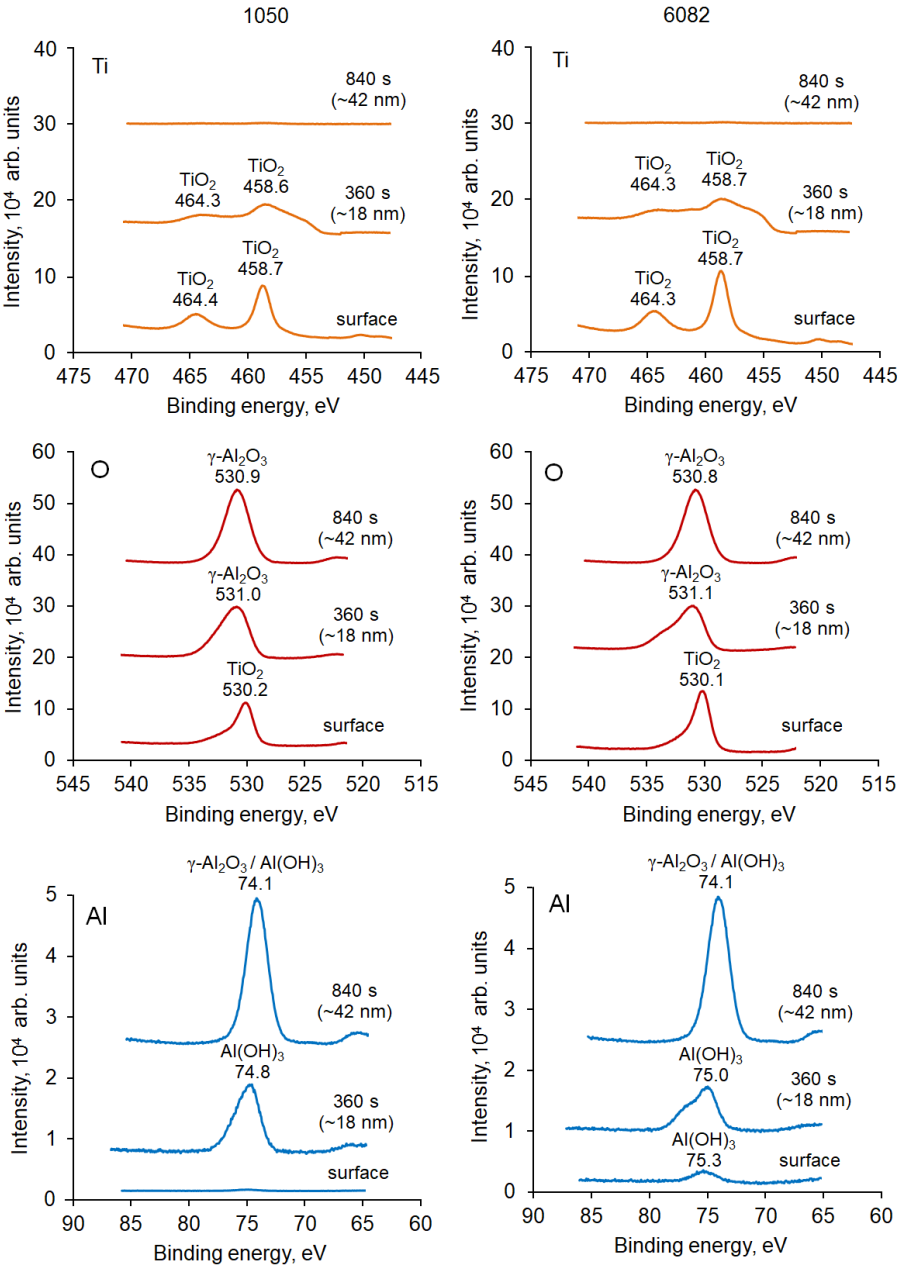

Fig. S11. *Titanium 2p (a), oxygen 1s (b) and aluminum 2p (c) XPS spectra of Ti layers deposited on anodized 1050 (left) and 6082 (right) alloys by sputtering before or after 360 s and 840 s of etching with Ar^+ ions*

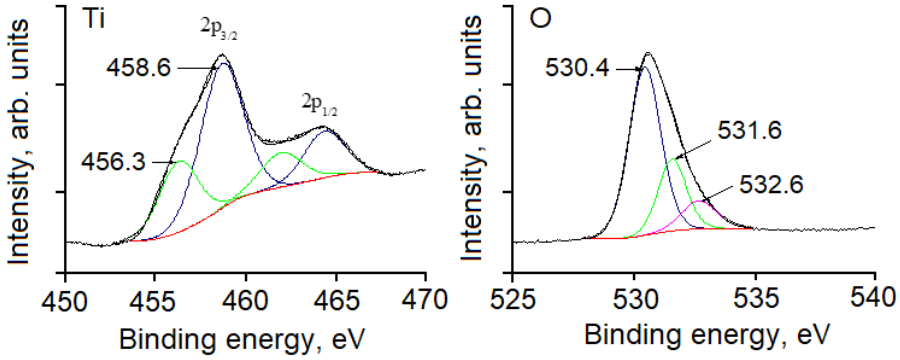

Fig. S12. *Titanium 2p (left) and oxygen 1s (right) XPS spectra and curve-fitting analysis of Ti layer deposited on anodized 6082 alloy by sputtering after 60 s of etching with Ar^+ ions*

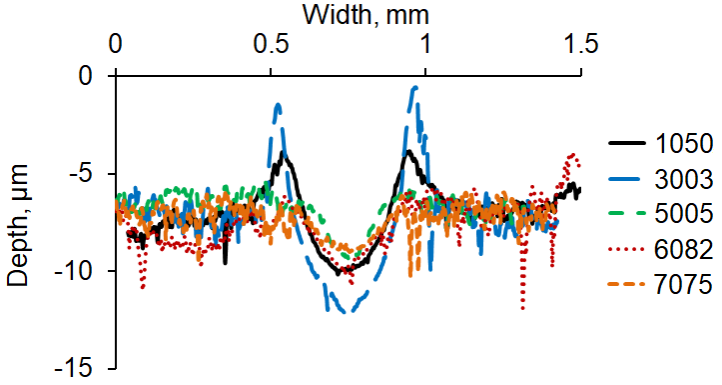

Fig. S13. *Wear profiles of hard anodized Al alloys after 500 friction cycles under 10 N load, against a steel ball*

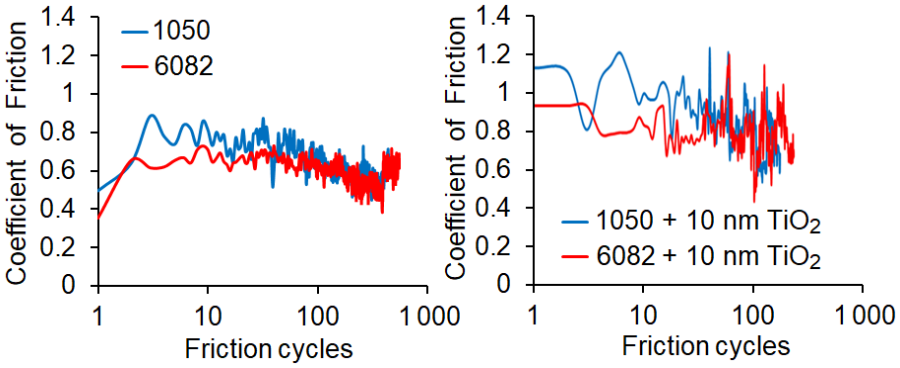

Fig. S14. *Influence of TiO_2 layer of 10 nm thickness on friction before (left) and after (right) ALD deposition of untreated 1050 and 6082 alloys under 1 N load, against a steel ball*

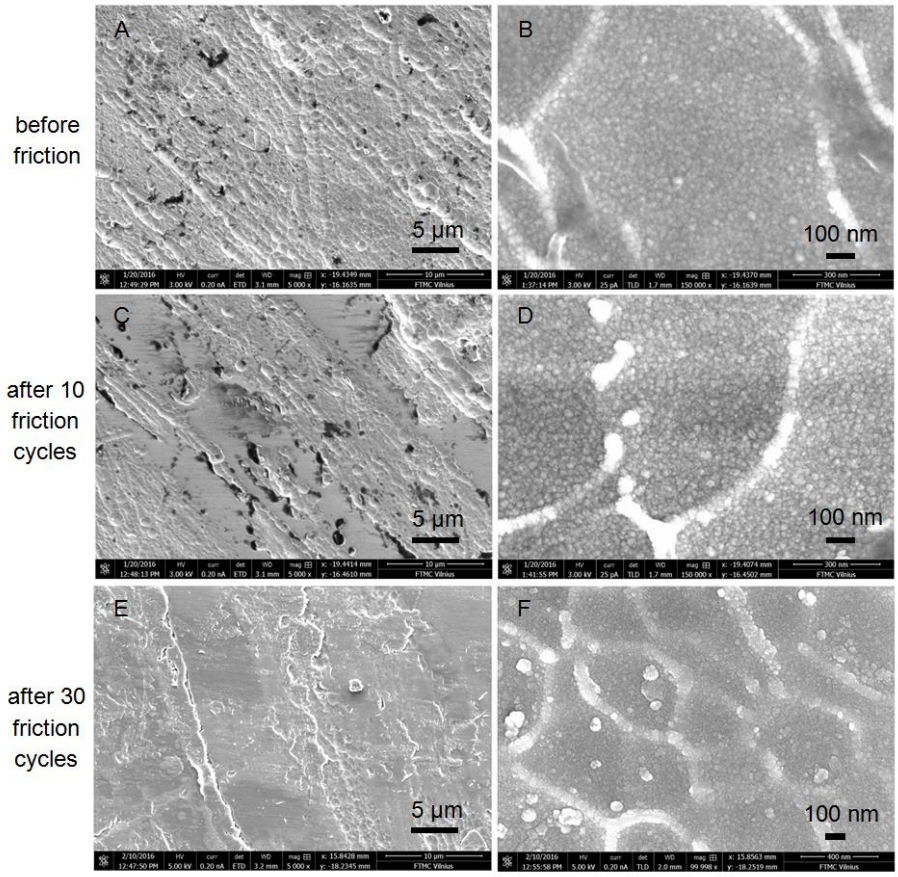

Fig. S15. *SEM images of friction-induced transformations of 75 nm Ti layer surface after 10 and 30 friction cycles on anodized 1050 alloy under 10 N load, copied from [150]*

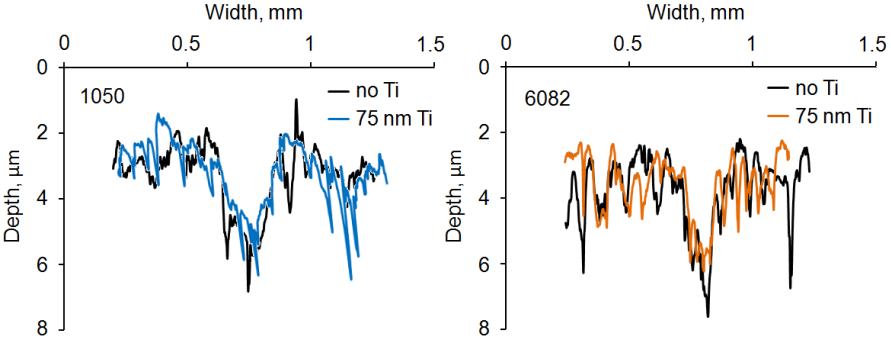

Fig. S16. *Wear profiles of hard anodized 1050 and 6082 alloys with 75 nm Ti layer after 30 friction cycles under 2 cm/s velocity and 10 N load*

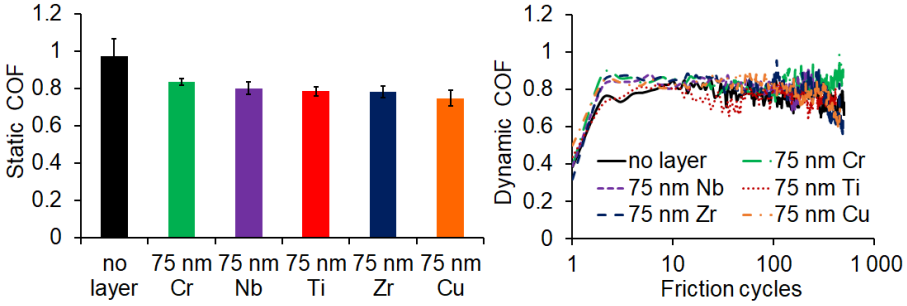

Fig. S17. *Influence of nanothin layers of 75 nm thickness on static (top) and dynamic (bottom) friction of untreated 6082 alloys under 10 N load*

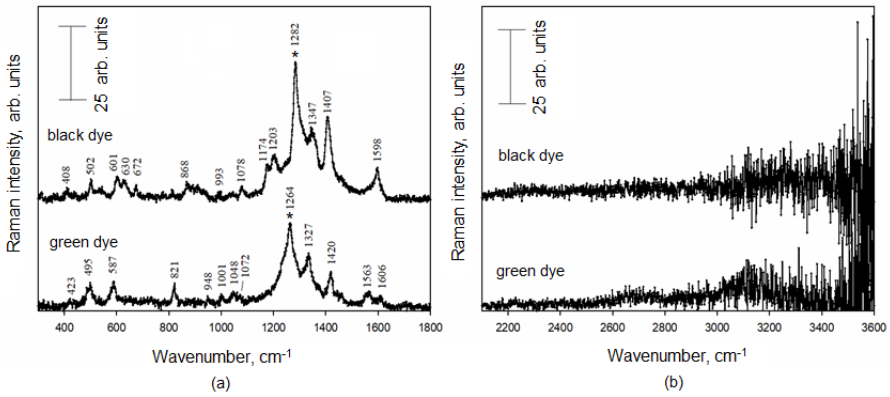

Fig. S18. *Near-field (a) and far-field (b) Raman spectra of azo dyes after 30 min of drop deposition on anodized Al foil (upper curve – black dye, lower curve – green dye)*

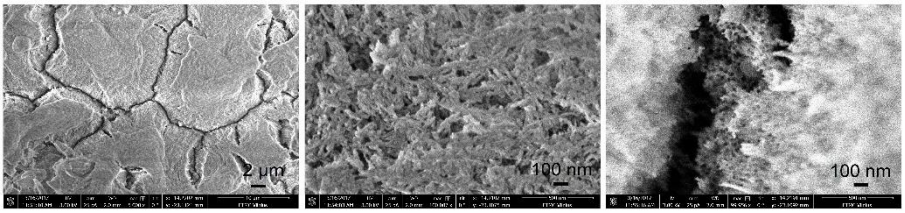

Fig. S19. *SEM images of hard anodized 6082 alloys obtained after 150 min at 30 °C under different magnifications*

ACKNOWLEDGMENTS

I want to thank my supervisor Dr Svajus Asadauskas for scientific advice, knowledge and support all those study years starting from Master degree. I am very grateful for everyone who helped me with the research, the preparation of the publications and the writing of the dissertation.

I am thankful for all colleges and scientists from the Department of Chemical Engineering and Technology and the Department of Electrochemical Material Science including Dr. Sigitas Jankauskas, Dr. Gedvidas Bikulčius, Dr. Alma Ručinskienė, Dr. Ignas Valsiūnas, Prof. Habil. Dr. Eimutis Juzeliūnas, Dr. Asta Grigucevičienė, Dr. Konstantinas Leinartas, Dr. Arūnas Jagminas, Dr. Svetlana Lichušina, Dr. Povilas Miečinskas, Laurynas Staišiūnas, Irina Demčenko and other scientists for the help, experimental assistance, technical advice, friendly working environment and assistance in preparing a dissertation. I am also grateful for Dr. Algirdas Selskis, Dr. Giedrius Stalnionis, Dr. Vitalija Jasulaitienė, Dr. Vidas Pakštas, Dr. Sandra Stanionytė from the Department of Characterisation of Materials Structure for assistance in characterization of anodized and nanostructured coatings. I am thankful for Prof. Habil. Dr. Gediminas Niaura, Dr. Ilja Ignatjev and other scientists from Department of Organic Chemistry for Raman spectroscopy studies. Also thankful for Dr. Mindaugas Gedvilas and Dr. Paulius Gečys from the Department of Laser Technologies for the advice of static friction evaluation and texturing studies. Experimental assistance of VU students Daiva Vozgirdaitė and Anastasija Kalužina is cordially appreciated.

I am also very grateful for Prof. Augustas Pivoriūnas and Dr. Alina Čebatariūnienė from the Department of Stem Cell Biology of Centre for Innovative Medicine and FTMC researchers Dr. Arūnas Stirkė, Justina Kavaliauskaitė, Auksė Kazlauskaitė, Monika Marija Kirsnytė and others from the Department of Functional Materials and Electronics for biocompatibility studies and collaboration in publishing the results presented in this thesis.

Thanks to the Agency for Science, Innovation and Technology for financial support participating in the international conference “Nanotech France 2018.” Also thankful for the Research Council of Lithuania for financial support.

LIST OF PUBLICATIONS AND THEIR COPIES

1. Matijošius, T., Ručinskienė, A., Selskis, A., Stalnionis, G., Leinartas, K. and Asadauskas, S.J. (2016). Friction reduction by nanothin titanium layers on anodized alumina. *Surface and Coatings Technology*, 307, pp.610-621.
2. Matijošius, T., Asadauskas, S.J., Bikulčius, G., Selskis, A., Jankauskas, S., Višniakov, J. and Ignatjev, I. (2019). Determination of the dye penetration rate in porous aluminum oxide using Raman spectroscopy. *Coloration Technology*, 135(4), pp.275-282.

1st publication

Friction reduction by nanothin titanium layers on anodized alumina

Matijošius, T., Ručinskienė, A., Selskis, A., Stalnionis, G., Leinartas, K. and Asadauskas, S.J.

Surface and Coatings Technology, 307, pp.610-621 (2016)
DOI: 10.1016/j.surfcoat.2016.09.083

Surface & Coatings Technology 307 (2016) 610–621

Contents lists available at ScienceDirect

Surface & Coatings Technology

journal homepage: www.elsevier.com/locate/surfcoat

Friction reduction by nanothin titanium layers on anodized alumina

Tadas Matijošius, Alma Ručinskienė, Algirdas Selskis, Giedrius Stalnionis, Konstantinas Leinartas, Svajus J. Asadauskas *

Institute of Chemistry, Center for Physical Sciences and Technology (FTMC), Vilnius, Lithuania

ARTICLE INFO

Article history:
Received 31 May 2016
Revised 15 September 2016
Accepted in revised form 30 September 2016
Available online 1 October 2016

Keywords:
Anodising
Aluminum oxide
Magnetron sputtering
Pin on disc
Titanium coatings

ABSTRACT

Anodization of aluminum improves hardness, paintability or corrosion resistance but incidental friction may lead to major surface damages of anodized parts. Industrial alloys 1050A and 6082 were anodized to produce 60 μm coatings, then Ti layers of 16 nm, 75 nm and 2.3 μm thickness were deposited by magnetron sputtering. Reciprocal ball-on-plate tribotests under relatively high load of 10 N was used and high friction was observed on alloys before anodization with or without Ti layers. On anodized coatings friction was much lower but abrasion remained rapid. Deposition of 16 and 75 nm Ti layers prevented abrasion for significant durations, especially on anodized 6082, whose substrate was harder. Counterintuitively, deposition of 2.3 μm Ti layers was much less effective. On specimens with 75 nm Ti layers Energy-Dispersive X-ray Spectroscopy showed major delocalization of Ti aggregates in the friction zone with Ti concentration gradients of 10 times within 30 μm. Such material transfer might relate to improved tribological characteristics. Surprisingly good performance of 16 and 75 nm specimens suggests that incidental friction can be successfully inhibited by depositing nanothin Ti layers. Further studies of Ti deposition may lead to significant improvements in industrial anodization technology.

1. Introduction

Aluminum alloys are often anodized (electrochemically oxidized) to increase surface hardness, provide better paintability, improve corrosion resistance and other technical features [1–3]. Usually, highly porous nanostructured coatings of alumina (Al_2O_3) with vertical nanopores of uniform size and distribution are produced after anodizing [4,5]. Industrially, anodization is often carried out in sulfuric acid-based electrolytes, where positively charged Al is attacked by anions (HSO_4^-, $RCOO^-$, etc.). This electrochemically oxidizes the metal mostly into Al_2O_3, forming anodized coatings of various thickness, sometimes 100 μm or more. Despite better hardness, wear rate of anodized coatings is still high [5] presenting a major problem in many field applications. Although expensive technologically, metal or polymer based solid lubricants are often applied to reduce friction and wear of anodized surface. Incorporation of MoS_2 [6], nickel composite (e.g. Co-Ni-P) [7] and other substances might give a needed success in improving wear resistance. Nevertheless, industrially the most widespread method is still based on polytetrafluoroethylene, which usually reduces Coefficient of Friction (COF) to less than 0.2 [8] by functioning as a barrier lubricant.

In previous studies [9,10] titanium oxides and nitrides showed some effectiveness as protective, anti-frictional layers for various substrates, including anodized coatings. Particularly, coatings of TiN, TiSiN, TiSiCN demonstrated excellent wear resistance and low friction with COF 0.15–0.25 [9]. When Ti is exposed to air, a passive oxide film is spontaneously formed on its surface. Usually, such amorphous film is 5–10 nm thick and contains three layers: TiO next to metallic Ti, Ti_2O_3 in the middle and anatase TiO_2 [11] on the outer part. Titanium dioxide (TiO_2) is very stable, insoluble, non-toxic and chemically inert, resistant to most acids, alkalis and organic compounds. Because of chemical stability, corrosion-resistance, biocompatibility, non-toxicity and other desirable properties, deposition of Ti/TiO_2 layers is used in many applications, including biomedical materials due to effective protective and osseointegrative (direct bone to implant anchorage) properties [12,13]. For various technological purposes Ti layers have also been deposited on anodized alumina by magnetron sputtering [14], chemical vapor deposition [15], spraying [16], plasma electrolytic oxidation [17] and other methods. Deposition of Ti layers gains recognition in many high-tech processes, while anodization remains a major tool in the manufacture of advanced materials. Manipulation with nanopore sizes, their density, roughness, application of fillers or deposited layers and other parameters gives an opportunity to control wettability, permeability, adhesion, resistance, biocompatibility, nanostructurization and other properties of anodized surfaces. Many industrial items are exposed to friction during field applications, however, tribological properties of Ti layers on anodized alumina have not yet been studied in detail.

Abbreviations: 1050A, high purity industrial aluminum alloy; 6082, industrial aluminum alloy suitable for anodization; COF, Coefficient of Friction; EDS, Energy-Dispersive X-ray Spectroscopy; SEM, Scanning Electron Microscopy; Ti, titanium.

* Corresponding author at: Sauletekio 3, Vilnius LT-10222, Lithuania.
E-mail address: asadauskas@chi.lt (S.J. Asadauskas).

http://dx.doi.org/10.1016/j.surfcoat.2016.09.083
0257-8972/

Some other types of substrates have already been investigated to some extent for tribological behavior of Ti or TiO_2 layers on fasteners [18], implants [19], turbine engines [20], aerospace or marine applications [21]. Still, the data volume remains limited, making it difficult or impossible to predict the effect of deposited Ti on frictional characteristics. In one particular study magnetron sputtering was used to deposit Ti/TiO_2 layers of ~200 nm thickness on Ti6Al4V substrate [19]. This reduced COF to 0.5 and assured stable friction for 10,000 cycles under 0.49 N load, 3 cm/s rotation speed with 4 mm rotation radius against 6 mm diameter SiC balls. From these and related studies it might appear that deposited Ti layers reduced friction only marginally compared to alloys without coating. In contrast, better achievements could be observed in Ti based multilayer coatings [9,22], where COF went down to 0.15. Such friction reduction was quite remarkable for dry coatings, unfortunately, no further study to investigate the causes of the tribological improvement was made available. Also, authors employed relatively light loads of 0.1 kgf and less, which would not always be relevant in field uses, where incidental friction might take place during manufacture, packaging, transportation, installation etc. So it remains unknown whether Ti-containing multilayers can provide friction reduction under more severe tribological regimes.

In this study the effectiveness of Ti layers was investigated under much higher load of 10 N. In addition, very few reports discuss the dependence of tribological properties on the thickness of Ti layers, so this aspect received particular attention in this investigation. Resistance to friction and wear under higher interfacial pressures is important for many applications, where anodized alumina is used, such as fasteners, positioners, biomedical devices [23], sliding surfaces, aerospace, robotic equipment, etc. Instead of pure aluminum, industrially relevant alloys 1050A and 6082 were utilized, while tribotests employed conventional ball-on-plate methodology, typically used in friction studies of anodized alumina and many other coatings.

2. Experimental

Two main processes were used for surface preparation: 1) anodization and 2) magnetron sputtering, see Fig. 1. The obtained specimens were evaluated by using optical and scanning electron microscopy. Then their friction and wear was compared using ball-on-plate tribotests. Most of the equipment, procedures and materials, which were used in this study, had already been previously presented in several proceedings articles [24–27]. Briefly, their descriptions are provided below.

2.1. Materials

Two Al alloys, 1050A of 99.62% purity (0.34% Fe; 0.1% Si; 0.01% Mn) and 6082 of 96.72% purity (1.1% Si; 1.02% Mg; 0.61% Mn; 0.54% Fe) with a sheet thickness of 1 mm and 2 mm respectively, from Aleris Rolled Products Germany GmbH were used as substrates. Reagent grade salts and electrolytes were employed for the anodization and laboratory grade solvents were used for cleaning and degreasing. Commercially available high purity Ti (99.995%) from Alfa Aesar GmbH (Germany) was used as magnetron sputtering target, Fig. 1, for deposition of Ti layers.

2.2. Anodization

The anodization was performed in H_2SO_4/oxalic acid electrolyte in compliance with Type III procedures. This type of electrolyte is widely used to produce relatively thick, hard Al_2O_3 coatings [2,4], so the referenced solutions and procedures were used as a basis for this study. Before anodization the disc-shaped specimens of 1.5 cm OD were etched in an alkaline solution of 30 g/L NaOH + 25 g/L Na_3PO_4 + 75 g/L Na_2CO_3 for 30 s at 60 °C. After rinsing in deionized water they were cleaned for 1–2 min in 10% HNO_3 and rinsed in water again. Then the discs were placed into the continuously mixed electrolyte of 175 g/L H_2SO_4 + 30 g/L $(COOH)_2 \cdot 2H_2O$ + 55.5 g/L $Al_2(SO_4)_3 \cdot 18H_2O$ at 15 °C and 200 A/m^2 anodic current density for 70 min. Coatings were periodically checked with CM-8825FN device (Guangzhou Landtek Instruments Co., China) to obtain 60 ± 10 μm thickness. After anodizing, the discs were immersed into 170 W ultrasonic bath VTUSC3 (Velleman, Belgium) and sonicated at full power for 10 to 20 min in deionized water without heat for rinsing. Then the discs were dried at 100 °C for 30 to 60 min and stored in dry environment for 1 to 7 days for further experiments.

2.3. Magnetron sputtering

Deposition of Ti layers of 16 nm, 75 nm and 2.3 μm thickness was performed on Al specimens with or without anodization by DC/RF magnetron sputtering device Univex 350 (Leybold Vacuum Systems, Germany). Before sputtering the discs of untreated alloys (without anodization) were etched in an alkaline solution for 30 s at 60 °C and cleaned for 1–2 min in 10% HNO_3 to remove all impurities of the surface. The specimens were placed into the rotary holder of the magnetron apparatus, the lid was closed and the chamber was vacuumized for at least 16 h before actual sputtering. The base pressure of the system was 250 μPa and the working pressure of Ar gas was kept constant at 250 mPa maintaining substrate temperature at 12 °C. Thermal regime was balanced using two controls: 1) cooling by circulating cold water through the magnetrons and the specimen holder; 2) heating with integrated quartz halogen lamps, interfaced via programmable "SHQ15A TC/PID" controller (AJA International, USA). The distance of 20–25 cm between the target and specimens was too large to significantly affect the temperature of substrate, when coating 16 nm and 75 nm Ti layers. Sputtering time, current and voltage were adapted to obtain a necessary thickness of Ti layers: 16 nm (t_1 = 15 min, I_1 = 100 mA, U_1 = 421 V),

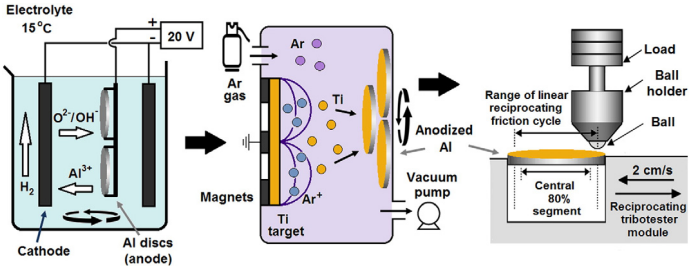

Fig. 1. The principal scheme of specimen preparation and investigation in three main stages (from left): anodization → magnetron sputtering → tribotesting / microscopy.

75 nm ($t_2 = 30$ min, $I_2 = 200$ mA, $U_2 = 420$ V) and 2.3 μm ($t_3 = 30$ min, $I_3 = 400$ mA, $U_3 = 375$ V). The rotary sample holder with 6 specimens was turning during the sputtering process at 18 rpm to assure uniform patterns of Ti deposition.

Along with Al discs, a quartz monocrystal was also inserted into the device when the thinnest Ti layer was deposited in order to determine its weight by quartz crystal microgravimetry via resonator frequency change according to Sauerbrey ratio [28]. The resonator mass changes were translated into Ti layer thickness of 16 nm. Cross-sections of several discs were made and SEM showed that 75 nm thickness was obtained, as described in §3. Deposition of the thickest Ti layer was performed by moving the specimens 3 times closer to Ti target. Profilometry of the discs showed that 2.3 μm thickness was obtained, as described in §3.

2.4. Tribological tests

For tribological measurements a Pin-on-Disc Tribometer (Anton Paar TriTec SA, Switzerland) was employed by utilizing a ball-on-plate linearly reciprocal configuration. As a stationary part, two types of 6 mm OD balls were used: 1) bearing steel 100Cr6 (96.5% purity, grade G20, hardness 800 HV and roughness R_a 0.02 μm) from SKF AB (Sweden) and corundum Al_2O_3 (99.8% purity, grade G16, hardness 2100 HV and roughness R_a 0.025 μm) from Ceratec (Belgium). The moving part was the Al disc, mounted on a pre-installed tribometer module. Linear reciprocal motion of 2 mm amplitude was maintained resulting in a track length of 4 mm and the total distance of 8 mm for one reciprocal friction cycle. At 2 cm/s velocity each friction cycle produced approx. 100 data points of 'instantaneous' friction force, whose values remained sufficiently similar throughout the selected range of the reciprocal motion, i.e. the middle 80% segment [24]. The average COF value was calculated automatically by taking an arithmetical average of modular friction values for the central 80% segment of the path. The results were presented as COF changes with progressing friction in terms of number of cycles. To ensure good reproducibility, each sample was tested 2 or more times at given conditions and the most representative runs were selected for the comparison between samples.

The tribotesting parameters of 10 N load, 2 mm amplitude and 2 cm/s velocity were held constant against a steel or corundum ball. Tribotest duration was either automatically limited due to excessive friction force because of increase in COF, or stopped after a specified number of friction cycles, such as 10, 30, 500 or 1000.

2.5. Microscopy studies

For optical microscopy analysis a B-353 MET model with Optikam B2.0 digital camera was used (Optika SRL, Italy). Topographical changes were evaluated under 200× and 400× magnifications. No polarization or color filters were used.

Scanning Electron Microscopy (SEM) images were obtained using dual beam system Helios NanoLab 650 (FEI, Netherlands) with a Schottky type field emission electron source and a Gallium (Ga) ion source at 1 500× and 150 000× magnification. Thin layers of Cr were applied on all specimens in order to obtain the necessary electrical conductivity on the surface by using a magnetron sputtering device Quorum Q150T ES (Judges Scientific Plc, UK), which led to the Cr coating thickness of 1.5 to 2.0 nm. SEM images were used to determine the nanopore diameter, distribution and surface porosity. Number of pores was established by calculating the nanopores in 0.2 × 0.2 μm segments of the surface in 3–4 random areas to get the average pore density.

Porosity (%) were calculated using the following equation [3]:

$$\eta = \frac{S_{pore} \cdot n}{S_{ox}} \cdot 100\% \quad (1)$$

where: S_{pore} is the average area of a nanopore opening, see Eq. (2), in μm^2;

S_{ox} is the area of surface oxide, obtained as the 2D area selected for the calculation minus S_{pore} n (i.e. minus the area of nanopore openings), in μm^2;

n is number of nanopores in the selected S_{ox} area.

The average area of a nanopore opening, S_{pore}, was calculated assuming a circular shape of the opening, Eq. (2):

$$S_{ox} = \pi \cdot ID^2/4 \quad (2)$$

where ID represented an average Internal Diameter (ID) of the nanopore from SEM measurements, in μm.

2.6. Cross-sectional evaluations

Several specimens were analyzed by producing localized cross-sections by focused Ga ion beaming with Helios NanoLab 650 (see above). Before the formation of cross-sections on the specimens (precoated with 1–2 nm Cr layers to increase conductivity for SEM inspection), a protective Platinum (Pt) overcoat of ~1 μm thickness was deposited by electron and ion beams. Such thick Pt overcoat helps avoiding the Ga ion damage to the edge regions of studied coating. The overcoat thickness was selected based on previous experimentation with this equipment [29–31] and recommendations of other researchers [32, 33]. Then the specimen was placed under the Ga ion beam exposure perpendicularly to the surface until the necessary depth was reached. Afterwards the specimen was shifted laterally several times for progressively shorter exposure to the Ga ion beam. In this manner a slope was formed on one side of the cross-section, so the observations could be made with the SEM probe, whose axis was tilted at 52° angle to the specimen surface. SEM images of the cross-section were studied at 3 kV accelerating voltage and 6.3 pA current. Horizontal field width was 2 μm and working distance about 4 mm.

The distribution of the elements in the cross-sections and wear tracks was also evaluated. Quantitative Energy-dispersive X-ray Spectrometry (EDS) was employed using a INCA spectrometer with X-Max 20 mm^2 Silicon-drift detector (Oxford Instruments, UK). EDS X-ray maps were obtained at 20 kV. Elemental composition was reported as wt.% percentage.

2.7. Surface roughness measurements

A contact profilometer Surftest SJ-210 was used to determinate roughness (R_a) of untreated, anodized and Ti coated surfaces. The contact needle with 2 μm tip radius was scanning the surfaces horizontally and transferred the data into the Image Plus software for the visualization. The R_a was calculated from at least 5 measurements on different locations within the same specimen. Four specimens were used to determine average R_a on samples before and after anodization, but without Ti layers, while 2 specimens were used to determine R_a of samples with Ti layers. For measuring the average elevation, the median planes were projected by equating the peak volumes above the planes with the void volumes underneath them.

2.8. Statistical analysis

Statistical analysis of tribological, surface roughness and nanopore measurements is presented as mean ± standard deviation. In case four or more runs were made on the same sample, *p*-value is listed also as "p =". In tribological experiments with samples without Ti layers the values were determined by testing 2 to 5 specimens. Roughness (R_a) was measured using 4 (without Ti layers) or 2 (with Ti layers) specimens for each sample. Nanopore density was calculated from 4 random 0.2 × 0.2 μm areas to obtain the average, meanwhile the nanopore diameters were determined from 10 measurements.

3. Results and discussion

As opposed to studies of anodized coatings on high purity aluminum, this report focused on two Al alloys with broad industrial recognition, 1050A and 6082. Due to dependence of friction mechanisms on inherent alloy characteristics, especially in the presence of metallurgical additives, it would be problematic to extend tribological observations from high purity aluminum to industrial metals. Being among the highest purity industrial alloys, 1050A contains 99.6 wt.% Al making it irrational to consider substrates with higher Al contents in this study. Both 1050A and 6082 alloys offer good anti-corrosive properties, but 1050A purity provides better formability and plasticity. Heat treatable 6082 alloy with 96.7 wt.% Al has higher strength and mechanical resistance primarily due to Mg and Si additives. A load of 10 N (or 1.02 kgf) was selected for comparing the tribological properties, which is higher than typical loads used in study of anodized alumina. However, this load is quite likely in field applications [34]. Also, 1050A and 6082 belong to different types of Al alloys. Therefore, the observations of relatively high loads and severe friction on both 1050A and 6082 alloys can be much more viable industrially than findings obtained solely from high purity aluminum studies under mild tribological regimes.

3.1. Effects of Ti layers on tribology of untreated Al surfaces

The tribological effectiveness of Ti layers was studied on both untreated and anodized Al alloys. Surface roughness of 1050A and 6082 was quite significant with R_a of 1.02 and 1.24 respectively. Their topography was somewhat irregular and contained many grain-like inclusions formed after Al rolling process. On 6082 grain boundaries of various sizes could be observed, some exceeding 100 μm, which would not be unusual in 6000 series alloys [35–36]. Although on 6082 grain boundaries remained visible even after depositing the 2.3 μm Ti layer, surface topography of both alloys could still be considered sufficiently similar for the purpose of tribological comparisons. Therefore, the alloys were not mechanically pre-treated before magnetron sputtering, anodization or tribotesting.

Initially, the influence of Ti layers on untreated Al surfaces without any anodization was evaluated. Magnetron sputtering was used to obtain separate specimens with 16 nm, 75 nm and 2.3 μm Ti layers on the top of untreated 1050A and 6082. The differences in surface characteristics before and after sputtering were not significant, as presented in Fig. S1 (see electronic Supplementary information).

As an interesting exception, it was observed that untreated surfaces with 75 nm Ti layers had blue color. As described by other researchers, such effect might be obtained due to light interference phenomena [37] of this layer thickness. Still, any changes in surface roughness were minor and could not be expected to lead to appreciable effects on friction and wear. The tribological properties of specimens with and without Ti layers (without anodization) were screened, showing high friction, Fig. 2.

Friction was so severe on 1050A specimen that COF even exceeded 1.0. On 6082 COF was also very high. Extreme friction was a result of abrasion, which began within just several friction cycles, forming clearly visible wear tracks. Even the thickest Ti layers of 2.3 μm showed COF in excess of 0.4, which should be considered high. This demonstrated that Ti layers of 16 and 75 nm thickness were not able to reduce dry friction on Al alloys. Hardness of Ti layers was expected to be much higher than that of Al substrate and this would not be beneficial to tribological properties. As discussed by other researchers [38–40], hard top layers could easily fracture due to rapid deformation of the softer substrate, which should produce abrasion. This could be compared to a hard shell of an egg, whose friction would increase dramatically, if cracked. Such supposition agreed with the observations of somewhat lower friction on 6082, compared to 1050A. Most likely higher hardness of 6082 was more favorable to the ability of Ti layers to withstand breakage. The differences in other substrate properties, such as elasticity, compressibility, etc., might also be important, rather than any effects of Ti layers or surface topography. However, further exploration of these differences would bear little significance in terms of technological viability, because COF on 1050A and 6082 was very high, wear was rapid and the arrangement "hard coating/soft substrate" could not be considered favorable tribologically.

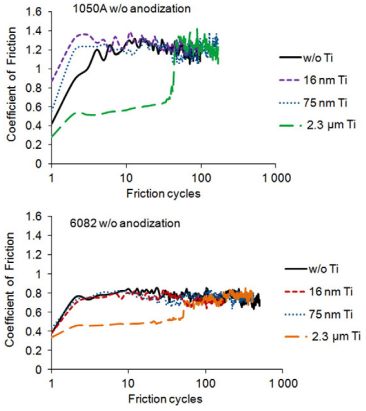

Fig. 2. Influence of Ti layer thickness on friction tendencies of untreated 1050A (top) and 6082 (bottom) alloys. Tribotests of alloys without anodization against an Al_2O_3 ball.

As displayed in Fig. 2, much thicker Ti layer of 2.3 μm showed some improvement in friction reduction. Better performance was not surprising, because the thicker Ti layer could withstand higher interfacial pressures and resist fracture or delamination. Nevertheless, even in case of 2.3 μm layer COF was still higher than 0.4, as an indication of rapid wear. Even more, a sudden increase in friction took place within fewer than 100 friction cycles, suggesting the layer cracking and onset of substrate abrasion, as discussed below in §3.4. Consequently, the friction reduction alone would be a very unlikely reason to justify depositing such a thick Ti layer on untreated aluminum in any technological application.

3.2. Anodization and magnetron sputtering

As discussed in §1 Introduction, anodization is often employed to make Al parts mechanically harder, easily paintable, more corrosion resistant and for many other purposes. In this study, Al discs were anodized using a conventional Type III "hard" anodization procedure in a technologically widespread electrolyte of sulfuric and oxalic acids [2, 41,42]. The process of electrochemical oxidation resulted in anodized coatings of 60 μm thickness and assured major increase in hardness compared to untreated 1050A and 6082 alloys [5,43]. The porosity and nanotopography of obtained surfaces was inspected using Scanning Electron Microscopy (SEM), Fig. S2 (see electronic Supplementary information).

As expected, anodized surfaces contained many nanopores, while untreated surfaces were quite uniform and nearly indistinguishable between 1050A and 6082. No porosity could be observed by SEM on surfaces before anodization. Grain boundaries of 1050A appeared much smaller in size than those of 6082. Nanopore size and distribution was clearly different, with their main characteristics given in Table 1.

SEM data showed that nanopores in 6082 were at least twice as wide as those in 1050A, with the former porosity nearly four times higher. Such differences could have significant influence not only on adhesion

Table 1
Characteristics of surface nanopores, obtained after anodization.

Alloy	Nanopore diameter, nm	Nanopore density, pores/μm^2	Porosity, %, per Eq. (1)
1050A	6.5 ± 1.3 (p = 0.027)	1560 ± 110 (p = 0.123)	5.45
6082	15.0 ± 2.2 (p = 0.044)	1040 ± 121 (p = 0.135)	22.50

Table 2
Average roughness R_a, standard deviation and p values of untreated and anodized surfaces with and without Ti layers, deposited by magnetron sputtering.

Alloy	w/o Ti	16 nm Ti	75 nm Ti	2.3 μm Ti
6082 w/o anodization	1.27 ± 0.08 (p = 0.034)	1.07 ± 0.13 (p = 0.057)	1.02 ± 0.19 (p = 0.085)	1.04 ± 0.11 (p = 0.049)
Anodized 6082	1.44 ± 0.14 (p = 0.060)	1.39 ± 0.14 (p = 0.059)	1.48 ± 0.11 (p = 0.049)	1.71 ± 0.17 (p = 0.076)
1050A w/o anodization	1.01 ± 0.09 (p = 0.041)	0.80 ± 0.13 (p = 0.059)	0.71 ± 0.12 (p = 0.054)	0.78 ± 0.07 (p = 0.032)
Anodized 1050A	0.84 ± 0.08 (p = 0.036)	0.82 ± 0.08 (p = 0.035)	1.03 ± 0.11 (p = 0.047)	1.10 ± 0.09 (p = 0.041)

of Ti during magnetron sputtering, but also on tribological tendencies. Therefore, the comparison of these two alloys could encompass a relatively broad range of properties, which might be affected by anodization and Ti layer deposition.

Anodized specimens were processed by magnetron sputtering to build Ti layers of 16 nm, 75 nm and 2.3 μm on their surface. Their topography was compared to that of untreated and non-sputtered alloys using optical microscopy and SEM. Optical images showed that anodized 1050A had a smoother surface than 6082. As shown in Fig. S3 (see electronic Supplementary information), the grain boundaries of 6082 were again quite pronounced, still being visible after depositing 75 nm Ti layer, but they disappeared under 2.3 μm Ti layer.

From the optical microscopy images it might appear that surfaces become smoother after the deposition of Ti layers by magnetron sputtering. However, contact profilometry could not confirm this supposition. Average surface roughness (R_a) of untreated, anodized and sputtered Al alloys showed that Ti layer deposition did not affect the surface roughness dramatically, despite some changes in R_a values, Fig. 3. The mean R_a values along with standard deviations and p-values are listed in Table 2.

Anodization did not affect roughness excessively either and R_a values stayed in the vicinity of 1 μm. Some increase or reduction in R_a was detectable, although more specimens would be necessary for better quantification. Standard deviations showed that R_a values remained well within the same order of magnitude. This might lead to an expectation that the changes in roughness alone would not affect tribological properties significantly. For better understanding of the Ti layer topography, the specimens were thoroughly inspected by SEM, in some cases using cross-sections obtained by focused Ga ion beaming after pre-depositing a Pt overcoat, Fig. 4.

At higher magnifications Ti layer differences between the alloys became more evident. On 1050A the material in Ti layers appeared relatively uniform and homogeneous, whereas on 6082 the sputtered matter formed aggregates and elongated segments 30–50 nm wide and hundreds of nanometers in length (Fig. 4A, B). This might suggest that sputtered 6082 had much higher roughness on the nano-scale level than 1050A. However, on macro-scale, i.e. as measured by contact profilometry, the increase in surface roughness was not so dramatic. Compared to anodized coatings before sputtering, the roughness changed only marginally, see Table 2 and Fig. 3. So it could not be stated that Ti layer deposition resulted in substantial increase of roughness on 6082 compared to that on 1050A. It might also be noted in Table 1 that nanopores on 6082 were at least twice as wide, compared to 1050A. In 6082, the nanopore diameter of 15 nm could have a much more pronounced effect on the uniformity of the 75 nm thick layer compared to the nanopores of 6.5 nm on 1050A. Consequently, homogeneity of the Ti layer on 6082 appeared much lower than that on 1050A only on nano-scale.

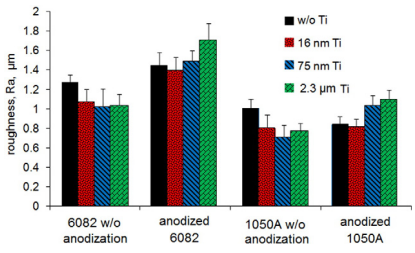

Fig. 3. Average roughness R_a of untreated and anodized surfaces with and without Ti layers, deposited by magnetron sputtering.

In order to study the quality of Ti coatings on 1050A and 6082 alloys, Ga-ion beaming was used to form cross-sections of surfaces with a protective Pt overcoat. These images, Fig. 4 E–F, also showed that the Ti layer was more uniform on 1050A than 6082. The layer thickness on 1050A fluctuated around 75 nm by less than ±3 nm, whereas the thickness variation on 6082 alloy was much greater. In fact, the Ti layer thickness on 6082 was calculated to average at 65 nm, rather than 75 nm, as determined by cross-sectional measurements. The amounts of Ti, deposited onto the surfaces, should be very similar, since 1050A and 6082 specimens were coated in a rotary holder during the same runs of magnetron sputtering. Therefore, the lower measured thickness in 6082 could be an outcome of more Ti penetrating into the nanopores. In addition, significant roughness and surface irregularities could also lower the measured thickness of Ti layers.

The thickness of 2.3 μm Ti layers was confirmed using contact profilometry, Fig. S4 (see electronic Supplementary information). Although the data showed significant scatter, the changes in height were clearly evident. Calculations of the average elevation corresponded well to each other, with the average thickness of 2.3 μm. An attempt was made to investigate the morphology of the thicker Ti layers on 1050A using X-ray diffraction. Unfortunately, several reasons made the spectra inconclusive. Roughness of the specimens was too high for the grazing-incidence method (GIXRD) to be effective even for 2.3 μm Ti layer, so the presence of Ti and possibly its partial oxides was evident only with some uncertainty. Neither Ti nor its oxides could be identified even qualitatively by GIXRD analysis of 75 nm Ti layer specimen. It must also be pointed out that several peaks of Al and Ti have similar 2-theta values, so a good spectral resolution is necessary. Since the specimen substrates were manufactured by rolling process, some directionality of the alloy domains and Ti layer patterns (Fig. 4B) could also affect GIXRD readings. Traces of air, present in the instrument chamber as well as within the anodized coating, made the formation of non-stoichiometric oxides (and possibly nitrides) of titanium very likely, which further impeded the resolution and peak identification. Consequently, no reliable findings could be obtained to learn more about the morphology of deposited layers. In order to establish crystallographic patterns of the Ti layers with sufficient reliability, a dedicated study should be set up using well-polished specimens, preferably higher purity aluminum and fewer variables in sputtering parameters.

In general, the investigations of the anodized coatings and sputtered Ti layers showed that obtained surfaces met the target expectations of

coating thickness and Ti layer nanotopography. Such consistency between expectations and obtained results further supported the viability of anodization and sputtering procedures. The anodized specimens with deposited Ti layers appeared suitable for further tribological studies.

3.3. Effects of Ti layers on tribology of anodized Al surfaces

Previous studies by other research groups described rather different effects of Ti layers on several substrates. When 200 nm Ti layer was deposited on Ti6Al4V alloy, friction was maintained around COF 0.5 beyond 10,000 cycles [19]. Multilayer coatings with Ti were able to bring down COF to 0.15 [9,22]. However, the role of Ti in friction reduction remained unclear, so this study looked into the tribological effectivess of Ti layers of several thicknesses. Just as in case of untreated alloys, friction tendencies of anodized 1050A and 6082 with or without Ti layers were evaluated using a reciprocal motion at 2 cm/s through a wear track of 4 mm length. Such speed and trajectory is relevant to many applications, involved in moving contacts, e.g. sliding over, fasterner opening, engagement of parts during transportation, etc. The load of 10 N was selected, because it approaches a capability of 60 μm anodized coating to withstand breakage on much softer substrate [38,40]. Ball-on-plate tests were carried out on anodized specimens with and without Ti layer deposition, Fig. 5.

Friction on anodized surfaces without Ti was again very high, although it increased much slower than that on untreated surfaces, described earlier in §3.1. Anodized specimens never reached COF of 1.0 and never showed as much friction fluctuations as did 1050A or 6082 specimens without anodization. This suggested that anodization of Al surfaces alone might provide some assurance against COF reaching 1.0. Nevertheless, recorded COF values still were high, exceeding 0.4 within just several friction cycles.

Deposition of Ti layers had essentially no positive effect on 1050A and 6082 without anodization. On anodized surfaces, however, Ti layers led to a significant reduction of friction, Fig. 5. Before sputtering, friction on anodized specimens exceeded COF = 0.4 almost immediately, but after depositing just 16 nm Ti layers they were able to sustain COF below 0.2 for 10 cycles or longer. Ti layers of 75 nm thickness showed even higher effectiveness, maintaining COF around 0.2 for 20 and 60 friction cycles on 1050A and 6082 respectively. Even more surprisingly, 2.3 μm Ti layers seemed not effective tribologically at all, succumbing to high friction in a very similar manner as the anodized coatings before sputtering. It was truly perplexing to find out that the 2.3 μm Ti layer

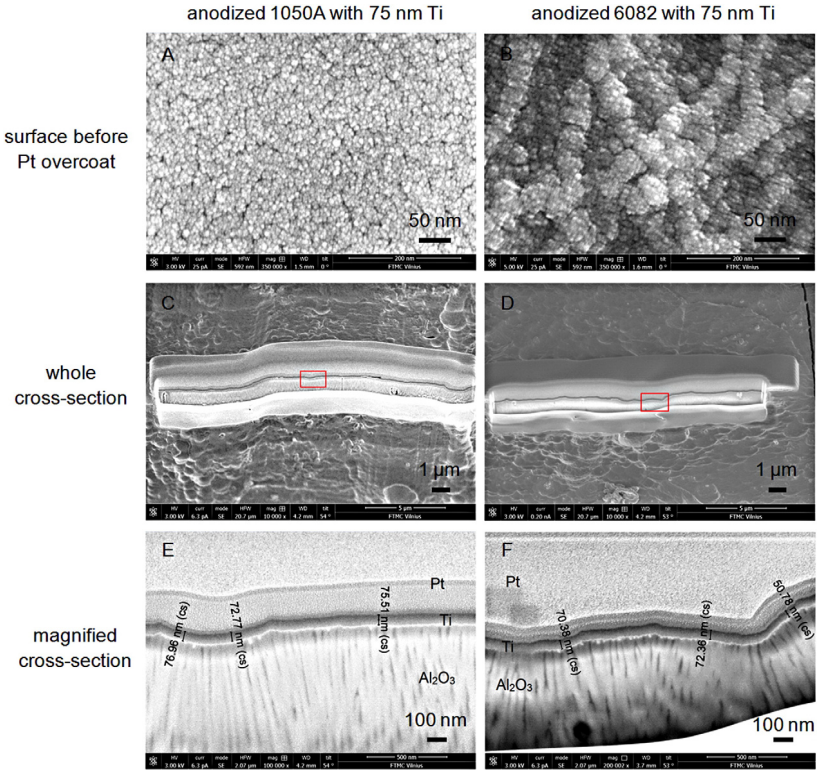

Fig. 4. SEM images of surfaces (A, B) and cross-sections (C—F) of anodized 1050A and 6082 alloys with 75 nm Ti layers. Cross-sections obtained with focused Ga ion beaming after predepositing a Pt overcoat.

performed so much worse than 16 nm or 75 nm Ti layers. Anodization and sputtering were re-run for the second time on several specimens. The whole experimental sequence of anodization – sputtering – tribotesting was highly reproducible and the results showed very good repeatability. Before Ti deposition the mean COF reached 0.753 ± 0.042 (p-value $= 0.006$) after 10 friction cycles on 1050A, while 75 nm Ti layer brought COF down to 0.172 ± 0.005 (p-value $=$ 0.036). it remained uncertain, which tribological or structural phenomena could result in such a paradox-like observation of nanothin Ti layers giving a clearly very beneficial tribological effect, while much thicker 2.3 μm Ti layers were not effective whatsoever.

Therefore, an additional exercise was initiated to verify the tribological ineffectiveness of thick Ti layers by replacing the mating material in the friction zone. Instead of ball-on-disc friction tests using a corundum (i.e. Al_2O_3) ball, the tests were performed using a steel ball, since friction against steel surfaces is quite widespread technologically. The whole sequence of untreated, anodized and sputtered specimens was screened using the same load, wear track length and velocity, i.e. 10 N, 4 mm and 2 cm/s respectively, Fig. S5 (see Electronic Supplementary information).

During tribotests with a steel ball on anodized coatings the tendency of 2.3 μm Ti layers to perform poorer than those of 75 nm and 16 nm was again evident, just that the difference was not as extreme as in case of a corundum ball. The specimens essentially confirmed the same tendency of improved tribological properties at 75 nm thickness and friction increase on 2.3 μm Ti layers, despite some changes in the magnitude of the friction values due to the difference in mating materials.

The influence of Ti layer thickness on friction tendencies was even more evident when the data was reprocessed to show COF values after 10 friction cycles, Fig. 6 (top). Such number of friction cycles was selected to simulate conditions of incidental mechanical contacts between moving surfaces, like those incurred during the industrial anodization of aluminum items, their transportation and installation. Even if properly manufactured and packaged, anodized items could still engage into some incidental friction. Therefore, the ability of anodized surfaces to sustain low COF for at least several friction cycles would be beneficial in many of those cases, so unwanted wear or other types of surface damage could be prevented.

The charts in Fig. 6 clearly showed that progressively higher thickness of deposited Ti layers had an opposite impact on untreated alloys than on anodized ones. On surfaces without anodization, thin Ti layers of 16 and 75 nm thickness resulted in major friction increase, while 2.3 μm Ti layer reduced COF somewhat. In contrast, the anodized alloys provided better Ti layer adhesion and resulted in significant friction reduction at Ti layer thickness of 16 and 75 nm independently of mating surfaces. This was even more evident for the data, extracted to show the number of friction cycles when COF stayed below 0.4, see Fig. 6 (bottom).

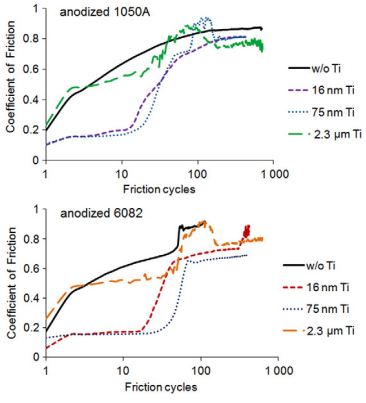

Fig. 5. Influence of Ti layer thickness on friction tendencies of anodized 1050A (top) and 6082 (bottom) alloys. Tribotests against an Al_2O_3 ball.

As a rule of thumb in industrial tribology, incidental friction could often be considered acceptable, if COF stayed below 0.3–0.4, assuming that relatively low COF would only lead to gradual wear, rather than abrasion, scuffing, pitting or other severe regimes. The latter modes of wear would usually take place under COF significantly above 0.4. After processing the data to display the influence of Ti layer thickness on the maximum number of friction cycles, which could be sustained with COF below 0.4 (Fig. 6 bottom), it appeared that 2.3 μm Ti layers performed clearly worse than those of 75 nm. Again, in case of tribotests with a corundum ball, 16 nm Ti layers performed significantly better than those of 2.3 μm, while in case of a steel ball the difference was not as significant. Nevertheless, it could again be claimed with certainty that friction of 2.3 μm Ti layers was higher than that of much thinner Ti layers, in spite of COF dependence on mating materials.

3.4. Effects of Ti layers on wear of anodized coatings

In order to assure long service time and extended durability, it is desirable to avoid surface wear and deterioration. Most applications require at least to assure low wear rates without inflicting severe surface damage, such as abrasion, pitting, scuffing, etc. In this study, resistance to wear of anodized coatings with and without Ti layers was assessed using several procedures of tribotesting and surface evaluation. The most attention was devoted to surface wear before the initiation of any significant abrasion processes. Therefore, 10 friction cycles were selected as the first milestone for wear measurements and analysis of surface transformations. This extent of tribological interaction could also be relevant to incidental friction in many applications, as discussed earlier in §3.3.

When Ti layers were deposited on anodized 1050A, their wear was clearly noticeable visually just after 10 friction cycles. Inspection with an optical microscope revealed rapid degradation of 75 nm Ti layer, Fig. 7. It might be noted that high rates of wear could possibly be measured by contact (mechanical) profilometry. However, any attempts to determine wear depth after only 10 friction cycles on anodized alloys with the mechanical profilometer were not sufficiently accurate due to relatively small wear scars. After 30 friction cycles the scars were deeper, approaching 2 μm, but still not enough for satisfactory quantification. Available AFM techniques could not be used because of excessive roughness. Therefore, in this study the evaluation of wear after 10 or 30 friction cycles could only be performed qualitatively by optical and electron microscopy.

Before friction, the appearance of Ti layers was bluish without significant discolorations. After 10 friction cycles the surface showed protrusions of grey tones. Grey color might be related to anodized coatings without any Ti on the top, so these discolorations implied a high rate of wear. Nevertheless, it could not be stated that the 75 nm Ti layer was completely removed from the discolored segments, because the grey protrusions might also appear as a consequence of optical effects at lower Ti layer thickness. In spite of this precaution, at least partial delamination of the Ti layer seemed likely. It could also be observed that 10 friction cycles were sufficient to produce some cracks on anodized coating of 1050A, Fig. 7 center. These cracks should not be viewed as a direct consequence of wear, because just the load of 10 N alone might be sufficient for damaging hard anodized coating on a relatively soft substrate of 1050A. This phenomenon was more evident when testing the deposited Ti layers on untreated 1050A without anodization, see

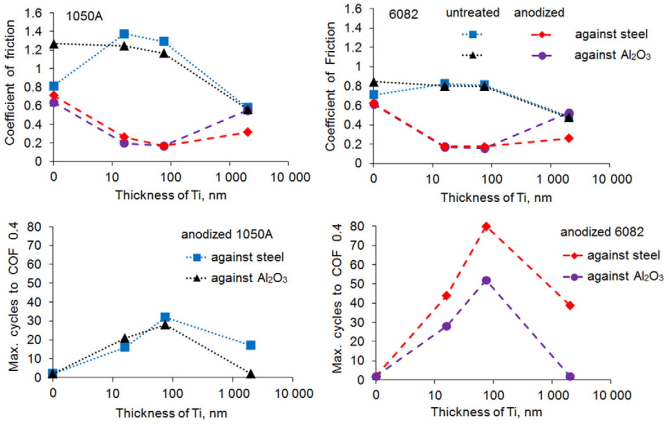

Fig. 6. Top: Influence of Ti layer thickness on Coefficient of Friction after 10 friction cycles. Bottom: Ability of anodized surfaces to sustain friction below COF 0.4 for a number of friction cycles. Left: 1050A. Right: 6082.

§3.1. Therefore, cracks could develop within the anodized coating itself just due to high interfacial pressure independently of the 75 nm Ti layer.

When the tribotester stopped automatically due to excessive friction force after 500 friction cycles, much more damage to the surface could be observed, Fig. 7 right. The wear track did not show any bluish color anymore, the absence of which implied that all original Ti layer could be destroyed. Very similar trends were observed on 6082 alloy as well. Surface discolorations were located in various areas of wear scars as a consequence of relatively high (R_a ~ 1 μm) surface roughness.

Wear scars after prolonged tribotesting at high COF were quite deep, however, it was too complicated to make a legitimate comparison between highly worn specimens. First of all, many specimens could not even last 500 friction cycles due to friction force becoming excessive and triggering an automatic tribotester shutdown. Also, after attaining high COF the whole Ti layer could be removed within just several friction cycles, making it unreasonable to look for any influence of Ti on wear rates. In essence, wear measurements after tribotesting at high COF would mostly characterize the properties of the anodized coating and substrate itself without much relation to Ti layers. Therefore, an attempt was made to look into wear resistance after 30 friction cycles on 1050A just after COF exceeded 0.4. SEM was employed for better understanding of friction-induced Ti layer transformations on micro- and nanoscale. Initially, the development of wear tracks was evaluated after 10 and 30 friction cycles, Fig. 8.

After 10 friction cycles the wear track was barely visible without direct evidence of removed material. However, some surface damage was evident in a form of cracks even after 10 friction cycles on 1050A, in agreement with optical photomicrographs, Fig. 7. It might be pointed out that no cracks could be observed after 10 or 30 friction cycles on 6082, whose COF was still well below 0.4 after that much of tribotesting. However, on 1050A after 30 friction cycles significant wear damage could be observed, Fig. 8. A deep, clearly defined pit was formed in the middle of the wear track. Many more smaller scars were also produced around the central part and near the edges of the track, where interfacial pressures were expected to be the highest [44]. The largest pit appeared to remove not just the 75 nm Ti layer, but whole anodized coating of 60 μm thickness. This showed that anodized coating on 1050A was quite fragile, at least compared to more industrially recognized 6082. Simple calculation shows that under 10 N load the interfacial pressure exceeds 150 MPa when the friction zone diameter is less than 0.4 mm, which is the case in most tests, at least during the initial friction stages. It appears that such pressure is already sufficient to crack the anodized coating of 60 μm thickness on 1050A. Deterioration of the whole anodized coating gave a proof that the abrasion began sooner than 30 friction cycles, because large amounts of wear debris were forming, resulting in gradual replacement of the surface-to-surface contact with a surface-to-debris regime. Sizes of the abrasive debris particles might vary over a broad range both on microscale and nanoscale level. As an example,

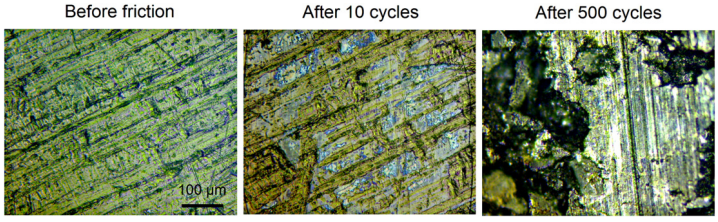

Fig. 7. Optical microscope images of tribotest wear scars of 75 nm Ti layers on anodized 1050A before and after 10 and 500 friction cycles. Tribotests of anodized alloys against an Al_2O_3 ball.

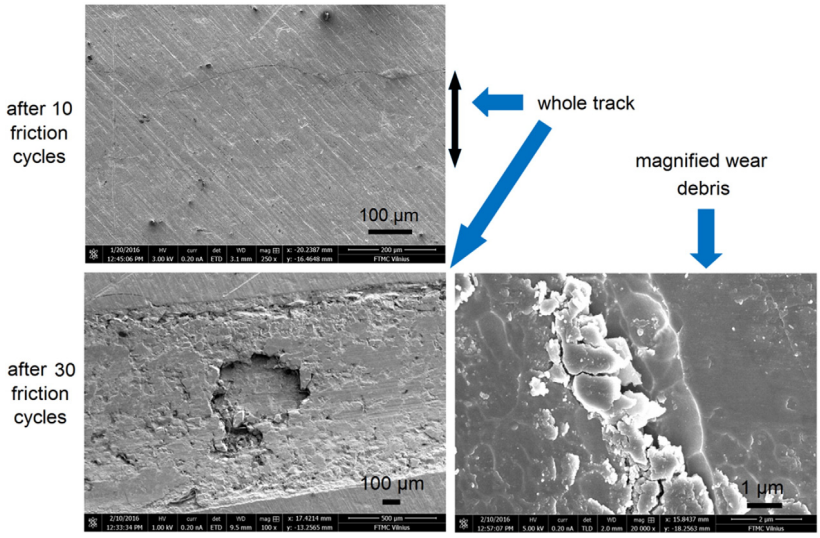

Fig. 8. SEM images of wear tracks on anodized 1050A with 75 nm Ti layers after 10 and 30 friction cycles, tribotests against an Al_2O_3 ball.

finer particles of cracked coating just before separating as wear debris were magnified in Fig. 8.

Further inspection of the wear tracks before cracking began was presented in Fig. 9. Surfaces after 10 friction cycles showed some flattening and a larger number of dark protrusions due to original roughness, but otherwise appeared quite similar to those before tribotesting. No difference between the two could be observed at higher magnification. But after 30 friction cycles the surface underwent significant transformation. Original roughness was essentially erased and the nanoscale texture appeared different, suggesting that most of the 75 nm Ti layer was removed. The abundance of small particles of ~0.1 µm in diameter was much higher, implying the presence of fine debris particles. The shapes and sizes of those particles showed some uniformity, which suggested that they might actually represent the remains of the delaminated Ti layer of 75 µm thickness with some tendency to aggregate. Therefore, Ti elemental mapping was performed on the zone without cracking after 30 friction cycles. Major variation in Ti contents could be observed, Fig. S6 (see Electronic Supplementary Information).

Beforehand, it might be noted that EDS measurements without tribotesting showed that 75 nm Ti layers were effectively deposited on Al surfaces, recording the average of 6.72 ± 0.4 wt.% of Ti. Since EDS consumed the material from about 1 µm depth of the anodized coating, the contribution of Al_2O_3 coatings was much higher than that of 75 nm Ti layers. So the Ti concentration readings should be considered semi-quantitative at best, although 6.7 wt.% might not appear very distant from 7.5% representing 75 nm of 1 µm. Interestingly, contents of S were very substantial at 2.9 wt.% and 4.4 wt.% in 1050A and 6082 respectively, which suggested considerable residues of the electrolyte in the nanopores. Since the electrolyte mostly contained sulfuric acid (plus oxalic a.), eventually $Al_2(SO_4)_3$, other salts and various hydrates could be formed. Residual sulfates and other salts might have a significant impact on tribology, but industrially it would not be realistic to eliminate S from the anodized coatings by washing out, especially from nanopores as narrow as 15 nm ID or less. However, the residues in the nanopores were not likely to have any significant effect on friction before the removal of the Ti layer due to abrasion. As a matter of fact, after 10 friction cycles at steady state regime Ti and S contents did not change, remaining at 6.85 wt.% and 2.82 wt.% respectively, while after 30 friction cycles the averages of 5.89 wt.% and 2.79 wt.% were recorded. This showed that most Ti still remained inside the wear scar with large fluctuations in concentration, as shown in Fig. S6 (see Electronic Supplementary information). In the wear track after 30 cycles Ti concentration gradient was very high, such as 0.77 wt.% to 8.73 wt.% within less than 30 µm, but no visible pits or major surface damage could be observed. These numbers should not be viewed as actual Ti concentrations due to 1 µm sampling depth during EDS scanning, as cautioned above. Nevertheless, it could be considered that Ti concentration might change more than 10 times within less than 30 µm on the wear track. This suggested that Ti layer might undergo a quasi-fluid type of material transfer [45–47] from one location to another within the wear track, assuring significantly lower friction and wear. More complex tribological mechanisms, such as selective transfer [48,49] as in Cu on steel or possibly others might also be involved, but a much more extensive study would be needed to identify the most probable pathways.

The effectiveness of thin Ti layers, such as 75 nm thickness, to reduce friction and wear on anodized alumina could not be easily explained from the accumulated data. Relatively high COF of 2.3 µm Ti layers might suggest that observed delocalization of Ti aggregates in the friction zone would probably not take place as easily in thick Ti layers as it would in case of 75 nm or 16 nm thickness. The latter one showed somewhat poorer tribological characteristics than those of 75 nm, which suggested that the 16 nm layer might simply be too thin to assure sufficient surface separation, as shown in tribotests with a steel ball. But COF and EDS data suggested that in case of 75 nm Ti layers a large portion of friction energy could be used for delocalization of Ti aggregates, rather than for abrasion, pitting or other modes of severe surface damage. Such energy dissipation would beneficially affect tribological properties. Intricacies of the Ti delocalization mechanism would need

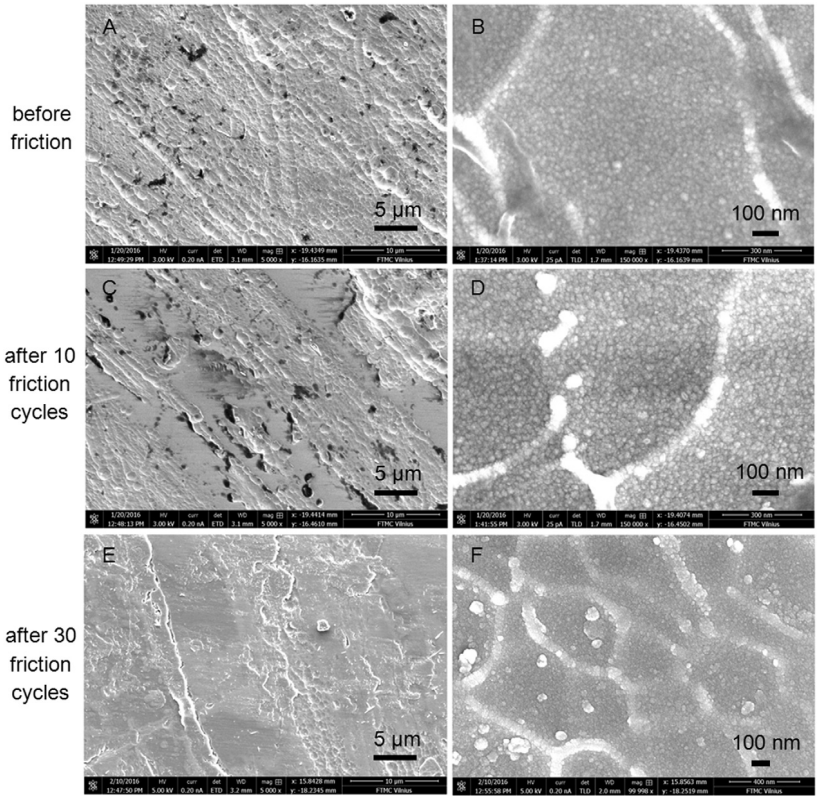

Fig. 9. SEM images of friction-induced transformations of 75 nm Ti layer surface after 10 and 30 friction cycles on anodized 1050A alloy, tribotests against an Al_2O_3 ball.

more studies. Other Ti layer thicknesses should be studied along with other loads, velocities, atmospheres, thermal regimes and other tribotesting parameters. Different types of anodization should also be investigated, especially considering the amount of sulfur in the anodized coatings.

Nevertheless, the current study has already provided a number of indications that deposition of Ti layers on anodized Al might eventually lead to major improvements in protection of industrially anodized items from surface damages due to incidental friction and wear. Quite frequently some Al alloys, including 1050A, are not anodized due to the concerns of detrimental effects of friction. Deposition of nanothin Ti layers can expand the selection of alloys for anodization and significantly improve the versatility of anodization technology along with longevity and durability of anodized items.

4. Conclusions

Industrial aluminum alloys 1050A and 6082 were anodized by Type III procedures and Ti layers of 16 nm, 75 nm and 2.3 μm thickness were deposited by magnetron sputtering, as confirmed by profilometry, SEM and EDS analysis. Incidental friction was simulated by applying 10 N load with a corundum (Al_2O_3) ball or a steel ball in reciprocal motion against flat specimen discs. Although such load is significantly higher than those typically investigated by other researchers, a number of observations agreed with their reports.

- On untreated Al alloys without anodization nanothin Ti layers showed high Coefficient of Friction (COF) with only minor improvements in tribological properties at 2.3 μm Ti layer thickness.
- On anodized coatings without Ti friction was somewhat lower, but nearly immediately COF exceeded 0.4 as a result of rapid abrasion.
- Since hard anodized coatings of 60 μm thickness were built on a relatively soft substrate of 1050A, the interfacial pressures in excess of 150 MPa resulted in cracking, generation of wear debris and abrasion within several friction cycles.

No cracking was observed in anodized coatings on 6082 after 30 friction cycles.

Further tests revealed a perplexing observation that deposition of nanothin Ti layers of 16 nm and 75 nm thickness makes it possible to reduce friction very effectively.

- COF dropped below 0.4 on anodized 1050A for at least 10 friction cycles, with even better performance on less brittle anodized 6082.
- Counterintuitively, 2.3 μm Ti layers were much less effective, especially when tested against a corundum ball.
- Incidental friction and onset of abrasion of anodized alumina appeared to be successfully inhibited by nanothin Ti layers, but not by much thicker 2.3 μm Ti layers.

The underlying cause of such puzzling performance of 75 nm Ti layers might be related to major delocalizations of Ti aggregates in the friction zone, as observed by SEM and EDS. Elemental analysis showed that Ti concentration can change at least 10 times within less than 30 μm. Further studies at various loads, velocities, atmospheres, thermal regimes and other testing parameters as well as usage of polished surfaces and intermediate thicknesses of Ti layers could provide more insight. Nevertheless, such tribological effectiveness of Ti layers is likely to lead to significant improvements of anodization technology and important advancements in reducing wear and friction.

Supplementary data to this article can be found online at http://dx.doi.org/10.1016/j.surfcoat.2016.09.083.

Acknowledgments

Internal budgetary funding of Institute of Chemistry FTMC was used to sponsor the study. Encouragement of Prof. Augustas Pivoriūnas and Ms. Alina Čebatariūnienė from Center of Innovative Medicine was very helpful in devoting more attention to Ti layer deposition. Experimental assistance and technical advice of Prof. Eimutis Juzeliūnas, Dr. Gedvidas Bikulčius, Dr. Povilas Miečinskas, Dr. Vidas Pakštas, Dr. Sigitas Jankauskas, Dr. Ignas Valsiūnas, Dr. Svetlana Lichušina, Dr. Asta GriguceviČienė, Laurynas Staišiūnas and Irina Demčenko (all from Institute of Chemistry) is cordially appreciated.

References

[1] Y. Goueffon, C. Mabru, M. Labarrère, L. Arurault, C. Tonon, P. Guigue, Investigations into the coefficient of thermal expansion of porous films prepared on AA7175 T7351 by anodizing in sulphuric acid electrolyte, Surf. Coat. Technol. 205 (2010) 2643–2648.
[2] W. Bensalah, K. Elleuch, M. Feki, M. Wery, H.F. Ayedi, Optimization of anodic layer properties on aluminium in mixed oxalic/sulphuric acid bath using statistical experimental methods, Surf. Coat. Technol. 201 (2007) 7855–7864.
[3] P. Bocchetta, C. Sunseri, G. Chiavarotti, F.D. Quarto, Microporous alumina membranes electrochemically grown, Electrochim. Acta 48 (2003) 3175–3183.
[4] M.A. Kashi, A. Ramazani, M. Rahmandoust, M. Noormohammadi, The effect of pH and composition of sulfuric–oxalic acid mixture on the self-ordering configuration of high porosity alumina nanohole arrays, J. Phys. D. Appl. Phys. 40 (2007) 4625–4630.
[5] H. Kim, D. Kim, W. Lee, S. Cho, J. Hahn, H. Ahn, Tribological properties of nanoporous anodic aluminum oxide film, Surf. Coat. Technol. 205 (2010) 1431–1437.
[6] S. Shi, J. Wu, T. Huang, Y. Peng, Improving the tribological performance of biopolymer coating with MoS_2 additive, Surf. Coat. Technol. 303 (2016) 250–255.
[7] C. Ma, S.C. Wang, L.P. Wang, F.C. Walsh, R.J.K. Wood, The electrodeposition and characterisation of low-friction and wear-resistant Co-Ni-P coatings, Surf. Coat. Technol. 235 (2013) 495–505.
[8] J. Escobar, L. Arurault, V. Turq, Improvement of the tribological behavior of PTFE-anodic film composites prepared on 1050 aluminum substrate, Appl. Surf. Sci. 258 (2012) 8199–8208.
[9] D. Goldbaum, P. Manimuda, G. Kamath, S. Descartes, J.E. Klemberg-Sapieha, R.R. Chromik, Tribological behavior of TiN and Ti (Si,C)N coatings on cold sprayed Ti substrates, Surf. Coat. Technol. 291 (2016) 264–275.
[10] C. Liu, C. Chen, H. Cheng, Growth mechanism of TiO_2 nanotube arrays in nanopores of anodic aluminum oxide on Si substrates by atomic layer deposition, J. Electrochem. Soc. 158 (2011) K58–K63.
[11] E. Gemelli, N.H.A. Camargo, Oxidation kinetics of commercially pure titanium, Revista Matéria 12 (2007) 525–531.
[12] Y. Okazaki, C. Chen, S. Zhang, I. Lee, Immobilizing bioactive molecules onto titanium implants to improve osseointegration, Surf. Coat. Technol. 228 (2013) S312–S317.
[13] P. Silva-Bermudez, S.E. Rodil, An overview of protein adsorption on metal oxide coatings for biomedical implants, Surf. Coat. Technol. 233 (2013) 147–158.
[14] S. Baradaran, W.J. Basirun, E. Zalnezhad, M. Hamdi, A.A.D. Sarhan, Y. Alias, Fabrication and deformation behaviour of multilayer Al2O3/Ti/TiO2 nanotube arrays, J. Mech. Behav. Biomed. Mater. 20 (2013) 272–282.
[15] X. Meng, M.N. Banis, D. Geng, X. Li, Y. Zhang, R. Li, H. Abou-Rachid, X. Sun, Controllable atomic layer deposition of one-dimensional nanotubular TiO_2, Appl. Surf. Sci. 266 (2013) 132–140.
[16] Y. Xie, H. Ao, S. Xin, X. Zheng, C. Ding, Enhanced cellular responses to titanium coating with hierarchical hybrid structure, Mater. Sci. Eng. C 38 (2014) 272–277.
[17] J.M. Wheeler, J.A. Curran, S. Shrestha, Microstructure and multi-scale mechanical behavior of hard anodized and plasma electrolytic oxidation (PEO) coatings on aluminum alloy 5052, Surf. Coat. Technol. 207 (2012) 480–488.
[18] C. Stocchi, P. Robinson, S.T. Pinho, A detailed finite element investigation of composite bolted joints with countersunk fasteners, Compos. A: Appl. Sci. 52 (2013) 143–150.
[19] Y.X. Leng, J.Y. Chen, P. Yang, H. Sun, N. Huang, The microstructure and properties of titanium dioxide films synthesized by unbalanced magnetron sputtering, Nucl. Inst. Methods Phys. Res. B 257 (2007) 451–454.
[20] C. Veiga, J.P. Davim, A.J.R. Loureiro, Properties and applications of titanium alloys: a brief review, Rev. Adv. Mater. Sci. 32 (2012) 133–148.
[21] M.R. Garsivazjazi, M.A. Golozar, K. Raeissi, M. Fazel, Evaluation of corrosion and tribocorrosion of plasma electrolytic oxidation treated Ti–6Al–4V alloy, Surf. Coat. Technol. 244 (2014) 29–36.
[22] J. Li, H. Zhang, A. Fan, B. Tang, Tribological properties characterization of Ti/Cu/N thin films prepared by DC magnetron sputtering on titanium alloy, Surf. Coat. Technol. 294 (2016) 30–35.
[23] D. Brüggemann, Nanoporous aluminium oxide membranes as cell interfaces, J. Nanomater. (2013) 1–18.
[24] A. Ručinskienė, G. Bikulčius, S. Jankauskas, S. Asadauskas, Ball-on-plate testing of nanopore fillers for tribologically effective anodized alumina coatings, Proc. Int. Conf. BaltTrib 73–78 (2013).
[25] S. Asadauskas, G. Stalnionis, A. Ručinskienė, G. Bikulčius, Analysis of tribofilm formation in lubricants on anodized alumina, Proc. International Conference Chemistry & Chemical TechnologyKaunas Univ. of Technology 2014, pp. 53–56.
[26] R. Juškėnas, V. Kapočius, P. Miečinskas, V. Karpavičienė, XRD studies of electrochemically hydrided–dehydrided thin films of the alloy AZ31 and AZ31 with Ti, J. Alloys Compd. 467 (2009) 524–527.
[27] L. Staišiūnas, K. Leinartas, M. Samulevičienė, P. Miečinskas, A. GriguceviČienė, R. Juškėnas, E. Juzeliūnas, Electrochemical and structural characterization of sputter-deposited Mg–Nb and Mg–Nb–Al–Zn alloy films, J. Solid State Electrochem. 17 (2013) 1649–1656.
[28] G. Sauerbrey, The use of quartz oscillators for weighing thin layers and for microweighing, Z. Phys. 155 (1959) 206–222.
[29] J. Juodkazytė, B. Šebeka, I. Savickaja, A. Selskis, V. Jasulaitienė, P. Kalinauskas, Evaluation of electrochemically active surface area of photosensitive copper oxide nanostructures with extremely high surface roughness, Electrochim. Acta 98 (2013) 109–115.
[30] G. Knott, H. Marchman, D. Wall, B. Lich, Serial section scanning electron microscopy of adult brain tissue using focused ion beam milling, J. Neurosci. 28 (2008) 2959–2964.
[31] D. Mustafi, A. Avishai, N. Avishai, A. Engel, A. Heuer, K. Palczewski, Serial sectioning for examination of photoreceptor cell architecture by focused ion beam technology, J. Neurosci. Methods 198 (2011) 70–76.
[32] R. Liske, S. Wehner, A. Preusse, P. Kuecher, J.W. Bartha, Influence of additive Co adsorption on copper Superfill behavior, J. Electrochem. Soc. 156 (2009) H955–H960.
[33] N. Hanief, C.J. Lang, M. Topic, Investigating the chromium-platinum coated system, J. South. Afr. Inst. Min. Metall. 114 (2014) 151–156.
[34] J. Padgurskas, R. Kreivaitis, V. Jankauskas, P. Janulis, V. Makarevičienė, S. Asadauskas, L. Miknius, Antiwear properties of lard methyl esters and rapeseed oil with commercial ashless additives, Meccanica 70 (2008) 67–72.
[35] T. Minoda, H. Yoshida, Effect of grain boundary characteristics on intergranular corrosion resistance of 6061 aluminum alloy extrusion, Metall. Mater. Trans. A 33 (2002) 2891–2898.
[36] L. Donati, A. Segatori, M.E. Mehtedi, L. Tomesani, Grain evolution analysis and experimental validation in the extrusion of 6XXX alloys by use of a lagrangian FE code, Int. J. Plast. 46 (2013) 70–81.
[37] A.T.K. Mizuno, Y.T.K. Fukui, K.T.K. Nakamoto, T.T.K. Yoshii, Titanium Oxide Films, Their Production and Uses, Patent EP0507545 A1, 1992 1–8.
[38] K. Holmberg, A. Laukkanen, H. Ronkainen, K. Wallin, S. Varjus, J. Koskinen, Tribological contact analysis of a rigid ball sliding on a hard coated surface part II: material deformations, influence of coating thickness and Young's modulus, Surf. Coat. Technol. 200 (2006) 3810–3823.
[39] T. Staedler, K. Schiffmann, Correlation of nanomechanical and nanotribological behavior of thin DLC coatings on different substrates, Surf. Sci. 482–485 (2001) 1125–1129.
[40] K. Holmberg, H. Ronkainen, A. Laukkanen, K. Wallin, Friction and wear of coated surfaces – scales, modelling and simulation of tribomechanisms, Surf. Coat. Technol. 202 (2007) 1034–1049.
[41] C. Yu, C. Hu, A. Bai, Y. Yang, Pore-size dependence of AAO films on surface roughness of Al-1050 sheets controlled by electropolishing coupled with fractional factorial design, Surf. Coat. Technol. 201 (2007) 7259–7265.
[42] M. Moradi, M. Noormohammadi, F. Behzadi, Three-dimensional structural engineering of nanoporous alumina by controlled sprinkling of an electrolyte on a porous anodic alumina (PAA) template, J. Phys. D. Appl. Phys. 44 (2011) 1–7.

[43] A.A.D. Sarhan, E. Zalnezhad, M. Hamdi, The influence of higher surface hardness on fretting fatigue life of hard anodized aerospace AL7075-T6 alloy, Mater. Sci. Eng. A 560 (2013) 377–387.
[44] D.H. Warner, J.F. Molinari, Micromechanical finite element modeling of compressive fracture in confined alumina ceramic, Acta Mater. 54 (2006) 5135–5145.
[45] A.I. Dmitriev, V.L. Popov, S.G. Psakhie, Simulation of surface topography with the method of movable cellular automata, Tribol. Int. 39 (2006) 444–449.
[46] I. Iordanoff, M.M. Khonsari, Granular lubrication: toward an understanding of the transition between kinetic and quasi-fluid regime, J. Tribol. 126 (2004) 137–145.
[47] A. Zmitrowicz, Wear debris: a review of properties and constitutive models, J. Theor. Appl. Mech. 43 (2005) 3–35.
[48] D.N. Garkunov, Triboengineering (Wear and Non-Deterioration), Agricultural Academy Press, Moscow, 2000.
[49] N.K. Myshkin, Friction transfer film formation in boundary lubrication, Wear 245 (2000) 116–124.

2nd publication

Determination of the dye penetration rate in porous aluminum oxide using Raman spectroscopy

Matijošius, T., Asadauskas, S.J., Bikulčius, G., Selskis, A., Jankauskas, S., Višniakov, J. and Ignatjev, I.

Coloration Technology, 135(4), pp.275-282 (2019)
DOI: 10.1111/cote.12404

doi: 10.1111/cote.12404

Determination of the dye penetration rate in porous aluminum oxide using Raman spectroscopy

Tadas Matijošius,[a,*] Svajus J. Asadauskas,[a] Gedvidas Bikulčius,[a] Algirdas Selskis,[a] Sigitas Jankauskas,[a] Jevgenij Višniakov[b] and Ilja Ignatjev[a]

[a]*Institute of Chemistry, Center for Physical Sciences and Technology (FTMC), Saulėtekio av. 3, LT-10257, Vilnius, Lithuania*
Email: tadas.matijosius@ftmc.lt

[b]*Semiconductor Physics Institute, FTMC, Saulėtekio av. 3, LT-10257, Vilnius, Lithuania*

Received: 14 June 2018; Accepted: 5 April 2019

Oxidised aluminum coatings are useful in various high technology applications to protect surfaces from negative environmental effects. In this study, aluminum discs and foils of industrial alloys were anodised in a sulphuric acid/oxalic acid electrolyte. Scanning electron microscopy was used to determine the pore diameter, distribution and surface porosity. The anodising procedure was adapted to produce near-hollow templates on aluminium foil, onto which aqueous solutions of commercial chromium-complexed anionic azodyes were dropped. Raman spectroscopy was used to detect the penetration of dye compounds based on the most intensive vibrational modes. Each dye was successfully monitored to assess its penetration rate and behaviour in the anodised coating. This method could be applied to characterise newly developed organic dyes for aluminum colouring.

Introduction

Many high technology manufacturers utilise oxidised aluminum coatings for parts such as laser assemblies, robots or information technology equipment. Electrochemical anodising of aluminium is often employed to build aluminimum oxide coatings of a thickness of 100 μm or greater. During electrochemical oxidation, aluminium forms self-organised arrays of cylindrical pores. After anodisation, the coatings are comprised of two distinct segments: (i) a barrier layer next to the metal, and (ii) an anodic layer, in which the pores are oriented perpendicular to the film surface [1]. Such alignment in anodic aluminium oxide takes place due to mechanical stress associated with generation of a repulsive force between neighbouring pores, which leads to the self-ordering process [2]. Basically, there are two competing processes: the formation of an oxide coating and its chemical dissolution in the anodising electrolyte. This balance is crucial to the formation of the anodic layer in the entire anodisation process [3,4].

Because of the capillary action of the pores, the anodised coating easily adsorbs the dyes. This property is very helpful in the utilisation of organic or inorganic dyes to colour anodised aluminium. Most dyes are designed so that the dyeing is performed by saturation of the pore to get the correct colour and stability. To achieve this, temperature, pH, concentration and duration must be controlled. Dyes need a certain depth of pore to achieve the colour, which makes the anodising step critical. Uniformity of thickness and pore structure are very important for consistent results.

Once the anodising is complete, fillers are applied with the purpose of imparting colour, corrosion resistance, and many application-related properties, such as reflectance, UV resistance, antibacterial/antifungal performance, etc. The anodised surface may be coloured with a dye and then sealed by placing it in boiling water, to block the openings of the pores [5].

Anodised aluminium can be coloured by three different methods, which are distinguished by the nature of the colouring material and its location within the film: adsorptive dyeing, electrolytic colouring and integral colouring [6]. In the case of electrolytic colouring, inorganic pigments accumulate at the bottom of anodised aluminium pores. Meanwhile, in adsorptive dyeing, an organic dyestuff is introduced into the pores and adsorbed onto the aluminium oxide in the region closest to the coating surface.

After dyeing it is often necessary to apply subsequent sealing, a hydrothermal process that blocks the pores, largely prevents any leaching of the colouring material, and greatly reduces the sorptive characteristics of the coating along with its susceptibility to chemical attacks [7]. The hydrothermal method of sealing is performed by dipping anodised aluminium in boiling water. The oxide on the surface and pores reacts to make hydroxides, hydrated metal oxides, and various other structures of lower density. They occupy greater volume and make an impermeable layer that is stable under various environmental conditions [8]. Although the dyes incorporated into pores by the adsorptive dyeing method are closer to the anodised aluminium oxide surface, what remains there is a risk that has to be washed out during hydrothermal filling. This obstacle may be encountered when dyeing anodised aluminium with organic dyes possessing a wider colour choice. Unfortunately, we are unaware of any methods to quantify dye penetration into the anodised aluminium coating.

It is known [9] that surface-enhanced Raman spectroscopy (SERS) is a highly sensitive technique that allows detection of molecules in very low concentrations and provides rich structural information. For SERS measurements, the surface

onto which the molecules of analytes will be adsorbed should be rough. Silver, gold and copper electrode surfaces can be chemically or electrochemically roughened [10–12], covered with or free from nanoparticles [13,14]. It was found that nearly hollow templates of anodic aluminium oxide, which were covered with silver by the magnetron-sputtering deposition, can be manufactured into highly sensitive and low-cost substrates for SERS [15]. Fully anodised aluminium foil can be used to estimate dye penetration rates. Therefore, we decided not to deposit any metal layer onto anodised aluminium to avoid the closure of the pores which were being formed. Deposition of a metal layer would also have a negative effect upon dye penetration into the pores.

Overall, Raman spectroscopy is a powerful and non-destructive analytical method for observing vibrational, rotational and other low-frequency modes of analytes, which enables investigation of spectral variation in real time. Raman spectra can target specific vibrational modes that relate to well-defined molecular moieties. Photometric measurements of colour reflectance or density using SpectroEye (X-rite, Inc., USA), GretagMacbeth (X-rite, Inc., USA), or similar techniques generally characterise the overall performance of the whole dye formulation, without segregating specific molecules. Therefore, it is more difficult to explain possible chemical transformations or kinetic pathways using conventional spectrophotometric techniques. To our knowledge, to date Raman spectroscopy has not been adapted to detect the rate of dye penetration throughout anodised coatings. The aim of this study was to investigate the potential of Raman spectroscopy for detection of the dye penetration rate in fully anodised aluminium foils.

Experimental

Materials

Sheets (0.8 mm thickness) of alloys 1050A and 6082 (Aleris Rolled Products, Germany) were used for anodisation and demonstrated 99.60% purity (0.34% iron, 0.1% silicon and 0.01% manganese) and 96.72% purity (0.54% iron, 1.1% silicon, 0.61% manganese and 1.02% magnesium), respectively. Aluminium foil of 50 μm thickness (made in Russia) demonstrated 99.95% purity (0.03% iron and 0.02% silicon). Reagent grade salts and electrolytes were employed for anodisation and laboratory grade solvents were used for cleaning and degreasing. The dyeing process was carried out with commercially available Sanodal Deep Black MLW and Sanodure Green LWN (Clariant, Switzerland) anionic dyes. Note that from now on they will be referred to as the "black dye" and "green dye", respectively. Both dyes were dissolved in deionised water with a concentration of 2 g/l; they represent widespread organic dyestuff compounds bearing the chromium-complexed azo moiety Cr (R-N=N-R')$_2$, typically with derivatised ortho-phenol substituents, in order to assemble colour-producing conjugated chains and one or more anionic functional groups ($-SO_3H$, $-Cl$, $-COOH$, etc.) for better hydrophilicity, adsorption, and other properties.

Procedure

The anodisation was performed in a sulphuric acid/oxalic acid electrolyte. This type of electrolyte is widely used to produce relatively thick aluminium oxide coatings [16,17], so the previously reported solutions and procedures were used as the basis in this study. Before anodisation, the disc-shaped specimens of 1.5 cm diameter were etched in an alkaline solution of 30 g/l sodium hydroxide + 25 g/l sodium phosphate + 75 g/l sodium carbonate for 30 s at 60 °C. After rinsing in deionised water, the specimens were cleaned for 1–2 min in 10% nitric acid then rinsed with water again. Next, the discs were placed into a continuously mixed electrolyte of 175 g/l sulphuric acid (H_2SO_4) + 30 g/l oxalic acid [$(COOH)_2{\cdot}2H_2O$] + 55.5 g/l aluminium sulphate [$Al_2(SO_4)_3{\cdot}18H_2O$] at 15 °C and 200 A/m² anodic current density for 70 min. The thickness of the anodic aluminium oxide layer was measured with a CM-8825FN device (Guangzhou Landtek Instruments Co., China). After anodising, the discs were immersed in a 170 W ultrasonic bath (VTUSC3, Velleman, Belgium) and sonicated at full power for 10–20 min in deionised water below 20 °C. Then the discs were dried at 60 °C for 60 min and stored in a dry environment for one to seven days for further experiments.

A template of evenly distributed pores, which extend continuously throughout anodised aluminium, may be made in one of three ways: (i) the anodised aluminium coating can be separated from the remaining metallic aluminium by dissolution of the latter. After the anodisation, the remaining aluminium substrate can be dissolved in a copper chloride-based solution [100 ml hydrochloric acid (HCl) (38%) + 100 ml water (H_2O) + 3.4 g copper chloride ($CuCl_2{\cdot}2H_2O$)] at 15 °C for *ca*. 2 h [18]. Excess metallic aluminium can be removed from the film using a saturated solution of iodine in methanol [19], or after the formation of pore arrays by anodisation then the anodised aluminium coating can be peeled off the aluminium substrate using a saturated mercuric chloride ($HgCl_2$) solution for *ca*. 30 min [20]; (ii) anodised aluminium coating can be electrochemically delaminated from the metallic substrate (known as the shock method) [21]; or (iii) aluminium foil can be anodised until all the aluminium turns into aluminium oxide [22]. Each of these methods has its own disadvantages. Of the three options described above, we have chosen the last one (iii).

Aluminium foil (99.95% pure and 50 μm thick) mounted in a special holder was anodised until the anodising current dropped to 0. It is apparent [23] that an aluminium oxide template consisting of two aluminium oxide layers (barrier and porous) was formed from the aluminium foil. It is known [23] that the barrier layer should comprise less than 0.08 μm, while the porous moiety grows throughout the rest of the foil volume due to electrochemical oxidation [24]. Caution was exercised to avoid complete destruction of the barrier layer, because this layer must remain intact to assure mechanical integrity of the anodised template. Thus, having measured the overall thickness of the aluminium oxide template by using a vertical optimeter with a ± 1 μm measurement error, we determined that the thickness of our template was equal to 70 ± 1 μm and 68 ± 1 μm for the foils anodised at 15 and 30 °C, respectively.

Characterisation

Scanning electron microscopy (SEM) images were obtained using a dual beam system (Helios NanoLab 650, FEI, The Netherlands) with a Schottky type field emission electron source and a gallium ion source at 1500× and 150 000×

magnification. To obtain the necessary electrical conductivity on the surface, nano-thin layers of chromium were applied to all specimens using a magnetron sputtering device (Quorum Q150T ES, Judges Scientific, UK), which resulted in a chromium layer thickness of 1.5–2.0 nm.

SEM images were used to determine the pore diameter, distribution and surface porosity. The number of pores was established by calculating the pores in 0.2 × 0.2 μm segments of the surface in three to four random areas to obtain the average pore density. Porosity was calculated using the equation described previously [25].

The Raman spectroscopy method was used to obtain the penetration rate of dye through anodised aluminium foil. Raman spectra were recorded with an Echelle type spectrometer (RamanFlex 400, PerkinElmer, USA) equipped with a thermoelectrically cooled charge coupled device detector and a fibre optic cable for excitation and collection of the spectra. A diode laser with a 785 nm beam was used as the excitation source. The laser beam was initially focused on a 200 μm diameter spot on the surface of the anodised coating; the laser power was 30 mW. For all specimens, photoluminescence (PL) scans were recorded to establish the feasibility of Raman spectra collection. For fully anodised foil specimens, the laser beam from the bottom was directed upwards into the barrier layer, which was sufficiently transparent for the scattered light spectra to be collected in the detector at the same location as the laser source. Then the aluminium foil holder was carefully moved towards the laser while monitoring the instant PL values. The maximum PL was attained at the point of highest aluminium oxide abundance, indicating that the beam's focus included the entire barrier layer. This focus position was retained until each spectrum was recorded, with an accumulation of three scans at an integration time of 10 s. All spectra were divided by the total accumulation time followed by subtraction of background fluorescence. The polystyrene standard (ASTM E1840) spectrum was used to calibrate Raman frequencies. Grams/AI 8 software from Galactic Industries (USA) was used for recorded spectra analysis. The experiments were carried out at room temperature.

Results and Discussion

Structural aspects of anodised specimens

The theoretical volume expansion factor of the porous oxide layer is 1.6 when the formation current efficiency is 100%. However, the laboratory results are lower than the theoretical value; the experimental expansion factor can range from 0.8 to 1.6. This variation results from varying anodising parameters such as a lower current efficiency [24]. Figure 1 shows SEM images of fully anodised aluminium foil: cross-section (a) and areas with magnification from the top to bottom side (b–d). This confirms the expectation that pores are distributed throughout the fully anodised foil. No significant differences in pore distribution, density, thickness or other properties could be observed when comparing the segments from the top, centre and bottom cross-sectional portions.

SEM micrographs of the surfaces of aluminium discs 1050A, 6082 and anodised foil are presented in Figure 2. They demonstrate that the alloys, after being anodised to a

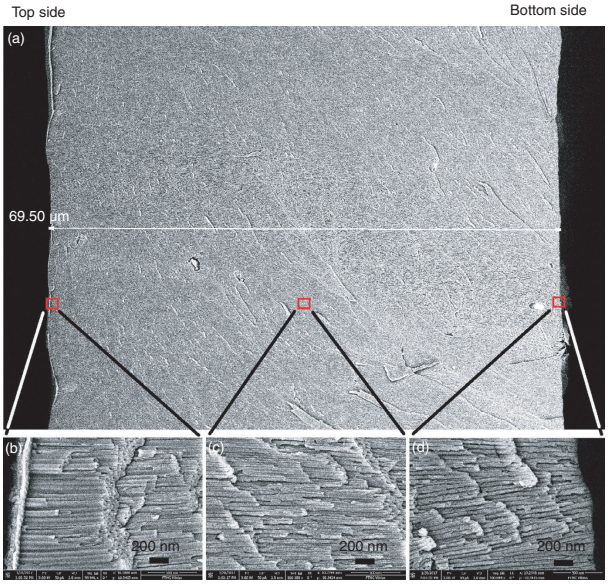

Figure 1 Scanning electron microscopy images of the cross-section of fully anodised foil: (a) the full cross-sectional view of the fully anodised foil; (b–d) magnified images of the pores in various cross-sectional spots. The foil was anodised at 15 °C [Colour figure can be viewed at wileyonlinelibrary.com]

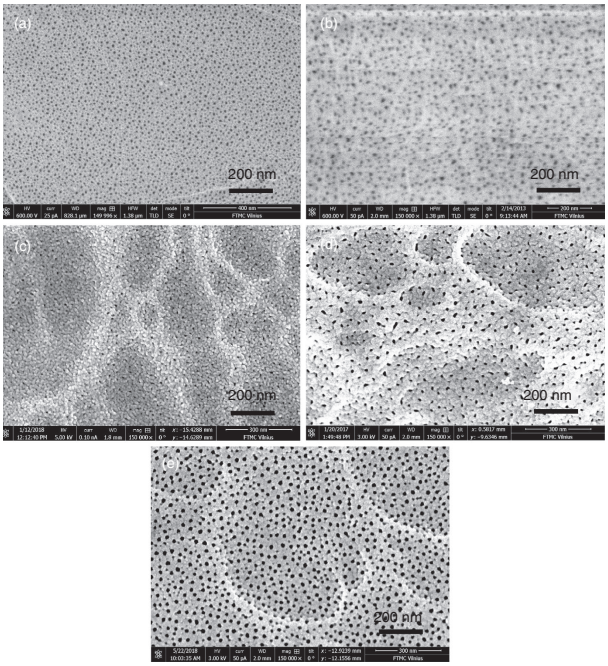

Figure 2 Scanning electron microscopy images of surfaces of partially and fully anodised aluminium specimens. Partial anodisation at 15 °C: (a) 1050A disc, (b) 6082 disc, and (c) foil. Fully anodised foils at (d) 15 °C and (e) 30 °C

Table 1 Characteristics of surface pores obtained after anodisation

Alloy; anodisation conditions	Anodic layer thickness, μm	Pore diameter, nm	Pore density, pores μm^{-2}	Porosity, %
1050A; partial at 15 °C	60 ± 1.0	6.5 ± 1.3	1560 ± 110	5.5
6082; partial at 15 °C	60 ± 1.4	15.0 ± 2.2	1040 ± 121	22.5
Aluminium foil; partial at 15 °C	20 ± 1.1	7.6 ± 2.9	1207 ± 39	5.8
Aluminium foil; full at 15 °C	70 ± 1.0	13.2 ± 2.1	530 ± 34	7.8
Aluminium foil; full at 30 °C	68 ± 1.0	15.9 ± 2.5	770 ± 39	18.0

depth of 60 μm, produce pores that differ in diameter (Figure 2a,b). Pore diameter is larger in the 6082 alloy despite its lower purity (Table 1).

Comparison of 1050A discs and aluminium foil after partial anodisation (Figure 2a,c) shows that their pore diameters are rather close at 7.6 nm and 6.5 nm, respectively (Table 1). This agrees well with the relatively high purity (over 99.5%) of both aluminium foil and 1050A discs in contrast to 6082 discs of only 96% purity, whose pores have a much larger diameter at 15 nm. When varying the anodisation temperature, it is known [26] that this leads to wider pores because of more intensive chemical dissolution of aluminium oxide in the anodising electrolyte. Our data demonstrate a similar tendency (Figure 2d,e). Meanwhile, the pore diameter of the fully anodised aluminium foil (Figure 2d) is greater than that of the partially anodised aluminium foil (Figure 2c), at 13.2 and 7.6 nm, respectively. When anodisation approaches nearly hollow pores in the aluminium foil, its ohmic resistance begins to increase rapidly and leads to higher spot temperatures within the pores. This accelerates the dissolution of aluminium oxide, resulting in larger pore diameters.

In general, the structural investigations showed that properties of obtained coatings and templates were in good agreement with the findings of other researchers. Variation of alloys and anodisation conditions produced pore diameters within the range of 6.5 to nearly 16 nm, with some diversity in porosity values and anodic layer thickness. These alloys and properties represent typical coatings in the aluminium anodising industry, because industrial coatings often contain pores of 5–20 nm in diameter, which assure good paint adsorption but are still narrow enough to be easily sealed in boiling water.

Spectroscopic observations of undyed surfaces

The laser of the Raman spectrometer was directed from the bottom upwards into the anodised aluminium template (Figure 3), which was mounted within a holder horizontally, that is, exposing the side with the barrier layer to the laser beam (Figure 3a). This barrier layer prevents the template from collapse, but because of its thinness it does not interrupt the laser beam completely, allowing it to focus inside fully anodised aluminium pores. The Raman spectrometer fibre optic cable position was changed in the XYZ directions according to the location of the template surface. The laser beam was focused inside the template using the Z direction by a PL maximum of 785 nm for the aluminium oxide.

Fully anodised aluminium foils were used to obtain the penetration rates of commercially available dyes. To establish whether the assembled Raman spectroscopy setup is suitable to analyse the anodised foils, Raman spectra from different anodised aluminium surfaces were recorded (Figure 4).

From previous studies, it is known that the PL of anodised aluminium oxide depends on acid electrolyte, anodisation voltage, pore diameter, anodisation regime, thermal treatment and other processing parameters [27–29]. It was observed that PL intensities of anodised aluminium, which was prepared in the oxalic acid electrolyte, are higher than the PL intensities of the one anodised in sulphuric or phosphoric acid [28]. For Raman scattering, which is the basis of Raman spectroscopy, PL is not beneficial. It was observed (Figure 4) when using a 785 nm laser source that the PL effect from anodised

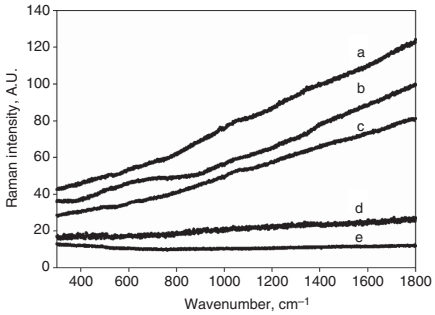

Figure 4 Raman spectra in the 'fingerprint' region of anodised aluminium: (a) partially anodised 1050A discs; (b) partially anodised 6082 discs; (c) partially anodised foil; (d) fully anodised foil; and (e) plain aluminium foil before anodisation

aluminium depends on alloy composition, anodisation extent, voltage, current density, pore sizes, electrolyte temperature, concentration and possibly other factors. It turned out that in the fully anodised foil the PL effect was negligible and similar to that of non-anodised foil (Figure 4d,e).

Characterisation of dyes

Two types of commercially available chromium-complexed anionic azodyes (black and green) were chosen for the detection of penetration rates through fully anodised aluminium foils. The composition of the dyes was confidential;

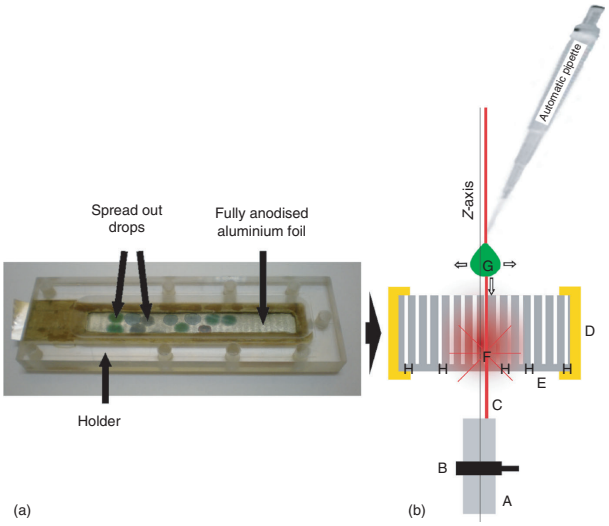

Figure 3 (a) Real image of the template (i.e. fully anodised aluminium foil) in the holder after dye was dropped onto it and Raman spectroscopy measurements were carried out; and (b) principal scheme of Raman spectroscopy measurements: A = fibre optic cable for working distance of 7 mm; B = holder, which shifts along the Z axis; C = 785 nm laser beam; D = holder with fixed position; E = the template, i.e. fully anodised aluminium foil of 70 μm thickness; F = approximate focus position of the laser beam; G = dye drop, with arrows showing overspread directions; H = barrier layer (*ca*. 10–20 nm) of anodised part of aluminium foil. Not to scale [Colour figure can be viewed at wileyonlinelibrary.com]

however, it might be reasonable to assume that they contained some variations of the most prevalent chromium-complexed azo moiety in commercial dyestuffs (Figure 5).

The substituents in the moiety are crucial for defining the colour, adsorption, hydrophilicity, degradation stability and the variety of other properties, which are important for commercial dyes. It should be noted that the dyes are unlikely to contain just one dominating molecular structure or packing shape, or even a particular dominating molecular size. It is more probable that dye formulations contain a number of molecular derivatives, which address a broad variation of target substrates. The dyes can be used on various anodised aluminium surfaces of different alloys, pore sizes and densities, under differing anodisation conditions and with other parameters. Some dye molecules are more effective in one type of anodised surface, while others are more effective in another. Furthermore, dye formulations can be fortified with additives to enhance their lightfastness, glossiness, adsorption, penetration properties, degradation stability, curing durations, wetting, spreading, shelf life, antibacterial and antifungal performance and possibly other characteristics. Therefore, exact chemical mechanisms describing the dye adsorption on anodised aluminium might be complex and diverse.

Nevertheless, some general trends of azodye interactions with the pores of anodised aluminium can still be established. The molecular size of the chromium-complexed anionic azo moiety should not exceed 3 nm, which is smaller than the pore diameters of anodised surfaces investigated in this study. After penetrating into the pore, the moiety is exposed to aluminum hydroxides, which are formed during anodisation in aqueous electrolyte. Sulphonates and other anionic functional groups of the dye moiety can interact with aluminium cations from the hydroxides, which are partially bound to the aluminium oxide within the anodised coating. Consequently, the dye molecules can form ionic bonds on the walls of the pores. However, several uncertainties cannot be answered without experimental investigations. The size of dye molecules can be too large to penetrate into the pores. The availability of aluminium cations can be limited within the pores due to residual acidic electrolyte. The reactivity of anionic functional groups within the dye molecule towards the cations can be too high, which would result in blockage of the pore openings. Inversely, the reactivity can be too low, resulting in dye migration out of the pores. Therefore, the measurement of penetration rates would be useful in evaluating the suitability of the selected dye for given surfaces and conditions.

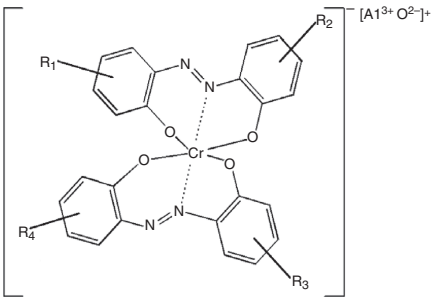

Figure 5 Molecular structure of the one of the most prevalent chromium-complexed azo moieties in commercial dyestuffs after adsorption within the pore of anodised aluminium. R_1 to R_4 represent a variety of substituents, ranging from halogens, anionic functional groups, alkyls, and other types of hydrophobic or hydrophilic chains

As is evident from the molecular structure, chromium-complexed anionic azodyes contain a lot of aromatic rings and some double bonds. The abundance of π electrons is very favourable for Raman spectroscopy, which is sensitive to such compounds. For investigation we chose the most intensive vibrational modes of each dye: 1285 cm^{-1} for black dye and 1264 cm^{-1} for green dye. Those two modes can be assigned to a CN functional group: 1285 cm^{-1} endocyclic and 1264 cm^{-1} exocyclic (Figure 6) [30]. High intensity of those vibrational modes is helpful for reducing the error values in spectra analyses.

Measurement of dye penetration rates

The volume of 5 μl of anionic dye was selected to avoid excessive overfilling of aluminium pores. The dye droplet was deposited onto the anodised foil and a number of Raman spectra were collected periodically within 1 h or less. Before the droplet deposition, a laser beam was focused within the inside of anodised aluminium pores from the bottom, according to the intensity of the background PL value. For kinetic curve construction from each Raman spectra the first spectrum, which was collected 30 s later from the droplet deposition, was subtracted to eliminate the vibrational modes of dye interactions with the environment on top of the aluminium foil. The results are shown in Figure 7.

On the aluminium foils, which were anodised at 15 °C, both dyes achieve the maximum Raman peak intensity within 25 min of drop deposition (Figure 7a,b). This duration appears to relate to the time required for the dye molecules to penetrate the anodised aluminium foil completely. The black dye curve gradually increases and reaches a plateau after 25 min. The green dye curve has a sharper growth and might show a period of delay at the beginning. Once it reaches its maximum value after 25 min it shows a slight tendency to decline, although this is not statistically significant. In addition, the green dye was partly washed out from the pores of anodised aluminium during the dyeing procedure. Also, it was observed that after 25 min the most intensive vibrational modes of each dye showed a small but distinct shift to lower frequencies. For black dye the shift registered was from 1285 to 1282 cm^{-1} and for the green dye it was from 1265 to 1263.6 cm^{-1}. Changes in these frequencies appear to be related to the interactions of the dye functional groups with the pores of anodised aluminium foil. Larger shifts suggest stronger interactions. Consequently, the black dye interacts with anodised aluminium foil more strongly than the green dye.

When aluminium foil was anodised at 30 °C, larger pore sizes were obtained. This led to respectively higher dye penetration rates through the anodised foils (Figure 7c,d).

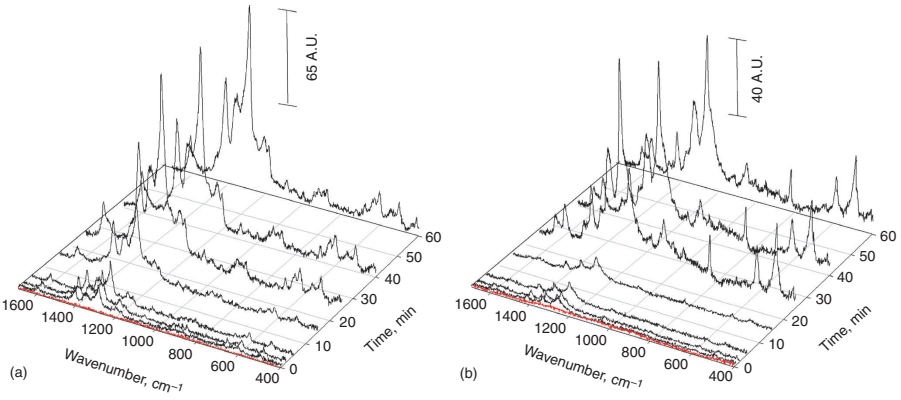

Figure 6 Raman spectra variations over time after 5 µl of each dye was dropped onto the fully anodised aluminium foil surface at 15 °C: (a) black dye and (b) green dye [Colour figure can be viewed at wileyonlinelibrary.com]

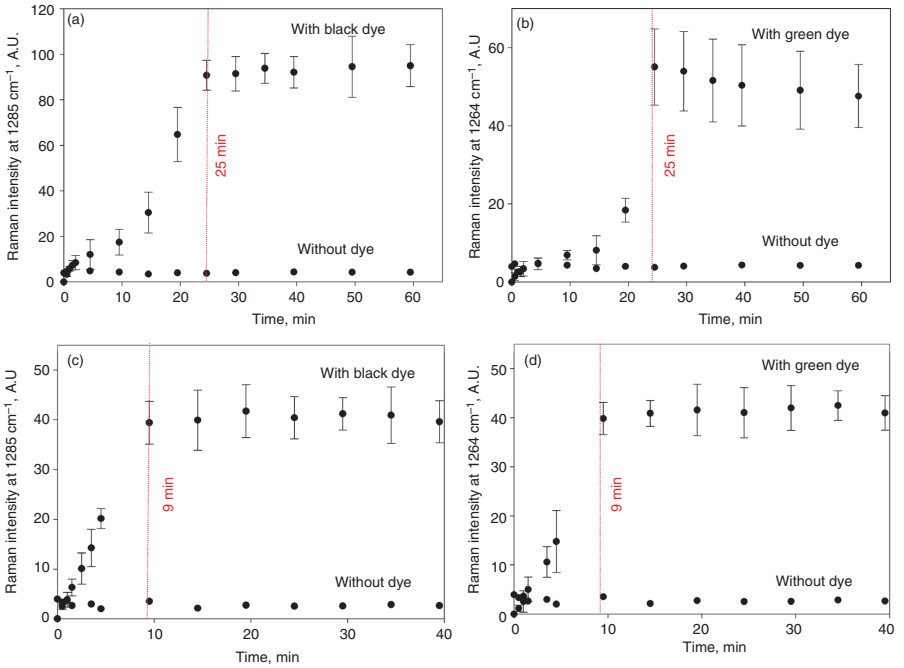

Figure 7 Penetration rate of two different dyes throughout fully anodised aluminium foil: (a) black dye and (b) green dye when aluminium foil was anodised at 15 °C; (c) black dye and (d) green dye when aluminium foil was anodised at 30 °C [Colour figure can be viewed at wileyonlinelibrary.com]

These tendencies agree well with the established values for pore diameter, density and porosity (Table 1).

It is known [23] that aluminium dyeing is carried out with anionic dyes, which react with the ionic sites within the pores of the anodised coating. Carboxylic acid moiety may even induce the formation of self-assembling nanostructures on aluminium hydroxides [31]. In the pores of anodised coating, the adsorption patterns of chromium-complexed anionic azodyes might be even more complex. Furthermore, the abundance of residual electrolyte, oxygen,

electrochemical triggers UV exposure, biocontamination and possibly other factors may induce rapid chemical degradation [32]. An understanding of the chemistry of the process must be based on knowledge of the ionising properties of the surface, and also an understanding of how they are influenced by the nature of the solution with which they are in contact. The anion, whether covalently bound or ionised, may be replaced by dye anions, and it is this reaction that is the basis of the aluminium oxide dyeing process.

On the other hand, it is known that the formation of an aluminium oxide coating may contain a considerable number of impurities, whose quantity depends on the nature of the electrolyte. For example [33,34], anodised coatings formed in sulphuric acid contain up to 17% sulphates. Those formed in phosphoric acid might contain 6% phosphates, while those formed in oxalic acid might contain up to 3% oxalates [35]. By contrast, the content of chromate in the coating that was anodised in chromic acid constitutes only 0.2%. Consequently, the behaviour of the Raman curve may be explained by the dye interactions with the sulphates and oxalates remaining in the pores of aluminium oxide.

These trends are also likely to hold for other dyes, not only chromium-complexed anionic azo-compounds. Dyestuffs frequently have molecules with many π-electrons, which result in vibrational modes of high intensity in Raman spectroscopy. Changes in their intensity or frequency can be monitored, just as in the case of chromium-complexed azo-compounds. Therefore, when new dye formulations are considered, the utilisation of Raman spectroscopy with anodised aluminium foil can be a valuable tool for assessing dye efficiency.

Conclusions

Three different aluminium alloys were anodised, characterised by SEM, and their PL values were established. Anodised coatings on alloy discs show high PL values, which have a negative effect on Raman scattering. Fully anodised aluminum foil has weak PL, making it possible to determine the penetration rate of commercially available anionic azo dyes throughout fully anodised coating. A new method was developed to focus the laser beam inside the coating and to record individual vibrational modes of each dye in Raman spectroscopy, which were then used to determine the penetration rate and assess the behaviour of each dye. The high intensity of those vibrational modes was helpful for reducing the error values in spectra analyses. The major Raman frequency shift of vibrational mode during dye penetration throughout aluminum foil indicated stronger interactions of certain functional groups of the dye molecules with the anodised coating. Black dye showed a higher frequency shift of the C-N vibrational mode than green dye. When aluminium foil was anodised at higher temperature, the penetration rate was 2.8 times higher than in the foil anodised at lower temperature, because of different pore diameter, pore density and porosity, as well as possible other factors. This method can be applied for evaluating the suitability of newly synthesised or formulated organic dyes for aluminium surfaces and coatings.

References

1. F Keller, M S Hunter and D L Robinson, *J. Electrochem. Soc.*, **100** (1953) 411.
2. O Jessensky, F Müller and U Gösele, *J. Appl. Phys.*, **72** (1998) 1173.
3. J R Davis, *Aluminum and Aluminum Alloys* (Ohio: ASM International, 1993) 296.
4. N Tsynsaru, *Chemistry*, **27** (2016) 17.
5. N Hu, X Dong, X He, J F Browning and D W Schaefer, *Corros. Sci.*, **97** (2015) 17.
6. H J Gõhausen, *Trans. IMF*, **60** (1982) 74.
7. R C Furneaux and G C Wood, *Trans. IMF*, **60** (1982) 14.
8. N Mathew, *J4R*, **2** (2016) 5.
9. A X Wang and X Kong, *Materials*, **8** (2015) 3024.
10. P Gao, D Gosztola, L-W H Leung and M J Weaver, *J. Electroanal. Chem. Interfacial Electrochem.*, **233** (1987) 211.
11. A Kudelski and J Bukowska, *Vibrat. Spectrosc.*, **10** (1996) 335.
12. G Niaura and A Malinauskas, *Chem. Phys. Lett.*, **207** (1993) 455.
13. X Kong, Q Yu, X Zhang, X Du, H Gong and H Jiang, *J. Mater. Chem.*, **22** (2012) 7767.
14. K C Grabar, R G Freeman, M B Hommer and M J Natan, *Anal. Chem.*, **67** (1995) 735.
15. K Wong-ek, P Eiamchai, M Horprathum, V Patthanasettakul, P Limnonthakul, P Chindaudom and N Nuntawong, *Thin Solid Films*, **518** (2010) 7128.
16. W Bensalah, K Elleuch, M Feki, M Wery and H F Ayedi, *Surf. Coat. Technol.*, **201** (2007) 7855.
17. M A Kashi, A Ramazani, M Rahmandoust and M Noormohammadi, *J. Phys. D: Appl. Phys.*, **40** (2007) 4625.
18. T T Xu, R D Piner and R S Ruoff, *Langmuir*, **19** (2003) 1443.
19. A Kirchner, K J D MacKenzie, I W M Brown, T Kemmitt and M E Bowden, *J. Membr. Sci.*, **287** (2007) 264.
20. X Chang, S Wang, H Luo and G Gong, *J. Fluoresc.*, **13** (2003) 421.
21. H L Lira and R Paterson, *J. Membr. Sci.*, **206** (2002) 375.
22. H Lv, Y Song, L Cao, C Yang, H Xiao and S Zhang, *J. Alloys Compd.*, **614** (2014) 182.
23. C H Giles, *Rev. Prog. Coloration*, **5** (1974) 49.
24. F Li, L Zhang and R M Metzger, *Chem. Mater.*, **10** (1998) 2470.
25. T Matijošius, A Ručinskienė, A Selskis, G Stalnionis, K Leinartas and S J Asadauskas, *Surf. Coat. Technol.*, **307** (2016) 610.
26. T Aerts, T H Dimogerontakis, I De Graeve, J Fransaer and H Terryn, *Surf. Coat. Technol.*, **201** (2007) 7310.
27. S Stojadinovic, Z Nedic, I Belca, R Vasilic, B Kasalica, M Petkovic and L J Zekovic, *Appl. Surf. Sci.*, **256** (2009) 763.
28. N I Mukhurov, S P Zhvavyi, S N Terekhov, A Y Panarin, I F Kotova, P P Pershukevich, I A Khodasevich, I V Gasenkova and V A Orlovich, *J. Appl. Spectrosc.*, **75** (2008) 214.
29. A Santos, M Alba, M M Rahman, P Formentín, J Ferré-Borrull, J Pallarès and L F Marsal, *Nanoscale Res. Lett.*, **7** (2012) 228.
30. M Mathlouthi, A M Seuvre and J L Koenig, *Carbohydr. Res.*, **146** (1986) 1.
31. I Liascukiene, M Steffenhagen, S J Asadauskas, J F Lambert and J Landoulsi, *Langmuir*, **30** (2014) 5797.
32. S Asadauskas, A Grigucevičienė, K Leinartas and D Bražinskienė, *Tribol. Int.*, **44** (2011) 557.
33. Y Goueffon, L Arurault, C Mabru, C Tonon and P Guigue, *J. Mater. Process. Technol.*, **209** (2009) 5145.
34. I Mínguez-Bacho, S Rodríguez-López, A Climent-Font, D Fichou, M Vázquez and M Hernández-Vélez, *Microporous Mesoporous Mater.*, **225** (2016) 192.
35. S Tajima, N Baba, K Shimazu and I Mizuki, *Electrocomp. Sci. Technol.*, **3** (1976) 91.

NOTES

Vilniaus universiteto leidykla
Saulėtekio al. 9, III rūmai, LT-10222 Vilnius
El. p. info@leidykla.vu.lt,
www.leidykla.vu.lt
Tiražas 16 egz.